AGARD-AG-160-VOL.15

AGARD-AG-160-VOL.15

AD A123249

AGARDograph No. 160

AGARD Flight Test Instrumentation Series

Volume 15

on

Gyroscopic Instruments and their Application to Flight Testing

by

B. Stieler and H. Winter

DTIC ELECTE JAN 1 1 1983 S E

DTIC FILE COPY

DISTRIBUTION AND AVAILABILITY ON BACK COVER

This document has been approved for public release and sale; its distribution is unlimited.

83 01 12 076

AGARD-AG-160
Volume 15

NORTH ATLANTIC TREATY ORGANIZATION

ADVISORY GROUP FOR AEROSPACE RESEARCH AND DEVELOPMENT

(ORGANISATION DU TRAITE DE L'ATLANTIQUE NORD)

AGARDograph No.160 Vol.15

GYROSCOPIC INSTRUMENTS AND THEIR APPLICATION TO FLIGHT TESTING

by

B.Stieler and H.Winter

Volume 15

of the

AGARD FLIGHT TEST INSTRUMENTATION SERIES

Edited by

A.Pool and K.C.Sanderson

Accession For
NTIS GRA&I ☒
DTIC TAB ☐
Unannounced ☐
Justification
By
Distribution/
Availability Codes
Dist | Avail and/or Special
A

This AGARDograph has been sponsored by the Flight Mechanics Panel of AGARD.

THE MISSION OF AGARD

The mission of AGARD is to bring together the leading personalities of the NATO nations in the fields of science and technology relating to aerospace for the following purposes:

- Exchanging of scientific and technical information;
- Continuously stimulating advances in the aerospace sciences relevant to strengthening the common defence posture;
- Improving the co-operation among member nations in aerospace research and development;
- Providing scientific and technical advice and assistance to the North Atlantic Military Committee in the field of aerospace research and development;
- Rendering scientific and technical assistance, as requested, to other NATO bodies and to member nations in connection with research and development problems in the aerospace field;
- Providing assistance to member nations for the purpose of increasing their scientific and technical potential;
- Recommending effective ways for the member nations to use their research and development capabilities for the common benefit of the NATO community.

The highest authority within AGARD is the National Delegates Board consisting of officially appointed senior representatives from each member nation. The mission of AGARD is carried out through the Panels which are composed of experts appointed by the National Delegates, the Consultant and Exchange Programme and the Aerospace Applications Studies Programme. The results of AGARD work are reported to the member nations and the NATO Authorities through the AGARD series of publications of which this is one.

Participation in AGARD activities is by invitation only and is normally limited to citizens of the NATO nations.

The content of this publication has been reproduced directly from material supplied by AGARD or the authors.

Published September 1982

Copyright © AGARD 1982
All Rights Reserved

ISBN 92-835-1433-5

Printed by Technical Editing and Reproduction Ltd
5–11 Mortimer Street, London, W1N 7RH

PREFACE

Soon after its founding in 1952, the Advisory Group for Aerospace Research and Development recognized the need for a comprehensive publication on flight test techniques and the associated instrumentation. Under the direction of the AGARD Flight Test Panel (now the Flight Mechanics Panel), a Flight Test Manual was published in the years 1954 to 1956. The Manual was divided into four volumes: I. Performance, II. Stability and Control, III. Instrumentation Catalog, and IV. Instrumentation Systems.

Since then flight test instrumentation has developed rapidly in a broad field of sophisticated techniques. In view of this development the Flight Test Instrumentation Group (now the Flight Test Techniques Group) of the Flight Mechanics Panel was asked in 1968 to update Volumes III and IV of the Flight Test Manual. Upon the advice of the Group, the Panel decided that Volume III would not be continued and that Volume IV would be replaced by a series of separately published monographs on selected subjects of flight test instrumentation: the AGARD Flight Test Instrumentation Series. The first volume of the Series gives a general introduction to the basic principles of flight test instrumentation engineering and is composed from contributions by several specialized authors. Each of the other volumes provides a more detailed treatise by a specialist on a selected instrumentation subject. Mr W.D.Mace and Mr A.Pool were willing to accept the responsibility of editing the Series, and Prof. D.Bosman assisted them in editing the introductory volume. In 1975 Mr K.C.Sanderson succeeded Mr Mace as an editor. In 1981 Mr R.W.Borek, Sr., replaced Mr Sanderson. AGARD was fortunate in finding competent editors and authors willing to contribute their knowledge and to spend considerable time in the preparation of this Series.

Special thanks and appreciation are extended to Professor T. van Oosterom, The Netherlands. Professor van Oosterom chaired the Group from its inception in 1968 until 1976 and established many of the ground rules under which the Group still operates. The Group also appreciates the efforts of the late Mr N.O.Matthews, UK, who chaired the Group during 1977 and 1978.

It is hoped that this Series will satisfy the existing need for specialized documentation in the field of flight test instrumentation and as such may promote a better understanding between the flight test engineer and the instrumentation and data processing specialists. Such understanding is essential for the efficient design and execution of flight test programs.

The efforts of the Group members (J.Moreau and N.Lapchine CEV/FR, H.Bothe DFVLR/GE, J.T.M. van Doorn and A.Pool NLR/NE, E.J.Norris A&AFE/UK, and R.W.Borek, Sr. NASA/US) and the assistance of the Flight Mechanics Panel in the preparation of this Series are greatly appreciated. Credit is due to former Group Member Mr K.C.Sanderson, US, who served as an editor during the preparation of this volume.

F.N.STOLIKER
Member, Flight Mechanics Panel
Chairman, Flight Test
Techniques Group

ACKNOWLEDGEMENT

The authors wish to express their gratitude to the members of the Flight Test Instrumentation Group (FTIG) for their assistance and for many helpful suggestions which have been incorporated into this volume. They are especially grateful to Mr Norris (UK), Mr Pool (NL), Mr Sanderson (US), Mr Stoliker (US) and Mr Wilcock (UK). They also express their appreciation to their colleagues, especially to Dr Rodloff, for many valuable hints and discussions. Special thanks are due to Mrs Lübs and Mrs Thumser who carried out the work of typing this volume.

VOLUMES OF THE FLIGHT TEST INSTRUMENTATION SERIES

AGARDograph No.160

Volume

1 Basic Principles of Flight Test Instrumentation Engineering
by A.Pool and D.Bosman

2 In-Flight Temperature Measurements
by F.Trenkle and M.Reinhardt

3 The Measurement of Fuel Flow
by J.T.France

4 The Measurement of Engine Rotation Speed
by M.Vedrunes

5 Magnetic Recording of Flight Test Data
by G.E.Bennett

6 Open and Closed Loop Accelerometers
by I.McLaren

7 Strain Gauge Measurements on Aircraft
by E.Kottkamp, H.Wilhelm and D.Kohl

8 Linear and Angular Position Measurement of Aircraft Components
by J.C. van der Linden and H.A.Mensink

9 Aeroelastic Flight Test Techniques and Instrumentation
by J.W.G. van Nunen and G.Piazzoli

10 Helicopter Flight Test Instrumentation
by K.R.Ferrell

11 Pressure and Flow Measurement
by W.Wuest

12 Aircraft Flight Test Data Processing – A Review of the State of the Art
by L.J.Smith and N.O.Matthews

13 Practical Aspects of Instrumentation System Installation
by R.W.Borek

14 The Analysis of Random Data
by D.A.Williams

15 Gyroscopic Instruments and their Application to Flight Testing
by B.Stieler and H.Winter
(The present Volume)

It is intended to publish the following further volumes in the Series

Trajectory Measurement for Take off and Landing and Other Short-Range Applications

Flight Test Signal Conditioning

CONTENTS

	Page
SUMMARY	1
1. INTRODUCTION	1
2. PRINCIPLES AND PROBLEMS OF INERTIAL MEASUREMENTS	3
2.1 Measurement of Translational Motion	3
2.2 Measurement of Rotational Motion	9
2.3 Accuracy Limitations of Inertial Measurements	10
3. INERTIAL SENSORS	11
3.1 Gyroscopic Sensors and their Application	11
3.2 Basic Performance Equations and Error Sources Common to Mechanical Gyros	13
3.3 The Use of Single-Degree-of-Freedom (SDF) Gyros as Angular Rate Sensors and Stabilization Devices	34
3.4 The Use of Two-Degree-of-Freedom Gyros as Angular Rate Sensors and Stabilization Devices	44
3.5 Optical Gyros	59
3.6 Accelerometers	73
4. ACCURATE DIGITAL READOUT OF INERTIAL SENSORS	79
4.1 Introduction	79
4.2 Methods for Digitizing the Measurements of Inertial Sensors	79
4.3 Stochastic Errors of the Digitizing Methods for Mechanical Inertial Sensors and Comparison with the Stochastic Errors of Laser Gyros	84
4.4 Review of Rules for Sampling Data	86
5. GYROS AS STABILIZATION DEVICES	89
5.1 Direct Gyroscopic Stabilization	89
5.2 Gyroscopic Stabilization by Means of Servo-Loops	91
5.3 Three-Gimbal Platforms	95
5.4 Four-Gimbal Platforms	97
6. ATTITUDE AND HEADING REFERENCES	99
6.1 Vertical Gyro	99
6.2 Directional Gyro	102
6.3 Gimballed Attitude and Heading Reference Systems	104
6.4 Attitude and Heading Platforms	107
6.5 Strapdown Attitude and Heading Reference Systems	107
7. INERTIAL NAVIGATION	110
7.1 Introduction	110
7.2 Mechanization of an Inertial Navigation System with its Sensors Pointing North, East and Down - the North Indicating System	111
7.3 The Error Dynamics of the North Indicating System	114
7.4 Other Mechanizations of Inertial Systems	130
7.4.1 Navigation Based on Inertial Measurements in the Wander Azimuth Coordinate Frame	130
7.4.2 Navigation Based on Inertial Measurements in the Pseudo-Pole Coordinate Frame	134
7.4.3 Navigation Based on Inertial Measurements in the Space-Stabilized Coordinate Frame	137
7.4.4 Navigation Based on Inertial Measurements in the Body-Fixed Coordinate Frame (Strapdown Systems)	138
7.5 The Linearized Error Dynamics of Inertial Navigation Systems	154
7.6 Self-Alignment of Platform and Strapdown Systems	155
7.7 Summary and Overview of Existing Inertial Navigation Systems	162
8. HYBRID INSTRUMENTATION SYSTEMS AND THEIR APPLICATION TO FLIGHT TESTING OF ON-BOARD AND GROUND EQUIPMENT	166
8.1 Models for the Sensor Errors	166
8.2 Filtering Procedures	168
8.2.1 Conventional (analog) Filtering	168
8.2.2 Kalman Filtering	171
8.2.3 Optimal Smoothing	171
8.3 Examples of Hybrid Systems	172
8.3.1 Hybrid Reference System for the Testing of a Microwave Landing System	172
8.3.2 Hybrid Reference System for the Flight Testing of a Doppler Navigation System	179

	Page
9. APPLICATION OF GYROSCOPIC INSTRUMENTS TO FLIGHT TESTING OF AIRCRAFT	185
9.1 Requirements for the Gyroscopic Instruments	185
9.2 Conventional Instrumentation Systems	193
9.3 Instrumentation System Using an Inertial Platform	194
9.4 Examples of Modern Instrumentation Systems	195
9.5 Future Trends	200

Since this volume was prepared, AGARDograph 254 "Advances in Inertial Navigation Systems and Components", edited by H. Sorg, has been printed and distributed. This volume does not include specific references to AGARDograph 254, but it is a valuable reference, particularly for NMR gyros (page 13), modern flexible joints for DTGs (page 55), comparative discussion of optical gyros (page 59), computation of error terms in 7.4.2 (page 151) and the problem of transfer-alignment from a master to a slave system in 7.6.1 (page 155).

LIST OF SYMBOLS

a $[m/s^2]$	sum of all forces per unit mass, Eqs. (2.1), (2.3) and Fig. 2.3
A $[m^2]$	area enclosed by light beams in an optical gyro
A_{ij}	cofactor of a matrix, Section 7.4.4.3.1
$\underline{A}$	accelerometer triad in Figs. 7.3.1/7.4.2/7.4.3/7.4.6
ADC	analog-to-digital converter
AHRS	attitude and heading reference system
b [m]	pivot diameter in SDF gyro gimbal bearing, Fig. 3.2.9
B $[m/s^2]$	accelerometer error, Chapter 3.7
$\underline{c}$ $[m/s^2]$	Coriolis acceleration vector, Chapter 7
c [m/s]	$= 3 \times 10^8$, speed of light in vacuum
c^m [m/s]	speed of light in medium, Eq. (3.5.10)
c [m]	length of the gimbal in SDF gyro, Fig. 3.2.9
C $\left[\frac{N\text{-}m}{rad/s}\right]$	viscous damping ratio, Eqs. (3.2.34), (3.3.2), (3.3.11), (5.2.2), (5.2.10)
$\underline{C}_{ij}$	matrix to transform vector from coordinate frame j into i
CEP	circular error probable, Section 7.3.4
d	drift coefficient of a gyro marked by subscript and superscript, e.g. d^g_I = unbalance drift due to g-load in direction I, Tables 3.2.1 and 3.2.2
d [m]	diameter of light beam, Eq. (3.5.12)
d [m]	length of laser tube, Eq. (3.5.11)
D [rad]	deviation of the normal, Eq. (2.11)
D [rad/s]	total gyro drift; if marked with superscript a subset of the total gyro drift, e.g. D^M = drift due to mass unbalance
D' [rad/s]	total gyro drift derived in Section 3.2.2
DG	directional gyroscope
DTG	dynamically tuned gyro
e	eccentricity of the earth's reference ellipsoid, Eq. (2.9)
E [ ]	expected value, Fig. 7.3.8
ERU	earth rate unit = 15 °/h
f $[m/s^2]$	specific force, Eq. (2.3) and Fig. 2.3
f [Hz]	frequency
f	flattening of the earth's reference ellipsoid, Eq. (2.8)
F, F(s) [N-m/rad]	control loop transfer function, Chapters 3, 4, 5
F', F'(s) [A/rad]	control loop transfer function = F/S^t, Chapters 3, 4, 5
$\underline{F}$	system matrix, Eq. (7.3.4)
F [N]	force, Fig. 3.2.9
F_m	DTG figure of merit, Eq.(3.4.35)
FGP	four-gimbal platform, Section 5.4
FRG	free rotor gyro
FFLG	form frequency laser gyro, Section 3.5.3.5
g $[m/s^2]$	gravity, Eq. (2.28)

g' [m/s^2]	negative specific force, Eq. (2.3)
G, $G(s)$ [rad/N-m]	gyro transfer function in the platform environment, Eqs. (3.3.12), (3.3.20), (3.4.4)
G', $G'(s)$ [rad/N-m]	gyro transfer function in the strapdown environment, Eqs. (3.3.15), (3.4.18)
G'', $G''(s)$ [rad/N-m]	TDF gyro transfer function without damping, Eqs. (3.4.5), (5.1.3)
G [m/s^2]	gravitation, Eq. (2.3)
$\underline{G}$	driving function matrix, Eq. (7.3.4)
h	hour
h	altitude above earth's reference ellipsoid, Fig. 2.1b
H [N-m-s]	angular momentum, Eqs. (2.38), (2.41), (3.2.4) to (3.2.6)
H [Gauss]	magnetic field intensity, Section 3.5.4
i [A]	current
I [kg-m^2]	moment of inertia of gyro rotor about spin axis
$\underline{I}$	unity matrix, Eq. (3.2.10)
$\hat{\underline{I}}$	skew symmetric unity matrix, Eq. (3.2.10)
INS	inertial navigation system
IMU	inertial measurement unit
J [kg-m^2]	moment of inertia
$\underline{J}$ [kg-m^2]	moment of inertia tensor, Eq. (2.39)
K [m/N]	structural compliance in a mechanical gyro, Eq. (3.2.30)
K [N-m/rad]	torsional spring coefficient, Eqs. (3.3.34), (3.3.2), (3.4.32)
K [N-m/rad]	servo loop gain, Chapters 5, 6
K	dummy integer, Eq. (7.3.28)
L [m]	length of light beams, perimeter of optical gyro, Section 3.5
Δl [m]	apparent difference in the length of the optical path in a RLG, Section 3.5.2.2
LSB	least significant bit, Chapter 4
m [kg]	mass, Chapter 3
m	dummy integer, Chapter 4
M [N-m]	torque, Eqs. (2.37), (3.2.1), (5.3.2)
MTBF [h]	mean time between failure
n [rad/s]	spin rate of gyro rotor, Chapters 3 and 5
n	refraction index, Section 3.5
n	integer, number of bits, Chapter 4
N	number of pulses of a RLG, Eq. (3.5.8)
$N(m, \sigma^2)$	Gaussian distribution with mean value m and standard deviation σ, Chapter 7
$N(q)$	norm of quaternion, Eq. (7.4.34)
NIS	north indicating system, Chapter 7
OG	optical gyro, Section 3.5
ORS	optical rate sensor, Section 3.5
$p = \frac{d}{dt}$	time derivative operator, Eq. (3.2.25), Fig. 3.4.7

$p(x)$	probability density, Fig. 7.3.6
$\underline{P}$	covariance matrix, Eq. (7.3.10)
P	platform, Fig. 7.3.1
ΔP [V-s]	voltage pulse, Chapter 4
PRL	pulse rebalance loop, Chapter 4
$\underline{q}'$	quaternion, Eq. (7.4.33)
$\underline{Q}$	quaternion matrix, Eq. (7.4.38)
$\underline{Q}$	matrix of uncorrelated noise, Eq. (7.3.30)
ΔQ [A-s]	electric charge, Chapter 4
r [m]	semiminor axis of the earth's reference ellipsoid, Eq. (2.7)
r [m]	distance between center of support and center of gravity, Eq. (3.2.25)
r [m]	radius of light beam, Eq. (3.5.1)
r	amplitude of backscattered light with respect to incident light of a mirror, Eq. (3.5.12)
$\underline{R}$ [m]	radius vector from origin O of inertial coordinate frame to point P of measurement, Eq. (2.1)
R [m]	semimajor axis of the earth's reference ellipsoid set equal to the radius of spherical earth, Eqs. (2.6), (7.3.1)
R	system reliability, Fig. 7.4.9
R [Ohm]	measuring resistance, Chapters 3, 4
$R_{N,E}$	radii of curvature of earth's reference ellipsoid, Eqs. (2.13), (2.14)
RIG	rate integrating gyro
RLG	ring laser gyro
s	second
s [rad/s]	Laplace variable
S [rad/s/V]	gyro scale factor, Eqs. (3.2.43), (4.2.2b)
S^t [dyn-cm/A]	torquer scale factor
S^T [rad/s/A]	torquer scale factor (= S^t/H)
S^u [rad/s/V]	scale factor of rate gyro
S [m]	distance flown, Chapter 7
S	signal generator, Fig. 7.3.1
SAP	single axis platform, Section 5.2.1
SM	servo motor, Fig. 7.3.1
SDF	single-degree-of-freedom
t [s]	time
T [s]	period
T [s]	time constant, Chapter 6
T^p [s]	pulse length, Chapter 4
T [K]	temperature, Section 3.5.4
T^s [s]	sampling time, Chapter 4
T^s [s]	Schuler period, Eq. (7.3.1)
ΔT [s]	time difference between two light beams travelling through optical path

ΔT [K/m]	temperature gradient, Section 3.5.4
T [s]	MTBF of a sensor, Fig. 7.4.9
TDF	two-degree-of-freedom
TGP	three-gimbal platform, Section 5.3
u [V]	sensor output voltage
$\underline{u}$	control vector, Eq. (7.3.4)
V [m/s]	velocity components with respect to ground, Eq. (2.26)
v [m/s]	total velocity vector with respect to ground, Eq. (2.26)
VFC	voltage-to-frequency converter
w	white noise, Fig. 7.6.3
x,y,z	axes of coordinate frame
x	state variable, Chapter 7
z	measurement variable, Chapter 7
Δz	relative shift of fringe pattern of two interfering light beams in an OG
α [rad]	constant misalignment angle of gyro axes with respect to reference axes, Fig. 3.2.4
α [rad]	angle between coordinate systems, Eq. (7.3.36)
α [rad]	wander angle, Fig. 7.4.1
α [rad]	angle to describe quaternion, Fig. 7.4.10
α [rad]	coning motion amplitude, Eq. (7.4.46)
β [rad]	coning motion amplitude, Eq. (7.4.46)
β [rad]	angle to describe quaternion, Fig. 7.4.10
β [rad]	platform rotation angle of Delco system, Fig. 7.4.3
β [rad]	misalignment angle between torquer axes and reference axes, Fig. 3.2.5
γ [rad]	angle between rotor reference axis and magnetic field vector, Chapter 3
γ [rad]	angle between gravitation vector $\underline{G}$ and gravity vector $\underline{g}$, Fig. 2.1
γ [rad]	angle to describe quaternion, Fig. 7.4.10
δ [rad]	angle to describe quaternion, Fig. 7.4.10
δ	sign to describe an error, e.g. δV = velocity error
Δ	sign to describe a difference, e.g. ΔS = distance from starting point
ϵ [rad]	error angle, misalignment of platform or strapdown system with respect to navigational frame or integral gyro drift
ζ	damping constant, Eq. (3.2.35), (3.4.8)
η [rad]	deflection of the vertical about north-south axis, Fig. 2.4 and Eq. (2.35)
θ [rad]	gyro pickoff angle, Chapter 3, 4, Fig. 3.2.3
θ [rad]	pitch angle, Chapters 6, 7, 8, 9
θ [rad]	rotation of polarization plane of light beam, Eq. (3.5.14)
κ	relative scale factor error = $\delta S/S$, Eq. (3.2.46)
κ [rad/s]	eigenvalue of unstable vertical channel, Eq. (7.3.38)
λ [rad]	geographic longitude
λ [m]	wavelength of light

Λ [rad]	celestial longitude = $\lambda + \Omega t$, Eq. (2.23b)
μ [rad]	position angle in pseudo pole coordinate frame, Fig. 7.4.4
μ	friction coefficient, Chapter 3
ν [rad/s]	frequency of light, Eq. (3.5.7)
ξ [rad]	deflection of the vertical about east-west axis, Fig. 2.4 and Eq. (2.3.5)
π	multiplication mode, Fig. 3.3.2, 3.3.5
ρ	correlation factor, Fig. 7.3.9
σ	standard deviation
σ [rad]	position angle in pseudo pole coordinate frame, Fig. 7.4.4
τ [s]	integration time
τ [s]	life time, Fig. 7.4.9
τ [s]	time constant, Eq. (7.4.4)
τ_α [s]	time constant due to fluid mass coupling, Eq. (3.3.7)
φ [rad]	geographic latitude, Fig. 2.1
φ_c [rad]	geocentric latitude, Fig. 2.1
φ [rad]	phase shift, Eq. (3.5.3) and (7.4.46)
ϕ [rad]	roll angle
ϕ [rad]	angular displacement of gyro with respect to inertial space, Eq. (3.4.6)
ϕ^P [arc sec]	pulse weight, Chapter 4
$\underline{\phi}$ [rad]	attitude angle vector, Eq. (5.1.1)
Φ	transition matrix, Eq. (7.3.5)
χ [rad]	total out-of-alignment angle between gyro frame and reference frame, Figs. 3.2.3, 3.2.4 and Eq. (3.2.12)
$\underline{\underline{\chi}}'$	matrix in quaternion computation, Eq. (7.4.40)
ψ [rad]	yaw angle
ω [rad/s]	angular rate
ω^n [rad/s]	natural frequency, Eq. (3.2.35)
ω^n [rad/s]	nutation frequency, Eq. (3.4.8)
ω^S [rad/s]	Schuler frequency, Eq. (7.3.1)
Ω [rad/s]	coning motion frequency, Fig. 7.4.11
Ω [rad/s]	magnitude of earth rate, Eq. (2.21)
Ω' [rad/s]	$= \Omega + \dot{\lambda}/2$, Eq. (7.2.5)
$\underline{\underline{\Omega}}$	$\underline{\omega}$ x matrix, Eqs. (3.2.9), (7.4.12)

Subscripts indicate the reference coordinate frame, axes orientation and directions

a	wander azimuth coordinate frame, Fig. 7.4.1
b	body, Section 7.4.4.1
c	related to center of the earth
D	down axis in navigational coordinate frame, Fig. 2.1
e	earth-fixed coordinate frame, Fig. 2.1

E	east axis in navigational coordinate frame, Fig. 2.1
g	gyro coordinate frame, Fig. 3.2.1
h	horizontal, Fig. 7.4.3
i	inertial coordinate frame, Fig. 2.1
i	dummy subscript, Table 3.2.2
I	input axis, Fig. 3.2.1
j	dummy subscript, Table 3.2.2
m	derivation of magnetic field, Eq. (3.2.3)
m	pseudo pole coordinate frame, Fig. 7.4.4
n	navigational coordinate frame, Fig. 2.1
N	north axis in navigational coordinate frame, Fig. 2.1
O	output axis, Fig. 3.2.1
P	platform, Chapter 5
r	gyro case reference coordinate frame, Fig. 3.2.4
r	rotor-fixed coordinate frame, Eq. (3.2.3)
S	spin axis, Fig. 3.2.1
t	torque generator coordinate frame, Fig. 3.2.5
v	vertical, Fig. 7.4.3
x,y,z	directions of coordinate frame axes

Superscripts

one superscript is used for physical criteria

a	accelerometer, Section 7.6
a	anisoelasticity, Eq. (3.2.31)
a	asymmetry error of scale factor, Eq. (3.2.46)
a	dummy superscript in Eq. (3.5.16)
b	dummy superscript in Eq. (3.5.16)
c	dummy superscript in Eq. (3.5.16)
c	constant value; Eq. (3.2.46)
c	cross coupling; Table 3.2.1b
d	Doppler, Chapter 3
D	dither, Section 3.5.4
f	fixed value, Sections 3.2 and 3.5.4
f	friction, Eq. (3.2.37)
F	Faraday, Section 3.5
g	gyro, Chapters 3.7
h	hunting, Eq. (3.2.33)
H	magnetic field coefficient, Section 3.5.4
i	dummy superscript
i	input, Eq. (3.4.2)
i	anisoinertia, Table 3.2.1b
k	dummy superscript

l	linearity error of scale factor, Eq. (3.4 2)
L	lock-in rate, Section 3.5
m	maximum, Chapter 4
m	magnetic field vector, Eq. (3.2.4)
m	misalignment, Tables 3.2.1a, 3.2.2a
n	nonlinearity error of scale factor, Eq. (3.4.2)
n	nutation, Chapters 3, 5
p	pulse, Chapter 4
p	pseudo coning, Tables 3.2.1b, 3.2.2b
p	platform, Chapters 5, 7
r	restraint torque, Eq. (3.2.21)
r	rotor, Eq. (3.2.4)
r	readout, Chapter 4
rw	random walk, Section 3.5.4
s	scale factor, Tables 3.2.1a, 3.2.2a
s	spin, Eq. (3.2.5a)
s	spring rate coupling, Eq. (3.2.39)
s	Schuler, Chapter 7
s	sampling, Chapter 4
st	saw tooth, Chapter 4
s	servo loop, Chapter 5
t	command torque and command rate, Eq. (3.2.19)
T	total angular momentum of a gyro, Eqs. (3.2.1) and (3.2.6)
T	transpose of a matrix
T	temperature coefficient, Section 3.5.4
ΔT	temperature gradient coefficient, Section 3.5.4
T	table, Section 3.5.4
u	unbalance, Section 3.2.2.1

two superscripts with vectors indicate the direction of motion, e.g.

$\underline{\omega}_n^{in}$	= angular rate vector of the navigational coordinate frame with respect to the inertial coordinate frame, measured in the navigational coordinate frame (as indicated by the subscript); the superscripts used are those of the coordinate frames, as defined above under "Subcripts"

Other symbols

$\frac{d}{dt}\Big\|_i$	time derivative with respect to inertial frame
~	variable in the Laplace domain
-	mean value
$\hat{x}$	computed value
—	vector
—	matrix
^	amplitude

GYROSCOPIC INSTRUMENTS AND THEIR APPLICATION TO FLIGHT TESTING

by

B. Stieler and H. Winter

Institut für Flugführung

Deutsche Forschungs- und Versuchsanstalt
für Luft- und Raumfahrt e.V. (DFVLR)
D-3300 Braunschweig-Flughafen, West Germany

SUMMARY

This AGARDograph is the 15th of the AGARD Flight Test Instrumentation Series and discusses the use of gyroscopic instruments to support flight testing. Gyroscopic instruments are used in flight tests to measure the aircraft angular accelerations and rates, attitude and heading and - in combination with accelerometers - the linear acceleration, the ground velocity and the position. This volume describes the measuring principles, the technical lay-out and the error behaviour of the sensors and systems used for these measurements: Gyros, accelerometers, attitude and heading references and inertial navigation systems. Attention is also given to integrated and hybrid sensor systems, as they are in use in modern instrumentation systems. Examples of actual flight instrumentation systems are described and the requirements for the gyroscopic sensors in these systems are discussed for applications in aircraft stability and control flight tests, in performance tests and in airborne and ground systems calibration and testing.

This AGARDograph has been sponsored by the Flight Mechanics Panel of AGARD.

1. INTRODUCTION

During the last decade the requirements for the instrumentation used for flight testing of aircraft have become more stringent for a number of reasons. First, the aircraft to be flight-tested - especially the new generation of high performance air-to-air combat aircraft - and their avionics system have become more complex with respect to flying qualities and performance. Second, flight test techniques have been developed to identify aircraft parameters in dynamic flight conditions in order to reduce flight time - in contrast to the steady state flight test procedures employed before. Finally, new mathematical tools have been developed to evaluate the flight test results - like Kalman filtering, system identification, etc. Using these tools more information about the aircraft parameters and their derivatives can be extracted from the flight test data if these data are sufficiently accurate, well synchronized and contain all required frequencies.

These factors make the design of an instrumentation system a complex task. In Volume 1 of this AGARDograph [1.1] the basic principles of flight test instrumentation engineering have been described in detail. For the gyroscopic instruments which will be discussed in the present Volume, we have to concentrate on the specific problems of these transducers, their measurement principles, range and frequency response and accuracy. Gyroscopic instruments are used for measuring

- angular rates; in an aircraft referenced coordinate system (turn rate instrumentation, sensors in flight control loops, flight test transducers)

- angles; in an earth referenced coordinate system (attitude angles, roll and pitch; yaw angle or heading). The gyros are used to store, physically, a reference frame as in artificial horizons, in attitude and heading reference systems or in inertial platform systems.

For angular rate measurement, the gyro is mounted on the aircraft frame and the sensing element - the gyro rotor - is subject to the full linear motion and to the angular motion to be measured. The torque required to slave the rotor to the vehicle's angular motion is a direct measure of this motion and is converted into the output signal. For angle measurement, use is made of the physics of a gyro with rotational freedom about all axes. The direction of its rotor axis stays fixed with respect to the fixed stars, unless a torque is applied to one of its transverse axes. The rotational freedom is achieved by mounting the gyro in a set of gimbals with low friction bearings or stabilization control loops. In this way the sensing element is isolated from the angular motion of the vehicle and subject only to its linear motion. Thus, the storage of a reference frame, e.g. north, east and vertical, is realized, which is a prerequisite for carrying out angular measurements as with vertical or directional gyros, or for measuring angular motion and linear acceleration with the gyro stabilized platforms of inertial navigation system.

The development of very accurate rate sensors with digital readout systems and of fast digital computers has made it possible to compute the reference frame by integration of the angular rates. These "strapdown" systems combine both measuring functions discussed above by providing the angular rates as well as the attitude and heading angles with high accuracy.

An important factor influencing the selection of the gyroscopic instruments for flight testing is the frequency spectrum of the angular rates and angles to be measured. Roughly speaking, in flight testing one may distinguish three frequency ranges:

- High frequency range (up to 100 Hz). This range is of interest mainly in aero-elasticity, structural, vibration and flutter studies.

- Medium frequency range (up to 10 Hz). Main interest is in aircraft performance, stability and control problems.

- Low frequency range (below 1 Hz). Main interest is in avionics and navigation system testing.

In the high frequency range angular and linear accelerometers and strain gages are generally used. These will be covered only partially in this volume. Gyroscopic instrumentation is used mainly for medium and low frequency applications. In aircraft performance, stability and control flight tests the angular rates, the attitude and heading angles and the linear accelerations in the medium frequency range are of interest. For the flight testing of avionics and navigation systems, the attitude and heading angles, the ground velocity and the aircraft trajectory have to be measured accurately.

The contents of this volume are presented in the following order: In the second chapter the basic principles, problems and limitations of inertial measurements (angular and linear measurements) are discussed. In the third chapter the measurement principles, technical lay-out and performance of the inertial sensors are discussed (mechanical and laser gyros and accelerometers). The accelerometers are discussed only briefly because a separate volume of this AGARDograph [1.2] is entirely devoted to these sensors. In the fourth chapter special attention is given to the problem of accurate digital readout of inertial sensors. In the fifth chapter the principles and problems of the use of gyros for platform stabilization are discussed. The sixth chapter describes attitude and heading reference systems and the seventh chapter inertial platform and strapdown systems. In the eighth chapter the principles and technical lay-out of hybrid systems are discussed. These systems have the highest potential for accuracy, but complicated software has to be designed to obtain full benefit of this potential. Finally, in the ninth chapter a survey of the spectra of applications of gyroscopic instruments to aircraft flight testing is given, with several examples of modern systems and a discussion of future trends.

The information contained in the present volume has been arranged so that the reader is familiarized with the principles, technical realization and performance of gyroscopic instruments of different accuracy classes:

Low accuracy transducers (Chapters 3 and 6)

- Spring restrained gyros and accelerometers with accuracies of about 1 % of full scale.

- Unaided vertical and directional gyros with accuracies of several degrees.

Medium accuracy transducers (Chapters 3 and 6)

- Gyros and accelerometers with electronic caging loops and accuracies of about 0.1 % of full scale.

- Velocity aided vertical gyro, gyroscopic compass systems, attitude and heading reference systems with accuracies of 0.5 to 1 degree.

High accuracy systems (Chapters 4, 7 and 8)

- Inertial platform and strapdown systems providing attitude angles within 0.1 degree, heading within 0.2 to 0.5 degrees, angular rates better than 0.1 % of full scale (strapdown systems), ground velocity within 3 m/s, position within 1 to 3 km per hour of flight time and acceleration better than 0.1 % of full scale.

- Hybrid reference systems with higher accuracies than those of inertial platform and strapdown systems, depending on the accuracy of the sensors used to aid the INS (see Chapter 8).

Conventional instrumentation systems for performance, stability and control flight tests in most cases use three accelerometers, three rate gyros and a vertical and a directional gyro of low accuracy (1 % of full scale for rate and acceleration, and a few degrees of error for the angle measurements). Modern instrumentation systems make use of medium to high accuracy inertial transducers and inertial platforms are coming into general use, especially for the performance testing of high performance aircraft in dynamic flight conditions [1.3 and 1.4]. For the flight testing of modern avionics and navigation systems hybrid, integrated systems are required in order to achieve the required high accuracy of the reference system. For angular rate measurement in these systems either rate gyros have to be used, or the platform angles have to be differentiated. The former method is preferred, because it is more precise. With the introduction and successful application of strapdown systems, the complete information can be obtained from one single source: the accelerations, angular rates, the angles, the ground velocity and position. For high precision flight testing under dynamic conditions, the strapdown system will be the ideal gyroscopic instrumentation system. For covering the medium and low frequency range external measurements of velocity and position must be made to aid the strapdown systems.

References for Chapter 1

[1.1] A. Pool and D. Bosman, Ed. — Basic Principles of Flight Test Instrumentation Engineering. AGARDograph No. 160, Volume 1, 1974.

[1.2] I. McLaren — Open and Closed Loop Accelerometers. AGARDograph No. 160, Volume 6, 1974.

[1.3] James N. Olhausen — The Use of a Navigation Platform for Performance Instrumentation on the YF-16 Flight Test Program. AIAA Aerospace Meeting, Pasadena, California, January 1975.

[1.4] E.G. Hoffmann — Aero Navigation Systems Flight Testing for Compliance with Airworthiness Regulations. Seventh Annual Symposium of the Society of Flight Test Engineers, August 1976.

2. PRINCIPLES AND PROBLEMS OF INERTIAL MEASUREMENTS

Newton's laws of classical mechanics are the basis for measuring the two states of motion of a rigid body, the translational motion and the rotational motion.

We shall derive in this chapter the formulas to evaluate the output of accelerometers and gyros measuring the translational and rotational motions. Accuracy limitations will be presented.

2.1 Measurement of Translational Motion

The translational motion of the rigid body's center of gravity caused by the forces acting on the body is described by Newton's second law

$$\underline{a} = \frac{d^2 \underline{R}}{dt^2}\Big|_i \, . \tag{2.1}$$

$\underline{a}$ is the applied force per unit mass including the gravitational forces if the body is within the gravity field of another body (earth, sun, moon), and

$\frac{d^2 \underline{R}}{dt^2}\Big|_i$ is the second time derivative of the radius vector $\underline{R}$ from the origin of the inertial coordinate frame i to the point of measurement P.

Assuming initially the origin of the i-frame to be located on one of the fixed stars, $\underline{R}$ to be the distance from there to the earth's center of gravity and $\underline{a}$ to be the sum of the gravitational forces of all celestial bodies on the earth's center of gravity, we immediately see that Eq. (2.1) is satisfied for the motion of this point around the sun. We may therefore relocate the origin of the i-frame into this point (s. [2.1], Section 3.4), which is more appropriate to describe the motion of a body with respect to the earth. $\underline{R}$ is then the radius vector from the earth's center of gravity to the point P of measurement (s. Figs. 2.1a and b).

As a matter of definition the axes of the i-frame must be non-rotating, for which the direction to the fixed stars may serve as a reference. Their relative motion causes an angular rate error of only $<3 \cdot 10^{-9}$ °/h, [2.2]. We assume initially that the axes of the i-frame are oriented with x pointing north, parallel to the instantaneous spin axis of the earth and with y and z orthogonal to x as shown in Fig. 2.1a. This axis orientation is in error by the following effects.

The earth itself has to be regarded as a big gyro with a pear-shaped body. The gravity field of the sun and the moon are exerting torques upon this gyro causing a precession ($<1.6 \cdot 10^{-6}$ °/h) and a nutation ($<10^{-7}$ °/h) of the instantaneous spin axis as shown in Fig. 2.2a (s. [2.2] and [2.3], Chapter 4).

Furthermore the earth is not a solid body but its mass distribution is affected by meteorological, geophysical and biological processes (rain, winds, ocean, currents, vegetation growth) which cause the instaneous spin rate to vary irregulary with time ($<10^{-6}$ °/h). Tidal friction of the sea and viscous damping between the earth's core and mantle cause it to decrease slightly (0.0016 s per 100 years), [2.2].

The effects just mentioned also cause the instantaneous spin axis, i.e., the direction of true north, to migrate with respect to the earth crust as shown in Fig. 2.2b. If the i-frame is oriented with its x-axis parallel to geographic north (mean direction of the earth spin axis in the year 1903), which is more convenient than the instantaneous spin axis, and with its y- and z-axes in the equatorial plane, the angular difference between the x-axis and the instantaneous spin axis gives rise to angular rate measurement errors (introduced by a small component of the earth's rotation rate) of:

$$\delta\omega \leq 5 \cdot 10^{-5} \text{ °/h}. \tag{2.2}$$

Accelerometers are instruments measuring the accelerations of a rigid body (e.g., an airplane) in the directions of their sensitive axes. Their output signal in three orthogonal directions is a vector $\underline{f}$ proportional to the force necessary to balance the proof mass of the accelerometer (s. Fig. 2.3 and Section 3.6).

We call $\underline{f}$ "the specific force" in the following. The sum $\underline{a}$ of all forces per unit mass acting on the proof mass is:

$$\underline{a} = \underline{f} + \underline{G} \tag{2.3}$$

where $\underline{G}$ represents the gravitation of the earth including the effects of other celestial bodies (sun, moon) changing with their relative positions to the point P of measurement. These effects near the surface of the earth amount to only (s. [2.1], Chapter 4 and [2.2]),

$$\delta G = 10^{-7} G \tag{2.4}$$

and are negligible in general. So we have with Eqs. (2.1) and (2.3):

$$\underline{f} = \frac{d^2 \underline{R}}{dt^2}\Big|_i - \underline{G} = -\underline{g}', \text{ where we introduce } g' \text{ only for convenience in the sequence.} \tag{2.5}$$

We shall now derive the relationship between the time derivatives of the radius vector $\underline{R}$ with respect to the inertial frame i and with respect to the coordinate frame in which the measurement is carried out. Let us assume this to be the navigational coordinate frame n with its x, y and z-axes pointing north, east and down as shown in Fig. 2.1a.

a) Reference Coordinate Frames

x, y, z	inertial frame i
x_e, y_e, z_e	earth-fixed frame e
x_n, y_n, z_n	navigational frame n

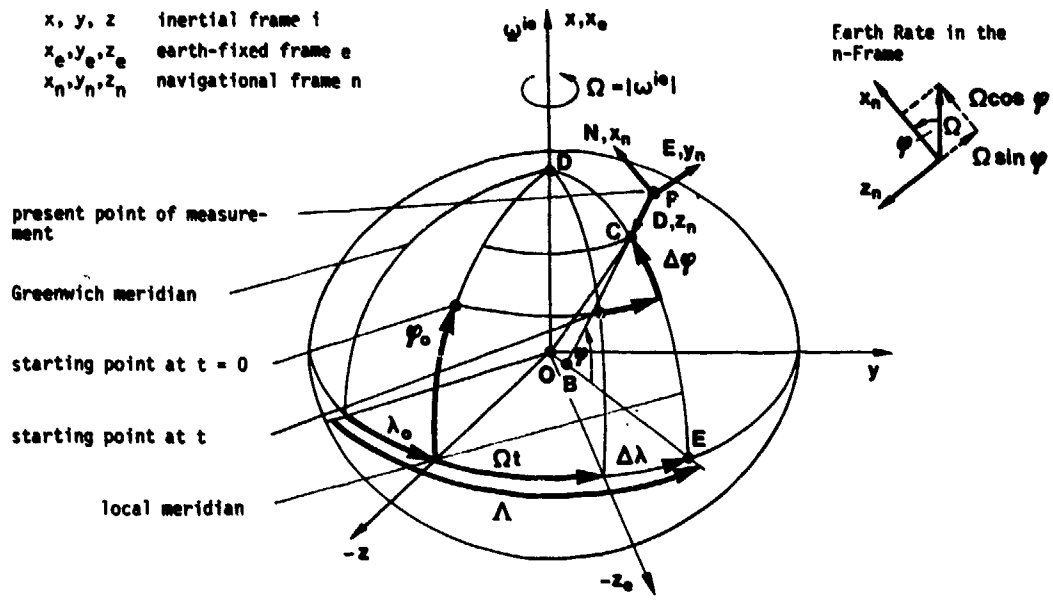

b) Radius Vectors, Radii of Curvature of the Reference Ellipsoid and Altitude

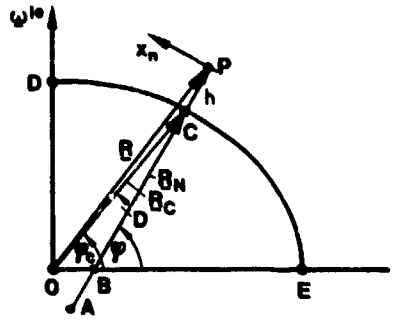

c) Gravitation and Gravity

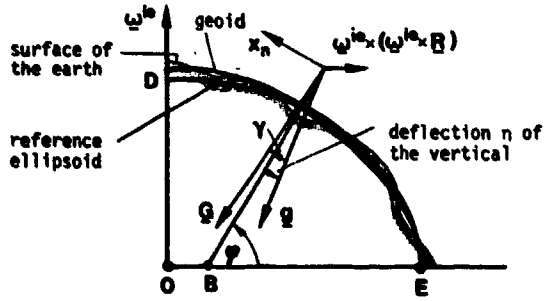

d) Shape of the Geoid with Respect to the Ellipsoid [2.4] (Δr in meters)

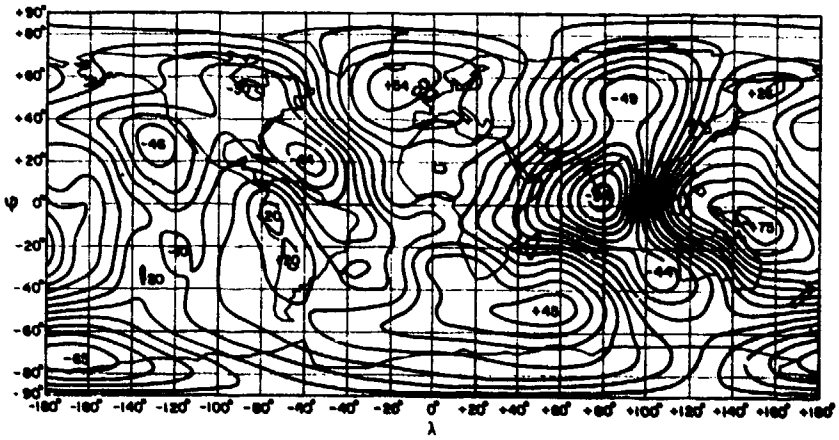

Fig. 2.1 Reference Coordinate Frames, the Reference Ellipsoid, Gravity and Gravitation and the Geoid

a)

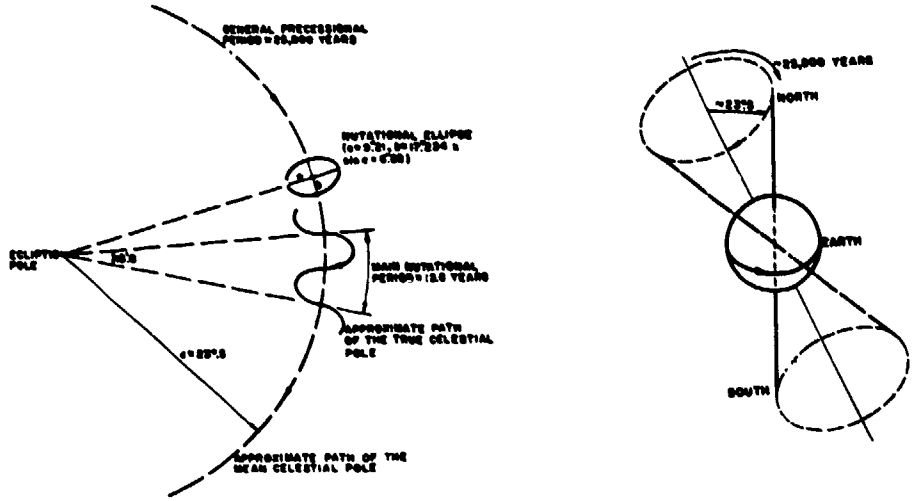

b)

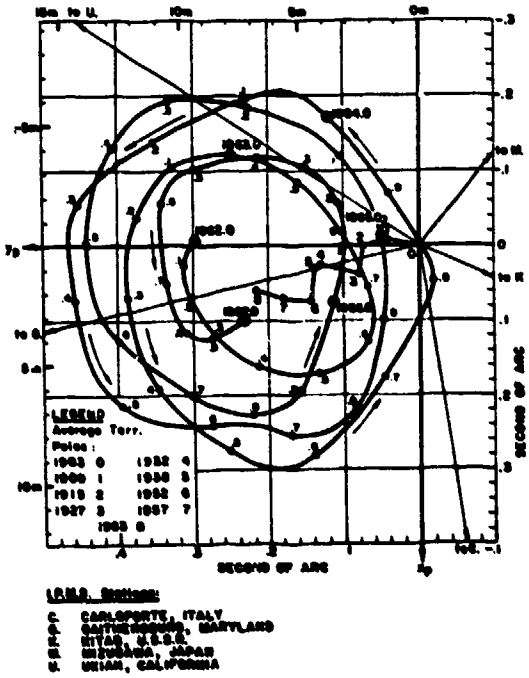

Fig. 2.2 Disturbance Motion of the Earth's Rotational Axis with Respect to the Fixed Stars (Nutation and Precession) and with Respect to the Earth (Migration of the North Pole) [2.3] and [2.4]

The direction "down" is defined as being normal to the reference ellipsoid, which is the best mathematical approximation to the pear-shaped geoid - the earth's body of equipotential surface at mean sea level (s. Figs. 2.1c and d).

It is inclined by the geographic latitude φ with respect to the equatorial plane. A few parameters have to be defined for the reference ellipsoid:

- the semimajor axis (OE in Fig. 2.1b)
  $R = 6{,}378{,}160$ m (2.6)

- the semiminor axis (OD in Fig. 2.1b)
  $r = R(1 - f)$ (2.7)

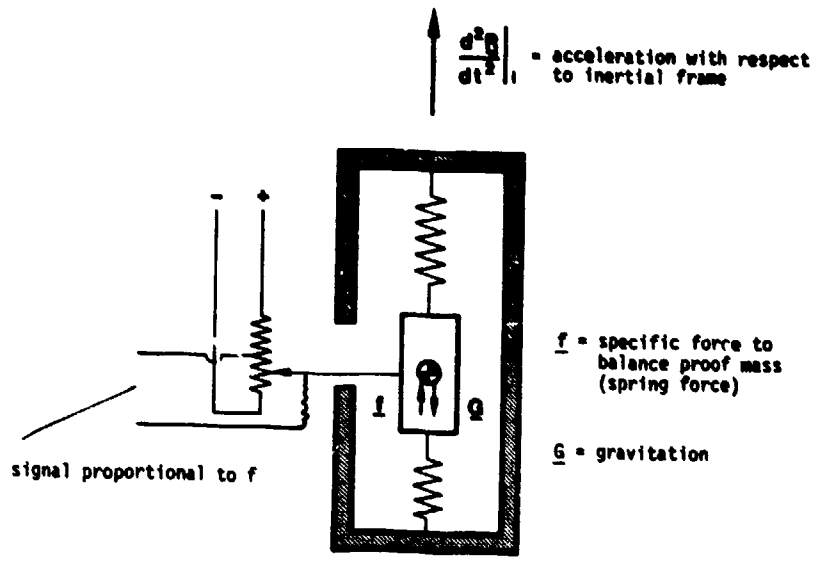

$$\underline{a} = \underline{f} + \underline{G} = \left.\frac{d^2\underline{R}}{dt^2}\right|_i$$

Fig. 2.3 Forces and Output Signal in an Accelerometer

- the flattening of the ellipsoid
  $f = (R-r)/r = 1/298.247$ (2.8)
- the numerical eccentricity e
  $e^2 = f(2 - f)$ (2.9)
- the geocentric latitude
  $\varphi_c = \tan^{-1}\left(\frac{r^2}{R^2}\tan\varphi\right)$ (2.10)
- the deviation of the normal (h = altitude above the reference ellipsoid, s. Fig. 2.1b)
  $D = \varphi - \varphi_c \approx f(1 - h/R_c)\sin 2\varphi$ (smaller than 11.6 arc min) (2.11)
- the geocentric radius
  $R_c = \frac{R(1-f)}{(1-e^2\cos^2\varphi_c)^{1/2}} = R(1-f)(1+\frac{e^2}{2}\cos^2\varphi)$ (2.12)
- the meridian radius of curvature
  $R_N = \frac{R(1-e^2)}{(1-e^2\sin^2\varphi)^{3/2}} \approx R[1 + e^2(\frac{3}{2}\sin^2\varphi - 1)]$, (2.13)
- the transverse radius of curvature
  $R_E = \frac{R}{(1-e^2\sin^2\varphi)^{1/2}} \approx R[1 + \frac{1}{2}e^2\sin^2\varphi]$, (2.14)
- the mean radius of curvature
  $R = (R_N R_E)^{1/2}$ (2.15)
- the radius of curvature in direction ψ with respect to north
  $\frac{1}{R_A} = \frac{\cos^2\psi}{R_N} + \frac{\sin^2\psi}{R_E}$. (2.16)

The figures quoted were laid down by the International Union for Geodesy and Geophysics at its General Meeting in Lucerne in 1967 and are part of the Geodetic Reference System 1967 [2.5].

Now we have defined the coordinate frames i and n and may derive the relationships for the velocities and accelerations within these frames:

The rate of change of the radius vector $\underline{R}$ (s. Fig. 2.1b) in the inertial frame and the navigational frame is connected through the theorem of Coriolis [2.1, Appendix A4]

$$\left.\frac{d\,\underline{R}}{dt}\right|_i = \left.\frac{d\,\underline{R}}{dt}\right|_n + \underline{\omega}^{in} \times \underline{R}. \tag{2.17}$$

This is the total velocity of the point P of measurement with respect to the origin O of the i-frame, i.e. the earth's center of gravity. Its acceleration with respect to this point is given by

$$\left.\frac{d^2\underline{R}}{dt^2}\right|_i = \left.\frac{d^2\underline{R}}{dt^2}\right|_n + \left.\frac{d\underline{\omega}^{in}}{dt}\right|_n \times \underline{R} + 2\underline{\omega}^{in} \times \left.\frac{d\underline{R}}{dt}\right|_n + \underline{\omega}^{in} \times (\underline{\omega}^{in} \times \underline{R}). \tag{2.18}$$

with vertical-, horizontal-, Coriolis-, centrifugal accelerations.

The total angular rate $\underline{\omega}^{in}$ is the sum of earth rate and transport rate:

$$\underline{\omega}^{in} = \underline{\omega}^{ie} + \underline{\omega}^{en}, \tag{2.19}$$

where in the n-frame the earth rate is given by:

$$\underline{\omega}_n^{ie} = \Omega \begin{pmatrix} \cos\varphi \\ 0 \\ -\sin\varphi \end{pmatrix} \tag{2.20}$$

with the magnitude

$$\Omega = |\underline{\omega}^{ie}| = \frac{2\pi}{86164.1} \ \frac{\text{rad}}{\text{s}}$$

$$= 7.292\,115 \cdot 10^{-5} \ \frac{\text{rad}}{\text{s}}$$

$$= 15.041\,067 \ \frac{\text{arc sec}}{\text{s}}. \tag{2.21}$$

The transport rate $\underline{\omega}_n^{en}$ and the total angular rate $\underline{\omega}_n^{in}$ of a vehicle are in the n-frame:

$$\underline{\omega}_n^{en} = \begin{pmatrix} \dot\lambda\cos\varphi \\ -\dot\varphi \\ -\dot\lambda\sin\varphi \end{pmatrix} = \begin{pmatrix} V_E/(R_E+h) \\ -V_N/(R_N+h) \\ -[V_E/(R_E+h)]\tan\varphi \end{pmatrix}, \quad \underline{\omega}_n^{in} = \begin{pmatrix} (\Omega+\dot\lambda)\cos\varphi \\ -\dot\varphi \\ -(\Omega+\dot\lambda)\sin\varphi \end{pmatrix} = \begin{pmatrix} \dot\Lambda\cos\varphi \\ -\dot\varphi \\ -\dot\Lambda\sin\varphi \end{pmatrix}, \tag{2.22a,b}$$

with the rate of change of geographic longitude λ, of celestial longitude Λ and of latitude φ given by:

$$\dot\lambda = \frac{V_E}{(R_E+h)\cos\varphi}, \qquad \dot\Lambda = \Omega + \dot\lambda \tag{2.23a,b}$$

$$\dot\varphi = \frac{V_N}{(R_N+h)}. \tag{2.24}$$

It should be pointed out that in these equations $R_{N,E}$ are not the components of the radius vector $\underline{R}$ but the radii of curvature of the ellipsoid (s. Eqs. (2.13) and (2.14)).

The relationships for the acceleration (2.18) simplifies considerably if we introduce the velocity of the point P of measurement with respect to the surface of the reference ellipsoid:

$$\left.\frac{d\underline{R}}{dt}\right|_e = \underline{v} = \left.\frac{d\underline{R}}{dt}\right|_n + \underline{\omega}^{en} \times \underline{R}, \tag{2.25}$$

which, expressed in n-frame coordinates, is:

$$\underline{v}_n = \begin{pmatrix} V_N \\ V_E \\ V_D \end{pmatrix} = \begin{pmatrix} (R_N+h)\,\dot\varphi \\ (R_E+h)\,\dot\lambda\cos\varphi \\ -\dot h \end{pmatrix}. \tag{2.26}$$

The resulting acceleration of P is:

$$\left.\frac{d^2\underline{R}}{dt^2}\right|_i = \dot{\underline{v}} + (2\underline{\omega}^{ie} + \underline{\omega}^{en}) \times \underline{v} + \underline{\omega}^{ie} \times (\underline{\omega}^{ie} \times \underline{R}). \tag{2.27}$$

The last term on the right side is compounded with the <u>gravitation $\underline{G}$</u> in Eq. (2.5) to give the <u>gravity $\underline{g}$</u> as shown in Fig. 2.1b:

$$\underline{g} = \underline{G} - \underline{\omega}^{ie} \times (\underline{\omega}^{ie} \times \underline{R}) = \underline{G} - \frac{R\Omega^2}{2} \cdot \begin{pmatrix} -\sin 2\varphi \\ 0 \\ 1 + \cos 2\varphi \end{pmatrix}. \tag{2.28}$$

So we obtain for the specific force vector $\underline{f}$ necessary to balance the proof mass of accelerometers on a moving vehicle:

$$\underline{f} = \dot{\underline{v}} + (2\underline{\omega}^{ie} + \underline{\omega}^{en}) \times \underline{v} - \underline{g}, \tag{2.29}$$

which is valid for any reference coordinate frame r when the subscript or superscript n is replaced by r.

The angle γ, by which the gravitation $\underline{G}$ is inclined about the east axis with respect to the gravity $\underline{g}$, is given by:

$$\gamma = \frac{R\Omega^2}{2g} \sin 2\varphi = \frac{D}{2} \text{ (smaller than 6 arc min).} \tag{2.30}$$

The maximum difference in magnitude between gravitation and gravity is at the equator:

$$|\underline{G} - \underline{g}| = \frac{R\Omega^2}{2} (1 + \cos 2\varphi) \leq 3.4 \cdot 10^{-3}\ g. \tag{2.31}$$

Gravity changes with position, not only because of the centrifugal acceleration, but also because gravitation itself is a function of longitude and latitude due to the inhomogeneous mass distribution of the geoid.

Its absolute measurement is only practicable in few places, since it requires much expense. Its relative measurement is easy to achieve on land by means of gravimeters, but again difficult on sea which covers 2/3 of the globe. Satellite observations from different places on the globe have opened additional means of defining gravitation, but the results are more or less integrated over a certain area.

A survey of methods and problems to describe gravitation $\underline{G}$ mathematically as a function of latitude and longitude is given in [2.6, Chapter 4]. It is shown here that it is possible to assume $\underline{G}$ as a function of latitude only, if one neglects terms of the order of 10^{-5} g. The results of satellite observations are summarized in [2.4].

Out of the parameters laid down in the Geodetic Reference System the following formulas are derivable for the magnitude of gravity at sea level (h = 0) and its gradient:

$$g(o) = 978.0318\ (1 + 5.3024 \cdot 10^{-3} \sin^2\varphi - 5.9 \cdot 10^{-6} \sin^2 2\varphi)\ \text{Gal} \tag{2.32}$$

$$\frac{dg(o)}{dh} = -0.308\ 77\ (1 - 1.39 \cdot 10^{-3} \sin^2\varphi)\ \text{mGal/m}, \tag{2.33}$$

where, in honor of Galileo

$$1\ \text{Gal} = 1\ \text{cm/s}^2. \tag{2.34}$$

Gravity $\underline{g}$ is commonly oriented "down" in the navigational coordinate frame, i.e. parallel to the normal of the reference ellipsoid. The "deflection of the vertical" due to the inhomogeneous mass distribution is comprised in the angles η about the north and ξ about the east axes so that

$$\underline{g}_n = g\ (\xi \quad -\eta \quad 1)^T, \tag{2.35}$$

for which Fig. 2.4 shows some results of satellite observations [2.4]. The deflection of the vertical decreases with altitude until at 10 000 km it reaches approximately half of the maximal values shown in this figure.

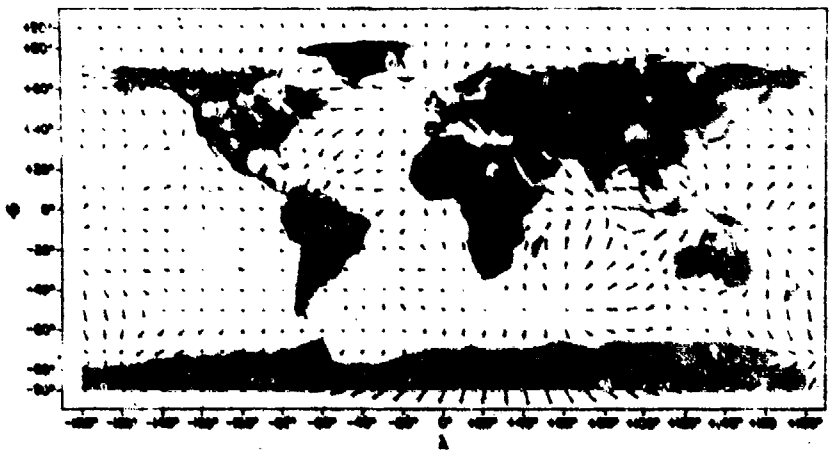

Scale ⟶ 10 arc sec

Fig. 2.4 Deflection of the Vertical at Sea Level in arc sec (total amount ν) [2.4]

The exact knowledge of the magnitude of gravity g becomes essential for testing accelerometers below 10^{-5} g. For the purpose of flight testing and of inertial navigation it is of lower significance, since

- the inertial navigation in the altitude channel, i.e., the computation of vertical velocity and altitude solely from the vertical acceleration, is unstable anyhow and has to be aided by external altitude measurements (e.g., barometric altimeter, s. Sections 8.2.1 and 7.5.1), thus lowering the requirements for the acceleration measurement accuracy;

- the navigation in the horizontal channels does not depend on the computation of the magnitude of g (s. Section 7.2).

Therefore it is often sufficient to assume

$$g(h) = g(o)/(1 + h/R)^2 \tag{2.36}$$

with g(o) derived from Eq. (2.32).

For high accuracy horizontal inertial navigation as in marine application, the exact knowledge of the deflection of the vertical does become important. This statement is also reversible in a certain sense: for the measurement of the deflection of the vertical inertial navigation systems do become increasingly important [2.7].

2.2 Measurement of Rotational Motion

Newton's second law, applied to describe the rotational motion of a rigid body, results in the formula [2.1, Chapters 3.5 and 3.6]:

$$\underline{M} = \left.\frac{d\underline{H}}{dt}\right|_i , \tag{2.37}$$

where $\underline{M}$ is the torque vector applied to the rigid body and $\underline{H}$ is the angular momentum vector, computed from

$$\underline{H} = \underline{J}\ \underline{\omega}^{ib}. \tag{2.38}$$

The symmetrical "inertia tensor" $\underline{J}$ is composed of three "moments of inertia J_{ii}" and three "products of inertia J_{ij}" (i = x,y,z and j = x,y,z):

$$\underline{J} = \begin{pmatrix} J_{xx} & J_{xy} & J_{xz} \\ J_{xy} & J_{yy} & J_{yz} \\ J_{xz} & J_{yz} & J_{zz} \end{pmatrix} . \tag{2.39}$$

They are computed from integrals over the whole volume of the body (designated as $\int_V$) according to:

$$J_{xx} = \int_V (y^2 + z^2)\, dm \qquad J_{yy} = \int_V (x^2 + z^2)\, dm \qquad J_{zz} = \int_V (x^2 + y^2)\, dm$$

$$J_{xy} = -\int_V xy\, dm \qquad J_{yz} = -\int_V yz\, dm \qquad J_{xz} = -\int_V xz\, dm. \tag{2.40 a-f}$$

For a certain orientation of the x, y and z-axes the products of inertia vanish to give

$$\underline{H} = \begin{pmatrix} J_x\, \omega_x^{ib} \\ J_y\, \omega_y^{ib} \\ J_z\, \omega_z^{ib} \end{pmatrix} . \tag{2.41}$$

These axes are called "principal axes" and the J_i the "principal moments of inertia".

Applying the theorem of Coriolis [2.1, Appendix A4] to Newton's rotational law for a rigid body (2.37) we obtain in any rotating reference coordinate frame r:

$$\underline{M} = \left.\frac{d\underline{H}}{dt}\right|_r + \underline{\omega}^{ir} \times \underline{H}. \tag{2.42}$$

In a gyro the r-frame is case-fixed, for instance, and the angular momentum is constant with respect to the case, so we may approximate this equation by:

$$\underline{M} = \underline{\omega}^{ir} \times \underline{H}, \tag{2.43}$$

showing that this sensor allows us to measure the angular rate $\underline{\omega}^{ir}$ of the case with respect to the inertial frame by means of the reaction torque $\underline{M}$.

The reader is referred to [2.9] and also [2.1] for a deeper insight into gyroscopic theory and application.

2.3 Accuracy Limitations of Inertial Measurements

The accuracy of inertial measurements is limited by the following effects

- fundamental limitations
- technical imperfections
- environmental influences
- effects of the digitizing process.

Fundamental limitations such as gravity effects from the sun and moon, migration of the north pole, imperfect knowledge of the earth's gravity field etc. discussed above, cause very small errors in comparison with the other effects. Typical values for such errors are given above and in Ref. [2.8] as:

$\delta\omega \leq 5 \cdot 10^{-5}\ {}^{\circ}/h$ with the migration of the north pole not modelled

$\delta\omega \leq 2 \cdot 10^{-6}\ {}^{\circ}/h$ with the migration of the north pole modelled (2.44a,b)

$\delta f \leq 10^{-5}\ g$ with gravity anomalies not modelled

$\delta f \leq 2 \cdot 10^{-7}\ g$ with gravity anomalies modelled. (2.45a,b)

Technical imperfections, such as friction, electronic noise, spurious torques, manufacturing defects, finite response times , etc., limit the measuring accuracy of the sensors. But inertial technology has reached such a degree of perfection in the last decades that sensors with sufficient accuracy and dynamic response for almost all flight test applications are on the market. Typical values for these errors are

$$\delta\omega \leq 10^{-3}\ {}^{\circ}/h \tag{2.46}$$

$$\delta f \leq 10^{-5}\ g. \tag{2.47}$$

Environmental influences such as the undetected motion of the foundation (s. Fig. 4.2.5), temperature dependence, vibrations can present severe problems. Proper selection of the sensors and careful analysis of the environmental conditions together with calibration and compensation techniques can help to reduce these errors to a large degree.

Calibration and compensation of the sensor errors are based on a proper error model. Emphasis is placed on the derivation of this model in Chapter 3 and on the error compensation in Chapter 7.

For digitizing the measurement of the inertial sensor techniques with different accuracy potential can be applied. Also certain mathematical rules have to be observed which again are the basis for the signal preparation and readout frequency. These problems are discussed in Chapter 4.

In Chapter 8 a completely different approach to overcome these accuracy limitations is discussed: the use of redundant measurements based on a different technology (cinetheodolites, radar, VOR, DME, Doppler radar, etc.) for a continuous inflight calibration of the inertial sensors. This method can produce a considerable improvement in accuracy for flight test data evaluation.

References for Chapter 2

[2.1] Wrigley, W. Hollister, W. M. Denhard, W. G. — Gyroscopic Theory, Design and Instrumentation. The MIT Press, Cambridge, Mass., 1969.

[2.2] Kayton, M. — Fundamental Limitations on Inertial Measurements. Progress in Astronautics and Rocketry, Vol. 8, Guidance and Control, Academic Press, New York, 1962, pp. 367 - 394.

[2.3] Mueller, I. I. — Spherical and Practical Astronomy as Applied to Geodesy. Frederic Ungar Publishing Co., New York, 1969.

[2.4] Lundquist, C. A. Veis, G. (Editors) — Geodetic Parameters for a 1966 Smithsonian Institution Standard Earth, Vol. 1 - 3. Smithsonian Astrophysical Observatory, Special Report 200, Cambridge, Massachusetts 02138, USA.

[2.5] Torge, W. — Geodaesie. Sammlung Goeschen.

[2.6] Britting, K. — Inertial Navigation System Analysis. Wiley Interscience, New York, 1971.

[2.7] — Proceedings of the 1st International Symposium on Inertial Technology for Surveying & Geodesy, Ottawa, Canada, 12 - 14 October 1977.

[2.8] Kayton, M. Fried, W. R. (Editors) — Avionics Navigation Systems. J. Wiley and Sons, Inc., New York, 1969.

[2.9] Magnus, K. — Kreisel. Springer-Verlag, Berlin, 1971

3. INERTIAL SENSORS

3.1 Gyroscopic Sensors and their Application

The mechanical gyro with the rotating wheel and the optical gyro will be subjects of this chapter. According to the angular freedom of the spin axis with respect to the case (s. Fig. 3.1.1) one distinguishes between single-degree-of-freedom (SDF) gyros and two-degree-of-freedom (TDF) gyros. The SDF gyro is basically an angular rate sensor and the TDF gyro an attitude reference sensor, but Table 3.1.1 shows that both sensors are not restricted to these specific applications.

Type of Gyro	Mode	Application
single-degree-of-freedom (SDF) gyro	spring restrained	turn indicator, sensor in control loop, sensor for flight test
"	analog caging loop	sensor in control loop, sensor for flight test, sensor in low to medium accuracy strapdown attitude or navigation systems
"	pulse caging loop	as with analog caging loop but potential of higher accuracy
"	uncaged	stabilization sensor for platforms, sight-lines, guns, etc.
conventional two-degree-of-freedom (TDF) gyro	uncaged	stabilizer in low to medium accuracy attitude and heading reference instruments as artificial horizon and compass gyro
conventional and dynamically tuned TDF gyro	analog caging loops or pulse caging loops or uncaged but null sensor in stabilization control loop	as SDF gyro but only one sensor for two axes
electrostatically supported gyro	only uncaged mode possible	null sensor for platform stabilization in high accuracy INS; reference for attitude with respect to inertial space in strapdown systems
other mechanical rate sensors	no caging loop required	in general low to medium accuracy angular rate sensors
optical rate sensor, laser gyro	no caging loop required	preferably high accuracy rate and angle displacement sensor in strapdown systems

Table 3.1.1 Gyroscopic Sensors and their Applications

The SDF gyro spans the whole spectrum from the conventional angular rate sensor for control and flight test purposes to the use as a stabilization sensor on attitude reference platforms or inertial navigation platforms, and to the use as a highly accurate rate or angular displacement sensor in strapdown systems.

The TDF gyro covers the same spectrum but is also used as a simple attitude and heading reference when the instrument is not equipped with a special stabilization control loop but stabilization is achieved by means of the spinning wheel's angular momentum which has an effect similar to that of an inert mass. The accuracy of the instrument in this mode is affected by the friction in the gimbal bearings. Very clever technical solutions exist to keep this friction low. Other adverse effects caused by the gimbal mass and "gimbal lock" limit the accuracy and angular freedom of the TDF gyro with angular momentum stabilization.

TDF gyros without gimbal suspension of the rotor exist in the following versions:

- TDF gyros with limited angular freedom of the rotor with respect to the case. Fig. 3.1.2 shows two examples, the TDF gyro with spherical gas bearing and the dynamically tuned gyro, also called "dry gyro", which has to a large degree replaced the SDF gyro in stabilization loops.

- TDF gyros with unlimited angular freedoms such as the electrostatically supported gyro (ESG) shown in Fig. 3.1.3. The spherical rotor of the ESG spins in an evacuated case and is supported by electrostatic forces. In this manner friction has been suppressed to a very large extent and the gyro, once brought to its nominal spin rate, runs without drive for months. The ESG serves as a stabilization sensor for high-accuracy inertial navigation platforms as well as an attitude reference in strapdown systems.

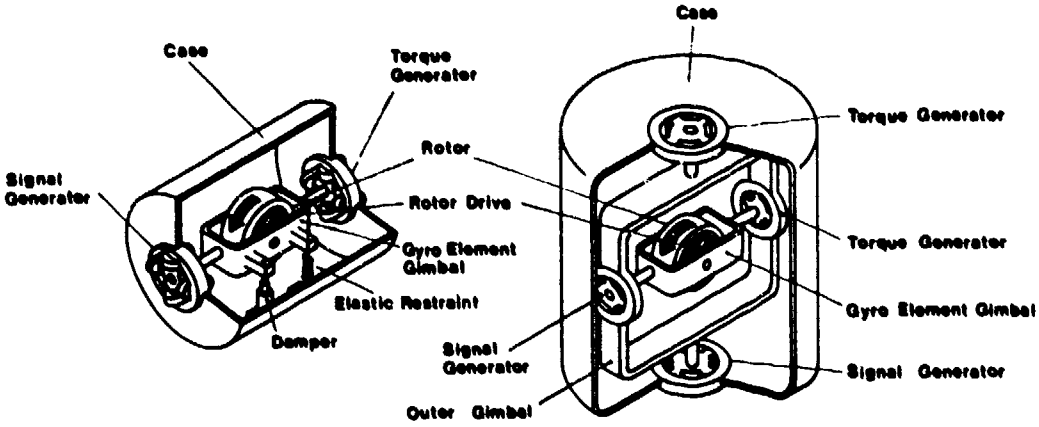

a) Single-Degree-of-Freedom (SDF) Gyro b) Two-Degree-of-Freedom (TDF) Gyro

Fig. 3.1.1 The Essential Elements of Mechanical Gyros

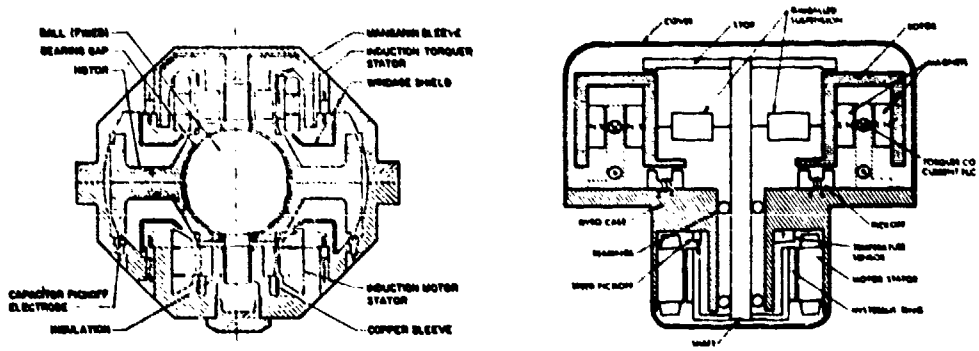

a) TDF Gyro with Spherical Gas Bearing (North American Aviation, Inc.)

b) Dynamically Tuned Gyro (Teledyne)

Fig. 3.1.2 Two Examples of TDF Gyros with Limited Angular Freedom of the Rotor with Respect to the Case

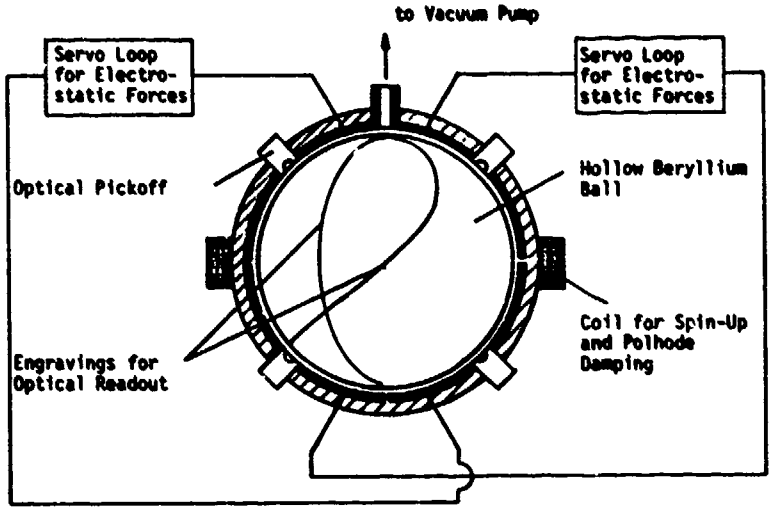

Fig. 3.1.3 Example of a TDF Gyro with Unlimited Angular Freedom of the Rotor with Respect to the Case - Electrostatically Supported Gyro (ESG)

Somewhat related to the ESG are the gyros with fluid rotors where the solid sphere is replaced by a fluid. Their application is limited.

There are gyros classified in Table 3.1.1 as "other mechanical rate sensors". The following physical effects are used in these mechanical rate sensors:

- The reaction of liquid metal within a spinning torus to a rotation normal to the spin axis generating an angular acceleration within the torus (Honeywell Magnetohydrodynamic (MHD) Two-Axes-Rate-Sensor),
- the reaction of an oscillating mass to a rotation (Honeywell Vibrating Wire Rate Sensor, tuning fork rate sensor),
- the deflection of a gas jet due to an angular rate normal to the jet flux (Hamilton Standard Superjet).

The optical rate sensors have a great potential for future flight tests and navigation. They use a physical effect first demonstrated by Sagnac in 1913 with a ring interferometer. Angular rate with respect to inertial space can be measured if two light beams travelling in opposite directions on a circular path in the plane normal to the angular rate to be measured are brought to interference. This physical effect is utilized in optical rate sensors or in optical rate integrating sensors, the latter being commonly known as ring laser gyros.

There are other proposals for angular rate sensors, such as nuclear magnetic resonance (NMR) gyros. To the authors' knowledge they have not passed the laboratory state. They are not included in this description.

The following discussions will mainly concern the conventional gyros with spinning wheels, which for the time being have the widest distribution in flight test, control and navigation systems. The reader's attention is also drawn with emphasis to the ring laser gyro which opens new aspects for flight test measurements.

3.2 Basic Performance Equations and Error Sources Common to Mechanical Gyros

In recent years strapdown systems (s. Chapter 7.4.4) have reached a rather mature state of the art as attitude and heading and navigation systems and they will also certainly find more and more favour as flight test systems (s. Chapter 9).

High accuracy angular rate measurements are the basis of any strapdown system, which makes it necessary to derive the deterministic and compensatable errors of a mechanical gyro in detail. Since both, single-degree-of-freedom (SDF) and two-degree-of-freedom (TDF) gyros, are used for this purpose, their dynamics and deterministic errors will be derived commonly in the next two Sections 3.2.1 and 3.2.2, thus opening the way for a better comparison of their application for this task discussed in Section 3.3 and 3.4.

The reader not interested in high accuracy performance of a mechanical gyro in a dynamic environment or the reader in a hurry will certainly find a way of scanning the next sections to familiarize himself some definitions and to arrive at the section of his interest. The results of Section 3.2 are listed in Table 3.2.1 for the SDF gyro and 3.2.2 for the TDF gyro.

3.2.1 The Performance Equation of Mechanical Single- and Two-Degree-of-Freedom Gyros

The derivation of the mechanical gyro's performance equation will be based upon Newton's law for the rotational motion (s. Eqs. (2.37) and (2.42)):

$$\underline{M} = \left.\frac{d\underline{H}^T}{dt}\right|_i = \left.\frac{d\underline{H}^T}{dt}\right|_g + \underline{\omega}^{ig} \times \underline{H}^T \qquad (3.2.1)$$

which will be applied to the gyro element shown in Fig. 3.2.1. $\underline{M}$ is the torque vector acting on the gyro element, $\underline{H}^T$ is the total angular momentum vector and

$\left.\frac{d}{dt}\right|_i$ or $\left.\frac{d}{dt}\right|_g$ denote "time derivative with respect to the inertial frame i or to the gyro element coordinate frame g, respectively".

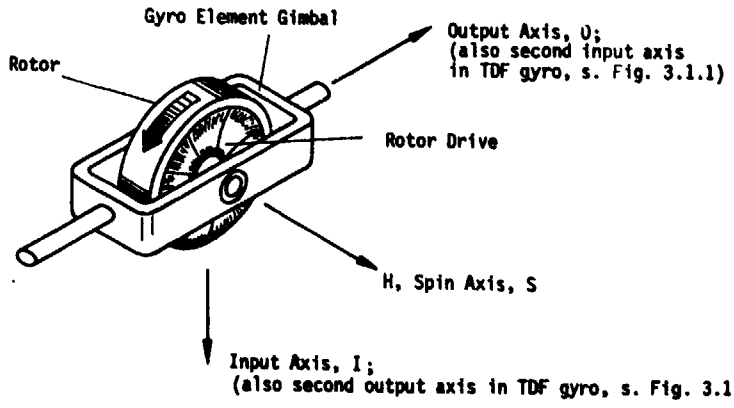

Fig. 3.2.1 Gyro Element Coordinate Frame and Notation

According to Section 2.1 we may, for most man-made instruments, establish as the inertial frame a coordinate frame, which is nonrotating with respect to the fixed stars and located with its origin in the earth's center of gravity. Its axes are oriented as shown in Fig. 2.1; its x-axis is pointing to the north pole, i.e. aligned with the earth's rotational axis, and its y- and z-axes are located in the equatorial plane. The g-frame shown in Fig. 3.2.1 will be assumed as an orthogonal coordinate frame with its origin in the center of support of the gyro element. Its S_g-axis is aligned with the spin axis of the rotor and the I_g- and O_g-axes are nonspinning and are aligned with the principal axes of the gimbal element such that products of the inertia tensor $\underline{J}$ (s. Eqs. (2.39) and (2.40)) vanish.

With the SDF gyro the O_g-axis is in general collinear with the gimbal axis, which again is approximately parallel to the torquer axis (s. Fig. 3.1.1a). With the TDF gyro the axes-orientation depends on the construction (s. Figs. 3.1.1b and 3.1.2). We will assume that its I_g- and O_g-axes are close to the torque generator axes.

Superscripts will be used in the following as physical characteristics and ω^{ig} means "angular rate of the gyro frame with respect to the inertial frame".

The main contribution to the total angular momentum vector $\underline{H}^T$ is $\underline{H}^r$ of the rotating wheel. It is, in the gimbal coordinate frame:

$$\underline{H}_g^r = \begin{pmatrix} 0 \\ 0 \\ I\,\omega_S^{ir} \end{pmatrix}_g , \tag{3.2.2}$$

with I = rotor moment of inertia about the spin axis and ω_{Sg}^{ir} = angular rate of the rotor with respect to inertial space in the direction of the spin axis. It is composed of

$$\omega_{Sg}^{ir} = (\omega_S^{ig} + \omega_S^{gm} + \omega_S^{mr})_g \tag{3.2.3}$$

where ω_{Sg}^{ig} is the angular rate of the gyro element with respect to inertial space, ω_{Sg}^{gm} is the angular rate of the motor's magnetic field vector with respect to the gimbal element and ω_{Sg}^{mr} is the angular rate of the rotor with respect to the magnetic field vector. We will use as short-hand notation

$$\omega_{Sg}^{gm} = n \qquad \omega_{Sg}^{mr} = \dot{\gamma} \qquad H = In. \tag{3.2.4a,b,c}$$

For inertial grade instruments the rotor speed n is carefully kept constant and is in the order of 400 Hz and H in the order of 10^{-3} to 10^{-1} Nms. We will define as spin angular momentum $\underline{H}_g^s$ and as gyro element angular momentum $\underline{H}_g^g$, both in the "g"-frame:

$$\underline{H}_g^s = \begin{pmatrix} 0 \\ 0 \\ I(n+\dot{\gamma}) \end{pmatrix}_g ; \qquad \underline{H}_g^g = \underline{J}\,\underline{\omega}_g^{ig} = \begin{pmatrix} J_I & 0 & 0 \\ 0 & J_O & 0 \\ 0 & 0 & J_S \end{pmatrix} \cdot \begin{pmatrix} \omega_I \\ \omega_O \\ \omega_S \end{pmatrix}^{ig} = \begin{pmatrix} J_I\,\omega_{Ig}^{ig} \\ J_O\,\omega_{Og}^{ig} \\ J_S\,\omega_{Sg}^{ig} \end{pmatrix} , \tag{3.2.5a,b}$$

where $\underline{J}$ is the inertia tensor mentioned above with components $J_{I,O,S}$, the moments of inertia of the total gyro element (e.g. gimbal plus rotor for the SDF gyro).

The total angular momentum vector in the "g"-frame is thus:

$$\underline{H}_g^T = \underline{H}^s + \underline{H}^g . \tag{3.2.6}$$

Before going more into details of the performance of a gyro in a high frequency environment, let us briefly review its performance for low input frequencies, when the spin angular momentum is predominant ($H^s >> H^g$) and constant with respect to the g-frame, i.e.

$$\left.\frac{d\underline{H}_g^s}{dt}\right| = 0.$$

With this assumption Eq. (3.2.1) can be written in the g-frame as:

$$\underline{M}_g = \left.\frac{d\underline{H}_g^g}{dt}\right|_g + \underline{\omega}_g^{ig} \times \underline{H}_g^s \tag{3.2.7}$$

where this is the torque applied to gyro element	this term causes nutation in a TDF gyro or time lag in an SDF gyro	this term describes the gyro element low frequency response, e.g. the precession in a TDF gyro.

Eq. (3.2.8) is the <u>basic law of motion of a practical gyroscopic element</u>, which simplifies for low input frequencies to:

$$\underline{M}_g = \underline{\omega}_g^{ig} \times \underline{H}_g^s . \tag{3.2.8a}$$

For the evaluation of vector equations in components the matrix notation is useful. We define an $\underline{\omega}\times$ matrix (s. [3.1] Chapter 1.9):

$$\underline{\omega}_g^{ig} \times = \begin{pmatrix} 0 & -\omega_S & \omega_O \\ \omega_S & 0 & -\omega_I \\ -\omega_O & \omega_I & 0 \end{pmatrix}_g^{ig} = \underline{\Omega}_g^{ig}; \tag{3.2.9}$$

and Eq. (3.2.8a) reads:

$$\underline{M}_g = \underline{\Omega}_g^{ig}\, \underline{H}_g. \tag{3.2.8b}$$

Evaluated in components we obtain:

$$\begin{pmatrix} M_I \\ M_O \end{pmatrix}_g = H \begin{pmatrix} \omega_O \\ -\omega_I \end{pmatrix}_g^{ig} . \tag{3.2.8c}$$

As short-hand matrix notation for this two component vector we will use

$$\underline{M}_g = H\, \hat{\underline{I}}\, \underline{\omega}^{ig}, \tag{3.2.8d}$$

where the skew symmetric unity matrix

$$\hat{\underline{I}} = \begin{pmatrix} 0 & 1 \\ -1 & 0 \end{pmatrix} \qquad \hat{\underline{I}}\,\hat{\underline{I}} = -\underline{I} = -\begin{pmatrix} 1 & 0 \\ 0 & 1 \end{pmatrix} \tag{3.2.10a,b}$$

takes into account a component and sign conversion of both sides, as with the torque and angular rate vector of a gyro. From Eq. (3.2.8d) and (3.2.10) it is easy to obtain:

$$\underline{\omega}^{ig} = -\frac{1}{H}\, \hat{\underline{I}}\, \underline{M}_g. \tag{3.2.11}$$

Eqs. (3.2.8) and (3.2.11) are the <u>practical gyro element performance equations</u> relating the torque $\underline{M}_g$ applied to the gyro element and its <u>angular rate ω^{ig} with respect to inertial space</u>. They may best be interpreted in the following way. If a torque vector $\underline{M}$ or angular rate vector $\underline{\omega}$ is applied to a gyro, the response vector - angular rate vector $\underline{\omega}$ or torque vector $\underline{M}$ - is orthogonal to both, the applied vector and the angular momentum vector $\underline{H}$ and directed in the sense which would take $\underline{H}$ by the shortest way towards the applied vector. <u>Fig. 3.2.2</u> gives an illustration of this interpretation, where we have to keep in mind that in the second case the response torque indicated <u>is the negative of the torque</u> applied to the gyro element.

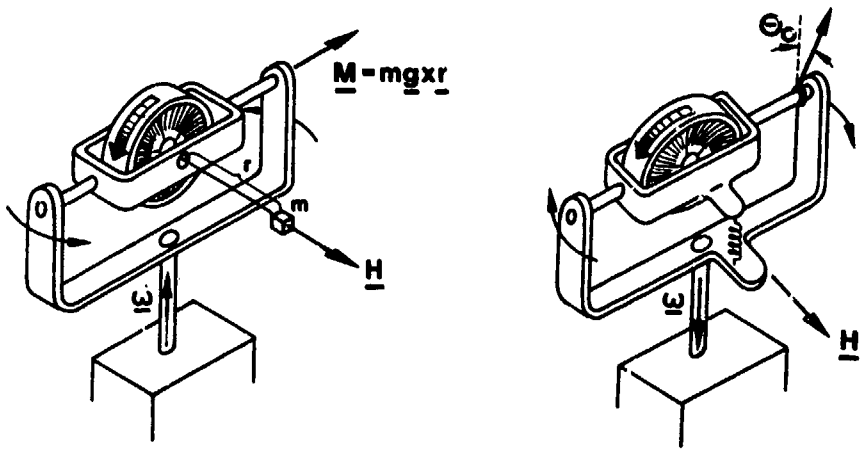

<u>M applied:</u>

Direction of response angular rate:
$\underline{H}$ vector is "hunting" the input torque vector $\underline{M}$ caused by mass m

<u>ω applied:</u>

Direction of response torque:
acts so as to take the $\underline{H}$ vector by the shortest way towards the input angular rate vector $\underline{\omega}$

Fig. 3.2.2 Illustration of the Gyro Reaction to Input Torques and Input Angular Rates

For strapdown gyros and systems, however, we cannot restrict our attention to low frequencies only. We also have to remember that until now we have carried out the derivation in the g-frame, which has angular freedom about one (SDF gyro) or two axes (TDF gyro) with respect to the gyro case. The corresponding pickoff angle depends on the input angular rate applied to the case, the torque applied to the gyro element via a torque generator and on the sensor errors. This angle is converted into the output signal. We will derive in the following the dependence of the pickoff angle on the input signals and sensor errors.

For this purpose coordinate frames have to be defined carefully because for high precision measurements, such as in strapdown systems (s. Chapter 7.4.4) where the angular rate measurements of the gyros are used for navigation purposes, misalignments of the order of arc minutes cause errors which may greatly exceed the required 1/100 °/h drift.

We will assume that the reference coordinate frame (subscript "r") in which the gyro is used within a system or on a test table is an orthogonal frame and that the axes of the gyro element coordinate frame are out-of-alignment with respect to the r-frame by the small angles $\chi_{I,O,S}$. It will also be assumed, at least for the moment, that the origins of both frames coincide. The angles $\chi_{I,O,S}$ are composed of the time varying angles $\theta_{I,O,S}$ describing the angular freedom of the orthogonal gyro element axes (s. Fig. 3.2.3) and the misalignment angles $\alpha_{I,O,S}$ (s. Fig. 3.2.4). The smallness of the angles allows us to treat them as vectors ([3.1], Appendix 3):

$$\underline{\chi} = \underline{\theta} + \underline{\alpha}. \tag{3.2.12}$$

The angles $\alpha_{I,O,S}$ may be due to imperfect mounting of the rotor within the gimbal and case, backlash of the gimbal pivots in the jewel bearings or misalignment of the gyro case with respect to the reference frame (s. Fig. 3.2.4).

The transformation matrix between the gimbal element and the reference coordinate frame is:

$$\underline{\underline{C}}_{rg} = \begin{pmatrix} 1 & -\chi_S & \chi_O \\ \chi_S & 1 & -\chi_I \\ -\chi_O & \chi_I & 1 \end{pmatrix} = \underline{\underline{I}} + \underline{\underline{\chi}}; \qquad \underline{\underline{C}}_{gr} = \underline{\underline{I}} + \underline{\underline{\chi}}^T = \underline{\underline{I}} - \underline{\underline{\chi}}, \tag{3.2.13a,b}$$

where $\underline{\underline{I}}$ is the unity matrix.

A third coordinate frame has to be defined; it is the one in which the torque is applied to the gimbal element via the torque generators. With the SDF gyro the torquer axis in general will be parallel to the case axis and to the gimbal axis. Misalignment may result from backlash in the gimbal bearings. With the TDF gyro shown in Fig. 3.1.2 the torquer axes are defined by the torquer coils. Their directions are subject to manufacturing inaccuracies. In practice the final adjustment of these axes is carried out electrically. We will assume that the torque generator coordinate frame (subscript "t"), which is nonorthogonal, may be misaligned with respect to the reference coordinate frame (by the small angles β_{ij} ($i = I,O,S$; $j = I,O,S$; $i \neq j$). The transformation matrix between the two frames (s. Fig. 3.2.5) is:

$$\underline{\underline{C}}_{rt} = \begin{pmatrix} 1 & -\beta_{IS} & \beta_{IO} \\ \beta_{OS} & 1 & -\beta_{OI} \\ -\beta_{SO} & \beta_{SI} & 1 \end{pmatrix} = \underline{\underline{I}} + \underline{\underline{\beta}}; \qquad \underline{\underline{C}}_{tr} = \underline{\underline{I}} + \underline{\underline{\beta}}^T. \tag{3.2.14}$$

Eq. (3.2.1) expressed in the torque coordinate frame, with the input signals ω contained in $\underline{\Omega}$ expressed in the reference coordinate frame, becomes:

$$\underline{M}_t = \underline{\underline{C}}_{tg}\,\underline{M}_g = \underline{\underline{C}}_{tg}\,\frac{d}{dt}\Big|_g\,(\underline{H}^s + \underline{H}^g)_g + \underline{\underline{C}}_{tr}\,\underline{\underline{\Omega}}_r^{ig}\,\underline{\underline{C}}_{rg}\,(\underline{H}^s + \underline{H}^g)_g, \tag{3.2.15}$$

where we have made use of the relationships $\underline{\underline{C}}_{tg}(\underline{\omega}_g \times \underline{H}_g) = C_{tr}(\underline{\omega}_r \times \underline{H}_r)$ and $\underline{\underline{C}}_{tg} = \underline{\underline{C}}_{rt}^T \cdot \underline{\underline{C}}_{rg}$.

Considering the freedom of the gyro element to move with respect to the gyro case, we split up $\underline{\omega}^{ig}$ into

$$\underline{\omega}_r^{ig} = \underline{\omega}_r^{ic} + \underline{\omega}_r^{cg}, \tag{3.2.16}$$

where

$$\underline{\omega}_r^{ic} = \begin{pmatrix} \omega_I \\ \omega_O \\ \omega_S \end{pmatrix}_r \tag{3.2.17}$$

is the angular motion of the case with respect to inertial space in the "r" frame. Similarly

$$\underline{\omega}_r^{cg} = \omega_g^{cg} = \begin{pmatrix} \dot{\theta}_I \\ \dot{\theta}_O \\ \dot{\theta}_S \end{pmatrix} \tag{3.2.18}$$

is the motion of the gyro element with respect to the case in the reference frame and equally in the gimbal frame when products $\dot{\theta} \times \chi$ are negligible.

Torques acting on the gimbal elements (s. Fig. 3.2.1) are composed of:

- the restraint torques $\underline{M}^r$
- the command torques $\underline{M}^t$ or command rates $\underline{\omega}^t$ applied through the torque generator

$$\underline{M}^t = \hat{\underline{\underline{I}}}\,H\,\underline{\omega}^t \tag{3.2.19}$$

- and the disturbance torques $\underline{M}^d$ causing gyro drifts $\underline{D}'$ to be derived in Section 3.2.2; they act in addition to the terms of Eq. (3.2.15).

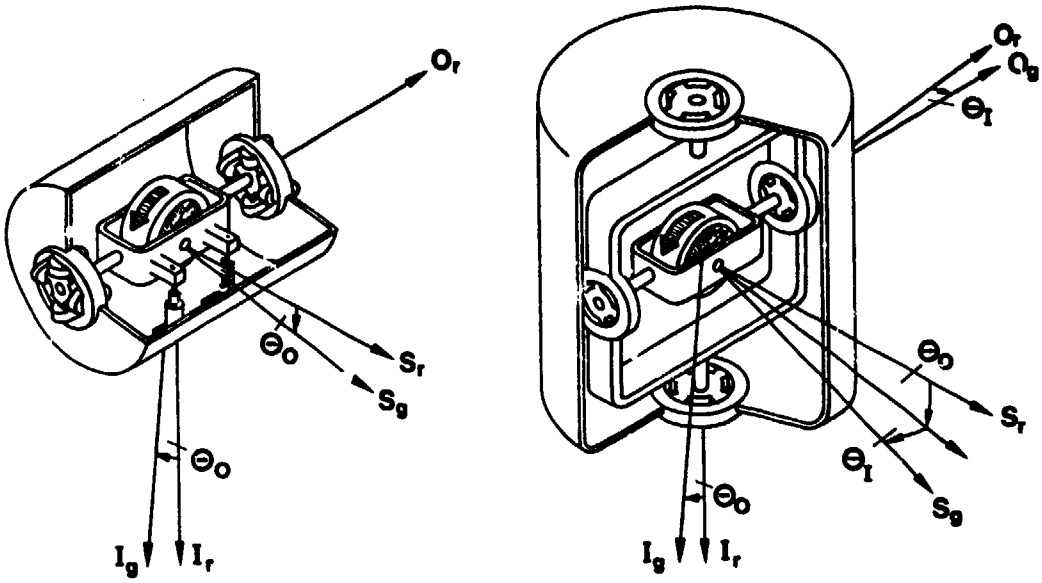

Fig. 3.2.3 Angular Freedom of the Gyro Element with Respect to the Case in the SDF and the TDF Gyro

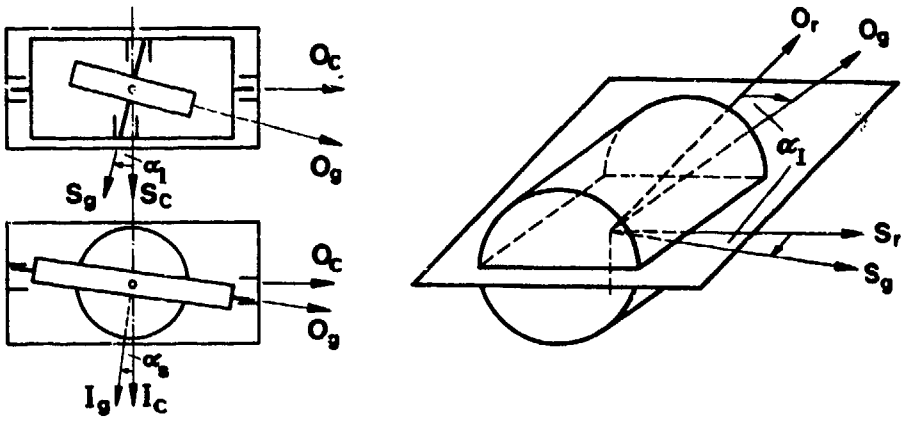

Fig. 3.2.4 Misalignment of the Gimbal Element with Respect to the Case and of the Gyro Case with Respect to the Reference Axes

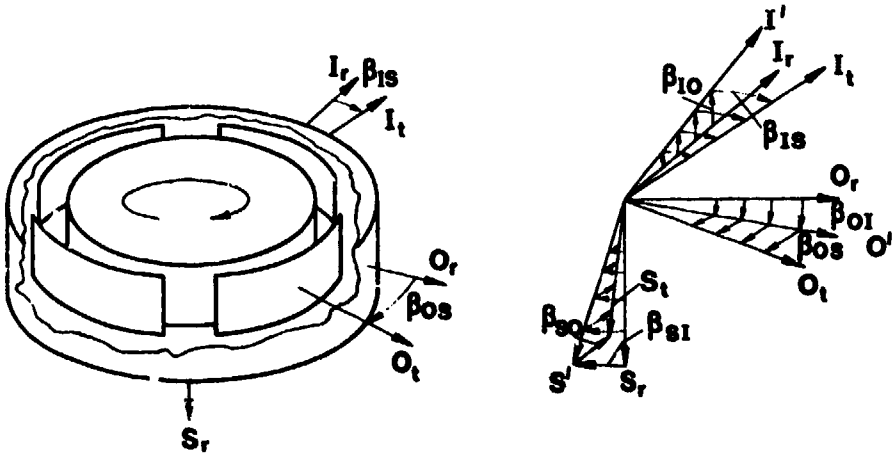

Fig. 3.2.5 Misalignment of the Torque Generator Axes with Respect to the Reference Axes

$$\underline{M}^d = \hat{\underline{I}}\, H\, \underline{D}'. \tag{3.2.20}$$

In summary

$$\frac{1}{H}\underline{M} = \frac{1}{H}\underline{M}^r + \hat{\underline{I}}\,\underline{\omega}^t + \hat{\underline{I}}\,\underline{D}'. \tag{3.2.21}$$

Introducing Eqs. (3.2.5/6/10/12/13/14/16/17/18/19/20/21) into Eq. (3.2.15) and reordering it such that the terms governing the interior dynamics of the sensor are combined on the left-hand side and the terms acting on the sensor are combined on the right hand side, we obtain the performance equation on the next page which is valid for the sensitive axes of single- and two-degree-of-freedom gyros. We have neglected in this derivation products of θ, α, β.

3.2.2 Additional Error Sources in Mechanical Gyros

3.2.2.1 Unbalance Drift

When the center of gravity of the gyro element in Fig. 3.2.1 is separated from the center of support (i.e. the origin of the "g"-frame) by

$$\underline{r} = (r_I \quad r_O \quad r_S)^T \tag{3.2.25}$$

and the acceleration vector g' acting on the center of gravity is (s. Eq. (2.5)):

$$\underline{g}' = (g'_I \quad g'_O \quad g'_S)^T \tag{3.2.26}$$

we obtain as mass unbalance drift D^u and with its time integral the error angle ε^u per velocity increment

$$\underline{D}^u = \frac{-1}{H}\hat{\underline{I}}\,\underline{M}^u = \frac{-m}{H}\hat{\underline{I}}\,\underline{r}\times\underline{g}' = \frac{m}{H}\begin{pmatrix} -r_S\, g'_I + r_I\, g'_S \\ \\ -r_S\, g'_O + r_O\, g'_S \end{pmatrix} = \underline{d}^u\,\underline{g}'\ ; \qquad \underline{\varepsilon}^u = \underline{d}^u\,\underline{\Delta V}\ . \tag{3.2.27a,b}$$

The mass unbalance drift or "g-dependent drift" defines the accuracy requirements for the calibration of gyros. The mechanical compensation is generally in the order of magnitude of d = 1 °/h/g.

For a gyro rotor with a diameter of 5 cm, a thickness of 2 cm and an angular rate of 24000 rpm the distance between the center of support and the center of gravity may only amount to:

$$r \le \frac{Hd}{mg} \approx 0.4\ \mu m. \tag{3.2.28}$$

The high quality gyros have special means to achieve this adjustment (s. Fig. 3.3.8).

According to the rule of thumb in inertial navigation the gyro drift has to be below 0.01 °/h for a navigational accuracy below 1 km/h. This number will be proved in Chapter 7. The difference between the drift of 1 °/h/g that can be obtained by adjustment and the required drift of 0.01 °/h is electrically compensated. In this regard the g-sensitive drift is considered constant, as, on an average, an aircraft is subject to only 1 g acceleration. This kind of compensation works only under the condition that the position of the float's center of support and center of gravity are stable within 1/100 of the above mentioned value, i.e.

$$\Delta r = 40\ \mathring{A} \text{ per } d = 0.01\ ^\circ/h/g. \tag{3.2.29}$$

3.2.2.2 Anisoelasticity Drift

This distance r between center of support and center of gravity can vary with the force acting on the center of gravity by (s. Fig. 3.2.6 for $K_{ii} \neq 0$ only, with i = I,S):

$$\underline{\Delta r} = m\cdot\underline{K}\cdot\underline{g}' = m\cdot\begin{pmatrix} K_{II} & K_{IO} & K_{IS} \\ K_{OI} & K_{OO} & K_{OS} \\ K_{SI} & K_{SO} & K_{SS} \end{pmatrix}\cdot\begin{pmatrix} g'_I \\ g'_O \\ g'_S \end{pmatrix}, \tag{3.2.30}$$

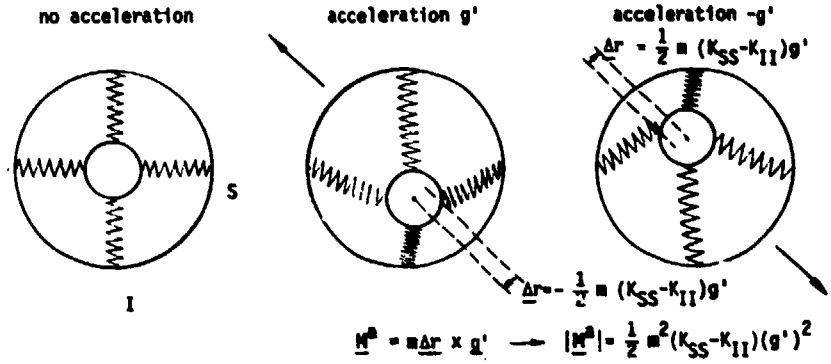

Fig. 3.2.6 Effect of Anisoelasticity

Parameters affecting the interior dynamics of the gyro

pickoff angle

restraint torque due to torsional spring and damping

$$\begin{pmatrix} J_I\, p^2 + H(1+\frac{\dot{\gamma}}{n})\,\omega_S + J_{S-0}(\omega_S^2 - \omega_0^2) & [H(1+\frac{\dot{\gamma}}{n}) + J_{S-I-0}\,\omega_S]\,p + J_{S-I}(\dot{\omega}_S + \omega_I\,\omega_0) + H\,\frac{\ddot{\gamma}}{n} \\ -[H(1+\frac{\dot{\gamma}}{n}) + J_{S-I-0}\,\omega_S]\,p - J_{S-0}(\dot{\omega}_I - \omega_I\,\omega_0) - H\,\frac{\ddot{\gamma}}{n} & J_0\,p^2 + H(1+\frac{\dot{\gamma}}{n})\,\omega_S + J_{S-I}(\omega_S^2 - \omega_I^2) \end{pmatrix} \begin{pmatrix} \theta_I \\ \theta_0 \end{pmatrix} - \begin{pmatrix} M_I^r \\ M_0^r \end{pmatrix} =$$

effect of hunting on scale factor

input signal

gimbal element and torquer misalignment error

pseudoconing and anisoinertia error

gimbal element misalignment errors

$$H(1+\frac{\dot{\gamma}}{n}) \begin{pmatrix} -\omega_0 - \alpha_I\,\omega_S + \beta_{0S}\,\omega_I \\ \omega_I - \alpha_0\,\omega_S + \beta_{IS}\,\omega_0 \end{pmatrix} - \begin{pmatrix} J_I\,\dot{\omega}_I + J_{S-0}\,\omega_0\,\omega_S \\ J_0\,\dot{\omega}_0 - J_{S-I}\,\omega_I\,\omega_S \end{pmatrix} - \begin{pmatrix} \alpha_I\,J_{S-0}(\omega_S^2 - \omega_0^2) \\ \alpha_0\,J_{S-I}(\omega_S^2 - \omega_0^2) \end{pmatrix} - \alpha_S\,J_{I-0} \begin{pmatrix} \dot{\omega}_0 - \omega_I\,\omega_S \\ \dot{\omega}_I + \omega_0\,\omega_S \end{pmatrix} - \begin{pmatrix} \alpha_0\,J_{S-I}(\dot{\omega}_S + \omega_I\,\omega_0) \\ -\alpha_I\,J_{S-0}(\dot{\omega}_S - \omega_I\,\omega_0) \end{pmatrix}$$

torquer misalignment errors

hunting misalignment error

command rate and additional gyro drift due to bias, mass-unbalance, etc. (s. Section 3.2.2)

$$- \begin{pmatrix} \beta_{0S}(J_0\,\dot{\omega}_0 - J_{S-I}\,\omega_I\,\omega_S) \\ -\beta_{IS}(J_I\,\dot{\omega}_I + J_{S-0}\,\omega_0\,\omega_S) \end{pmatrix} - \begin{pmatrix} -\beta_{S0} \\ \beta_{SI} \end{pmatrix} (J_S\,\dot{\omega}_S - J_{I-0}\,\omega_I\,\omega_0) - H\,\frac{\dot{\gamma}}{n} \begin{pmatrix} \alpha_0 - \beta_{S0} \\ -\alpha_I + \beta_{SI} \end{pmatrix} - H \begin{pmatrix} -\omega_0^t - D_0' \\ \omega_I^t + D_I' \end{pmatrix} \tag{3.2.22}$$

We have used in this relationship the abbrevations

$$J_{S-I} = J_S - J_I, \tag{3.2.23}$$

and

$$p = \frac{d}{dt}. \tag{3.2.24}$$

where $\underline{\mathfrak{K}}$ is the compliance tensor. So we obtain as anisoelasticity drift:

$$\underline{D}^a = \frac{-m^2}{H}\,\hat{\mathfrak{I}}(\underline{\mathfrak{K}}\,\underline{g}') \times \underline{g}' = \frac{m^2}{H}\begin{pmatrix} -K_{SI}g_I'^2 + K_{IS}g_S'^2 - (K_{SS} - K_{II})\,g_I'g_S' - K_{SO}g_I'g_O' + K_{IO}g_O'g_S' \\ K_{OS}g_S'^2 - K_{SO}g_O'^2 + (K_{OO} - K_{SS})\,g_O'g_S' + K_{OI}g_I'g_S' - K_{SI}g_I'g_O' \end{pmatrix} . \qquad (3.2.31)$$

The anisoelasticity causes a static drift in a vibrating environment. Its minimization puts a challenge on the design engineer and the bearing engineer to properly match the anisoelasticity of the gimbal element, the rotor and its bearings so that the total assembly is isoelastic [3.2]. The isoelasticity of the ball bearings is effected by the preload and the contact angle between the balls and the inner and outer rings. Isoelastic bearings have a contact angle of (s. Fig. 3.2.7, [3.2] and [3.3]):

$$\alpha = \tan^{-1} 1/\sqrt{2} = 35.3^0. \qquad (3.2.32)$$

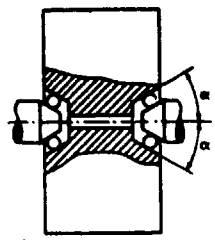

Fig. 3.2.7 Bearings of a Gyroscope Rotor

3.2.2.3 Motor Hunting Drift

The drift due to motor hunting, i.e. in Eq. (3.2.22) the terms:

$$\frac{\dot{\gamma}}{n}\begin{pmatrix}\omega_I \\ \omega_O\end{pmatrix} = \frac{1}{n}\left(\frac{\dot{\gamma}}{\omega_S}\right)\omega_S\begin{pmatrix}\omega_I \\ \omega_O\end{pmatrix} = \underline{D}^h \qquad (3.2.33)$$

may cause trouble at higher input frequencies in single- and two-degree-of-freedom gyros. The rotor may oscillate with respect to the constantly rotating magnetic field vector at higher amplitudes, especially if the damping of the motor is low - as for instance in hysteresis motors - and the gyro case is vibrating about the spin axis near the hunting frequency. For hysteresis motors this is in the range of 1 to 10 Hz. Modern strapdown gyros use motors with electronic speed control. This control network raises the damping to values of $\zeta = 0.2$, approximately. Fig. 3.2.8 is valid also for these motors.

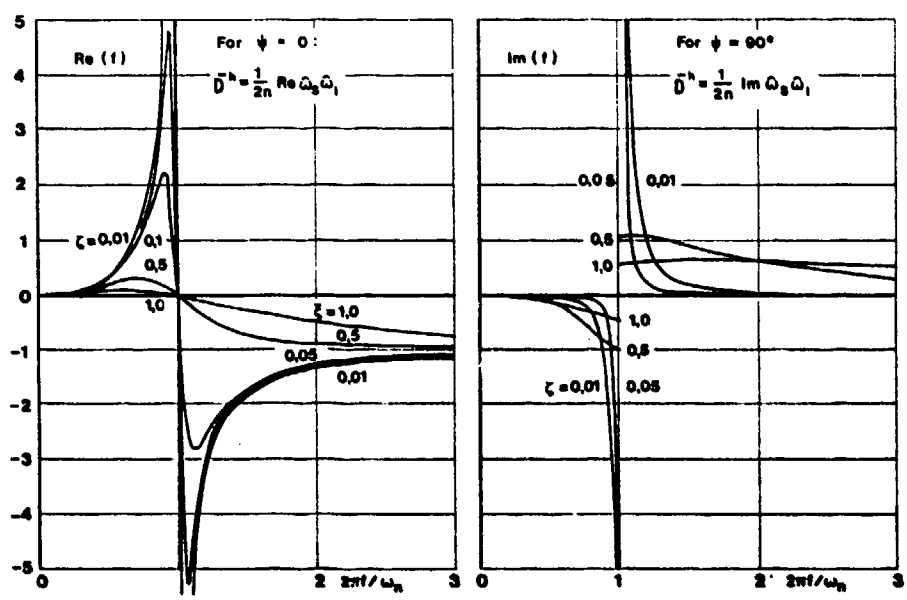

Fig. 3.2.8 Frequency Plot of the Drift Coefficients Due to Motor Hunting

The dynamics of the relative motion $\dot{\gamma}$ between rotor and magnetic field vector due to case vibration ω_s about the spin axis is comparable to that of the balance wheel in a wrist watch (~ indicates Laplace domain):

$$\frac{\tilde{\gamma}_0}{\tilde{\omega}_i} = \frac{\dot{\tilde{\gamma}}}{\tilde{\omega}_s} = \frac{-Is^2}{Is^2 + Cs + K} = \frac{-(s/\omega^n)^2}{(s/\omega^n)^2 + 2\zeta(s/\omega^n)+1} = Re + jIm \qquad (3.2.34)$$

with the natural frequency ω^n, the damping ratio ζ,

$$\omega^n = (K/J)^{1/2} \qquad \zeta = \frac{C}{2K}\,\omega^n \qquad (3.2.35)$$

the real part Re and the imaginary part Im of the transfer function $\frac{\dot{\tilde{\gamma}}}{\tilde{\omega}_s}$.

With $\omega_{I,0} = \hat{\omega}_{I,0} \sin 2\pi ft$ and $\omega_s = \hat{\omega}_s \sin(2\pi ft+\psi)$, we obtain for the mean hunting drift:

$$\bar{D}^h_{I,0} = \frac{\hat{\omega}_s\,\hat{\omega}_{I,0}}{2n}\,(Re\cos\psi + Im\sin\psi), \qquad (3.2.36)$$

where Re and Im have to be taken from Fig. 3.2.8. Re approaches -1 at high frequencies, when the rotor can no longer follow the gyro case vibration about the spin axis. Im is different from zero only in the neighbourhood of the resonance frequency. The compensation of this error is discussed in Section 7.4.4.

3.2.2.4 Errors Due to Gimbal Bearing Friction in SDF Gyros

In floated SDF and TDF gyros the gyro element is in general supported by pivot/jewel bearings or ball bearings. Uncertainties due to the friction in the bearings may arise, primarily if these gyros are used in strapdown systems (e.g. SDF gyros).

Fig. 3.2.9 shows the forces acting in the gimbal bearings of an SDF gyro due to an angular rate about the output axis ($F' = H\,\omega_0/c$). These again cause an uncertainty torque ($M = \mu b|F'|$) and an angular rate insensitivity ($\delta\omega_I = 2M/H$) of twice the amount of the friction effect in one direction (s. Fig. 3.2.10a).

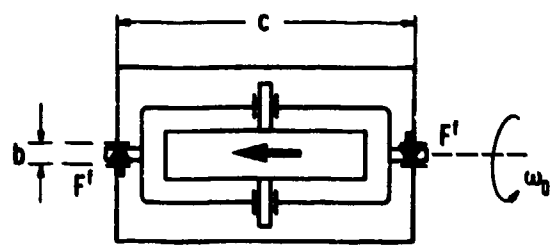

Fig. 3.2.9 Forces Acting on the Gimbal Bearing in an SDF-Gyro and Causing Friction Torques

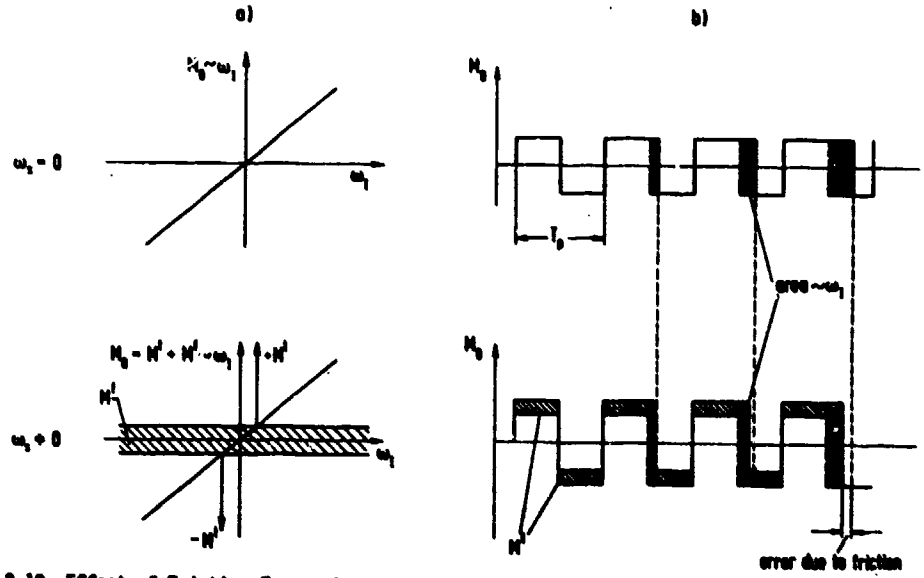

Fig. 3.2.10 Effect of Friction Torque in an SDF-Gyro on the Output Characteristics in an Analog Rebalance Loop (a) and Binary Pulse-Width-Modulation Rebalance Loop (b)

$$d_0^f = \frac{\delta\omega_I}{|\omega_0|} = 2\mu\,\frac{b}{c} = \frac{1\ ^\circ/h}{^\circ/s}\,. \tag{3.2.37}$$

where we used the following values: for the friction coefficient $\mu = 0.01$ (tungsten carbide pivots [3.4]), for the pivot diameter $b = 0.05$ cm and for the gimbal length $c = 5$ cm.

So far we have assumed that the SDF strapdown gyro with gimbal friction is equipped with an analog caging loop, where the torque M of the torque generator is proportional to the input rate ω_I. If the caging loop is a binary pulse-width modulation loop (s. Chapter 4), the SDF gimbal is constantly torqued from the negative to the positive direction about the output axis by means of torque pulses, the sum of which is proportional to the input rate. Friction reduces the torque pulses by M^f resulting in a drift, or a scale factor error of (s. Fig. 3.2.10b)

$$D^f = \mu\,\frac{b}{c}\,\frac{|\omega_0|}{\omega_{Imax}}\,\omega_I\ ; \qquad \kappa^f = \frac{\delta S}{S} = \mu\,\frac{b}{c}\,\frac{|\omega_0|}{\omega_{Imax}} = 1 \text{ ppm per } \omega_0 = 1\ ^\circ/s. \tag{3.2.38a,b}$$

3.2.2.5 Errors Due to Hydrodynamic Effects in TDF Gyros

The following considerations apply only to the "free rotor gyro (FRG)" and the "dynamically tuned gyro (DTG)" shown in Figs. 3.1.2a and b and not to the gimballed TDF gyro shown in Fig. 3.1.1b. The FRG and the DTG exhibit error sources due to constant and changing misalignments ($\chi = \theta + \alpha$, s. Eq. (3.2.12) and Fig. 3.2.3) of the rotor and the motor shaft with respect to the case. They are called "gyro spring rate coupling errors" acting as direct and cross-coupling components whereby:

- the direct coupling drift terms $d_{II}^s\,\chi_I$ and $d_{00}^s\,\chi_0$ are primarily due to hydrodynamic viscous shear torques and motor torques and
- the cross coupling drift terms $d_{I0}^s\,\chi_0$ and $d_{0I}^s\,\chi_I$ are primarily due to hydrodynamic pressure torques and electromagnetic interference between rotor, torquer and pickoff (s. Fig. 3.2.11).

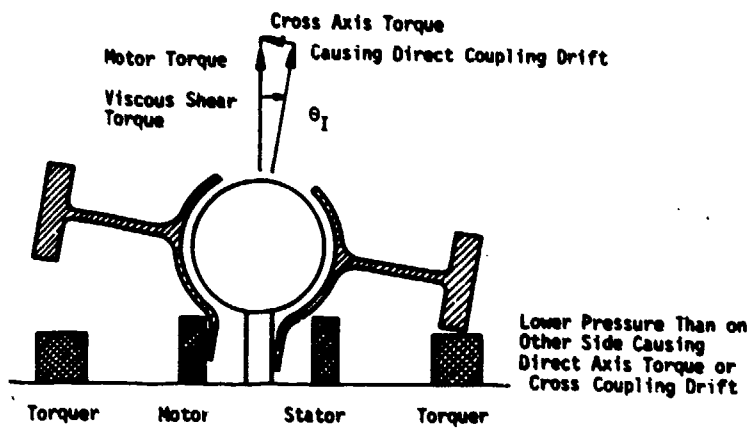

Fig. 3.2.11 Direct and Cross Coupling Drift in a Free Rotor Gyro

To include these terms into the performance equation for the FRG we have to introduce into Eq. (3.2.22) as additional drift components:

$$\underline{D}^s = \begin{pmatrix} -d_{II}^s & d_{I0}^s \\ -d_{0I}^s & -d_{00}^s \end{pmatrix} \cdot \begin{pmatrix} \theta_I + \alpha_I \\ \theta_0 + \alpha_0 \end{pmatrix} \tag{3.2.39}$$

It will be shown in Section 3.4.3 that these drift terms affect the dynamics of the sensor and cause the misaligned gyro rotor to carry out a coning motion which spirally converges to its equilibrium. The time constant and the period of this motion are for the Autonetics G 10B FRG [3.5] whose torquers are placed in a way similar to Fig. 3.2.11:

$$T_{II} = 1/d_{II} = T_{00} = 50\ s \qquad\qquad T_{I0} = 1/d_{I0} = T_{0I} = 5\ s. \tag{3.2.40a,b}$$

This gyro is fairly sensitive to rotor misalignments, since the periods T_{I0} and T_{0I} are small. Other Autonetics FRG's have larger values for these periods. In a DTG they can be easily increased by properly setting the tuning frequency, i.e. by causing the residual negative or positive spring constant due to mistuning to cancel d_{I0} or d_{0I}. This will be discussed more in detail in Section 3.4.5. In this respect the DTG is superior to the FRG. Routine adjustments to 0.002 °/h/arc-sec are made on standard DTG's and 0.0002 °/h/arc-sec is achievable.

The stability of the direct and cross coupling drift depends on the tightness of the rebalance loop and the stability of the pickoff plane.

3.2.2.6 Gyro Scale Factor Error

If mechanical gyros are used as angular rate sensors, they are in general equipped with a rebalance loop through an electronic network from the gyro pickoff to the gyro torquer, as described in Section 3.3.3.2 for the single-degree-of-freedom gyro. The rebalance loop acts similarly to the spring in Fig. 3.2.2.

For low input frequencies the torque M^t of the torque generator which drives θ to zero is a measure for the input angular rate ω_I minus gyro drift discussed in the previous sections:

$$M_0^t = -H(\omega_I - D). \tag{3.2.41a}$$

The torque M_0^t again is related to the current i by the torquer scale factor S^t or the command rate scale factor S^T:

$$M_0^t = S^t\, i = HS^T\, i. \tag{3.2.42}$$

In general the command rate scale factor is called the torquer scale factor of the gyro. We thus obtain:

$$i = \frac{-H}{S^t}(\omega_I - D) = \frac{-1}{S^T}(\omega_I - D). \tag{3.2.41b}$$

The corresponding output voltage u = Ri taken over a precision resistor is:

$$u = -R\frac{H}{S^t}(\omega_I - D) = \frac{-R}{S^T}(\omega_I - D) = \frac{-1}{S}(\omega_I - D). \tag{3.2.41c}$$

The actual gyro scale factor is thus:

$$S = \frac{S^t}{RH} = \frac{S^T}{R}. \tag{3.2.43}$$

The nominal gyro scale factor S^x used for the evaluation of the output voltage u is based on the nominal values of R^x, H^x and S^{tx} and is in error against the actual gyro scale factor S by

$$\frac{\delta S}{S} = \kappa = \frac{\delta S^t}{S^t} - \frac{\delta R}{R} - \frac{\delta H}{H}, \tag{3.2.44a}$$

so that

$$S^x = S\,(1 + \kappa). \tag{3.2.44b}$$

The measured angular rate is thus:

$$\omega^x = -S^x\, u = (1 + \kappa)\,(\omega_I - D), \tag{3.2.45}$$

where κ comprises all scale factor errors, the uncertainties of the precision resistor (δR), of the angular momentum (δH) and above all of the torque generator (δS^t). The drift D comprises all error terms which are summerized in Section 3.2.3.

Eq. (3.2.44a) shows the dominant role of the linearity and stability of the torquer scale factor S^t and the constancy of the gyro's angular momentum H in the accurate readout of the sensor. It is interesting to note that these requirements for linearity and stability do not exist for the gain of the caging loop electronics (caging loop without torquer, s. Section 3.3.3.2).

A typical model for the scale factor error of mechanical inertial instruments in the electrical rebalance mode of operation is given by (s. [3.6], Chapter 2, Eqs. (10), (41) and (62)):

$$\kappa = \kappa^c + \kappa^a \frac{\omega_I}{|\omega_I|} + \kappa^l\, \omega_I + \kappa^n\, \omega_I^2 \tag{3.2.46}$$

where, as illustrated in Fig. 3.2.12:

κ^c = basic "fixed" scale factor; depends primarily on the torque generator stability, hysteresis and temperature sensitivity, which for Samarium Cobalt magnets, a commonly used material in permanent magnet torque generators, is in the order of magnitude of

420 ppm/K; (3.2.47)

κ^a = scale factor asymmetry error, when the positive scale factor S^+ is different from the negative one S^- and a common value is used for both; κ^a causes a rectified drift if the sensor is exposed to a vibrating environment; for $\omega_I = \hat{\omega}_I \sin 2\pi ft$ we obtain the following mean drift:

$$D^s = \frac{\hat{\omega}_I}{\pi}\left(\frac{S^+ - S^-}{S}\right)$$

or the requirement that

$$\frac{S^+ - S^-}{S} \leq 10 \text{ ppm for } \omega_I = 1\ ^\circ/\text{s and } D^s \leq 0.01\ ^\circ/\text{h}; \tag{3.2.48}$$

κ^l, κ^n = linearity errors that modify the scale factor error under high rates; they depend among others:

- on the tightness of the rebalance loop (small pickoff angle minimizes the electromagnetic interference between rotor, pickoff and torquer)
- and also on the torquer design in a binary pulse-width modulation rebalance loop (the torque pulses may cause eddy currents depending on the input signal [3.7]).

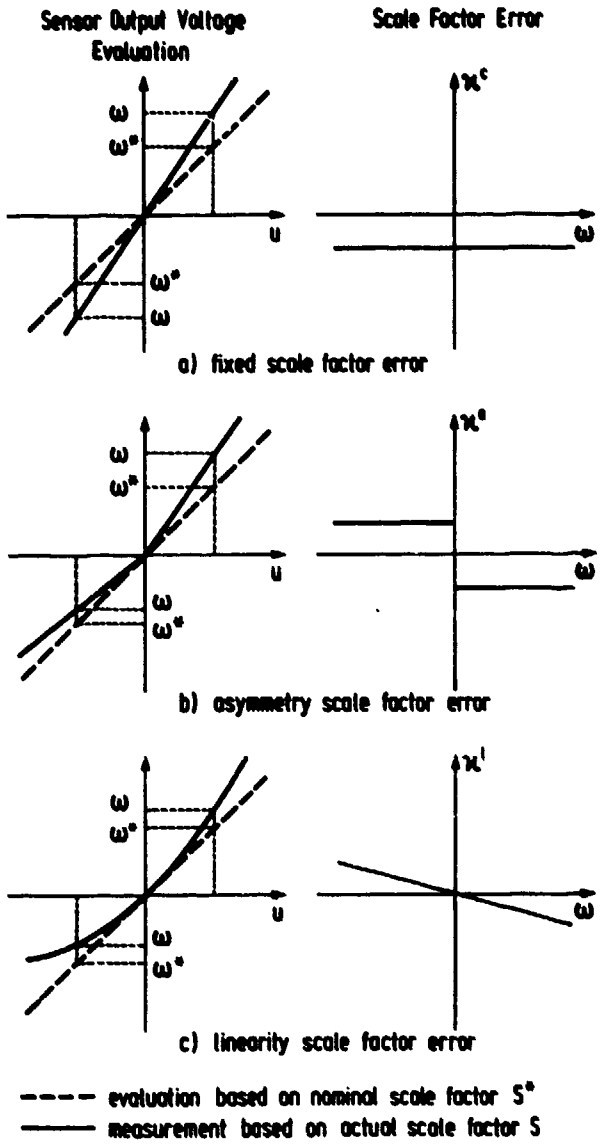

Fig. 3.2.12 Gyro Scale Factor Error Model

3.2.2.7 Errors not Included in the Analysis

There are error sources which vary from sensor to sensor and which can hardly be analysed in general. If stable from test to test, they can be modelled empirically. Some of them are listed below. They may be due to

- a residual spring torque of the "pig tails", i.e. the thin current leads from the gyro case to the gimbal element
- magnetic interferences from the pickoff and torquer; they depend on the angle between the gyro case and the sensitive element, i.e. on the stability of the pickoff plane
- temperature changes, especially in floated gyros, where the drift due to mass unbalance depends on the temperature
- the flow of the flotation liquid due to temperature gradients in floated gyros, where the gyro element is kept buoyant in the liquid (s. Section 3.3.3)
- the unsymmetric flow of the gas in double integrating gyros, where the gyro element is kept buoyant by means of a hydrostatic gas bearing (s. Section 3.3.4)

- the sensitivity to vibrations at spin frequency when the rotor has mass unbalance

- the sensitivity to vibrations at twice the spin frequency in dynamically tuned gyroscopes (DTG, s. Section 3.4.4)

- the random torques, due to ball bearing noise, for instance (random errors due to the digitizing process are treated in Chapter 4).

3.2.3 Summary of Deterministic Errors and Comments on their Compensation

The results of the previous sections are summarized in the Tables 3.2.1a to 3.2.2b on the next pages. As compared to Eq. (3.2.22) terms of no significance have been omitted.

The Tables 3.2.1a and 3.2.1b apply to the SDF gyro and include the nomenclature and symbols as used by the "Gyro and Accelerometer Subcommittee of the IEEE Aerospace and Electronic Systems Society" in its Standard Specification Format Guide and Test Procedure for Single-Degree-of-Freedom Rate Integrating Gyros" and its "Supplement for Strapdown Application" [3.8]. Also included in these tables are assessments on the requirements for error compensation in an INS (drift $\leq$ 0.01 °/h) and in an AHRS (attitude and heading reference system, drift $\leq$ 5 °/h), whereby we have assumed a fairly benign dynamic environment of 1 °/s RMS random angular rate, 0.1 g mean acceleration and 0.5 g RMS random acceleration.

The Tables 3.2.2a and 3.2.2b apply to the TDF gyro. We have assumed for the numerical evaluation of dynamic errors depending on the gyro's moments of inertia that the rotor is a ring with an outer diameter of 50 mm, an inner diameter of 30 mm and a width of 10 mm. We thus obtain the following moments of inertia

$I = 416 \text{ gm cm}^2$ about the spin axis,

$J = 216 \text{ gm cm}^2$ about the transverse axes. (3.2.49a,b)

The single-degree-of-freedom floated gyro and the dynamically tuned two-degree-of-freedom gyro have proven excellent performance in platform systems. The terms in Tables 3.2.1a and 3.2.2a are fairly stable for sensors of "inertial quality" and are hence compensable.

When mechanical gyros are exposed to the dynamic environment of strapdown systems their performance deteriorates condiderably, primarily

- due to the sensors' misalignment (s. Table 3.2.1a, Row 4 and Table 3.2.2a, Row 5),

- due to the command rate scale factor errors (s. Table 3.2.1a, Row 5 and Table 3.2.2a, Row 8) and

- due to the fact that the sensing element is not massless and dynamic errors arise (s. Tables 3.2.1b and 3.2.2b).

The deterministic error model in these cables may serve as a basis for error compensation once the coefficients have been defined as a result of laboratory tests and flight tests (s. [3.8] and [3.9]). The assessment of the compensation accuracy leaves the impression that the requirements for the use of both sensors, the SDF and the TDF gyro, in an attitude and heading reference system (AHRS) can be met easily, but seem very hard to meet in an inertial navigation system (INS). However publications on flight test results with strapdown navigation systems using DTG's (Litton LN-50, Teledyne TDY-704A) on board an executive jet [3.11] and a civil transport aircraft [3.12] are promising in this respect ($\leq$ 1 NM/h).

Gyro error compensations were implemented in the LN-50 for [3.11]:

- Bias
- g-dependent drift
- misalignment of pickoff plane and gyro spin axis
- motor hunting
- anisoinertia and
- output axis angular acceleration.

In a more severely dynamic environment additional performance degradation will arise

- due to the limited bandwidth of the sensors (in the order of 80 to 200 Hz) and the compensation algorithms and

- due to non-detected error terms.

Scientists put much hope on the ring laser gyro which at the expense of size promises improved performance in a dynamic environment.

In the next few sections we will discuss the use of SDF and TDF gyros as angular rate sensors and as stabilization devices.

No.	D =	IEEE Subcommittee Error Model and Symbols [3.8]	Nomenclature and Symbols Used in this Volume
1	D^c	D_F	acceleration insensitive drift rate D^c
2	$-\frac{m}{H}[r_S g_I' - r_I g_S']$	$+ D_I g_I' + D_0 g_0' + D_S g_S'$	acceleration sensitive drift rate $D^u = d_I^u g_I' + d_0^u g_0' + d_S^u g_S'$
3	$+\frac{m^2}{H}[K_{IS} g_S'^2 - K_{SI} g_I'^2$ $- (K_{SS} - K_{II}) g_I' g_S'$ $- K_{S0} g_I' g_0' + K_{I0} g_0' g_S']$	$+ D_{II} g_I'^2 + D_{SS} g_S'^2$ $+ D_{IS} g_I' g_S'$ $+ D_{I0} g_I' g_0' + D_{0S} g_0' g_S'$	acceleration-squared sensitive drift rate or anisoelasticity drift rate $D^a = d_{II}^a g_I'^2 + d_S^a g_S'^2$ $+ d_{IS}^a g_I' g_S'$ $+ d_{I0}^a g_I' g_0' + d_{0S}^a g_0' g_S'$
4	$-\alpha_0 \omega_S + \beta_{IS} \omega_0$		misalignment drift rate $D^m = d_S^m \omega_S + d_0^m \omega_0$
5	$+ \kappa \omega^t$	$+ \delta K_T i$	drift rate due to gyro scale factor error $D^s = [\kappa^c + \kappa^a \frac{\omega^t}{\lvert\omega^t\rvert} +$ $\kappa^l \omega^t + \kappa^n (\omega^t)^2]\omega^t$
6	+ other terms	+ other terms	

a) $g_i' = \hat{g}_i' \sin 2\pi ft$ $\qquad g_k' = \hat{g}_k' \sin (2\pi ft + \psi)$

Table 3.2.1a Deterministic Error Model of a Single-Degree-of-Freedom

Remarks	Requirements for Compensation in an INS (D<0.01 °/h)	AHRS (D<5 °/h)
due to residual torques (pig tails, inductive pickoff and torquer), fluid and gas flow, temperature effects; may vary with time and has to be recalibrated	<0.01 °/h	<5 °/h
s. Sections 3.2.2.1 and 3.3.4; due to unbalance (temperature sensitive), turbine torques	<0.1 °/h/g if mean acceleration < 0.1 g	<50 °/h/g
s. Section 3.2.2.2; due to compliance of gimbal element and bearing; always rectifying in a vibrating environment; varying with high frequencies [3.9]	<0.04 °/h/g² if linear vibration < 0.5 g (RMS)	<20 °/h/g²
rectifying only when g_i' and g_k' are correlated; $\overline{D^a} = \frac{1}{2} d^a_{ik}\ \hat{g}_i'\ \hat{g}_k'\ \cos\psi^{a)}$		
for unidirectional angular rates α and β may be regarded as error angles per 1 rad angular motion	in strapdown systems α and β <20 arc sec for a tolerable error angle per turn of <2 arc min	<3 arc min <20 arc min
s. Section 3.2.2.6; ω^t = earth rate + transport rate in platform environment; ω^t = vehicle's angular rate in strapdown environment;		
i fixed scale factor error due to temperature sensitivity of torquer resulting in error angle per turn;	in strapdown systems κ: <100 ppm for a tolerable error angle per turn of <2 arc min	<1000 ppm <20 arc min
ii asymmetry scale factor error resulting in rectified drift in vibrating environment (s. Eq. (3.2.48));	<10 ppm if angular vibration <1 °/s (RMS)	<4000 ppm
iii nonlinearity scale factor error, troublesome at high rates, resulting in error angle per turn, s. above.	<200 ppm	<1000 ppm

Gyro in a Platform and Strapdown Environment

No.	ΔD	IEEE Subcommittee Error Model and Symbols [3.8]	Nomenclature and Symbols Used in this Volume
1	$\frac{\dot{\gamma}}{n}\omega_I$		drift due to motor hunting rate $\dot{\gamma}$ $D^h = f(\omega_S, \omega_I)$
2	$-\frac{J_0}{I}\frac{\dot{\omega}_0}{n}$	$-\frac{J_0}{H}\dot{\omega}_0$	angular acceleration $D^p = d^p\,\dot{\omega}_0$
3	$+\frac{(J_S - J_I)}{I}\frac{\omega_S\,\omega_I}{n}$	$+\frac{J_S - J_I}{H}\omega_S\,\omega_I$	anisoinertia drift rate $D^i = d^i_{SI}\,\omega_S\,\omega_I$
4	$-\theta_0\,\omega_S$	$-\theta_0\,\omega_S$	cross coupling drift rate $D^c = f(\omega_I\,\omega_S)$
5a	$2\mu\frac{b}{c}\lvert\omega_0\rvert$		measurement dead band due to gimbal bearing friction if analog caging loop is used $D^f = d^f_0\,\lvert\omega_0\rvert$
5b	$\mu\frac{b}{c}\frac{\lvert\omega_0\rvert}{\omega_{Imax}}\omega_I$		drift or scale factor error due to gimbal bearing friction if binary pulse-width modulation caging loop is used $D^f = d^f_{0I}\,\lvert\omega_0\rvert\,\omega_I = \kappa^f\,\omega_I$
6		$+D_\omega(\omega_0)$	output axis rate error
7	+ other terms	+ other terms	

a) $\omega_{I,0} = \hat{\omega}_{I,0}\sin 2\pi ft$ $\qquad \omega_S = \hat{\omega}_S \sin(2\pi ft + \psi)$

b) $\omega_0 = \hat{\omega}_0 \sin 2\pi ft = \omega_I$ for a second gyro in a system; s. Section 7.4.4 for computation of this pseudo-coning error at system level

Table 3.2.1b Additional Deterministic Error Terms of a

Remarks	Requirements in an INS ($D < 0.01\ ^{o}/h$)	AHRS ($D < 5\ ^{o}/h$)
s. Section 3.2.2.3; rectifying if ω_I and ω_S are correlated; $\overline{D^h} = \frac{\hat{\omega}_S\ \hat{\omega}_I}{2n}(\mathrm{Re}\cos\psi + \mathrm{Im}\sin\psi)$ a) with Re and Im from Fig. 3.2.8; for frequencies above hunting frequency (1 to 10 Hz): Re → -1.	above hunting frequency $\hat{\omega}_S\ \hat{\omega}_I \leq 1(^{o}/s)^2$; otherwise compensation, s. Section 7.4.4.4	no special means required for suppressing this effect
s. Section 7.4.4.3.4; giving rise to pseudoconing error on system level; $\overline{D^p} = \frac{J_0}{2I}\frac{\hat{\omega}_0^2}{n}$ b) can be optimized by proper output axis orientation;	for $J_0/H = 10\ ^{o}/h(^{o}/s^2)$, as typical value for an SDF gyro, and $\hat{\omega}_0 = 1\ ^{o}/s$ (RMS): $\bar{d} = 5\ ^{o}/h$ compensation necessary	$\bar{d} = 5\ ^{o}/h$ compensation not absolutely necessary
rectifying only if ω_S and ω_I are correlated: $\overline{D^T} = \frac{J_S - J_I}{2I}\ \frac{\hat{\omega}_S\ \hat{\omega}_I}{n}\ \cos\psi$ a)	for $(J_S-J_I)/H = 0.03\ ^{o}/h(^{o}/s)^2$ as typical value for an SDF gyro, and $\hat{\omega}_S\ \hat{\omega}_I = 1(^{o}/s)^2$: compensation necessary	no compensation necessary
rectifying only if ω_S and ω_I or ω_0 are correlated; can be kept low with high loop gain; attributable to scale-factor error, s. Eq. (3.3.3).		
Spin-input rectification: $\overline{D^C} = [\frac{\theta_0}{\omega_I}]\ \omega_I\ \ \omega_S = \frac{\hat{\omega}_I\ \hat{\omega}_S}{2}(\mathrm{Re}\cos\psi + \mathrm{Im}\sin\psi)$ a) with Re and Im = real and imaginary part of gyro closed-loop transfer function, $[\theta_0/\omega_I]$ s. Eq. (3.3.18).	requirement for closed loop transfer function: Re or Im $<0.6\ \frac{\text{arc sec}}{^{o}/s}$ per $\hat{\omega}_{I,0}\ \hat{\omega}_S \leq 1\ (^{o}/s)^2$	no demanding requirements for closed-loop transfer function
Spin-output rectification: $\overline{D^C} = [\frac{\theta_0}{\omega_0}]\ \omega_0\ \ \omega_S = \frac{\hat{\omega}_0\ \hat{\omega}_S}{2}(\mathrm{Re}\cos\psi + \mathrm{Im}\sin\psi)$ a) with Re and Im = real and imaginary part of gyro closed-loop transfer function $[\theta_0/\omega_0]$.		
s. Section 3.2.2.4; μ = friction coefficient; b = pivot diameter; c = gimbal length; countermeasures: dithered jewel bearings, ball bearings, taut wire suspension.	for pivot/jewel bearings ≈ 1 $^{o}/h/(^{o}/s)$ not tolerable	tolerable
s. Section 3.2.2.4; scale factor error $\kappa^f = \mu\frac{b}{c}\frac{\lvert\omega_0\rvert}{\omega_{Imax}}$ apparent input axis misalignment; function of various orders of ω_0; may be discontinuous; depending on gimbal support including flotation fluid [3.8]	for pivot/jewel bearings ≈ 1 ppm/$(^{o}/s)$ tolerable	tolerable

No.	D_I	D_0 =	Nomenclature and Symbols Used in this Volume
1	D_I^c	D_0^c	acceleration insensitive drift rate $D^c_{I,0}$
2	$-\frac{m}{H}[r_S g'_I - r_I g'_S]$	$-\frac{m}{H}[r_S g'_0 - r_0 g'_S]$	acceleration sensitive drift rate $D^u = \sum i\, d_i^u\, g'_i$
3	$+ D_0^g g'_0$	$+ D_I^g g'_I$	"
4	$+\frac{m^2}{H}[K_{IS} g'^2_S - K_{SI} g'^2_I$	$+\frac{m^2}{H}[K_{0S} g'^2_S - K_{S0} g'^2_0$	acceleration - squared sensitive drift rate or anisoelasticity drift rate
	$- (K_{SS} - K_{II}) g'_I g'_S$	$- (K_{SS} - K_{00}) g'_0 g'_S$	$D^a = \sum i \sum j\, d^a_{ij}\, g'_i g'_j$
	$- K_{S0} g'_I g'_0 + K_{I0} g'_0 g'_S]$	$+ K_{0I} g'_I g'_S - K_{SI} g'_I g'_0]$	"
5	$- \alpha_0 \omega_S + \beta_{IS} \omega_0$	$+ \alpha_I \omega_S - \beta_{0S} \omega_I$	misalignment drift rate $D^m = \sum i\, d_i^m\, \omega_i$
6	$- d_{II} \alpha_I + d_{I0} \alpha_0$	$- d_{00}\alpha_0 - d_{0I} \alpha_I$	direct and cross axis spring rate coupling due to misalignment $D^\alpha = \sum i\, d_i^\alpha\, \alpha_i$
7	$- d_{II} \theta_I + d_{I0} \theta_0$	$- d_{00} \theta_0 - d_{0I} \theta_I$	direct and cross axis spring rate coupling due to control offset $D^\theta = \sum i\, d_i^\theta\, \theta_i$
8	$+ \kappa_I \omega_I^t$	$+ \kappa_0 \omega_0^t$	drift rate due to gyro scale factor error $D^s = [\kappa^c + \kappa^a \frac{\omega^t}{\lvert\omega^t\rvert} + \kappa^l \omega^t + \kappa^n (\omega^t)^2]\, \omega^t$
9	+ other terms	+ other terms	

a) $g'_i = \hat{g}'_i \sin 2\pi ft$ $\quad g'_k = \hat{g}'_k \sin (2\pi ft + \psi)$

Table 3.2.2a Deterministic Error Model of a Two-Degree-of-Freedom in a Platform and Strapdown Environment

Remarks	Requirements for Compensation in an INS (D<0.01 °/h)	AHRS (D<5 °/h)
due to residual torques (magnetic interference of pickoff and torquer; in floated gyros fluid flow; in FRG and DTG flow condition on rotor periphery (laminar, turbulent) [3.5], effect of pickoff plane variation on pickoff angle-dependent drift terms, s. Rows 6 and 7); may vary with time and has to be recalibrated	<0.01 °/h	<5 °/h
s. Section 3.2.2.1; due to unbalance (temperature sensitive); in FRG and DTG: $r_{I,O} = 0$	<0.1 °/h/g if mean acceleration < 0.1 g	<50 °/h/g
in FRG due to rotor compliance [3.5], in DTG due to quadrature pendulosity [3.10 and 3.20]	"	"
s. Section 3.2.2.2; in floated gyro and DTG: due to gimbal compliance; always rectifying in vibrating environment	<0.04 °/h/g² if linear vibration < 0.5 g (RMS)	<20 °/h/g²
in floated gyro and DTG: due to gimbal compliance; in FRG due to gas bearing incompressible effect [3.5], rectifying only when g_i' and g_k' are correlated; $\overline{D^a} = \frac{1}{2} d^a_{ik}\, \hat{g}_i'\, \hat{g}_k' \cos\psi$ a)	"	"
s. Row above; in FRG due to gas bearing compressible effect [3.5]	"	"
for unidirectional angular rates α and β may be regarded as error angles per 1 rad angular motion	in strapdown systems α and β <20 arc sec for a tolerable error angle per turn of <2 arc min	<3 arc min <20 arc min
effective in FRG and DTG only; due to hydrodynamic torques, motor torques, windage torques; additional error sources in DTG: mistuning and damping of flexures cause spring rate coupling in cross axis and in direct axis, respectively [3.10]; sensitive to adjustment and stability of pickoff plane, s. Section 3.2.2.5; in DTG: d_{IO} and d_{OI} can be compensated by variation of tuning condition, s. Sections 3.2.2.5 and 3.4.5	for $d_{II} = d_{OO} \approx 0.02$ °/h/arc sec (s. Eq. (3.2.40a)): α < 0.5 arc sec	α < 8 arc min
s. Row 6; causing random-drift in platform environment and maneuver-dependent drift in strapdown environment $\overline{D}^\theta = d^\theta_i \left[\frac{\theta_i}{\omega_j}\right] \omega_j$ b)	requirements for θ not so tight as for α in Row 6 since θ depends on aircraft maneuvers which change with time	
i = I,O; j = I,O, with $[\theta_i/\omega_j]$ = transfer functions; can be kept low with high loop gain, s. Eq. (3.4.23)		
s. Section 3.2.2.6; ω^t = earth rate + transport rate in platform environment; ω^t = vehicle's angular rate in strapdown environment;	in strapdown systems κ	
i. fixed scale factor error due to temperature sensitivity of torquer resulting in error angle per turn;	<100 ppm for a tolerable error angle per turn of <2 arc min	<1000 ppm <20 arc min
ii. asymmetry scale factor error resulting in rectified drift in vibrating environment (s. Eq. (3.2.48));	<10 ppm if angular vibration < 1 °/s (RMS)	<4000 ppm
iii. nonlinearity scale factor error, troublesome at high rates, resulting in error angle per turn, s. above i	<200 ppm	<1000 ppm
in DTG especially drift rate due to twice spin frequency angular motion and torques [3.10 and 3.58]; giving rise to turn-around error of DTG on platform due to differing structural compliance of platform with azimuth angle.		

Gyro (Gimballed, Free-Rotor Type and Dynamically Tuned)

No.	$\Delta D_I =$	$\Delta D_0 =$	Nomenclature and Symbols Used in this Volume
1	$\frac{\dot{\gamma}}{n}\omega_I$	$\frac{\dot{\gamma}}{n}\omega_0$	drift due to motor hunting rate $\dot{\gamma}$ $D^h = f(\omega_S, \omega_{I,0})$
2	$-\frac{J}{I}\frac{\dot{\omega}_0}{n}$	$+\frac{J}{I}\frac{\dot{\omega}_I}{n}$	angular acceleration drift rate $D^p = d^p\,\dot{\omega}_{I,0}$
3	$-(1-\frac{J}{I})\frac{\omega_S\omega_I}{n}$	$+(1-\frac{J}{I})\frac{\omega_S\omega_0}{n}$	anisoinertia drift rate $D^i = d^i_{j,k}\,\omega_j\,\omega_k$
4	$-\theta_0\,\omega_S$	$+\theta_I\,\omega_S$	cross coupling drift rate $D^c = d^c\,\omega_S$
5	+ other terms	+ other terms	

a) $\omega_{I,0} = \Omega_{I,0}\sin(2\pi ft)$ $\qquad$ $\omega_S = \Omega_S\sin(2\pi ft + \psi)$

Table 3.2.2b Additional Deterministic Error Terms of a Two-Degree-of-Freedom

Remarks	Requirements in an INS ($D<0.01\ ^{\circ}/h$)	Requirements in an AHRS ($D<5\ ^{\circ}/h$)
s. Section 3.2.2.3; rectifying if $\omega_{I,0}$ and ω_S are correlated: $\bar{D}^h_{I,0} = \frac{\Omega_S\,\Omega_{I,0}}{2n}(\mathrm{Re}\cos\psi + \mathrm{Im}\sin\psi)$ a) with Re and Im from Fig. 3.2.8; for frequencies above hunting frequency of 1 to 10 Hz: Re → -1	above hunting frequency: $\Omega_S\,\Omega_{I,0} < 1(^{\circ}/s)^2$; otherwise compensation, s. Section 7.4.4.4	no special means required for suppressing this effect
s. Section 7.4.4.3.4; giving rise to pseudoconing error on system level $\bar{D}^p_{I,0} = -\frac{J}{2In}\Omega^2_{0,I}$ b)	for $J/I = 0.5$, $n = 180$ Hz and $\Omega_{I,0} = 1\ ^{\circ}/s$ (RMS): $\bar{D}^p_{I,0} = 0.014\ ^{\circ}/h$	
	compensation recommended	no compensation necessary
rectifying only if ω_S and $\omega_{I,0}$ are correlated $\bar{D}^i_{I,0} = \frac{I-J}{2I}\frac{\Omega_S\,\Omega_{I,0}}{n}\cos\psi$ a)	for $(I-J)/I = 0.5$, $n = 180$ Hz and $\Omega_{I,0}\,\Omega_S = 1\ (^{\circ}/s)^2$ $\bar{D}^i_{I,0} = 0.014\ ^{\circ}/h$	
	compensation recommended	no compensation necessary
Rectifying only if ω_S and $\omega_{I,0}$ are correlated; can be kept low with high loop gain; attribute to scale factor error, s. Eq. (3.4.23).	requirement for closed-loop transfer function in direct and cross axis: Re or Im $< 0.6\ \frac{\text{arc sec}}{^{\circ}/s}$ per $\Omega_{I,0}\,\Omega_S \leq 1(^{\circ}/s)^2$	no demanding requirements for closed-loop transfer function
Spin-input rectification: $\bar{D}^c_{I,0} = \left\lvert\frac{\Theta_{0,I}}{\omega_{I,0}}\right\rvert \omega_{I,0}\,\omega_S = \frac{\Omega_{I,0}\,\Omega_S}{2}(\mathrm{Re}\cos\psi + \mathrm{Im}\sin\psi)$ a) with Re and Im = real and imaginary part of gyro cross-axis closed-loop transfer function $[\Theta_{0,I}/\omega_{I,0}]$, s. Eqs. (3.4.21) and (3.4.23).		
Spin-output rectification: $\bar{D}^c_{I,0} = \left\lvert\frac{\Theta_{0,I}}{0,I}\right\rvert \omega_{0,I}\,\omega_S = \frac{\Omega_{0,I}\,\Omega_S}{2}(\mathrm{Re}\cos\psi + \mathrm{Im}\sin\psi)$ a) with Re and Im = real and imaginary part of gyro direct axis closed-loop transfer function $[\Theta_{0,I}/\omega_{0,I}]$. s. [3.10] and [3.58]; in DTG especially due to twice spin frequency sensitivity		

b) $\omega_{0,I} = \Omega_{0,I}\sin(2\pi ft) = \omega_{I,0}$ for a second gyro in a system; s. Section 7.4.4 for the computation of this pseudoconing error at system level

Gyro (Free-Rotor Type and Dynamically Tuned) in a Strapdown Environment

3.3 The Use of Single-Degree-of-Freedom (SDF) Gyros as Angular Rate Sensors and Stabilization Devices

3.3.1 Dynamics of the SDF Gyro

The SDF Gyro shown with elastic restraint and damper in Fig. 3.1.1 and 3.2.3 has angular freedom about the y-axis only ($\theta_I = 0$) and we will evaluate this component from Eqs. (3.2.22 ff.).

The restraint torque M_0^r is composed of the spring and damper torques as shown in Fig. 3.1.1.

$$M_0^r = -K\theta_0 - C\dot{\theta}_0, \tag{3.3.1}$$

which we introduce into the remaining part of Eq. (3.2.22). Combining some terms into the effective spring coefficient K', we obtain as performance equation of the SDF gyro:

$$(J_0\, p^2 + Cp + K')\theta_0 = H(\omega_I - D) + M_0^t = H(\omega_I - \omega^t - D) \tag{3.3.2a,b}$$

where ω_I is the input signal including its errors listed in Tables 3.2.1a and b and ω^t is the command rate.

The effective spring coefficient is:

$$K' = K[1 + \frac{H}{K}(1 + \frac{\dot{\gamma}}{n})\,\omega_s + \frac{1}{K}(J_S - J_I)(\omega_S^2 - \omega_I^2)] = K\,(1 + \frac{H}{K}\,\omega_s). \tag{3.3.3a,b}$$

This term depends on the vehicle's dynamics as does the gyro's scale factor regardless of whether K is the mechanical spring coefficient or the gain of the rebalance loop (electrical spring coefficient). A high loop gain minimizes this dependence as shown in Table 3.2.1b, Row 4 (s. also Section 3.3.3.2).

For very high frequencies the compliance of the gimbal support and the gimbal bearings has to be taken into account and provides the SDF gyro with additional freedom about the input axis.

Introducing into Eq. (3.2.22) the restraint torque about the input axis

$$M_I^r = -K_I\,\theta_I \tag{3.3.4}$$

one may show that the performance equation of the SDF gyro is affected in two aspects:

- the effective moment of inertia of the sensor about the output axis is changed (s. [3.1], Chapter 6, and [3.9], Chapter 5):

$$J_0' = J_0 + H^2/K_I \tag{3.3.5}$$

- and the gyro float may carry out an oscillation with respect to the case about the input and output axes similar to the nutation oscillation of the two-degree-of-freedom gyro (s. Eq. (3.4.8)); the natural frequency of this oscillation is:

$$\omega^{ni} = (\frac{K_I}{J_I} + \frac{H^2}{J_I J_0})^{1/2} = (\frac{K_I}{J_I}\frac{J_0'}{J_0})^{1/2}. \tag{3.3.6}$$

This oscillation can in general be neglected, since in practice the gimbal support is so stiff that $\omega^{ni} > 100$ Hz.

In floated SDF gyros another effect takes place at high frequencies when the fluid couples to the "dry" inertia of the float and increases its moment of inertia about the output axis. In [3.8], Section 6.3 this phenomenon is taken into account by introducing

$$\frac{J_0'}{H} = \frac{J_0}{H} + \tau_a \tag{3.3.7}$$

with τ_a = time constant increment due to fluid mass coupling. The text in [3.8] reads:

"[illegible] is a [illegible] of dynamic fluid effects and is negligible at frequencies below the inverse of the nominal [illegible]teristic time. It is considered basically due to the mass of damping fluid. The degree to which the fluid mass is coupled-in depends on the gyro design and the fluid velocity and acceleration at each point in the damping gap and is therefore also a function of the frequency of angular accelerations applied to the output axis."

We will discuss in the next three sections three typical SDF gyros.

3.3.2 The Rate Gyro

As its name indicates, the rate gyro is used for measuring the angular rate of a vehicle. It has already been mentioned that this can also be achieved with other sensors, e.g. rate integrating gyros with servo loops, non-gyroscopic angular rate sensors or even the laser gyro. But the rate gyro provides a good combination of simplicity and accuracy.

In Fig. 3.3.1 we find the cut-away view of a rate gyro which may be representative for the great number of products of similar design offered by the different manufacturers. The layout is similar to the sketch in Figs. 3.1.1 and 3.2.3.

In this sensor the rotor is mounted within a capsule which is semi-floated. Paddles provide hydrodynamic damping which can be held constant over a wide temperature range by means of a mechanical bellow-controlled compensation, where gaps between paddles, affecting the viscous torque, change due to the temperature.

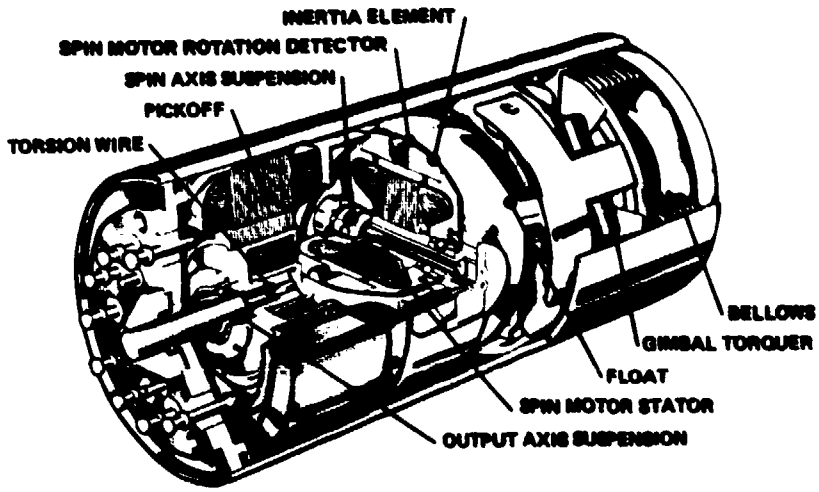

Outer dimensions: length 51 mm, diameter 24 mm.

Fig. 3.3.1 The Northrop GR-G5 Subminiature Rate Gyro

In the rate gyro the elastic restraint is predominant and we obtain from Eq. (3.3.2) in the Laplace domain(marked with ~) if in K' (s. Eq. (3.3.3)) the terms due to the vehicle's dynamics are neglected (K' = K):

$$\tilde{\theta}_0 = \frac{H/K}{(J_0/K)s^2 + (C/K)s+1} (\tilde{\omega}_I - \tilde{\omega}^t - \tilde{D}). \tag{3.3.8}$$

Except in the turn indicator where θ_0 is directly used to move the hand of the indicator, the output angle is converted into a voltage u as a measure for the input rate ω_I:

$$u = \frac{1}{S^u}\theta_0 \qquad S = S^u \frac{K}{H}, \tag{3.3.9}$$

whereby S =actual scale factor of the rate gyro. Based on the nominal scale factor S^u which may be in error by κ with respect to S, the voltage u is evaluated on system level to obtain the measured angular rate ω^κ. So we find as transfer function of the rate gyro including the error terms:

$$\tilde{\omega}^\kappa = S^\kappa \tilde{u} = S(1+\kappa)\tilde{u} = \frac{1+\kappa}{(\frac{s}{\omega^n})^2 + \frac{2\zeta s}{\omega^n} + 1} (\tilde{\omega}_I - \tilde{\omega}^t - \tilde{D}), \tag{3.3.10}$$

for which the different symbols and characteristic figures are presented in Table 3.3.1. Fig. 3.3.2 shows a detailed and a combined block diagram for the rate gyro. In Fig. 3.3.3 we find the normalized frequency plot for any second order system described by Eq. (3.3.10), where the natural frequency and the damping ratio correspond to Eq. (3.2.35).

The accuracy of the rate gyro depends to a large extent on the stability of the mechanical spring and the pickoff plane. Thus the accuracy is limited and in general one may ignore the error model in Table 3.2.1a,b for these instruments. From the standpoint of high signal to noise ratio a weak spring in the rate gyro would be desirable(Eq. (3.3.9)). But with a weak spring the cross coupling $H\omega_I$ in the effective elastic restraint Eq. (3.3.3) becomes more dominant and the sensor's scale factor changes with the angular motion of the vehicle. Gyros for measuring angular rates with high precision must therefore have an "electric spring" which allows a good signal to noise ratio ($<10^5$) and keeps the cross coupling low. The problem of high quality rate measurement will be discussed in Section 3.3.3.

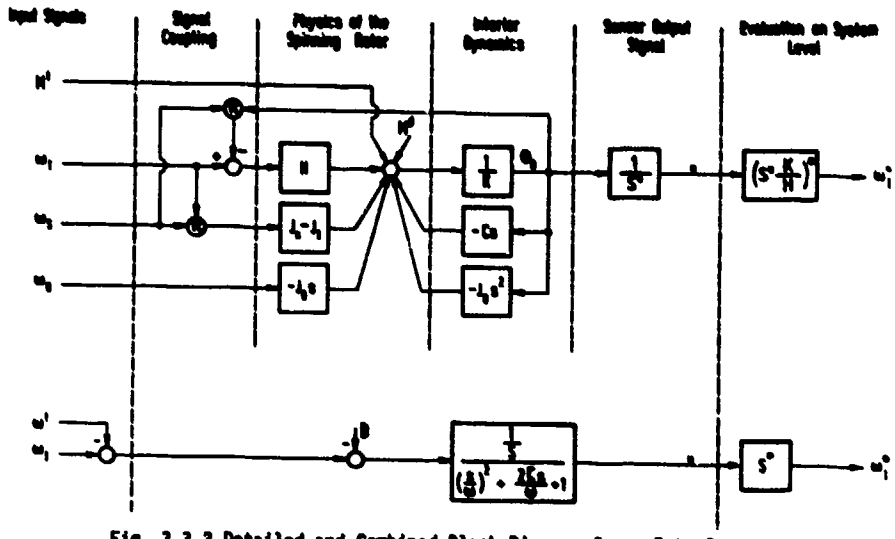

Fig. 3.3.2 Detailed and Combined Block Diagram for a Rate Gyro

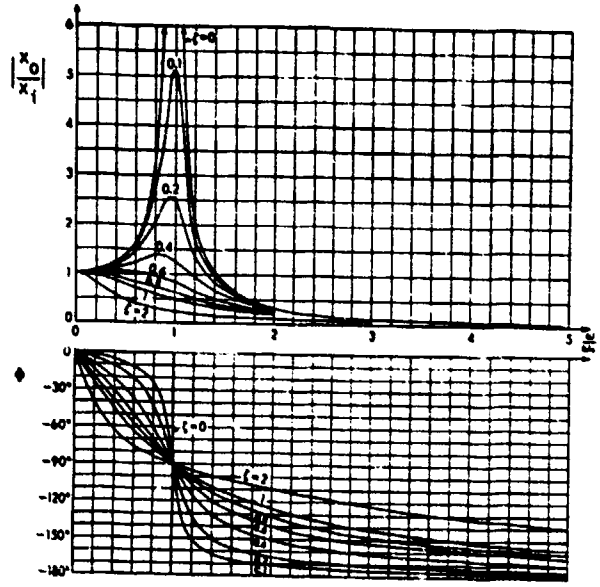

Fig. 3.3.3 Frequency Response of a Second-Order-System

Parameter	Units	Characteristic Value	Nomenclature
ω_{Imax}	$^o/s$	10 to 5000	maximum input rate
ω_{Imin}	$^o/s$	0.01 to 0.08	threshold and resolution
-	% of applied rate	0.1	hysteresis
-	$^o/s$	0.1 to 0.5	zero offset
M^d/H	% ω_{Imax}/g	<0.1	disturbance torque (mass unbalance)
$S = \frac{S^u K}{H}$	$(^o/s)/V$	adjustable	scale factor
J_o/H	$(^o/s)/(rad/s^2)$	<0.1	angular acceleration sensitivity
$\omega^n = (K/J_o)^{1/2}$	Hz	10 to 120	natural frequency
$\zeta = C\omega^n/(2K)$	-	0.1 to 1.0 typical	damping ratio

Table 3.3.1 Parameters and Figures Specifying a Rate Gyro

In general rate gyros do not have a torque generator except for self-test-purposes. Some manufacturers of rate gyros offer a gimbal torquer and/or spin motor detection for self-test as options. These options are very useful in aircraft control loops such as in blind landing systems which require high reliability. The rate gyro equipped with a torquer will react to a torquer current in a fashion similar to an input angular rate. In this way gimbal freedom, downstream electronics and system response can be checked. The spin rotor detector measures the angular speed of the gyro rotor optically or inductively. Thus the functioning of the sensor can be tested and in case of any failure the electronics can switch over automatically to the standby gyro.

3.3.3 The Rate Integrating Gyro (RIG)

The rate integrating gyro is similar to the rate gyro shown in Fig. 3.3.1 (Northrop GR-G5), but without the spring restraint. It is used as a stabilization device on attitude reference platforms or inertial platforms or as a strapdown rate sensor. In the former application it has been replaced in recent years by the tuned gyro because of certain advantages of the latter which will be shown later (s. Section 3.4.4). It is used in systems of very high accuracy such as marine systems. Efforts have been undertaken by the Charles Stark Draper Laboratory and Northrop to develop it as the "Third Generation Gyro TGG", i.e. in its most accurate version for strapdown space application. In the application as a strapdown rate sensor the RIG is equipped with a control loop from the pickoff to the torquer in order to keep the pickoff angle θ_0 near zero. Since the servo loops and especially the dynamic environments are different in both applications we will discuss the corresponding RIG performance separately.

3.3.3.1 The RIG for the Relatively Benign Platform Environment

In the platform environment we may neglect in Eq. (3.3.2) all errors due to angular rates and vibrations. With zero elastic restraint ($K' = 0$) we obtain the following performance equation of the RIG, where D includes only the error terms listed in Table 3.2.1a:

$$\frac{C}{H}\left(\frac{J_0}{C}p + 1\right)\dot{\theta}_0 = \omega_I^x - \omega^t + \omega_I - \omega^t - D. \tag{3.3.11}$$

Defining as RIG transfer function in the benign platform environment:

$$G(s) = \frac{H/C}{s(J_0/C\, s + 1)}, \tag{3.3.12}$$

the RIG performance equation reads in the Laplace domain (marked with ~):

$$\tilde{\theta}_0 = G(\tilde{\omega}_I - \tilde{\omega}^t - \tilde{D}). \tag{3.3.13}$$

The untorqued gyro ($\omega^t = 0$) with zero drift ($D = 0$) and zero time lag ($J_0/C = 0$) indicates the angular rotation of the case with respect to inertial space:

$$\dot{\theta}_0 = \frac{H}{C}\omega_I. \tag{3.3.14}$$

Thus the RIG can be compared with a bevel gear, the input shaft of which is fixed to inertial space. The gyro gain H/C corresponds to the gear ratio of the bevel gear.

Fig. 3.3.4 shows the cross section of a rate integrating gyro for use on platforms. The rotor is enclosed by the hermetically sealed gimbal (float), which is supported by a flotation liquid (e.g. fluorolube F 55; at 71 °C, the usual operating temperature of floated gyros, the specific weight $\gamma = 1.815$ g/cm^3). The gimbal supports - thin pivot/jewel bearings or magnetic suspension in high precision instruments - are thus relieved of the weight and the gyro can sustain very high shock accelerations. Through this buoyancy the friction in the gimbals, which would cause gyro drift, is correspondingly low. To further reduce the friction of pivot/jewel bearings, the jewels may be dithered (Honeywell GG 334). They are mounted in a piezoelectric ceramic disc polarized in the axial direction. The dither excitation frequency is high (e.g. the same as the spin motor frequency). The pivot to jewel friction is thus reduced by 10 : 1.

The flotation liquid has still another purpose. In the narrow gap between float and case (approx. 0.1 mm) it ensures heavy damping of the gyro, so that the gyro gain H/C in Eqs. (3.3.11 and 12) is in the order of magnitude of 1. The current supply from the case to the float takes place via very thin leads, the so-called "pig-tails". The latter have a diameter of 1/10 of a human hair, that means within the magnitude of µm. In high quality gyros the energy transfer is done inductively, as shown in Fig. 3.3.4.

The state of buoyancy, i.e. the friction forces in the pivot/jewel bearings, the damping constant C and the torquer scale factor are affected by temperature changes, and a good temperature control is in general a prerequisite for obtaining accurate results from the RIG. For many applications this might be a hindering factor. There are RIG's on the market in which the damping coefficient is constant over a wide temperature range. Means to achieve this goal are [3.4]:

- the use of silicone fluid with 0.9 gm/cm^3 density and a virtually constant damping over a temperature of -45 °C to 115 °C.
- the use of a bellows-controlled damping mechanism.

The temperature sensitivity of the torquer scale factor is a more severe problem in strapdown gyros and is discussed in Sections 3.2.2.6 and 3.3.3.2.

The design of the rotor bearing requires special emphasis. Any shift of the rotor causes a change in mass unbalance, i.e. gyro drift. For inertial quality the rotor bearings have to be stable within 0.4 µm as stated by the Eqs. (3.2.28 and 29). They also have to be designed as isoelastic as possible. Special ball

a)

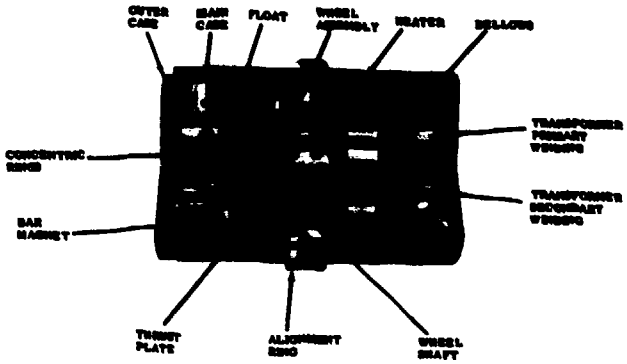

AC651G Gyro Cutaway

b)

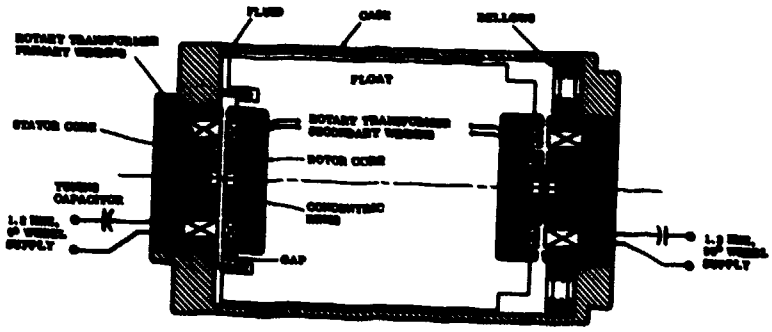

Wheel Power Rotary Transformer and Triaxial Suspension

c)

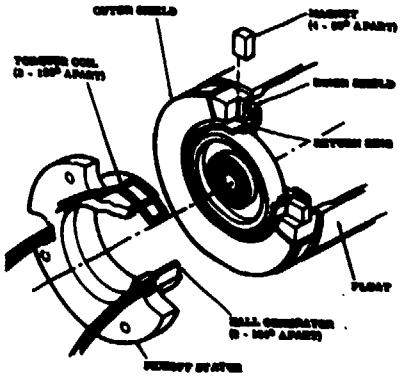

Permanent Magnet Torquer and Hall-Coil Pickoff

Fig. 3.3.4 The Delco AC651G Rate Integrating Gyro for Use in the Carousel IV-Platform

bearings (s. Section 3.2.2.2) and hydrodynamic gas bearings are used for this purpose. With the latter, the running life is theoretically infinite. Contact between rotor and stator occurs only during start-stop. But special materials (steel bonded carbide or high density ceramic surfaces) allow start-stops exceeding 10^4 without reduction in performance.

For keeping the time constant J_0/C low and for reducing the weight of the float (mass unbalance) many manufacturers prefer the "moving coil" torque generators where the heavy permanent magnet is case-fixed and the coil is mounted on the float. Ref. [3.1], Chapter 14 gives more details on gyroscopic design.

Table 3.2.1a shows us that the SDF gyro has better performance with the output axis in the vertical (s. Rows 2 and 3) and on a platform the gyros for stabilizing the horizontal axes are mounted in this fashion, leaving the gyro for the azimuth axis with highest drift rate in general.

We will come back to the use of the RIG for the stabilization of platforms in Chapter 5. Table 3.3.2 summarizes some details on RIG's for platform and strapdown application.

3.3.3.2 The RIG for the Strapdown Environment

According to Eqs. (3.3.2) and (3.3.3) the RIG transfer function should read in the strapdown environment:

$$G'(s) = \frac{1}{J_0 s^2 + Cs + H\left(1 + \frac{J}{H}\right)\omega_s + (J_S - J_I)(\omega_S^2 - \omega_I^2)} = \frac{1}{J_0 s^2 + Cs + H\omega_s} . \qquad (3.3.15a,b)$$

In practice terms due to the vehicle's dynamics are treated as error terms as indicated in Table 3.2.1b, Row 4 for the cross coupling term and the rebalance loop design is based on G(s) in Eq. (3.3.12). The open loop input-output relationship reads in the Laplace domain (marked with ~):

$$\tilde{\theta}_0 = G'[M_0^t + H(\tilde{\omega}_I - \tilde{D})] . \qquad (3.3.16)$$

For angular rate measurements a rebalance loop F(s) is implemented from the gyro pickoff to the torquer as indicated in Fig. 3.3.5; this will be discussed in more detail in Chapter 4. For convenience we put in

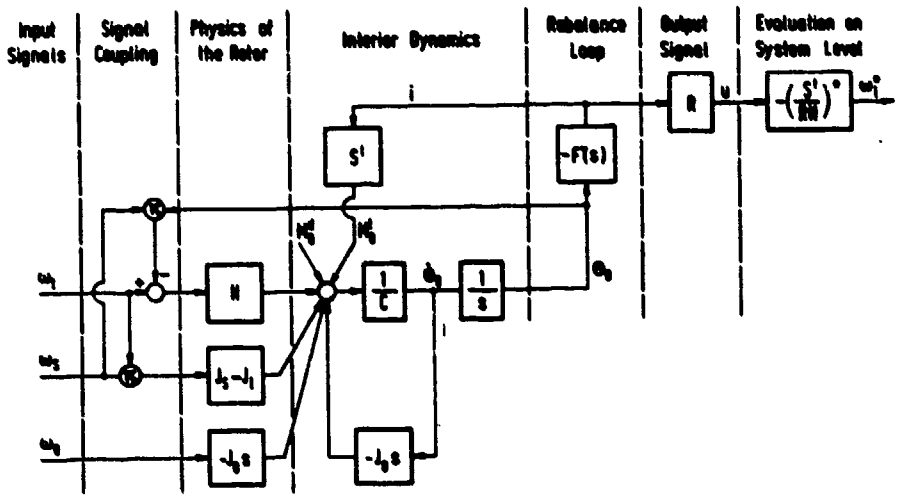

Fig. 3.3.5 Block Diagram for the Rate Integrating Gyro Plus Rebalance Loop

Fig. 3.3.5: $F = S^t F'$ with S^t = actual torquer scale factor (s. Section 3.2.2.6). We now introduce in Eq. Eq. (3.3.16):

$$\tilde{M}_0^t = -F(s)\,\tilde{\theta}_0 = -S^t F'(s)\,\tilde{\theta}_0 \qquad (3.3.17)$$

and the closed loop pickoff angle θ_0, the torquer current i and the measured angular rate $\omega^* = -S^* R\, i = -S^* u$ (with S^* =nominal gyro scale factor, R = measurement resistor, s. Section 3.2.2.6) become:

$$\tilde{\theta}_0 = \frac{H(\tilde{\omega}_I - \tilde{D})}{1/G' + F} \qquad (3.3.18a)$$

$$\tilde{i} = \frac{-FH(\tilde{\omega}_I - \tilde{D})}{S^t(1/G' + F)} \qquad (3.3.18b)$$

$$\tilde{\omega}^* = (1 + \kappa)\, F \frac{(\tilde{\omega}_I - \tilde{D})}{(1/G' + F)} = (1 + \kappa) \frac{(\tilde{\omega}_I - \tilde{D})}{(1 + 1/(G'F))} , \qquad (3.3.18c)$$

with κ = gyro scale factor error (s. Section 3.2.2.6). This shows us that the effective gyro scale factor depends on the product G'(s) F(s) defining the bandwidth of the sensor which can be up to 100 Hz. Only for G'(s) F(s) → ∞ do we obtain the desired output:

$$\omega^{*} = (1 + \kappa)\ (\omega_I - D). \tag{3.3.19a}$$

For low input frequencies (s=0) with no angular rate about the spin axis of the gyro ($\omega_S = 0$) G'(0) is large (s. Eq. (3.3.15b), and the above mentioned requirement G'(0) F(0) → ∞ is met and thus the angular rate measurement becomes independent of the rebalance loop's gain F(o) = K.

For $\omega_s \neq 0$ the gyro scale factor changes according to:

$$\omega^{*} = (1 + \kappa)\ \left(\frac{1}{1+H\omega_S/K}\right)(\omega_I - D) \tag{3.3.19b}$$

as indicated already in Eq. (3.3.3). A high rebalance loop gain K keeps this effect low, as mentioned in Table 3.2.1b, Row 4. The RIG rebalance loop includes an integrating network, in general whose gain grows with decreasing input frequency.

The block diagram for angular measurements about two axes by means of two rate integrating gyros with rebalance loops is shown in Fig. 3.3.6. The two-axes measurement is shown here for better comparison with the application of a two-degree-of-freedom (TDF) gyro for this purpose, where only one sensor is needed (s. Fig. 3.4.4). This will be discussed later.

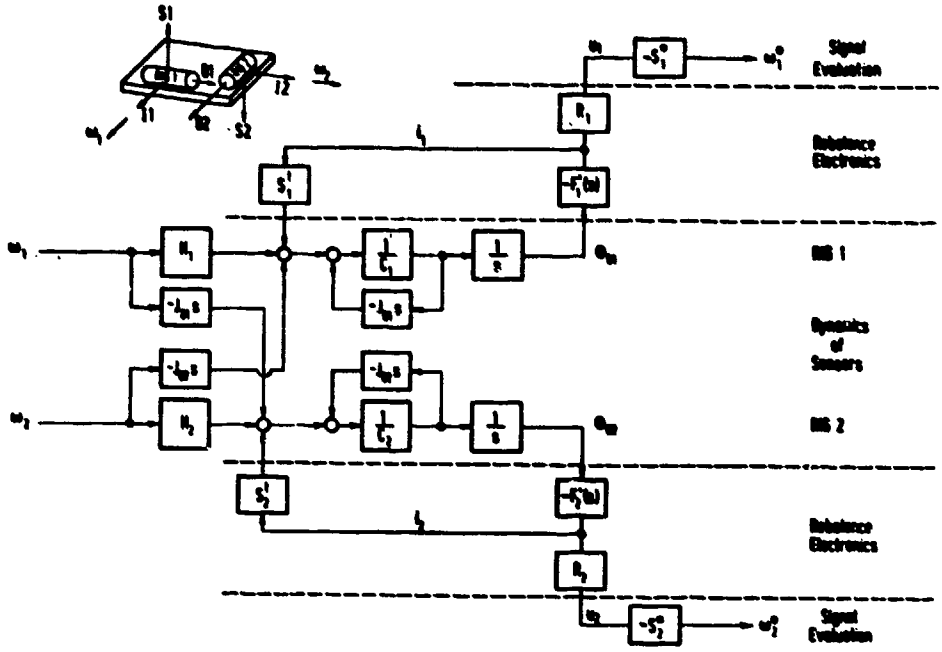

Fig. 3.3.6 Angular Rate Measurement About Two Axes by Means of Two Rate Integrating Gyros

As mentioned in Section 3.2.2.4 the gimbal bearings of RIG's in strapdown systems are always subject to forces and they have to be designed correspondingly. For a high dynamic environment the gimbal suspension of RIG's is implemented with dithered jewel bearings (Honeywell GG 8200 A), with ball bearings (Hamilton Standard RI 1010, Steinheil Lear Siegler 1903) or with taut wire suspension (Northrop K7G-5B). One of the most critical parts of all strapdown gyros is the torquer. The importance of the torquer scale factor has already been shown in Section 3.2.2.6 and in Tables 3.2.1a and 3.2.2a. Its linearity has to be within 10 ppm if the RIG is to be used in a strapdown INS (s. Table 3.2.1a, Row 5). Ref. [3.4] gives interesting details on torquer design for this application and mentions that its temperature sensitivity is 420 ppm/°K. As a consequence of this problem RIG's for strapdown use must have an excellent thermocontrol or means to compensate this effect, whereby it has to be taken into account that the torquer current is proportional to the input rate, i.e. the corresponding energy fed into the sensor changes correspondingly. This can be improved with digital caging loops, s. Chapter 4. It has already been mentioned that electronically rebalanced rate integrating gyros or double rate integrating gyros (s. Section 3.4) are more accurate for measuring angular rates than the conventional rate gyro. For angular rate measurement the rate gyro's accuracy may be sufficient, but if the angular rate measurements are used for the attitude computation as in strapdown systems (s. Section 7.4.4) the electrically rebalanced gyro has to be used.

In Table 3.3.2 the main characteristics of some RIG's are listed which may be regarded as representative for products in this field. Fig. 3.3.7 shows the cut-away view of a typical strapdown gyro.

No.	Manufacturer Type	Units	Delco DE 651G	Ferranti Type 125	Honeywell GG 8200 A	Northrop K7G-5B	SAGEM Gyroscope F	SLS 1903-SB
1	Weight	gm	227	450	205	283.5	160	200
2	Diameter	mm	45.2	52.9	38.1	42.1	27	37.5
3	Length	mm	64.3	83	77.7	82.6	71	88.5
4	Angular Momentum H	$gm\text{-}cm^2/s$	$1.0 \cdot 10^5$	$4.4 \cdot 10^5$	$7 \cdot 10^4$	$1.2 \cdot 10^5$	$3.75 \cdot 10^4$	$2.18 \cdot 10^4$
5	Characteristic Time J_0/C	ms	2.2	2	0.17	< 3	1	6.28 (at 65 °C)
6	Gyro Gain H/C	1	1.6	5	0.23	6	1.56	3.16 (at 65 °C)
7	Maximum Torquing Rate	deg/s	0.3	1.4	50	4	2.5	200 (600 for 5s)
8	Torquer Scale Factor	deg/h/mA	1.2	42.2	1450	140	170	5364
	Torquer Scale Factor Error							
9	Linearity	ppm	not applicable	200	150(up to 15°/s)	300		< 200 (up to 200 deg/s)
10	Stability	ppm/yr	40		300	100		40
11	Day to Day Drift[1)]	deg/h	0.3(1σ)	0.05(1σ) (0.0026)	0.05	0.15	0.1(1σ) (0.025)	0.6 (1σ)
12	g-insensitive Drift	deg/h	< 9	< 1	< 3	< 3	< 2	3
13	g-sensitive Drift	deg/h/g	< 6	< 0.3	< 2	< 3	< 2	3
14	g^2-sensitive Drift	$deg/h/g^2$	< 0.05	< 0.04		0.05	< 0.1	0.2
15	Short Term Drift[1)]	deg/h	0.015(1σ) (0.002)	0.012(1σ) (0.0007)	0.005 (0.003)	0.02 (0.01)		0.15 (0.1)
16	Operating Temperature	°C	62	55 or 70	82.2		70	65
17	Vibration	g	24(0to500Hz) 10(500to1000Hz)	30(55to2000Hz)	25	15(20to2000Hz)	12(20to2000Hz)	12 (20to2000Hz)
18	Shock	g	15 (11 ms)	60 (11 ms)	50 (10 ms)	50	50 (11 ms)	40 (11ms)
19	Linear Acceleration	g	24	30	30	20	50	40
20	Float Material		Beryllium	Beryllium	Beryllium	Beryllium	Beryllium	Aluminum
21	Float Suspension		Magnetic	Pivot/Jewel	Pivot/Jewel Dithered	Taut Wire		Ball Bearing
22	Rotor Bearing		Gas Bearing	Ball Bearing (Gas bearing Typ 126 available)	Gas Bearing	Gas Bearing	Ball Bearing	Ball Bearing

[1)] figures in () for output axis vertical

Table 3.3.2

Data for Some Rate Integrating Gyros

Fig. 3.3.7 The Steinheil Lear Siegler Rate Integrating Strapdown Gyro 1903-HJ

3.3.4 The Double Integrating Gyro (DIG)

If the flotation fluid in the rate integrating gyro (s. Fig. 3.3.4) is replaced by flowing air, we obtain the double integrating gyro, shown schematically in Fig. 3.3.8. In the discussion of the characteristics of this sensor we will follow [3.9] Chapter 13.

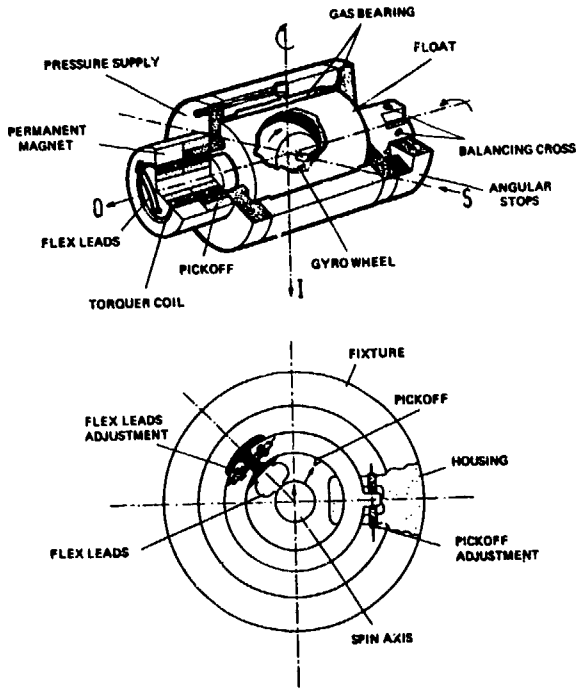

Fig. 3.3.8 Double Integrating Rate Gyro Schematically and Calibration Principle

The transfer function of the DIG in the Platform environment (negligible angular rates and vibrations) can be easily derived from Eq. (3.3.2) by putting C = K = 0:

$$G(s) = \frac{H}{J_0 s^2} . \tag{3.3.20}$$

With this relationship all the formulae (3.3.13 to 19) derived for the rate integrating gyro in the platform environment (s. Section 3.3.3.1) and in the strapdown environment (s. Section 3.3.3.2) are also valid for the DIG.

As to the drift terms, Tables 3.2.1a and b are also applicable to the DIG with the exception of the error terms due to fluid effects (e.g. $D_\alpha \dot{\omega}_0$). New error terms arise from the flowing air, which causes turbine torques depending on the applied acceleration (s. [3.9] Chapter 13), i.e., they are similar to mass unbalance drift. A typical drift due to turbine torques can be 0.8 °/h/g.

The DIG is at present applied only to the stabilization of inertial platforms, but has not found the broad utilisation as the RIG, though it offers the following advantages:

- the hydrostatic gas bearing of the precession axis or output axis provides a complete lack of solid friction;

- no problems arise for designing the gyro float for the state of buoyancy and controlling it to this state, i.e. as compared to the floated gyro, discussed in the previous sections and consequently:

  - heavier materials can be used for the gyro rotor of the DIG thus making it possible to obtain a greater angular momentum for the same diameter;
  - there is no requirement to operate the gyro at a fixed temperature (thanks to this advantage, an optimum temperature can be chosen which is most suitable with respect to the total system and the environmental conditions) and the temperature control need not be as precise as with the floated gyro; and
  - all measuring and adjustment elements are freely accessible: the gas bearing gyros require only a cover for protection against dust and external electric and magnetic fields and not the hermetic sealing of gyros with fluid flotation.

On the other hand there are the following drawbacks of the hydrostatic bearing:

- it is necessary to have available compressed gas which has to be fed to the sensors through the bearings of the platform gimbals, unless each sensor has its own pressurized gas supply; and
- the associated servo loop is somewhat more complex on account of the absence of a mechanical damping feature.

One would expect that the float support by means of the hydrostatic gas bearing of the DIG is fairly soft and the following effects discussed in Chapter 3.3 become significant:

- the increase in the effective moment of inertia about the output axis due to gimbal support compliance (s. Eq. (3.3.5)) and
- the occurance of a float oscillation within the case at a fairly low natural frequency ω^{ni} (s. Eq. (3.3.6)).

Values obtained from the above mentioned formulas for the gas-bearing gyro GWK 28 are listed in Table 3.3.3. This gyro is a smaller version of the GWK 38 discussed in [3.9], Chapter 13. The figures laid down for it were taken from a unpublished report of the Teldix Company, Heidelberg. Though the effective moment of inertia J_0 is doubled, the natural frequency ω^{ni} of the float oscillation within the case is above the range to cause problems.

H [gm cm²/s]	$2.94 \cdot 10^5$
J_0 [gm cm²]	98.1
J_I [gm cm²]	141.3
K_I [dyne cm/rad]	$8.83 \cdot 10^8$
J_0'/J_0	2.
ω^{ni} [Hz]	562.4

Table 3.3.3 Effect of Gas Bearing Compliance of Float Support in the Teldix GWK 28 Double Integrating Gyro on the Effective Moment of Inertia and Resonance Frequency

3.4 The Use of Two-Degree-of-Freedom Gyros as Angular Rate Sensors and Stabilization Devices

3.4.1 Dynamics of the Gimballed TDF Gyro

The gimballed TDF gyro shown in Fig. 3.1.1b is used

- as an unfloated gyro with heavy gimbals supported by ball bearings in vertical and directional reference instruments (VG, DG) and
- as a floated gyro with light gimbals supported by pivot/jewel bearings in platform systems.

In both cases the rotor moves very little with respect to inertial space and for the derivation of its dynamics we may discard all terms in Eq. (3.2.22) due to vibratory inputs.

In general the TDF gyros are used without elastic restraint. Damping is caused by the flotation fluid or friction in the bearings and we assume as restraint torque in Eq. (3.2.22):

$$\underline{M}^r = -C \begin{pmatrix} \dot{\theta}_I \\ \dot{\theta}_O \end{pmatrix} \tag{3.4.1}$$

resulting in the following performance equation of the gimballed TDF gyro:

$$\begin{pmatrix} (J_I p + C) & H \\ -H & (J_O p + C) \end{pmatrix} \underline{\theta} = \begin{pmatrix} -J_I p & -H \\ H & -J_O p \end{pmatrix} \underline{\omega}^i + H \hat{\underline{I}} (\underline{\omega}^t + \underline{D}) \tag{3.4.2}$$

where the skew-symmetric "unity-matrix" is defined in Eqs. (3.2.10a,b).

The vector $\underline{D}$ contains all the drift terms listed in Tables 3.2.2a and b except those due to scale factor error κ (Table 3.2.2a, Row 8) and angular acceleration (Table 3.2.2b, Row 2).

For $\underline{D} = \underline{\omega}^t = 0$ and $C = 0$ we can obtain one solution of Eq. (3.4.2) by inspection:

$$\theta_{I,O}(t) = \theta_{I,O}(0) - \int_0^t \omega_{I,O}(\tau)d\tau \tag{3.4.3}$$

which shows the characteristics of the "free gyro": as the rotor stays fixed with respect to inertial space, the pickoff angle will be equal to the initial pickoff angle minus the time integral of the angular rate of the case with respect to inertial space. This can be seen from the straight upper and lower branches of the block diagram in Fig. 3.4.1. As compared to the rate integrating gyro discussed in Section 3.3.3, which also indicated the angle of the case with respect to inertial space (s. Eqs. 3.3.13 and 14)), the TDF gyro does it with a gain identical to unity and no time lag. In principle this output is independent of wheel speed and stability of viscosity.

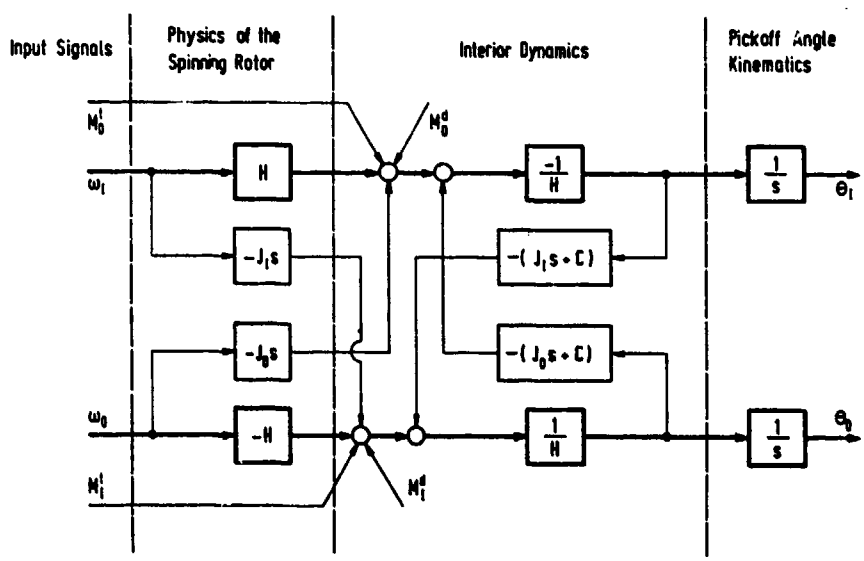

Fig. 3.4.1 Block Diagram of the Two-Degree-of-Freedom Gyro

We define as TDF transfer function:

$$\underline{G}(s) = \begin{pmatrix} (J_I s + C)s & Hs \\ -Hs & (J_O s + C)s \end{pmatrix}^{-1} \tag{3.4.4}$$

and as undamped TDF transfer function:

$$G''(s) = \begin{pmatrix} J_I s^2 & Hs \\ -Hs & J_O s^2 \end{pmatrix}^{-1} = G(s)\big|_{C=0} \tag{3.4.5}$$

So we obtain as <u>TDF performance equation</u> in the Laplace domain (marked with ~):

$$\tilde{\underline{\theta}} = \underline{G}[-\frac{1}{s}(\underline{G}'')^{-1}\,\tilde{\underline{\omega}}^i + H\,\hat{\underline{I}}\,(\tilde{\underline{\omega}}^t + \tilde{\underline{D}})] = -\tilde{\underline{\phi}} + H\underline{G}\,\hat{\underline{I}}\,(\tilde{\underline{\omega}}^t + \tilde{\underline{D}}), \tag{3.4.6a,b}$$

where ϕ is the angular displacement of the sensor with respect to inertial space. For slowly varying command rates ω^t and drift rates D, Eq. (3.4.6) reduces to

$$\dot{\underline{\theta}} = -\omega^i + \underline{\omega}^t + \underline{D}. \tag{3.4.6c}$$

In the Eq. (3.4.6b) we have put $\underline{G}(\underline{G}'')^{-1} = \underline{I}$, i.e. we have assumed that the gyro float will not be affected by the motion of the case. This is realistic, since the damping in floated TDF gyros is low, e.g. $\zeta = 10^{-3}$ for the Litton G-200 [3.13] .

Any stepwise command rate will stimulate the interior dynamics of the TDF gyro. Its characteristic equation:

$$s^2\,[(\frac{s}{\omega^n})^2 + \frac{2\zeta}{\omega^n}\,s + 1] = 0 \tag{3.4.7}$$

allows us to obtain the eigenvalues s_1 to s_4 of the TDF gyro. The first two eigenvalues $s_{1,2}$ of the bracketed term describe the <u>nutation</u> with the natural frequency ω^n and the damping ratio ζ:

$$\omega^n = \frac{H}{(J_I\,J_O)^{1/2}} = n\,\frac{I}{(J_I\,J_O)^{1/2}}\;; \qquad \zeta = \frac{C(J_I + J_O)}{2H\,J_I\,J_O}\;; \tag{3.4.8a,b}$$

the other two eigenvalues describe the <u>precession</u>, which are explained in Fig. 3.2.2.

$$s_{3,4} = 0. \tag{3.4.9}$$

The nutation frequency ω^n is in the order of magnitude of the spin frequency n. It is exactly equal to it if $I = J_I = J_O$, i.e. for a spherical rotor.

If all inputs are zero except for a step function in the torque about the O-axis, i.e. a negative command rate ω_I^t about the input axis, we obtain for the undamped TDF gyro (C = 0):

$$\theta_I(t) = -\omega_I^t\,(t - \frac{1}{\omega_n}\sin\omega^n t)$$

$$\theta_O(t) = \omega_I^t\,\frac{J_I}{H}\,(1 - \cos\omega^n t) = (\omega_I^t/\omega^n)(1 - \cos\omega^n t), \tag{3.4.10}$$

i.e. a high frequency coning motion of the spin axis is superimposed on the continuous precession as shown in <u>Fig. 3.4.2</u>.

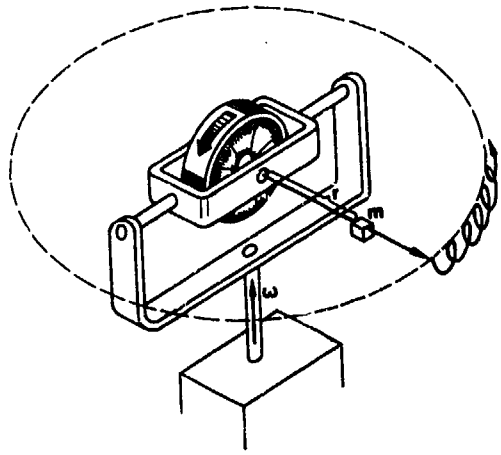

Fig. 3.4.2 Response of a Gimballed Two-Degree-of-Freedom Gyro to a Step Function in I-Axis Torque of O-Axis Command Rate

Assuming that the ratio H/C would be in the same order of magnitude for a floated TDF gyro as it is for a floated SDF gyro (H/C = 1), we see from Eq. (3.4.8) for $J_I = J_O$ that $\zeta = C/H = 1$, i.e. the nutation frequency would be heavily damped. For the unfloated instruments, the engineer should always bear in mind that the instrument may nutate (s. [3.1], Chapter 5.2).

Fig. 3.4.3 shows the floated gimballed TDF gyro Litef K 250 G which is used for the platform stabilization in the Litef PL-41 marine navigation system. It is equipped with hydrodynamic gas bearings for the rotor. The ball bearing version (K 250 K) is used in the secondary attitude and heading reference system (SAHRS) of the Tornado fighter aircraft.

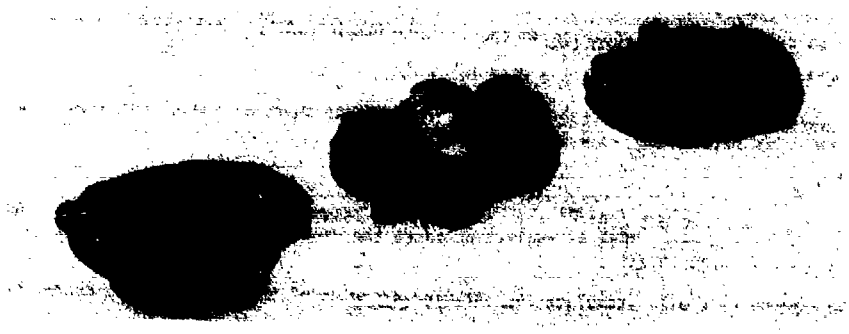

Fig. 3.4.3 Floated and Gimballed Litef K 250 G Two-Degree-of-Freedom Gyro for Platform Stabilization

It seems likely that in new designs the floated TDF platform gyros will be replaced more and more by the "dry gyros". The former ones suffer from all disadvantages already mentioned in connection with the rate integrating gyros concerning fluid, pig tails, gimbal and rotor bearings. The "dry gyros" and the "free rotor gyros" have considerable advantages in this respect as will be shown in the next sections.

We will come back to the use of gimballed TDF gyros as vertical and directional references and stabilizing devices on platforms in Chapters 5 and 6.

3.4.2 The Dynamics of the Free-Rotor Gyro (FRG) in the Benign Platform Environment

From the design viewpoint there are considerable advantages in the ungimballed TDF gyro, such as the free rotor gyro (FRG) in Fig. 3.1.2a, as compared to the gimballed TDF gyro in Fig. 3.1.1b:

- the motor, the pickoff coils and torquer coils are mounted case-fixed, and
- no "pig tails", no gimbal bearings and no flotation fluid are required resulting in lower temperature sensitivity and the fact that the drift adjustment can be carried out during the test.

But the free-rotor gyro (FRG) shown in Fig. 3.1.2 exhibits the additional error sources due to aerodynamic effects as discussed in Section 3.2.2.5.

The performance equation of the free rotor gyro in the platform environment Eq. (3.4.2) has to be completed by the additional drift terms:

$$\underline{d}^s = \begin{pmatrix} -d^s_{II} & d^s_{I0} \\ -d^s_{0I} & -d^s_{00} \end{pmatrix} \cdot \begin{pmatrix} \theta_I + \alpha_I \\ \theta_0 + \alpha_0 \end{pmatrix} . \tag{3.4.11}$$

These terms are also mentioned in the error model of Table 3.2.2a.

The FRG transfer function is:

$$\underline{G}(s) = \begin{pmatrix} (J_I s^2 + Cs + Hd_{0I}) & H(s + d_{00}) \\ -H(s + d_{II}) & (J_0 s^2 + Cs + Hd_{I0}) \end{pmatrix}^{-1} , \tag{3.4.12}$$

where we may assume:

$$J_I = J_0 = J. \tag{3.4.13}$$

Therefore we obtain as FRG performance equation in the Laplace domain:

$$\underline{\tilde{\theta}} = \underline{G} \left[- \frac{1}{s} (\underline{G}^*)^{-1} \underline{\tilde{\omega}}^i + H \hat{\underline{I}} (\underline{\tilde{\omega}}^t + \underline{\tilde{D}}) \right] = -\underline{\tilde{\theta}} + H \underline{G} \hat{\underline{I}} (\underline{\tilde{\omega}}^t + \underline{\tilde{D}}) \tag{3.4.14a,b}$$

where $G^*(s)$ is the same as in Eq. (3.4.5).

Eq. (3.4.14b) is only valid for high input frequencies when we may neglect the damping and the additional drift terms in the FRG transfer function (s. Eq. (3.4.12 and 3.4.5)).

In order to demonstrate the response of the FRG to an initial pickoff angle of $\theta_I(o)$, we assume in Eq. (3.4.14a) $C \ll H, Jd_{ij} \ll 4$ (with $i = I,0$ and $j = I,0$) and $H(J_I + J_0) \gg J_I J_0 (d_{I0} + d_{0I})$. The resulting characteristic equation may be approximated by:

$$\Delta = \{\frac{J_I J_0}{H^2} s^2 + \frac{1}{H^2} [C(J_I + J_0) - J_I J_0 (d_{II} + d_{00})] s + 1\} [s^2 + (d_{II} + d_{00}) s + (d_{00} d_{II} + d_{I0} d_{0I})],$$

(3.4.15)

where the first bracket on the right hand side describes the eigenvalues of the nutation whose damping has decreased due to the direct coupling drift and the second bracket describes the precession due to the direct and cross coupling drift rate. Increasing damping in precession causes decreasing damping in nutation [3.13, 3.14]!

Concentrating only on the slow motion we assume zero inertia, i.e. zero nutation, and find with $d_{II} = d_{00}$ and $d_{I0} = d_{0I}$:

$$\theta_I(t) = \theta_I(0)\, e^{-t\, d_{II}} \cos d_{I0}\, t \qquad \theta_0(t) = -\theta_I(0)\, e^{-t\, d_{II}} \sin d_{I0}\, t$$

$$\dot\theta_I(0) = -\theta_I(0)\, d_{II} \qquad \dot\theta_0(0) = -\theta_I(0)\, d_{I0}, \qquad (3.4.16a,b,c,d)$$

i.e. the FRG rotor carries out a coning motion which spirally converges to its equilibrium. According to [3.5] the time constant and period of this motion for the Autonetics G 10 B FRG are:

$$T_{II} = 1/d_{II} = T_{00} = 50\ \text{s} \qquad T_{I0} = 1/d_{I0} = T_{0I} = 5\ \text{s}. \qquad (3.4.17a,b)$$

This shows us that the direct axis torque or cross coupling drift can be serious in an FRG designed in a fashion similar to Fig. 3.2.11. As compared to the gimballed and floated TDF gyro the FRG exhibits the additional drift terms mentioned in Table 3.2.2. The other drift terms are alike though the physics which produces them may be quite different.

3.4.3 The Dynamics of the Free Rotor Gyro (FRG) in the Strapdown Environment

Though for the time being no FRG is used to the authors' knowledge as a strapdown gyro in a rough environment, we will briefly discuss the steps which have to be undertaken to do so. The reason for this discussion is not purely academic, because the dynamically tuned gyro (DTG), which ideally operates like a FRG, is used at present in quite a number of strapdown systems. We will regard the FRG as a reference for the DTG, which is discussed in Section 3.4.4.

For the derivation of the FRG performance in a strapdown environment we will follow the logic of Section 3.3.3.2. In an FRG we often find $J_I = J_0 = J = I/2$, which we assume in the following. Based on Eqs. (3.2.22) and (3.4.11) the FRG transfer function should read:

$$\underline{G}'(s) = \begin{pmatrix} J s^2 + H(\omega_s + d_{0I}) + J(\omega_s^2 - \omega_0^2) & (H + I\dot\gamma) s + H d_{00} + J(\dot\omega_s - \omega_I \omega_0) + I\ddot\gamma \\ -(H + I\dot\gamma) s - H d_{II} - J(\dot\omega_s - \omega_I \omega_0) - I\ddot\gamma & J s^2 + H(\omega_s + d_{I0}) + J(\omega_s^2 - \omega_I^2) \end{pmatrix}^{-1} \qquad (3.4.18)$$

In practice the rebalance loop design is based on the undamped TDF transfer function $G''(s)$ of Eq. (3.4.5) in general, and the additional terms in Eq. (3.4.18) are added to the gyro drift as shown in Tables 3.2.2b. We thus may assume the following open-loop input-output relationship for the FRG in the Laplace domain (marked with ~), which is similar to Eq. (3.4.14b):

$$\tilde{\underline{\theta}} = -\tilde{\underline{\phi}} + \underline{G}''(\tilde{\underline{M}}^t + H\, \hat{\underline{I}}\, \tilde{\underline{D}}). \qquad (3.4.19)$$

For the angular rate measurement, rebalance loops are implemented from the 2 pickoffs of the gyro to the 2 torquers as indicated in Fig. 3.4.4a, where we have introduced for convenience $\underline{F} = \underline{S}^t \underline{F}'$:

$$\tilde{\underline{M}}^t = -\underline{F}(s)\, \tilde{\underline{\theta}} = -\underline{S}^t \underline{F}'(s)\, \tilde{\underline{\theta}}, \qquad (3.4.20a)$$

with $\underline{F}$ and $\underline{F}'$ as matrices for the loop electronics and $\underline{S}^t$ as matrix for the actual torquer scale factor:

$$\underline{F}(s) = \begin{pmatrix} F_{II} & F_{I0} \\ -F_{0I} & F_{00} \end{pmatrix}, \quad \underline{S}^t = \begin{pmatrix} S_I^t & 0 \\ 0 & S_0^t \end{pmatrix}, \quad \underline{F}'(s) = \begin{pmatrix} F'_{II} & F'_{I0} \\ -F'_{0I} & F'_{00} \end{pmatrix}. \qquad (3.4.20b,c,d)$$

So we find as vector for the closed-loop pickoff angle:

$$\tilde{\underline{\theta}} = -(\underline{I} + \underline{G}''\, \underline{F})^{-1} (\tilde{\underline{\phi}} - H\, \underline{G}''\, \hat{\underline{I}}\, \tilde{\underline{D}}). \qquad (3.4.21)$$

Both components of this vector become decoupled from each other if we meet the following condition in the rebalance loop (3.4.20b) [3.15].

$$F_{II} = F_{00} = \frac{s}{\omega^n} F_{I0} = \frac{s}{\omega^n} F_{0I} \qquad (3.4.22a)$$

or

$$\underline{F}(s) = \frac{F}{Hs} [\underline{G}''(s)]^{-1} \qquad (3.4.22b)$$

where $\omega^n = H/J$ = nutation frequency as mentioned in Eq. (3.4.8a). The decoupled closed loop FRG transfer functions for the pickoff angle vector $\underline{\theta}$, the torquer current vector $\underline{i}$ and the measured angular rate vector $\underline{\omega}^x$ become:

a)

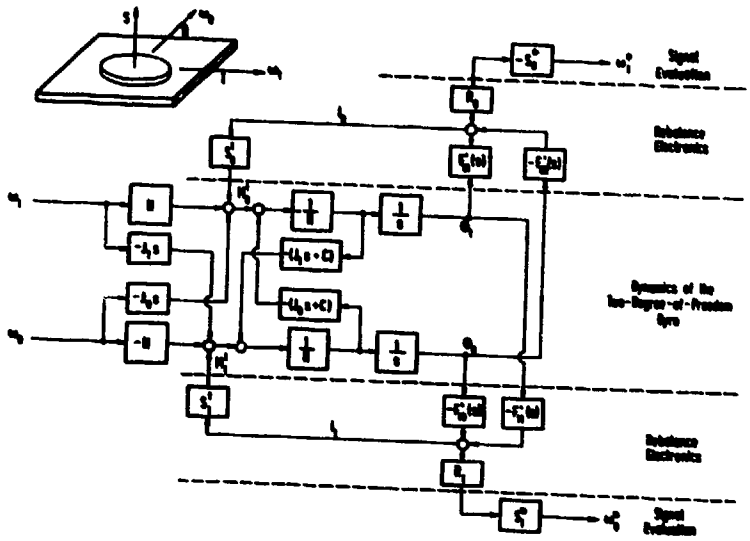

b)

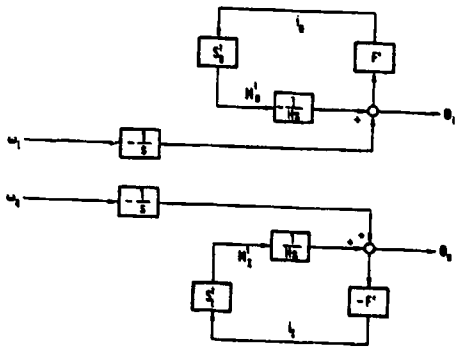

c)

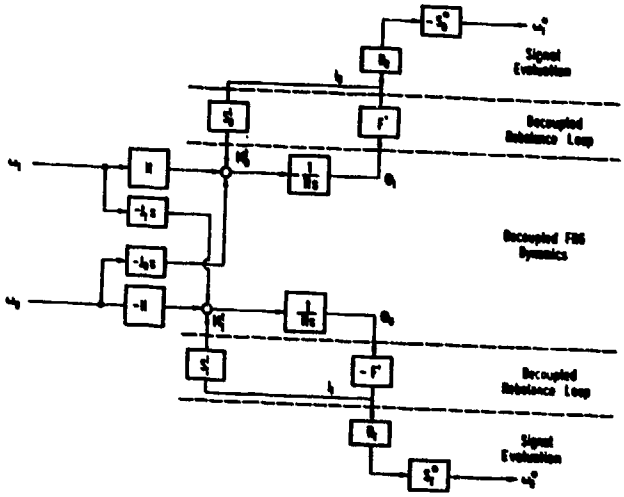

Fig. 3.4.4 Block Diagram for the Use of a Two-Degree-of-Freedom Gyro for Angular Rate Measurement (b and c with decoupling in the rebalance loop)

$$\tilde{\underline{\theta}} = \frac{-1}{1+F/(Hs)} \left(\tilde{\underline{\phi}} - H\, \underline{\underline{G}}''\, \hat{\underline{\underline{I}}}\, \tilde{\underline{D}}\right)$$

$$\tilde{\underline{i}} = \frac{F/(Hs)}{1+F/(Hs)} \left(\underline{\underline{S}}^t\right)^{-1} \left[\frac{1}{s} \left(\underline{\underline{G}}''\right)^{-1} \tilde{\underline{\omega}} - H\, \hat{\underline{\underline{I}}}\, \tilde{\underline{D}}\right]$$

$$\tilde{\underline{\omega}}^{\times} = \underline{\underline{S}}^{\times} \tilde{\underline{u}} = \underline{\underline{S}}^{\times}\, \underline{\underline{R}}\, \tilde{\underline{i}} = \frac{-F/(Hs)}{1+F/(Hs)} \left(\underline{\underline{I}} + \underline{\underline{\kappa}}\right) \hat{\underline{\underline{I}}} \left[\frac{1}{Hs} \left(\underline{\underline{G}}''\right)^{-1} \tilde{\underline{\omega}} - \hat{\underline{\underline{I}}}\, \tilde{\underline{D}}\right] \qquad (3.4.23a,b,c)$$

where $\omega = \dot{\phi}$; following the course of Section 3.2.2.6, we have introduced as resistor matrix $\underline{\underline{R}}$, as nominal gyro scale factor matrix $\underline{\underline{S}}^{\times}$ and its error matrix κ ($\underline{\underline{S}}^t$ s. Eq.(3.4.20c)):

$$\underline{\underline{R}} = \begin{pmatrix} R_I & 0 \\ 0 & R_O \end{pmatrix}, \quad \underline{\underline{S}}^{\times} = \begin{pmatrix} 0 & -[S_O^t/(HR_O)]^{\times} \\ [S_I^t/(HR_I)]^{\times} & 0 \end{pmatrix}, \quad \underline{\underline{\kappa}} = \begin{pmatrix} \delta S_O^t/S_O - \delta R_O/R_O - \delta H/H & 0 \\ 0 & \delta S_I^t/S_I - \delta R_I/R_I - \delta H/H \end{pmatrix}. \qquad (3.4.24a,b,c)$$

Figs. (3.4.4b,c) show in comparison to the coupled FRG in Fig. 3.4.4a the block diagrams for the pickoff angle components and the output signal components of the decoupled FRG, the former being truly decoupled in both axes, whilst the latter are coupled via the angular acceleration sensitivity of the sensor. In their structure they correspond exactly to Fig. 3.3.6 showing the use of two rate-integrating gyros (RIG) for the angular rate measurement about two axes. But they reveal an additional advantage for the use of a FRG for this purpose: in the decoupled mode the FRG dynamics are reduced to (s. Eq. (3.4.5)):

$$\underline{\underline{G}}(s) = -\frac{1}{Hs}\, \hat{\underline{\underline{I}}} \qquad (3.4.25)$$

i.e. the FRG acts as an ideal integrator, whilst the two RIG's in Fig. 3.3.6 act as integrators with time lag. But this advantage takes effect only at very high frequencies.

The reason for the decoupled FRG axes lies in the fact that the nutation is not excited by the input angular rate, due to proper compensation in the rebalance loop. In order that this compensation is "proper", the FRG parameters (nutation frequency) have to be exactly matched in the electronics, which is difficult to do. If the decoupling condition (3.4.22a) is not implemented exactly:

$$F_{II} = F_{OO} = (1+e)\, \frac{s}{\omega_n}\, F_{IO} = (1+e)\, \frac{s}{\omega_n}\, F_{OI}, \qquad (3.4.26)$$

the damping of the nutation is directly affected. The requirement for stable nutation is:

$$e > 0. \qquad (3.4.27)$$

Let us once more cast a glance at the output signals in Eqs. (3.4.23a,b,c) of the FRG with decoupling in the rebalance loops. For constant input rates ($s \to 0$) the output signals are:

$$\underline{\theta} = \frac{-H}{K} \left(\underline{\omega} - \underline{D}\right)$$

$$\underline{i} = H\left(\underline{\underline{S}}^t\right)^{-1} \hat{\underline{\underline{I}}} \left(\underline{\omega} - \underline{D}\right)$$

$$\underline{\omega}^{\times} = \left(\underline{\underline{I}} + \underline{\underline{\kappa}}\right) \left(\underline{\omega} - \underline{D}\right), \qquad (3.4.28a,b,c)$$

showing that only the pickoff angles, but not the output signals, depend on the gain K of the loop. By putting integrators into the loop, the pickoff angles are driven to zero for constant input rates, thus lowering the corresponding drift rates discussed in Table 3.2.2b, Row 4.

For input frequencies exceeding the bandwidth of the sensor, which is in the order of magnitude of 50 to 100 Hz (-3 db), the rebalance loop will be blocked ($F \to 0$) and the gyro will react like an uncaged sensor:

$$\underline{\theta} = -\underline{\phi}$$

$$\underline{i} = \underline{0}$$

$$\underline{\omega}^{\times} = \underline{0}. \qquad (3.4.29)$$

Let us close the discussion on the use of an FRG as angular rate sensor with an additional hint at the rebalance loop layout. Since the pickoff angles are measured directly at the spinning rotor any manufacturing intolerances will modulate the pickoff output signal with the spin frequency and its harmonics. Notch-filters are recommended to filter out the noise and prevent rectification in the closed rebalance loop.

The items discussed in this and the former sections apply in principle also to the dynamically tuned gyro (DTG) whose peculiarities will be described in the next section.

3.4.4 The Dynamically Tuned Free Rotor Gyro (DTG) in a Platform and Strapdown Environment

In platform inertial navigation systems of the class 1 NM/h performance as used in civil and military aircraft the DTG has achieved triumphant success. Invented by Howe and Savet at Bosch Arma Company the idea was put into mass-production by the Singer Kearfott Company (Gyroflex) and later also by Ferranti (Oscillo Gyro) and Litton (Vibrarotor, Vibragimbal). Because of the excellent experience the engineers had with this sensor the Teledyne Systems Company was the first to use it for strapdown application (SDG 5). Kearfott, Litton, SAGEM, INCOSYM and Litef followed this line and the first flight test results of strapdown systems using DTG's are promising.

The principles of operation of various DTG's will be discussed using Fig. 3.4.5. The figure illustrates three generations of dry gyros. In the early versions the gyro rotor was connected to the motor by means of a slightly flexible shaft or Hooke's joint (Ferranti gyroscopic gunsight [3.2]). The torsional spring torques cause the cross coupling drift rates d_{IO} and d_{OI} as discussed already in the previous section and shown in Fig. 3.2.11. As we know from Eqs. (3.4.11 to 17) this cross coupling drift rate causes the spinning rotor to precess in a cone, once it is misaligned from its equilibrium. Means to avoid this effect were sought in implementing negative "torsional spring"-torques as with permanent magnets or proper caging loops.

The invention of Howe and Savet brought the mechanical solution: the Hooke's joint with proper mass distribution, i.e. the gimbal suspension as shown in the center of Fig. 3.4.5. The forced motions of the gimbal when the rotor is misaligned with respect to the shaft, as more distinctly illustrated in Fig. 3.4.6, provide a negative net torque proportional to $J^g n^2$ (J^g = gimbal moment of inertia and n = rotor angular rate) which can be made to cancel the torsional spring torque proportional to the spring coefficient k by properly choosing J^g and n.

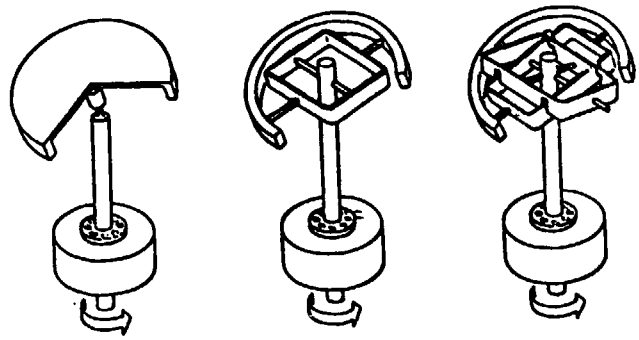

Fig. 3.4.5 Three Versions of Dry Gyroscopes

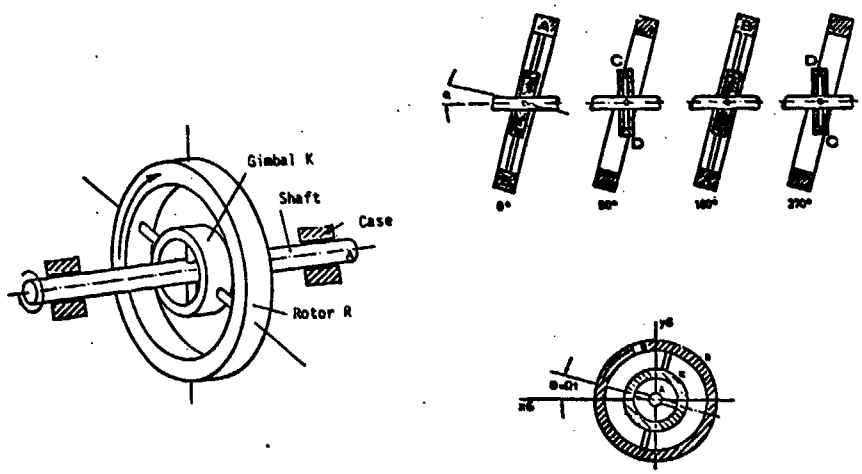

Fig. 3.4.6 Motion of the Gimbal in a Dynamically Tuned Gyroscope

Fig. 3.4.5 shows also a DTG with two gimbals which has advantages from viewpoint of performance as will be shown below.

The block diagram in Fig. 3.4.7 (derived from [3.25]) allows us to discuss the performance of the DTG with one gimbal (superscripts $k \neq 0$, $l = 0$) as compared to the free-rotor gyro (FRG, no gimbal, i.e., superscripts $k = l = 0$, and no torsion spring coefficients $K_{x,y} = 0$) whose block diagram is shown in Fig. 3.4.1.

The center of Figure 3.4.7 represents the dynamics of the rotor and gimbal in the shaft-fixed coordinate frame. We see the gyro dynamics in the forward loops and the coupling of both axes including the nutation as indicated in Fig. 3.4.1 for the FRG. The direct and cross coupling drift terms, discussed in Section 3.2.2.5, have been included in the diagram under the assumption that they are symmetric ($d_{II} = d_{OO}$, $d_{OI} = d_{IO}$).

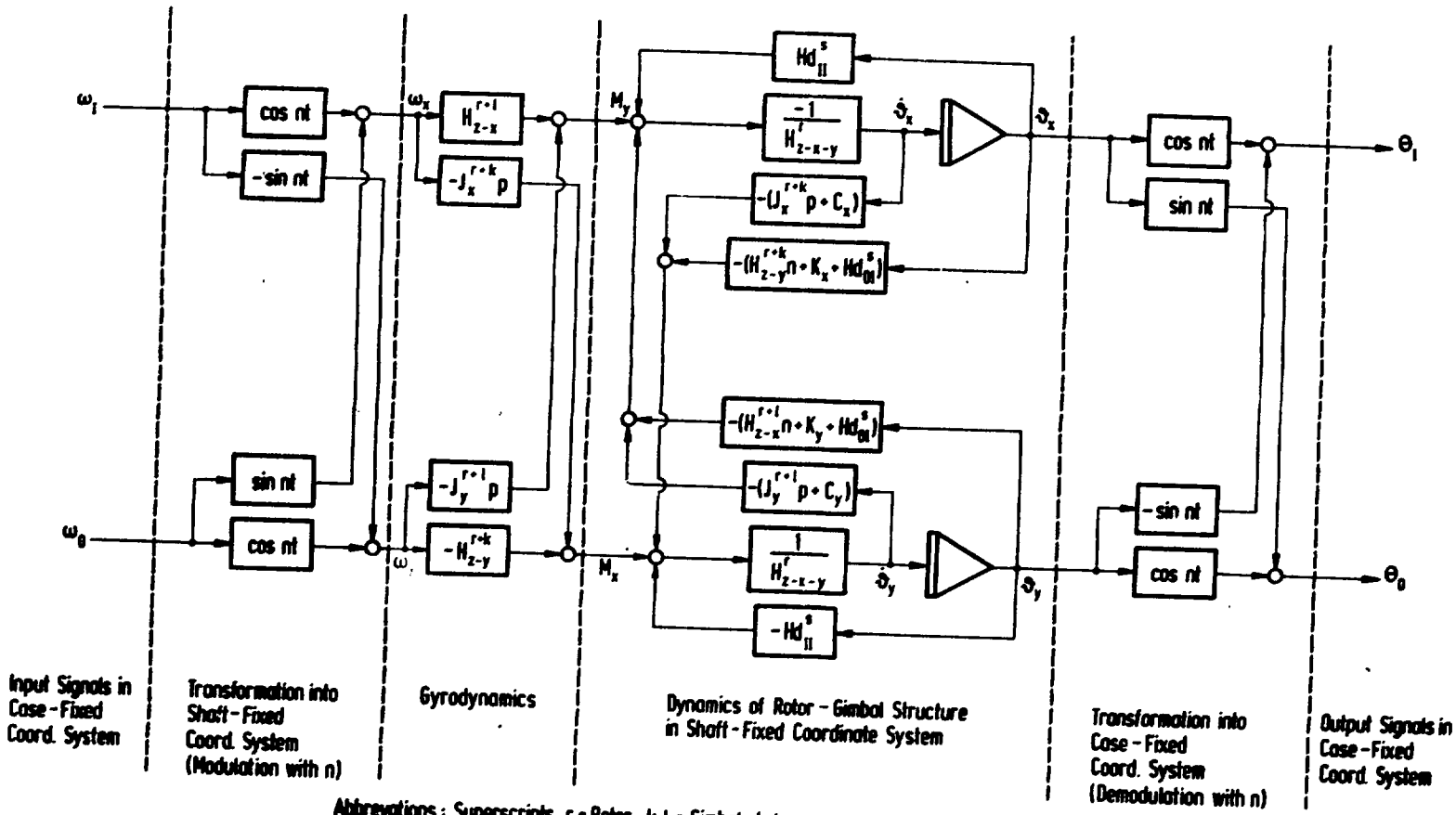

Abbrevations: Superscripts r = Rotor; k,l = Gimbals k,l
Subscripts I = Input Axis 1 = Output Axis for 0; 0 = Input Axis 2 = Output Axis for 1;
S = Spin Axis; x,y,z = Shaft-Fixed Axes

$H^{r+l}_{z-x} = J^{r+l}_{z-x} n$ $\qquad$ $J^{r+l}_{z-x} = J^r_z - J^r_x + J^l_z - J^l_x$

Fig. 3.4.7 Block Diagram of the Dynamically Tuned Gyroscope

The transformation of the input signals $\omega_{I,O}$ or $M_{I,O}$ from the case-fixed coordinate frame into the shaft-fixed frame causes a modulation with the spin frequency n. The transformation of the shaft-fixed angles $\delta_{x,y}$ into the case-fixed angles $\theta_{I,O}$ is achieved by demodulation with the same frequency.

In order to familiarize with this block diagram let us use it to derive the already known characteristics of the ideal FRG, i.e. we assume no damping (C = 0), no direct and cross coupling drift (Hd_{ij} = 0), no torsion spring constants ($K_{x,y}$ = 0) and no gimbal (no superscripts k and l). The word "shaft-fixed coordinate system" is a bit misleading with the FRG since the one shown in Fig. 3.1.2 does not have one. We cling to this definition by reason of convenience and assume that in this sensor the "shaft-fixed" z-axis is always parallel to the motor axis and that the other axes are rotating with the spin speed n.

The dynamics of the FRG-rotor are governed in the shaft-fixed coordinate system by the eigenvalues:

$$s_{1,2} = jn \qquad s_{3,4} = jn\left(\frac{I}{J} - 1\right), \tag{3.4.30a,b}$$

where $j = \sqrt{-1}$ and $J_z^r = I$ and $J_x^r = J_y^r = J$ in agreement with Sections 3.4.2 and 3.4.3. The eigenvalues describe the spin frequency and the nutation frequency diminished by the spin frequency (s. Eq. (3.4.8)). An initial misalignment angle of the rotor $\theta_I(o)$ is in the shaft-fixed coordinate system equivalent to the initial conditions $\delta_x(o) = \theta_I(o)$ and $\dot{\delta}_y(o) = n\,\delta_x(o)$ and causes the motion

$$\delta_x(t) = \theta_I(o)\cos n\,t \qquad \delta_y(t) = \theta_I(o)\cos(n\,t + \pi/2). \tag{3.4.31a,b}$$

This oscillation is seen in the case-fixed frame as a constant angle $\theta_I(o)$ as we would have expected for the ideal FRG.
Coming back to the DTG, this sensor with M sets of gimbals is "tuned" if the first two eigenvalues are the same as for the FRG, i.e. if the initial misalignment angle $\theta_I(o)$ remains constant - at least in the mean. The tuning condition is (s. [3.10], Eq. (11), [3.16] and [3.17]):

$$n = \left(\frac{\sum_1^M K_{xm} + K_{ym}}{\sum_1^M J_{xm}^g + J_{ym}^g - J_{zm}^g}\right)^{1/2}, \tag{3.4.32}$$

where the x-axis is along the torsion springs connecting gimbal and shaft, the y-axis is along the torsion springs connecting gimbal and rotor and the z-axis is along the spin axis (s. Fig. 3.4.6).

If the DTG is not perfectly tuned the residual torsional torques cause a gyro precession, i.e. coning motion of the initially misaligned rotor, which in principle is similar to the effect of the cross coupling drifts d_{IO} and d_{OI} in the FRG (s. Fig. 3.2.11 and Eq. (3.4.16a,b)). We obtain for the frequency of the coning motion due to mistuning (s. [3.10], Eqs. (25), (26) and (4)):

$$\omega^m = \frac{\delta n}{F_m}, \tag{3.4.33}$$

with

$$\delta n = n - n_o \qquad n_o = \text{tuning spin rate} \qquad n = \text{actual spin rate} \tag{3.4.34}$$

and the so called "figure of merit" (s. [3.10], Eq. (20)):

$$F_m = \frac{J_z^r + \sum_1^M J_{xm}^g}{\sum_1^M (J_{xm}^g - J_{ym}^g - J_{zm}^g)}. \tag{3.4.35}$$

The higher the figure of merit (the order of magnitude of 800 is achievable, s. [3.18]), the more the DTG approaches the ideal FRG. The drift due to mistuning, i.e. the gradient of the coning motion at t = 0, can be derived from Eqs. (3.4.16) and (3.4.33) as:

$$D_{0,I}^m = \pm\,\theta_{I,O}(o)\,\frac{n-n_o}{F_m}. \tag{3.4.36}$$

Because of the similarity of the effect of mistuning (s. [3.10], Eqs. 25 to 28) and cross coupling drift rate (s. Eqs. (3.4.16a,b)) which is inherent in all FRG's and DTG's, the latter can be compensated by properly changing δn or δn_o (s. also Fig. 3.4.7, where Hd_{II} acts in the same way as the torsional spring torques K).

In this respect the DTG is superior to the FRG. Routine adjustments to 0.002 °/h/arc sec are made on standard instruments and 0.0002 °/h/arc sec is achievable [3.19]. Compared to the FRG discussed in the previous sections these figures are lower by one to two orders of magnitude (s. Eq. (3.4.17)).

The direct coupling drift due to damping in the torsion springs and the other error sources inherent in all FRG's (s. Fig. 3.2.11) cannot be overcome in such an elegant way. As in any FRG, evacuating the case is a means for reduction of damping, and corresponding drift values of less than 0.01 °/h/arc sec are achievable. To prevent out-gassing of the bearing lubricants, the sensor is filled with hydrogen at a low pressure.

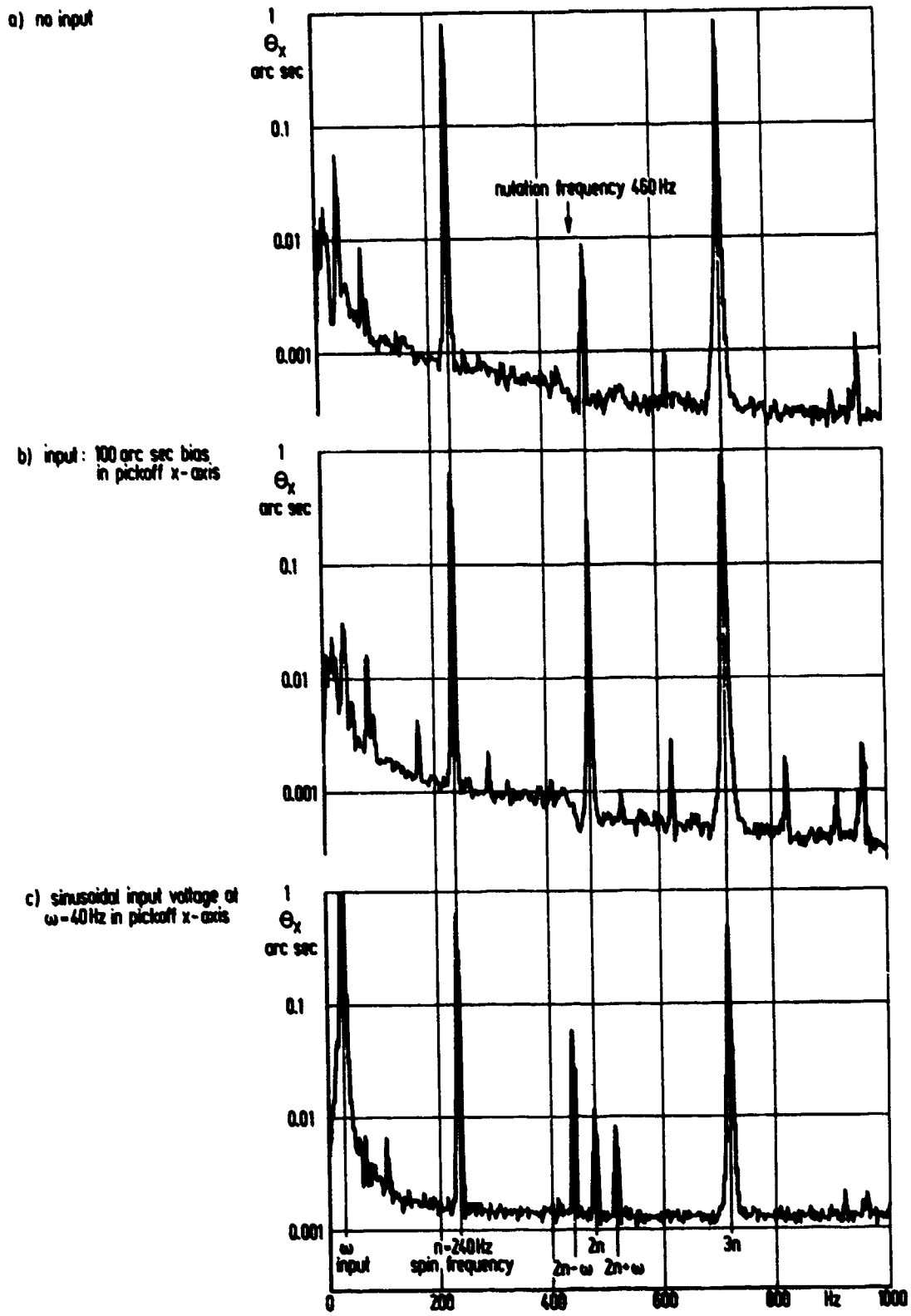

Fig. 3.4.8 Single-Gimbal DTG Pickoff Frequency Plot for Different Input Signals
(elder model of a Gyroflex; measurements filtered with first order lag, T = 0.7 ms)

The two branches in Fig. 3.4.7 describing the rotor dynamics in the shaft-fixed frame are symmetric for the FRG. For the DTG with one gimbal they are asymmetric, since the gimbal moment of inertia appears in the lower branch only.

In order to illustrate one peculiarity of the asymmetric DTG let us estimate its response to an initial misalignment $\theta_I(0)$, similar to the FRG discussed above. We assume that the asymmetry causes an amplitude difference of the oscillations in both axes of the shaft-fixed frame (s. Eq. (3.4.31)):

$$\delta_x(t) = \theta_I(o) \cos n\,t \qquad \delta_y(t) = \theta_I(o)(1+\varepsilon) \cos (n\,t + \pi/2) \tag{3.4.37}$$

which transform into the case-fixed frame as:

$$\theta_0(t) = -\,\theta_I(o)\,\frac{\varepsilon}{2} \sin 2\,n\,t$$

$$\theta_I(t) = \theta_I(o)\,[1 + \frac{\varepsilon}{2}(1 - \cos 2\,n\,t)], \tag{3.4.38}$$

i.e. a minute oscillation at twice the spin frequency is superimposed on the expected solution $\theta_I(t) = \theta_I(o)$. This is confirmed by comparing the two pickoff angle frequency plots for a single-gimbal DTG with analog rebalance loops shown in Figs. 3.4.8a and b. In Fig. 3.4.8a the measurements were carried out with no input into the sensor. The spin frequency and its second and third harmonics are clearly visible. If the rotor is slightly tilted by a pickoff voltage bias, the amplitude of the second harmonic is raised (s. Fig. 3.4.8b).

In [3.17] it is shown that the asymmetric single gimbal DTG not only has the eigenvalues describing the nutation ω^n and precession ω^p but also eigenvalues at beat frequencies, i.e. $2n \pm \omega^n$ and $2n \pm \omega^p$. The nutation frequency cannot be seen in Figs. 3.4.8a to c; in the design of the rebalance loops the Eqs. (3.4.26) and (3.4.27) have been observed.

The adding of a second gimbal (Litton Vibragimbal) or even of a third one, each 120° apart (Teledyne SDG5), causes symmetric rotor-gimbal dynamics and in theory the complete reduction of the twice-spin frequency sensitivity.
But with the single-gimbal DTG or the multigimbal DTG with gimbal imperfections the oscillation at this frequency remains, and excitations in the case-fixed coordinate frame of twice the spin frequency cause a rectified drift rate. Examples for the excitations are:

- angular vibrations of the case;
- oscillating torques on the rotor due to an input from the oscillating pickoff angles into the rebalance loops; and
- oscillating torques on the rotor due to linear vibrations from the ball bearings or from another DTG running at the same speed when the gimbals and the rotor have direct or quadrature pendulosity [3.58].

For a detailed discussion on the origin of the quadrature pendulosity in the case of a cruciform-type flexure refer to [3.20].

Formulas for the sensitivity of a single or multigimbal DTG to twice the spin frequency excitation are derived in [3.10]. For the single gimbal DTG the Eqs. (43) and (51) of [3.10] read:

- for an angular case vibration of

$$\phi_I = \phi_I(o) \sin 2\pi n t \tag{3.4.39}$$

the DTG drift is:

$$D_I = -\phi_I(o)\,\frac{n_o}{2F_m}\,\frac{K_x}{K_x+K_y} \tag{3.4.40}$$

where $K_{x,y}$ = torsional spring coefficient of the inner, outer spring;

- for a vibratory torque on the rotor of

$$M_I = M_I(o) \sin 2\pi n t \tag{3.4.41}$$

the DTG drift is:

$$D_I = -M_I(o)\,\frac{n_o}{4F_m}\,\frac{K_x}{K_x+K_y}\,. \tag{3.4.42}$$

These equations confirm again the benefit of a high figure of merit. From the viewpoint of performance this sensitivity at twice the spin frequency is the basic difference between the DTG and the FRG.

The sensitivity at twice the spin frequency is nonlinear since the gyro will react to an oscillatory input of a certain frequency ω at the same frequency and at the frequencies $2n + \omega$ as shown in Fig. 3.4.8c, where the sensor was excited with a sinusodial pickoff voltage at 40 Hz behind the measurement output. Therefore conventional transfer functions do not describe exactly the DTG dynamics [3.16] and [3.17] and the control engineer puts harmonic filters (comb filters) into the servo loop for the stabilization of a platform with a DTG or into the rebalance loop if the DTG is used for angular rate measurements. These filters allow the rejection of all spin frequencies and their harmonics which otherwise would circulate in the control loop.

In the servo loop for platform stabilization comb filters prevent pickoff oscillations at spin frequency (generated by ball bearing imperfections) and its harmonics from exciting the platform with a corresponding angular vibration. They cannot prevent the mechanical cross-talk between the two gyros - an effect which depends on the mechanical compliance of the platform-gimbal structure. Since this compliance changes with the angular orientation of the platform with respect to the case, the DTG shows more or less a so-called turnaround error, i.e. a drift changing with heading of an aircraft. A means of reducing this effect is to operate of the two DTG's at different speeds.

The advantage of strapdown systems is that the compliance of the inertial measuring unit does not change and the turnaround error does not exist. As long as the vibration is constant, the corresponding drift may be compensated. This may be one reason why modern DTG's for strapdown use are again designed as single-gimbal sensors, s. Table 3.4.2a. Another reason is that modern flexible joints can be fabricated with small dimensions resulting in a high figure of merit (up to 800, s. [3.18]). Valuable hints on their design can be found in [3.18] and [3.21] to [3.23].

With its three gimbals the Teledyne SDG5 gyro is an exception among the strapdown DTG's, but one may regard it as a forerunner of DTG's for this purpose.

The comb filters in the caging loop of strapdown DTG's also suppress the effect of pickoff-angle oscillation at multiples of the spin frequency on the feedback torque which are generated by ball bearing imperfections, rotor imperfections and oscillatory vibrations of the IMU. Once the comb/notch filters are implemented the DTG and the FRG should not differ from the control-loop-analysis point of view and the reader is referred to Sections 3.4.3 and 3.4.4 for more details on its behaviour in a platform and strapdown environment.

Due to the complex interior dynamics of the DTG its rebalance loop design is more complicated than the single-degree-of-freedom (SDF) gyro. Also the implementation of range switching, i.e. the automatic switching of the DTG rebalance loop gain to higher values at high input rates, results in improved sensor performance (s. Section 4.3), but raises special problems (s. [3.24]).

Once the rebalance loop is optimized, the error budget of the SDF gyro, the FRG, and the DTG do not differ too much in principle from each other (s. Tables 3.2.1a to 3.2.2b).

In summary the DTG compares in the following manner with respect to the floated SDF gyro:

Advantages of the DTG:

- two measurement axes with one sensor;
- fewer parts;
- no drift due to shift of the motor bearings;
- no "pig tails" because the motor, torquer coils and pickoff coils are fixed to the case;
- no flotation fluid, and correspondingly:

  lower temperature sensitivity;

  drift adjustment during test;
- no backlash and friction in the gimbal bearings.

Disadvantages of the DTG when used for strapdown angular rate measurements:

- design of the caging loop is more difficult;
- lower angular momentum required for high input rates.

This last disadvantage arises because in the DTG the dimensions of the rotor and those of the torquer depend on each other (Fig. 3.1.2), in contrast to the SDF gyro (s. Fig. 3.3.7). Because of this limitation of construction the torquer scale factor S^t [dyn-cm/mA] of the DTG is lower as compared to that of the SDF gyro. To achieve a gyro scale factor $S^T = S^t/H$ of the same magnitude as the SDF gyro, the DTG has to run at a lower speed (s. Tables 3.3.2 and 3.4.2a). An exception is again the Teledyne SDG-5 which has a very high angular momentum, but this sensor has a low gyro scale factor and requires a very high torquing power at high input rates (≈1 kW at 500 °/s!).

Fig. 3.4.9 shows the cross section of the Litton DTG "Vibragimbal" family G2, G4, G1200 for use on platforms (LTN 72, LTN 71, LN 33, LN 40). In Fig. 3.4.10we see the Litef K 273 DTG which is the sensor in the strapdown attitude and heading reference system LTR-80. Finally, Table 3.4.2 summarizes some details on DTG's for platform and strapdown application.

Parameter	Ferranti Oscillogyro Type 142	Incosym Incoflex DTG No. 7	Litef K 273	Litton G-6	Sagem GSD	Singer Kearfott Conex	Singer Kearfott Gyroflex	Teledyne SDG-5
Weight [gm]	227	100	250	400	130	140	275	< 1045
Diameter [mm]	42.6	25.4	38	46	40	37	54	76
Length [mm]	44.1	38.1	49	38	34	45	46	76
Spin Frequency [Hz]	175	160	180	100	180	200	240	100
Angular Momentum H [gm-cm^2/s]	$1.3 \cdot 10^4$		$2.8 \cdot 10^4$	$8.1 \cdot 10^4$	$1.4 \cdot 10^4$	$2.7 \cdot 10^4$	$1.8 \cdot 10^5$	$1 \cdot 10^6$
Moment of Inertia								
Spin Axis [gm-cm^2]			25	129		22	119	1600
Transv. Axis [gm-cm^2]	18		23			12	62	
Figure of Merit			200	550		45	440	300
Maximum Torquing Rate [^{o}/s]	0.28	1200	200(400)	40(200)	300	200(400)	7.0	400
Torquer Scale Factor [^{o}/h/mA]	1.8 ^{o}/h/V[1)]	3600	1100	1250		900	46(125)	170
Torquer Scale Factor								
Linearity [ppm]	30	100		50	500	100	10	25
Stability [ppm]				20		50	20	27
g-insensitive, Bias Drift [^{o}/h]	< 0.5	< 10.	< 25	0.005	5($\pm$0.05)	5.0	1.0	< 2.0
Day to Day Drift [^{o}/h]	0.01(0.005)	1.0	0.3	0.01	< 0.05	0.03	0.003	0.005
g-sensitive Drift [^{o}/h/g]	< 2.0	< 1.0	< 25($\pm$0.3)	5	2($\pm$0.03)	5.0	1.0	< 0.2
g^2-sensitive Drift [^{o}/h/g^2]	< 0.06	0.10	0.15	0.02	0.2($\pm$0.03)	0.03	0.001	< 0.03
Short Term Drift [^{o}/h]	0.005	1.0	0.3	0.002	<0.01	0.003	0.0003	0.001
(figures in ( ) for spin axis vertical)	0.005(0.002)	1.0	0.3	0.002	<0.01	0.003	0.0003 (0.0005)	0.001
Operating Temperature [^{o}C]	-40 to +80	-40 to 90	-40 to 90	-40 to 80		-40 to 93	-40 to 71	-40 to 93
Vibration [g]	30 (10 to 1000 Hz)	30 (5 to 2000 Hz)	10 (5 to 2000 Hz)	10 (10 to 1000 Hz)		200 (10 to 1600 Hz)	100 (10 to 1000 Hz)	
Shock [g]	60(11ms)	250(6ms)	30(100, 2 ms)	100(0.5 ms)		225(1.5ms)	100(11ms) 225(6ms)	150(7.5ms)
Linear Acceleration [g]	20		< 20	50		225	200	150
Number of Gimbals	0 (beam shaped rotor with single degree of freedom elastic hinge)	1	1	1	1	1	2	3

[1)] capacitive torquer

Table 3.4.2a Data for Some Dynamically Tuned Gyroscopes

No.		Singer Kearfott Gyroflex	Singer Kearfott Conex	Teledyne SDG-5
1	Gyro Mechanical Resonant Freq. [Hz]	240	200	100
2	Gyro Time Constant [s]	100	50	250
3	Rotor Angular Freedom [°]	0.5	1.0	<0.5
4	Torquer Axis Adjustment [arc min]	0.5	30.0	<1
5	Spin Axis Adjustment [arc min]	0.5	3.0	<1.5
6	Mass of Rotor [gm]	44	22	260
7	Mass of Gimbals and Weights [gm]	0.6	0.7	33
	Rotor CG-Adjustment			
8	Axial [μm]	0.3	0.61	80
9	Radial [μm]	0.1	12.2	130
10	Gimbal Axis Separation Adjustment [μm]	20	6.7	50
11	Quadrature g-Sensitivity [°/h/g]	0.25		<1.5
12	Spin Axis Mass Unbalance [°/h/g]	1.5	10	<1
13	2n-Translational Sensitivity [°/h/g peak]	0.5	20	0.2
14	2n-Angular Sensitivity [°/h/arc sec]	0.1	5	0.1
15	Quadrature g-Sensitive Drift [°/h/g]	0.25	1.5	3
16	Torquing Power [Watt]	26 for 10 °/s	3.5 for 100 °/s	40 for 100 °/s
	Uncompensated Temperature Sensitivity			
17	g-Intensitive Drift [°/h/K]	0.0005	0.03	0.001
18	g-Sensitive Drift [°/h/g/K]	0.003	0.05	<0.02
19	Torquer Scale Factor [ppm/K]	25	25	-115 ± 25
20	Pickoff Offset [arc/sec/K]	0.05	0.1	0.1

Table 3.4.2b Additional Data on Some Dynamically Tuned Gyros

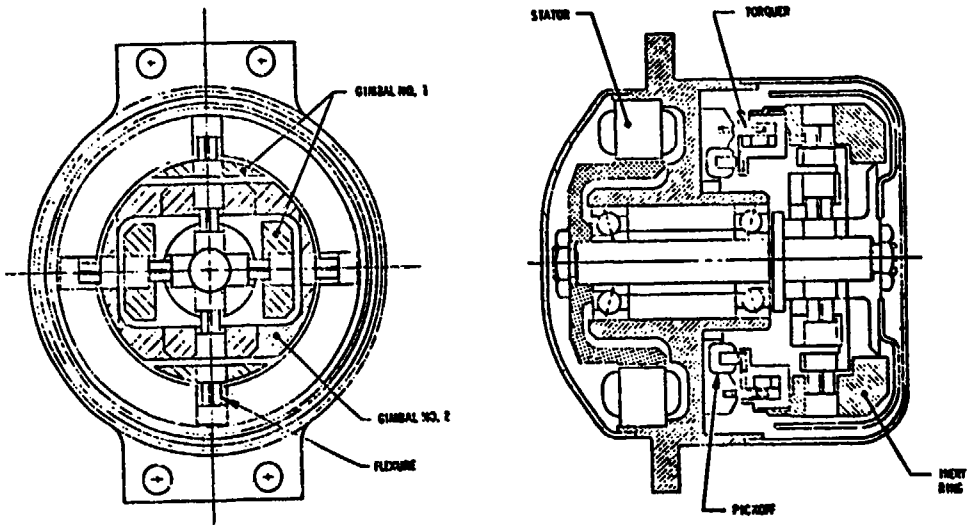

Fig. 3.4.9 The Litton Vibragimbal Gyro Assembly

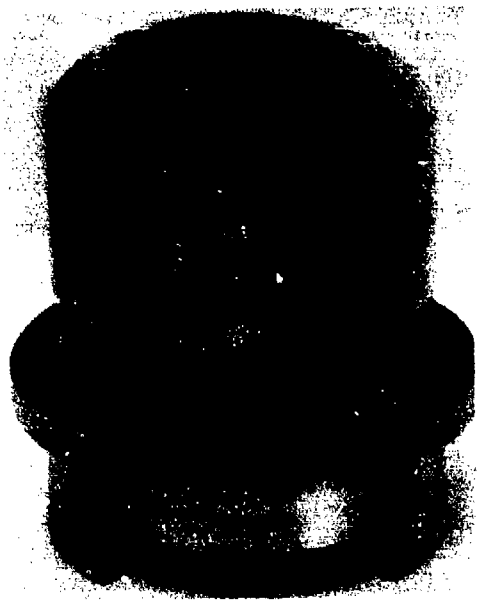

3.4.10 The Litef K 273 Strapdown Gyro

3.5 Optical Gyros (OG)

3.5.1 Introduction

Optical gyros make use of the so-called "Sagnac" effect, i.e. two light beams travelling in opposite directions in an optically closed path are affected by the rotation around the axis normal to the optical ring. This phenomenon was first observed by Harres in 1912 and by Sagnac in 1913 [3.26, 3.27].

The sensing element of the optical gyro thus is massless and the sensor should show no errors due the dynamic environment. This feature appears to offer enormous advantages when compared to the mechanical gyro, especially when the gyro is integrated into a strapdown navigation system (Section 7.4.4). Therefore, optical gyros would seem to be the ideal sensors for use in flight tests over a wide range of different applications and, consequently, are of special interest to the flight test engineer.

The following types of optical gyros are in development or in use already:

- optical rate sensors (ORS), where the output signal is a phase shift between two light beams; and
- rate integrating sensors (ring laser gyro RLG), where the output signal is a frequency shift between two light beams which can be directly converted into pulses proportional to input angular increments.

The sensitivity of the optical gyro depends on the area A enclosed by the light path. For a given outer dimension, the use of fibre optics to increase this enclosed area by numerous windings would appear to be an ideal way of increasing this sensitivity.

For the optical rate sensor, i.e. the classic Sagnac ring interferometer, the scale factor is proportional to the area A enclosed by the light beams (s. Eq. (3.5.3)) and the use of fibre optics opens a way to increase its sensitivity. This is essential if the sensor is to be of tolerable dimensions, because its sensitivity for one fibre winding is extremely low (e.g. 3.5 arc min phase shift per 1 rad/s input rate for a circular path of 10 cm diameter, s. Eq. (3.5.3)). However, once this technique will be available, the instrumentation engineer will gain freedom to further reduce the outer dimensions.

The development of the fibre optic rotation sensor is being actively pursued by many institutions. It is hampered by the fact that in this sensor the light beams are in contact with matter throughout their long path and consequently suffer adverse effects.

For the optical rate integrating sensor the scale factor is proportional to the enclosed area A divided by the length L of the path (s. Eq. (3.5.7)) and the use of the above mentioned multiturn path does not present any advantage. Nor is there a need for increasing the sensitivity, because it is already extremely high (e.g. 18 Hz per 1 Earth Rate Unit ERU for a diameter of 10 cm, or, expressed in different dimensions, 2.3 arc seconds input angle for 1 pulse output, see Eq. (3.5.9)). High quality sensors are being built using three or more mirrors within a linear dimension of 10 cm.

At the present time the main drawbacks to the use of optical gyros, compared with mechanical gyros, are their availability, cost and size. The mechanical gyros will certainly be retained for use as stabilization devices and strapdown sensors for lower accuracy (drift $\geq 0.1\ ^{o}/h$) for some time to come.

In the following paragraphs a brief review of the physics of the Sagnac interferometer is given together with its application to the optical rate sensor (ORS) and the ring laser gyro (RLG). The main sources of error are also discussed and examples of the RLG are given. No similar examples for the ORS are presented because this sensor has not yet left the laboratory development stage.

3.5.2 The Sagnac Ring Interferometer (SRI) as a Basis for the Optical Rate Sensor (ORS) and Ring Laser Gyro (RLG)

Around the turn of the century, discussions took place among physicists about the nature of light. In 1881 Michelson investigated the nature of a moving source of light using a linear interferometer [3.28], but this investigation did not show any measurable effect, thus proving that the speed of light (c) emitted from a moving source remains constant with respect to inertial space. However, for the same reason, the Sagnac ring interferometer, see Fig. 3.5.1, showed an effect.

The SRI shown in Fig. 3.5.1a consists of a light source (LS), a beam splitter (BS), three fully reflecting mirrors, M1, M2 and M3 for guiding the two light beams I and II on a square path back to their common origin on BS where part of their power is combined and projected onto the screen (SC). If the optical paths for both beams are identical, a photon emitted from BS on paths I or II will reach the origin again after time $T = L/c$, where L is the length of the path and c the speed of light. If the ring interferometer is rotated in the direction shown with respect to inertial space it can be seen that, since c is constant with respect to inertial space, the light beam I will reach the origin on BS at a time Δt_I later than T. Similarly the light beam II will reach BS at time Δt_{II} earlier. The equations for Δt can easily be derived for the circular path interferometer with radius r and area A (see Fig. 3.5.1b) as:

$$\Delta t_{I,II} = \mp L\,\omega\, r/c^2 \text{ and}$$

$$\Delta T = \Delta t_{II} - \Delta t_I = \frac{2L\omega r}{c^2} = \frac{4A}{c^2}\,\omega \qquad (3.5.1a,b)$$

with ΔT being the time difference between both beams. This time difference can also be interpreted as if the beams had travelled optical paths differing by the length

$$\Delta L = c\Delta T = \frac{2Lr}{c}\,\omega = \frac{4A}{c}\,\omega. \qquad (3.5.2a,b)$$

This interpretation helps us to understand the ring laser gyro very easily. It is shown in [3.29] that the formulas (3.5.1b and 3.5.2b) are independent of the shape of the enclosed area A.

The time difference ΔT between the beams causes a relative phase shift $\Delta\varphi$ or a relative shift Δz of the fringe pattern once they are brought to interference:

$$\Delta z = \frac{c\Delta T}{\lambda} = \frac{4A}{c\lambda}\,\omega = 1.65 \cdot 10^{-4} \text{ per } \omega = 1 \text{ rad/s} \qquad \Delta\varphi = 2\pi\Delta z = \frac{8\pi A}{c\,\lambda}\,\omega = 3.57 \text{ arc min per } \omega = 1 \text{ rad/s} \tag{3.5.3a,b}$$

where for the figures the following assumptions have been made: a circular path of 10 cm diameter, a light source of He-Ne ($\lambda = 6.33 \cdot 10^{-5}$ cm) and $c = 3 \cdot 10^{10}$ cm/s. The numbers reveal how weak the signal is.

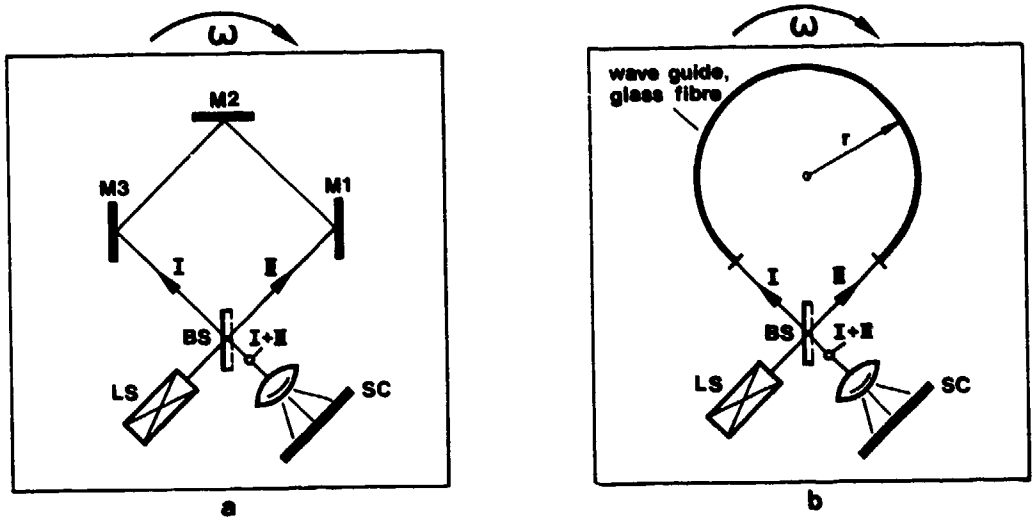

Fig. 3.5.1 Sagnac Ring Interferometer (a) and its Circular Substitute (b)

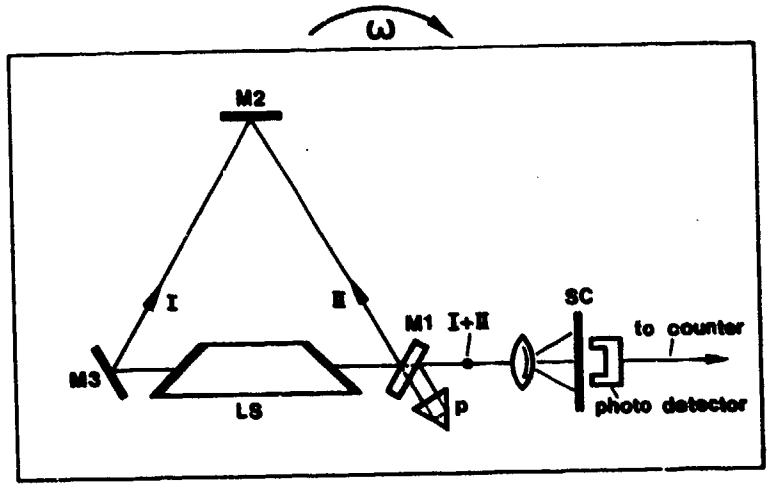

Fig. 3.5.2 The Ring Laser Gyro in Principle

Threshold values of Δz and $\Delta\rho$ found in the literature [3.30] are:

$$\Delta z_{min} = 10^{-3} \qquad \Delta\rho_{min} = 2 \cdot 10^{-7} \text{ rad} = 4 \cdot 10^{-2} \text{ arc sec.} \tag{3.5.4a,b}$$

These equations show that, with the ORS evaluating the direct phase shift, it should theoretically be possible to measure,

$$\omega_{min} = 40\ ^{o}/h. \tag{3.5.5}$$

This readout method was investigated at Lear Siegler for the development of an ORS. Though the above mentioned threshold was confirmed, other adverse effects limited the sensitivity of a 20 cm square set-up to over 25 °/s [3.30].

The readout method of the fringe pattern shift was used by Michelson and Gale in 1925 and they even managed to measure the rotation of the earth with $\Delta z = 0.25$! But their interferometer was of unwieldy outer dimensions, namely 340 m and 610 m separation of the four mirrors [3.31].

3.5.2.1 The Optical Rate Sensor

At present scientists in different countries have high expectations for the use of fibre optics in the SRI in order to develop an ORS of high accuracy and acceptable dimensions [3.32 to 3.37].

The expectations are nourished by the following advantages of the ORS as compared to the RLG discussed in the next section:

- the use of integrated optics promises that the ORS will become a very cheap sensor; and
- a solid state laser may be used in the ORS instead of a gas laser of limited life time which is at present required for the RLG.

For the ORS, the scale factors given in Eqs. (3.5.1 to 3.5.3) are increased by every turn of the fibre optic coil by substituting for A in these equations.

$$A = n\,A' \tag{3.5.6}$$

where A' is the mean area enclosed by each fibre optic turn and n is the number of turns.

Assuming that the threshold for measuring the relative fringe shift is, in accordance with Eq. 3.5.4a, $\Delta z = 10^{-3}$ then, in order to measure 1 Earth Rate Unit (ERU) with an ORS having a circular path diameter of 10 cm, the number of turns (n) required would be 82918 and thus the length (L) of the fibre optic 26 km!

If the method of direct phase shift measurement could be exploited with the corresponding threshold of Eq. (3.5.4b), then only 3 turns with a length L = 1 m would be required.

In present breadboard sensors frequency modulation techniques using acousto-optical elements for varying the light frequency are applied to convert the ORS output signal (phase shift or fringe pattern shift) into an output frequency.

The present state of the art is characterized by the fact that in the laboratory short-term noise equivalent rotation rates below 3 °/h have been accomplished with sensors of 30 cm diameter and 200 m fibre length [3.37].

The development of an ORS is beset with problems and the following are just three important ones. They indicate why the ORS has not yet progressed beyond the laboratory development stage.

- Expansion of the optical fibre and stress due to a temperature variation, for instance, affect the ORS scale factor and/or the optical properties of the fibres; though the corresponding effects are reciprocal[1]) and in general separable from the non-reciprocal effect due to sensor rotation, they do affect the measurement and have to be compensated.
- Time varying expansion and stress due to temperature gradients, for instance, as well as magnetic stray fields cause non-reciprocal effects which are not separable from the signal to be measured. These rate errors have been estimated [3.38]. For an ORS with an optical path diameter of 20 cm a thermal gradient of 10^{-2} K/s over a length of 1 m will induce an error of 0.1 °/h. A similar error will also be introduced if the magnetic field in the same ORS changes by 1/60 of the earth's magnetic field.
- Backscattering noise within the fibre and noise in the readout, which is reduced by using phase modulation techniques or an incoherent light and subsequent filtering [3.37].

3.5.2.2 The Ring Laser Gyro (RLG)

The set-up for the ring laser gyro (RLG) in Fig. 3.5.2 differs in principle from the one for the ORS in Fig. 3.5.1 in the following way. The light source - a gas laser - is mounted into the optical path replacing the exterior light source plus beam splitter of Fig. 3.5.1; the end mirrors of this laser tube are replaced by Brewster mirrors[2]): the optical path mirrors M1, M2, M3 are turned in such a way that, instead of the laser tube alone, the whole optical path acts as a resonance cavity.

1) Non-reciprocal effects are caused by motion or magnetism, whereby light beams travelling in matter in opposite directions are affected differently.

2) Brewster windows: material glass; angle of 57° with respect to optical axis; allow transmission without loss of light linearly polarized in the plane of incidence and reflect light linearly polarized normal to the plane of incidence [3.28].

In this particular device the optical path is composed of three mirrors only, as it is pursued at present by all manufacturers with the exception of Litton, which selected four mirrors. The mirror (M1) is partially transmitting and the prism (P) is part of the interference optics.

The ring laser is tuned to an oscillation with a frequency ν and a wavelength λ, which is an integer of the cavity length L as in a normal laser. Due to the Sagnac effect, the cavity length of both light beams I and II will apparently be displaced from L by an amount $\Delta l_I = c\Delta t_I$ and $\Delta l_{II} = c\Delta t_{II}$, or relative to each other by an amount ΔL (s. Eq. 3.5.2a,b)). This results in a frequency difference $\Delta\nu$.

With $\Delta\nu/\nu = \Delta L/L$ and $c/\nu = \lambda$, where λ is the mean wavelength of both beams, the frequency difference becomes:

$$\Delta\nu\ [\mathrm{Hz}] = \frac{4A}{L\lambda}\,\omega\,[\mathrm{rad/s}] = 9.12 \cdot 10^4\,\omega\,[\mathrm{rad/s}] \tag{3.5.7}$$

for a triangular path with a side length of 10 cm and $\lambda = 6.33 \cdot 10^{-7}$ m (He-Ne laser).

This frequency difference causes a wandering of the interference pattern at the screen (SC) proportional to the angular rate with respect to inertial space.

A photodiode mounted on the screen (SC) will count the number of fringes that pass it. Each fringe may then easily be converted into a pulse which indicates the angle increment through which the sensor has rotated with respect to inertial space. The number N of pulses for the total input angle displacement $\Delta\phi$:

$$N = \frac{4A}{L\lambda}\,\Delta\phi \tag{3.5.8}$$

defines the RLG nominal scale factor S, which for $\lambda = 6.33 \cdot 10^{-7}$m and a triangular RLG of 10 cm side length has the following magnitude:

$$S = \frac{\Delta\phi}{N} = \frac{L\lambda}{4A} = 2.3\left[\frac{\text{arc sec}}{\text{pulse}}\right]. \tag{3.5.9}$$

This result indicates that the RLG is ideally suited for use as a flight test sensor and in strapdown navigation systems.

3.5.3 Design Criteria for the Ring Laser Gyro and Sources of Error

3.5.3.1 Characteristics Common to All Ring Laser Gyros

Let us first comment on the selection of the laser - gas laser, liquid laser or solid state laser. Not only can any laser amplify light of a fixed frequency but also light within a broad spectrum due to the Doppler effect of its moving atoms. Yet the laser will oscillate at the frequency whose wavelength is an integer of the resonance cavity $L = n\lambda$.

In the RLG the need for the independent amplification of two light beams of different frequencies in one laser makes it necessary to use a gas laser. For the He-Ne gas laser, which is most commonly used in RLGs, the amplification bandwidth is 1500 MHz, approximately. The intensities of the two light beams vary periodically with the resonator length as shown in Fig. 3.5.3 ("mode distance" in this special case = 500 MHz).

Here the intensities I_1 and I_2 of the two light beams countertravelling in the ring laser are drawn over the variation of tube length. The curves are periodic with the wavelength λ of the centre frequency (the small apparent shift between both intensities is due to the construction of the plotter).

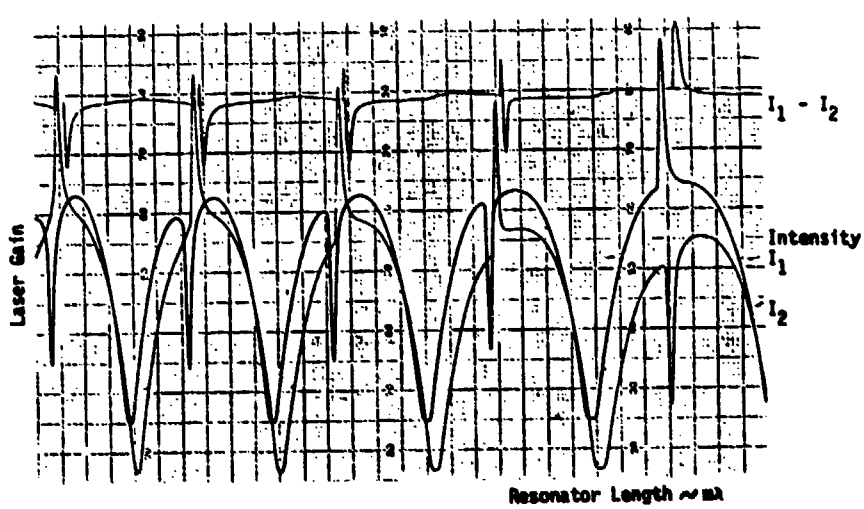

Fig. 3.5.3 Amplification Spectrum of Input Light in a He-Ne Laser Tube

Distinctly to be seen in Fig. 3.5.3 is the so-called "Lamb dip" near the maxima of the intensity curves, a condition in the RLG, when both light beams have the same frequency (zero input rate), i.e., when both beams have to be amplified by atoms of zero velocity [3.39]. When only one isotope is used this "Lamp dip" is only possible for one of the two beams, the intensity of which increases abruptly at the expense of the intensity of the other beam. If two isotopes are used with their gain curves and centre frequencies shifted slightly relative to each other, this "Lamb dip" effect is reduced. Therefore, two Ne isotopes (^{20}Ne and ^{22}Ne) in a mixture of 1:1 are mostly used (s. also Fig. 3.5.10).

The velocity of the gas within the laser tube, caused by the high voltage electrical field (Langmuir flow) and temperature gradients, will result in a constant frequency shift between the two counter-travelling light beams, which will be detected at the screen as an angular input rate. This is due to the so-called "Fizeau effect", describing the effect of the velocity V of an illuminated flowing medium of refraction index n on the speed c^m of light [3.39]:

$$\frac{c^m}{c} = \frac{1}{n} \pm \frac{V}{c}(1 - 1/n^2) = (0.9997 \pm 1.999 \cdot 10^{-14}). \qquad (3.5.10)$$

The numbers are good for V = 1 cm/s, $c = 3 \cdot 10^8$ m/s and n = 1.0003 for air. In the RLG this causes a change of optical length or an apparent frequency difference $\Delta\nu$ or angular rate $\Delta\omega$ [3.40]:

$$\Delta\nu = 2(n^2 - 1)\frac{d}{\lambda L} V = 6 \text{ Hz, i.e. } \Delta\omega \approx 4\ ^{\circ}/h \approx \frac{1}{4} \text{ ERU} \qquad (3.5.11)$$

for a ratio of the laser tube length d to the total length L of the cavity of d/L = 1/3 and $\lambda = 6.33 \cdot 10^{-7}$ m as for He-Ne.

To overcome the Fizeau effect, RLG's are always fitted with lasers having two anodes and one cathode or vice versa mounted symmetrically within the tube as indicated by Fig. 3.5.4, which shows the basic design principles of a Honeywell laser gyro. If only one anode were to be used the result would be an apparent rotation of the sensor proportional to a multiple of 100 °/h [3.41]. The sensor may be biased to compensate for some of these effects by adjustment of the high voltage (ca. 1500 V) in both branches. The number just quoted indicates that a highly stabilized control of voltage and of temperature is required.

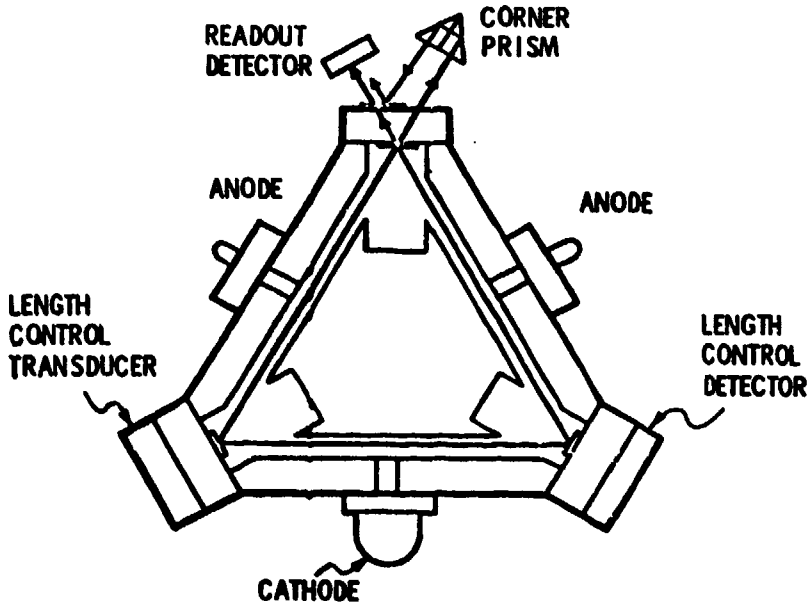

Fig. 3.5.4 Basic Configuration of the Honeywell Ring Laser Gyro

Another source of error is due to the fact that the refraction index n depends upon the frequency ν of the transmitted light. This causes the prism spectra of white light, and is known as the "dispersion effect". For the RLG this means that the optical cavity length $L = \int n(\nu)\, dl$ (with dl a length increment) and thus its scale factor (s. Eq..(3.5.7)) are functions of ν. This nonlinearity in the order of 0.1 % to 1 % is compensable if the operating characteristics of the laser remain constant [3.40].

However, the dispersion effect defines the stability required of the mean light frequency, i.e. the stability of the cavity length. This is firstly accomplished by using material of a very low thermal expansion coefficient (Cer-Vit, Zerodur) and secondly by controlling the mean intensity of the two light beams to its relative maximum. This is accomplished by means of a control loop from a photodiode on the partially transmitting mirror to a piezo element, adjusting one of the mirrors to the constant cavity lenght. The intensity maximum can be sensed by additionally dithering the piezo element.

The path lenght control to the maximum of the mean light intensity makes any other temperature control of the sensor unnecessary. We may thus state two essential advantages of the RLG over other gyroscopic sensors: digital output and temperature insensitivity - at least in theory!

A RLG incorporating the above design features will work satisfactorily for high input rates of ω; in fact the upper input rate is only limited to values above 800 to 1000 °/s by the fact that the modulation amplitude decreases with the output frequency [3.42]. But the RLG has a lower limit on input rates of a few hundred degrees per hour (Fig. 3.5.5).

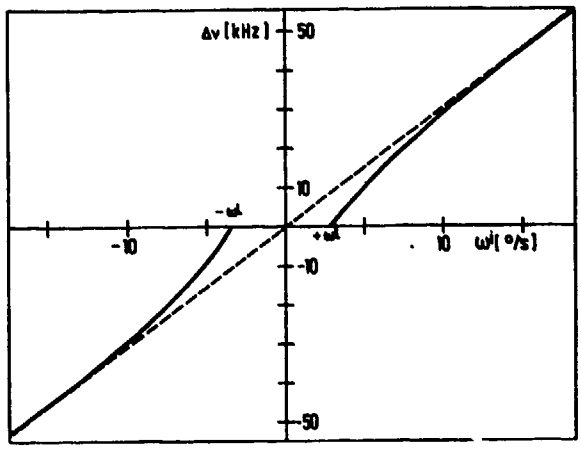

$A = 0.017\ m^2$
$L = 0.6\ m$
$\lambda = 6.33 \cdot 10^{-7}\ m$

Fig. 3.5.5 The Lock-In Effect of the Ring Laser Gyro

This is due to the so-called "lock in" effect experienced by any two weakly coupled oscillators with neighbouring natural frequencies. If this type of oscillating system is excited near the natural frequencies, both coupled oscillators will have the same period. Beat frequencies will be experienced only if the excitation frequency is distinctly different from the natural frequencies.

In the RLG the coupling of both oscillators, i.e. the two light beams, is caused primarily by the scattering of light at the mirror surfaces and within the laser tube. The relationship between the "lock in" rate (ω^L), the mirror backscattering amplitude ($r = 10^{-2}$) into the whole solid angle, the beam diameter ($d = 1$ mm), the enclosed area ($A = 43.3\ cm^2$ for a triangular optical path of 10 cm side length), the speed of light ($c = 3 \times 10^8$ m/s) and the wave length ($\lambda = 6.33 \times 10^{-7}$ m for Ne-He) is given as [3.40]:

$$\omega^L = 2.063 \cdot 10^5 \cdot \frac{c\,\lambda^2 r}{32\pi A\,d} = 570\ ^\circ/h. \qquad (3.5.12)$$

This corresponds fairly well with experimental values. It is interesting to note that $\omega^L \sim \lambda^2$, i.e. reduction of the wave length is beneficial, because it increases the scale factor (s. Eq. (3.5.9)) and reduces the value of ω^L (s. Fig. 3.5.4). Another approach for the analysis of the lock-in problem is presented in [3.42].

The "lock in" effect cannot be completely overcome. Its reduction through the development of improved mirrors with low backscattering and high reflectivity is the central topic of RLG research. Typical results from an analysis and laboratory measurement are presented in [3.44] and [3.45]. "Lock-in" rates as low as 100 °/h have already been accomplished [3.43]. However, the value would still be too high for a sensor with these characteristics to be used in navigation systems.

The "lock in" effect can be overcome by exposing the two light beams to an environment which causes nonreciprocal effects, i.e. effects which influence the light beams differently according to the directions in which they are travelling. As stated earlier these effects may be induced by:

- motion, or
- magnetism.

These effects may be introduced by employing "bias techniques", (s. Fig. 3.5.6) namely:

- as a continuous bias, or
- as a periodical bias or dither.

Different accuracy problems arise from the use of these "bias techniques", i.e.

- if the bias is applied continuously (s. Fig. 3.5.6a), it must be high enough (e.g. 100 °/s) to ensure that the RLG never enters the "lock in" region, and it must be stable enough to ensure that after compensation sufficient accuracy is achieved, (e.g. 10^{-2} °/h). The requirement for relative stability is thus:

$$\delta\omega/\omega = 3 \cdot 10^{-8}. \qquad (3.5.13)$$

- if the bias is applied periodically (s. Fig. 3.5.6b to d), the gyro will enter the "lock in" region twice per dither cycle and, on leaving this region the two beams will attempt to pull into phase lock. The

a) Lock-In Compensation: Constant Bias Rate ω^c

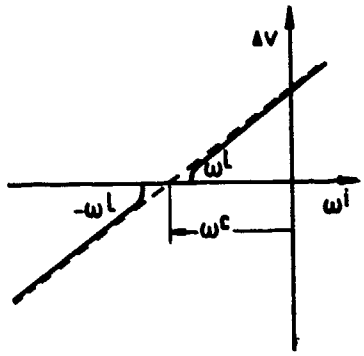

b) Lock-In Compensation: Rotational Dither

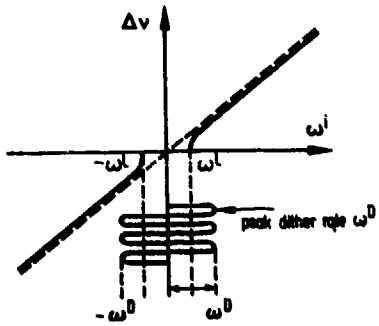

typically : ω^D = 100 to 300 deg/s

c) Input-Output with Dither

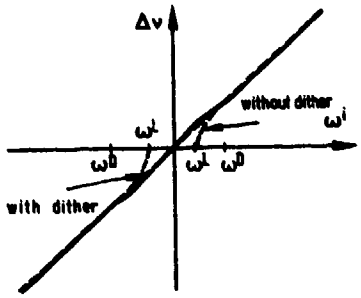

d) Scale Factor for Dithered Ring Laser Gyro

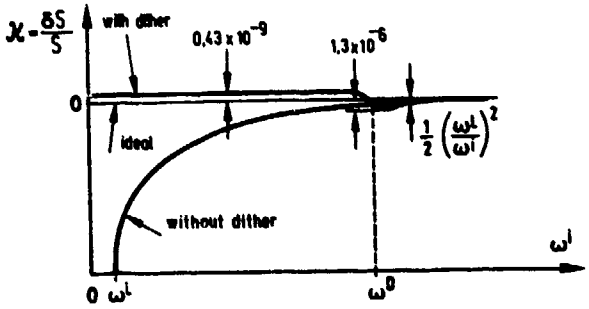

ω^L = 300 deg/h
ω^D = 200,000. deg/h = 55 deg/s

Fig. 3.5.6 Effects of a Continuous or a Periodical Bias in a Ring Laser Gyro on Input-Output Characteristics and Scale Factor [3.40]

resulting phase shift (order of magnitude some 10^0) will, at the best, constitute a source of rate noise which can never be made zero. These errors will accumulate in a random manner when the RLG output is summed up giving rise to a "random walk" cumulative output error, whose loband increases with the square root of the elapsed time. This is particularly serious when short measurement times are employed for the extraction of the sensor's drift; the apparent drift due to the random walk will be quite large [3.46].

- A second error source with this dither compensation is due to the fact that the gyro does not measure the vehicle's angular motion while passing the "lock in" region; this also contributes to a "random walk" drift depending on the dynamic environment and the time during which the RLG passes this region. A high dither frequency, or preferly a square-wave dither motion, are of advantage.
- A third error source with the dither compensation is the scale factor nonlinearity at input rates near the maximum dither rate (s. Fig. 3.5.6d). It arises from the fact that at this input rate the highly nonlinear maximum dither sinewave dives into the lock-in region. This scale factor nonlinearity shows an almost square law dependence on the lock-in rate [3.46] amounting to 50 ppm at a lock-in rate of approximately 0.4 °/s.

An obvious technical solution to a continuous bias would be a mechanical rotation of the RLG at >100 °/s. This would require an exact knowledge of the angular rate applied in order to compensate accurately for this rotation or, conversely an exact measurement of the angle between the rotating RLG and the base. As far as it is known, this technique is not currently being porsued.

The required stability in Eq. (3.5,13) for a continuous bias cannot be achieved by using magnetism.

The concept first pursued by Hamilton Standard under the name of "DILAG" (differential laser gyro) and later by Raytheon under the name of "FFRL" (four frequency ring laser gyro), in which constant magnetic bias techniques are used, is not that employed in a conventional RLG. In these instruments two RLGs are implemented in one cavity with the constant bias acting in a positive or negative sense upon both. Errors in the bias cancel out in the combined output and thus the stability requirements of Eq. (3.5.13) are not applicable [3.46]. We will come back to it in Section 3.5.3.5.

Technical solutions which have been applied by various design agencies using these concepts are discussed below and their characteristics are compiled in Table 3.5.1.

3.5.3.2 The Ring Laser Gyro Using the Mechanical Bias Technique (Mechanical Dither)

(Manufacturer: Honeywell US, Honeywell G, Litton, Rockwell, Sperry UK, CROUZET-SFENA F)

The RLG is mounted to the case via a torsion spring (s. Fig. 3.5.7a) which is excited to angular vibrations of 0.3° amplitude and 50 Hz frequency i.e. of 100 °/s angular rate amplitude, approximately. The dither compensation is done in an elegant way by mounting the readout prism and the detectors case-fixed as shown in Fig. 3.5.7b.

Beside the drawback that mechanical motion is used in a sensor which is solid state from its physics, the mechanical dither has another drawback: the bias motion is a sinusoid and not a square wave (which would bring about better performance since the lock-in region is traversed in the shortest time possible). But so far this concept is pursued by nearly all manufacturers (s. Table 3.5.1) which may be due to the following factors:

- most of the research time has been invested in this concept
- mechanical dither does not have a problem concerning symmetry, since even with asymmetric dither rate its integral will not increase with time
- the readout concept compensates the dither regardless of its time dependence.

3.5.3.3 The Ring Laser Gyro Using the Magnetic Mirror Bias Technique

(Manufacturer: Sperry)

In this RLG a magnetic environment is used to create a non-reciprocal effect. In 1876 Kerr (UK) [3.47] showed that the use of magnetic mirrors affected the properties of light. The transverse Kerr effect is used in this RLG to separate the frequencies of both light beams at zero input angular rate (s. Fig. 3.5.8). The maximum effect occurs when the two beams are polarized linear in the plane of incidence and the magnetization (M) is in the plane of the magnetic mirror and normal to the plane of incidence.

The magnetic mirror consists of a very thin transparent layer of especially composed iron garnet, together with a high reflectivity multilayer dielectric stack |3.48| to |3.50|. A reflectivity of over 99.8 % is obtained. The differential phase shift for the oppositely directed waves is 2.0 arc minutes which produces a bias equivalent to 60 degrees per second in a 0.4 m path length gyro operating at 1.15×10^{-6} m wavelength.

By periodically switching the sense of the applied magnetic field the bias is likewise periodically reversed. The garnet material has a very square hysteresis loop with 16 A/m coercive force. As a result the bias obtained reverses very suddenly, in 10^{-6} seconds, and there is essentially no time spent in the zero rate dead band. This eliminates the lock-in effect as a source of gyro random walk drift, allowing the quantum noise limit to be reached.

The square loop magnetic property also makes the bias mirror very insensitive to stray magnetic fields, or variation in the strength of the deliberately applied field, since the mirror is operated well into saturation.

With the garnet mirror, a random walk drift of 0.006 deg/$\sqrt{hr}$ at $\lambda = 1.15 \times 10^{-6}$ m is achieved using a 0.4 m optical path gyro. At $\lambda = 0.63 \times 10^{-6}$ m a random walk of 0.001 or lower is realized, owing to lower scale factor and higher lasing intensity.

a)

b)

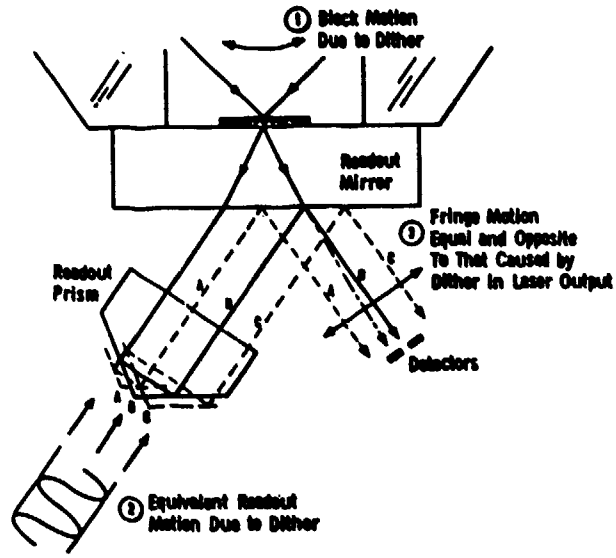

Fig. 3.5.7 The Honeywell GG 1300 Ring Laser Gyro and its Readout Compensation for Dither

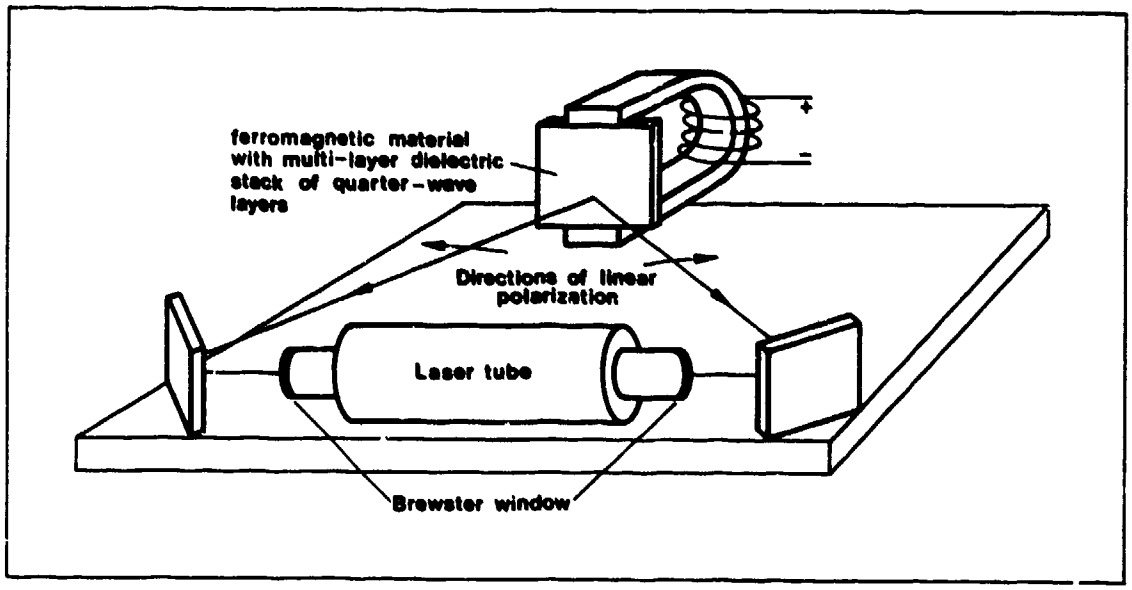

Fig. 3.5.8 The Ring Laser Gyro with Magnetic Mirror Bias Technique

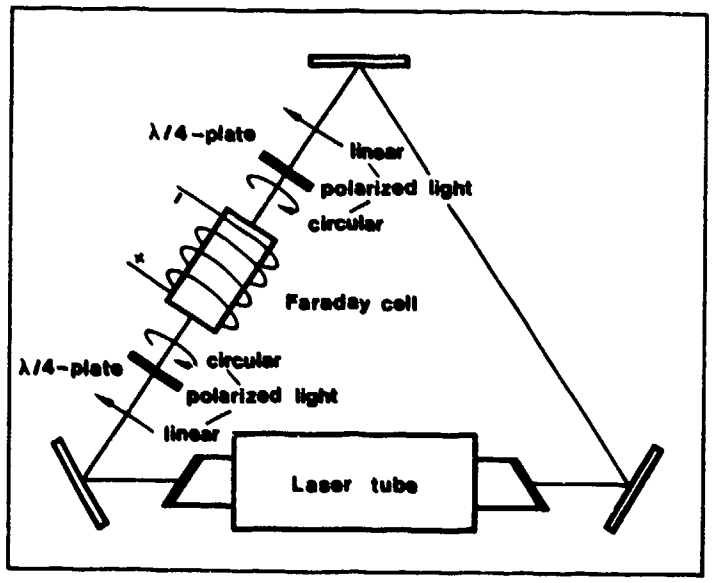

Fig. 3.5.9 The Ring Laser Gyro with Faraday Cell Bias Technique

3.5.3.4 The Ring Laser Gyro Using the Faraday Cell Bias Technique

The use of a Faraday cell is an alternative method for separating the two light beams in a RLG (s. Fig. 3.5.9). In 1845 Faraday showed that the plane of polarization is rotated by a magnetic field whose intensity is parallel to the direction of the polarized light beams transversing the isotope matter [3.47]. The sense of rotation is opposite for positive and negative propagation directions parallel to the applied magnetic field. This may be understood as occuring because the index of refraction of the material depends on whether the precession of its electrons about the applied longitudinal magnetic field is in the same or the opposite sense as the rotation of the circularly-polarized light's electric field. Equivalently stated, the Faraday effect introduces a differential phase shift between circularly polarized modes travelling in opposite directions.

In a RLG this rotation of the circular polarized light may be transformed into a corresponding phase shift of linear polarized light by means of two $\lambda/4$ plates in front of and behind a Faraday cell. The weakness of this method is that the effect is proportional to the length of the Faraday cell and the magnetic field, and thus the stability requirements of Eq. (3.5.13) can never be achieved. Temperature changes which affect the length of all intra-cavity elements can, to a certain extent, be overcome by proper design [3.46], and by periodically switching the direction of the magnetic field. However, any stray magnetic field will generate a false angular rotation signal.

Thus a general requirement for any RLG may be derived as:

"The length of the intra-cavity elements transversed by the beams has to be reduced to a minimum since they may act as unwanted Faraday cells."

The use of garnet as a Faraday cell material theoretically opens up the possibility of reducing the sensitivity of the RLG to stray magnetic fields since this material can be brought to magnetic saturation. However, its ability to transmit light is rather low thus preventing its use in a straightforward manner.

The above mentioned problems may give an indication why the Faraday cell bias technique is at present not used in a conventional RLG by any design agency. The Faraday cell in an external cavity or the Faraday mirror are discussed in [3.49].

3.5.3.5 The Four Frequency Laser Gyro (FFLG)

(Manufacturer: Raytheon [3.46])

The FFLG takes advantage of the fact that one single cavity can not only serve as resonator for two counter travelling light beams, but for four light beams - two in each direction, once they are polarized. Only two circular polarized light beams (right-and left-hand circular polarized, rcp and lcp) can be brought to resonance in each direction.

Fig. 3.5.10a indicates the elements of a FFLG resonator: four mirrors, the laser tube, the reciprocal (direction independent) polarization rotator and a Faraday cell as non-reciprocal element. The polarization rotator (typically, a piece of quartz cut normal to its main symmetrical crystalline axis) allows only rcp or lcp beams to come into resonance in each direction. It simultaneously splits the frequencies of the rcp and lcp beams, since after traversing the rotator the rcp and lcp beams are rotated by 2θ with respect to each other, corresponding to a relative phase shift of the same amount and to a frequency shift of

$$\Delta\nu = \frac{\theta c}{\pi L} \tag{3.5.14}$$

c/L being the free spectral range of the original (empty) cavity. For the case of a 90^0 rotator, the modes are split by one half of the free spectral range and therefore have a symmetric spectral distribution. Thus in the clockwise (cw) and counter clockwise (ccw) directions rcp and lcp light beams are brought to resonance, i.e. a rcp and a lcp ring laser gyro is implemented at frequencies split by

$$\Delta\nu = \frac{c}{2L} \tag{3.5.15}$$

as indicated in Fig. 3.5.10b. The lock-in effect in the two gyros requires the application of the bias techniques discussed in the previous sections. For this purpose a non-reciprocal polarization rotator, e.g. a Faraday cell, is used as shown in Fig. 3.5.10 with a frequency splitting lower than the one mentioned in Eq. (3.5.15) for the two gyros.

The non-reciprocal rotation effect of the Faraday cell further splits, in opposite senses, the counter travelling modes of each gyro. The resulting four frequencies are shown under a composite gain in Fig. 3.5.10b. The Faraday frequency splitting is:

$$\Delta\nu^F = \nu^b - \nu^a = \nu^d - \nu^c = \frac{c}{L}\,\frac{\theta^F}{\pi} \tag{3.5.16}$$

with θ^F = Faraday rotation in radians.

The Sagnac or laser gyro effect (s. Eq. (3.5.7)) in the two gyros is:

a)

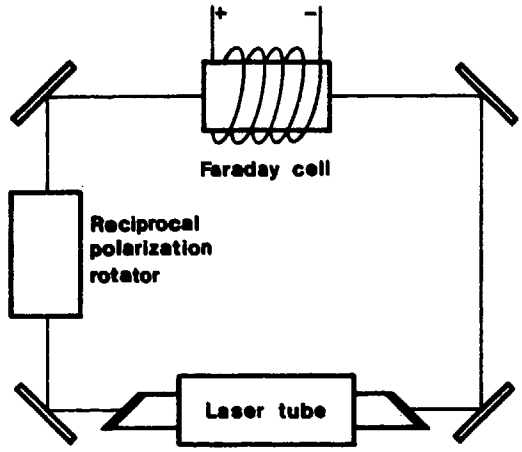

b)

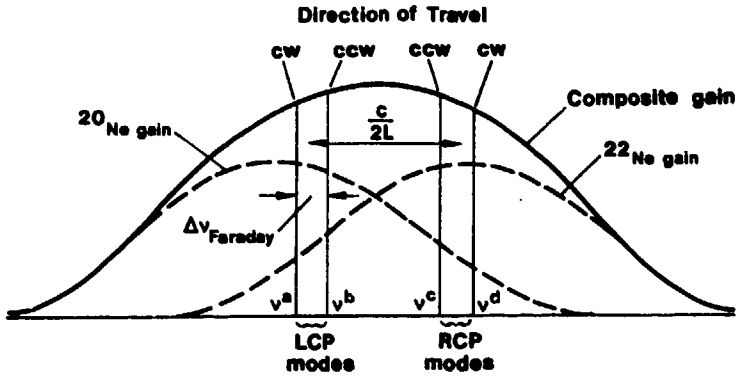

Fig. 3.5.10 The Four Frequency Laser Gyro and its Output Signals

$$\nu^b - \nu^a = \Delta\nu^F - \frac{2A\omega}{\lambda L} \; ; \qquad \nu^d - \nu^c = \Delta\nu^F + \frac{2A\omega}{\lambda L} \, . \tag{3.5.17a,b}$$

If the differential output between the two gyros is taken

$$\Delta\nu = (\nu^d - \nu^c) - (\nu^b - \nu^a) = \frac{4A\omega}{\lambda L} \tag{3.5.18}$$

the Faraday bias $\Delta\nu^F$ will cancel and the rotation-generated counts of the two gyros (rcp and lcp modes) add. Thus the sensitivity of a FFLG is twice that of a conventional ring laser.

The advantage of the FFLG is that both gyros, sharing a common optical path are statically biased, thus enabling the two gyros to avoid the "lock in" region. The random walk error should thus be avoided providing a sensor of low noise. The test results discussed in [3.44] and [3.51] are promising in this respect.

3.5.4 Error Model of the Ring Laser Gyro

So far we have discussed the functioning of optical gyros (OG) and some error sources. An error model as basis for calibration and compensation is still pending. The situation for the OG is in this respect different as compared to the mechanical gyro, for which we have found in Section 3.2 the main contributions to an error model as result of an analysis. With the OG the error model is at the present time primarily based on experience, i.e., found empirically, with the exception of some errors as for instance due to misalignment, scale factor nonlinearities near the lock-in threshold (s. Fig. 3.5.6d) and signal readout.

Contributions for standardizing the error model, for calibration techniques and for methods to analyse the results can be found in [3.52] and [3.53].

In summary the RLG output signal in these references is written as (s. Eq. (3.5.8), (3.5.9) and (3.2.45)):

$$N\,[\text{arc sec}] = S \int_0^t (1 + \kappa)\,(\omega_I - D)\,d\tau \tag{3.5.19}$$

where

D = drift

S = nominal gyro scale factor, being in error with the actual one by κ (s. Section 3.2.2.6):

$$\kappa = \delta S/S. \tag{3.5.20}$$

The scale factor error κ and the gyro bias again are functions of a number of external parameters, such as temperature, temperature gradient, time, switch-on to switch-on, and the applied magnetic field which are modelled for calibration in the following way:

$$\kappa = \kappa(\omega_I) + \kappa^T(T - T_o) + \underline{\underline{\kappa}}^{\Delta T}\,\underline{\Delta T} \tag{3.5.21}$$

$$D = D^f + D^t(t) + d^T(T - T_o) + \underline{\underline{d}}^{\Delta T}\,\underline{\Delta T} + \underline{\underline{d}}^H\,\underline{H} + d_0^m\,\omega_0 + d_S^m\,\omega_S + D^{rw} \tag{3.5.22}$$

where

$\kappa(\omega_I)$ = scale factor error as function of input rate ω_I, which may be highest near the lock-in bias rate, s. Fig. 3.5.6d, but small compared to the mechanical gyro

κ^T = temperature sensitivity of scale factor

$\underline{\underline{\kappa}}^{\Delta T}$ = $[\kappa^{\Delta T}{}_I \quad \kappa^{\Delta T}{}_0 \quad \kappa^{\Delta T}{}_S]$ = row matrix representing the sensitivity of the scale factor for temperature gradients in the three axes I, O, S

$\underline{\Delta T}$ = $[\Delta T_I \quad \Delta T_0 \quad \Delta T_S]^T$ = temperature gradient vector along gyro axes I, O, S

D^f = fixed RLG bias

$D^t(t)$ = deviation of the bias as function of time

d^T = bias temperature sensitivity

$\underline{\underline{d}}^{\Delta T}$ = $[d^{\Delta T}{}_I \quad d^{\Delta T}{}_0 \quad d^{\Delta T}{}_S]$ = row matrix representing bias sensitivity to temperature gradients in the three axes I, O, S

$\underline{\underline{d}}^H$ = $[d^H{}_I \quad d^H{}_0 \quad d^H{}_S]$ = row matrix representing bias sensitivity to magnetic fields along the three axes I, O, S

$\underline{H}$ = $[H_I \quad H_0 \quad H_S]^T$ = magnetic field vector along the three axes I, O, S

$d^m_{0,S}$ = misalignment drift coefficients, s. Table 3.2.1a, Row 4

D^{rw} = random walk drift.

The random walk drift D^{rw} is calculated from the test results if the moving avarage is taken out of the raw data, the remaining noise is integrated up and the error angle ε is divided by the elapsed time:

$$D^{rw} = \varepsilon/t. \tag{3.5.23}$$

Since according to theory the time dependence of the standard deviation $\sigma(\varepsilon)$ of the error angle is

$$\sigma(\varepsilon) \sim \sqrt{t}, \tag{3.5.24}$$

the standard deviation of the random walk drift is

$$\sigma(D^{rw}) \sim 1/\sqrt{t}. \tag{3.5.25}$$

The assumption made in [3.53] for D^{rw} is:

$$D^{rw} = R^\Theta/\sqrt{t} \tag{3.5.26}$$

with R^Θ = random walk parameter.

D^{rw} may be affected by the dither motion bias compensation (s. Section 3.5.3.2) because this motion causes sinusoidal disturbance torques about the input axis of the sensor and consequently during the test a corresponding motion of the table-mounted RLG case, if the compliance of the table differs from zero. For infinite compliance, i.e. no table restraint about its drive axis when the table servo electronics cannot follow the high frequency motion any longer, the table motion is governed by:

$$\frac{\phi^T}{\phi^D} = \frac{J^D}{J^T} \tag{3.5.27}$$

where

ϕ^T = amplitude of table motion

ϕ^D = amplitude of dither motion

J^D = moment of inertia of RLG dithering Zerodur block

J^T = moment of inertia of test table.

This test table motion will not be constant for each dither period and consequently will contribute to the random error. It is called "spillover" in [3.53] and [3.54]. These references include an analysis and test experiences of this effect.

The sampling time should be synchronized with the period of the lock-in bias compensation because any deviation may also contribute to an error in D^{rw} (s. [3.53]).

3.5.5 Summary of Some Hardware Examples

The main data on RLG's available today are listed in Table 3.5.1.

No.	Manufacturer Type	Units	Honeywell GG-1342	Rockwell -	Litton LG-2717	Litton LG-2728	Sperry SLIC-7(3axes)	Sperry SLG-15	Raytheon RB-25
1	Perimeter	cm	32	43	17	28	20	40	25
2	Weight	kg	1.9	3.63	1.5	1.5	2.3	7.2	-
3	Size	cm	15.7x14.7x5.3	22.9x22.9x7.6	14x11x6.5	14x17.7x5	10.2diax11.4	10.2x20.3x27.9	-
4	Material	-	CERVIT	CERVIT	ZERODUR	ZERODUR	CERVIT	CERVIT	CERVIT
5	Lock-in technique	-	mech.dither	mech.dither	mech.dither	mech.dither	magn.mirror	magn.mirror	Faraday cell 4 modes
6	Number of mirror	-	3	3	4	4	3x3	3	4
7	Number of anodes/ cathodes	-	2/1	1/2	2/1	2/1	2/1 each axis	2/1	-
8	Power requirements	-	28Vdc/1.1A	28Vdc/0.6A	3 Watt	3 Watt	0.6x3 Watt	0.6 Watt	-
9	Maximum input rate	deg/s	800	-	800	400	1500	750	-
10	Bias stability (1 - 10 hr)	deg/h	0.007	0.01	0.02	0.005	0.2	0.02	0.005
11	Bias stability (day to day)	deg/h	0.01	0.02	0.04	0.01	0.5	0.05	-
12	Random walk	deg/$\sqrt{h}$	0.003	0.005	0.015	0.003	0.05	0.006	0.001
13	Scale factor (s)	arcsec/pulse	2.0	1.57	3.0	1.8	3.2	1.6	1.5
14	S-linearity	ppm	5	10	5	3	200	100	5
15	S-stability	ppm	5	-	5	5	200	100	-
16	Bias temp. sensitivity	deg/h/°C	0.002	0.02	-	-	0.008	0.002	0.0004

Table 3.5.1 Data for Some Ring Laser Gyros

3.6 Accelerometers

In another volume of this AGARDograph [3.55] the application of accelerometers to flight-testing has been treated. For a better understanding of the following chapters the basic principles of accelerometer measurements are briefly summarized in this section.

3.6.1 Principle of Operation of an Accelerometer

In Chapter 2 the basic ideas of inertial measurements have been described. From Eq. (2.3) it could be seen that the "specific force" $\underline{f}$ to balance the proof mass in an accelerometer

$$\underline{f} = \underline{a} - \underline{G}$$

$$\underline{a} = \left.\frac{d^2 \underline{R}}{dt^2}\right|_i \tag{3.6.1}$$

is equal to the sum $\underline{a}$ of all forces accelerating the proof mass minus gravitation $\underline{G}$. The accelerometer output signal is proportional to $\underline{f}$.

The basic principle of construction of an accelerometer is explained in Fig. 2.3. A proof mass is suspended in a case and confined to a zero position with the help of a spring or a rebalance loop as described below. In general, damping is added to give the spring/mass system a proper dynamic transfer function. Aircraft accelerations act upon the accelerometer case and cause the mass to react with a displacement with respect to the zero position so that the resulting spring force compensates the acting acceleration. The displacement of the mass with respect to the case is then proportional to f.

High-quality accelerometers can be regarded as having a second-order transfer function. The bandwidth is in general much higher than the acceleration frequencies to be measured (s. Table 3.6.1), so that the output signal $f^{\times}$ is practically identical to the input specific force f plus the accelerometer errors:

$$f^{\times} = (1 + \kappa)(f + B) \tag{3.6.2}$$

where (s. Table 3.6.1)

κ = scale factor error, corresponding to that of the single-degree-of-freedom gyro discussed in section 3.2.2.6 and

B = accelerometer error, consisting, for instance, of the bias, the misalignment of the input axis and the cross coupling term discussed below [3.56].

Given the specific force $\underline{f}$ acting upon an aircraft, travelling in the earth's gravitational field $\underline{G}(\underline{R})$, the aircraft inertial acceleration

$$\left.\frac{d^2 \underline{R}}{dt^2}\right|_i$$

can be computed using Eq. (3.6.1). This again can be transformed into a navigation coordinate system to obtain the acceleration with respect to ground:

$$\dot{V}_N, \quad \dot{V}_E, \quad \ddot{h}$$

by use of Equation (7.2.4b). From this acceleration the velocity and position of the aircraft can be computed by integration, if initial values of velocity and position are known. How this is carried out in the computer of an inertial navigation system is discussed in Chapter 7. It is obvious from these considerations that the angular orientation of the accelerometer input axes with respect to the navigation coordinate system must also be known accurately.

3.6.2 Restrained Pendulum Accelerometer

The type of accelerometer that is presently used in most operational inertial navigation systems is the restrained pendulum accelerometer. Fig. 3.6.1 shows the principle of construction of such a device. A pendulous mass is suspended and restrained to a zero position by a control loop from the pickoff to the torquer, similar to a gyro (s. Fig. 4.2.1a). Optical, capacitive or inductive pickoffs detect a deflection of the pendulum and torquers force it back to its zero position. The torquer current i that is necessary to compensate an acceleration and to bring the pendulum back to its null position is then a measure of the specific force f.

Fig. 3.6.2 shows as an example the exploded view of the Sundstrand Q-FLEX Accelerometer in which the principles of construction of Fig. 3.6.1 are implemented. Flexure and proof mass are formed from a single blank of specially processed quartz. A slot is cut in the blank in such a manner as to form an annular section and central disc connected by a narrow bridge. The central disc serves as part of the proof mass, the bridge as a flexure, and the annular section as the flexure support. The bridge section is chemically milled in order to form the flexure. A portion of the central disc is made conductive by vacuum vapor-depositing metallic films to provide electrical surfaces, as required for the capacitance pickoff. Conducting leads for the pickoff signals and the torquer coil drive current are formed across the flexure by similarly vacuum-vapor-depositing metallic films. Finally, attaching the torquer coils onto the central disc completes the proof mass, flexure, and flexure support sub-assembly. This sub-assembly is then clamped between the magnet structures. The magnet structures hold the magnets in proper position and keep the proof mass assembly from moving [3.57].

No.	Manufacturer Model No.	Litef B250	Sundstrand Q-FLEX QA-1400	Systron Donner 4852
1	Weight [gm]	85	80	< 65
2	Diameter [mm] (Width)	26	26	25
3	Length [mm]	21	25	45
4	Natural Frequency [Hz]		< 800	
5	Damping Ratio		0.4-0.7	0.5 to 1.6
6	Bandwidth [Hz]	300	300(±5%)	> 300
7	Maximum Input Acceleration [g]	10	30	up to 400
8	Scale Factor (adjustable)	4.0 mA/g	1.3 mA/g	1.0 mA/g
	Scale Factor Error			
9	Linearity	$<3\cdot10^{-5}$g (for <1g)	20 μg/g^2	20 ug/g^2
10	Stability		500 ppm/yr	
11	Threshold	10^{-6}g	10^{-6} g	10^{-6}g
12	Bias (untrimmed)	$<5\cdot10^{-3}$g	$5\cdot10^{-3}$ g	$<4\cdot10^{-3}$g
13	Day-to-Day Repeatability	$6\cdot10^{-5}$g	$5\cdot10^{-5}$ (benign)	$3\cdot10^{-5}$g
			10^{-3} g (all environments)	
14	Transverse Sensitivity [g/g] (Misalignment)	$1.5\cdot10^{-4}$	$2\cdot10^{-3}$	$7\cdot10^{-3}$ (untrimmed)
	Temperature Sensitivity			
15	Bias	10μg/K	30 μg/K	< 10ug/K
16	Scale Factor	20μg/K	< 180 ppm/K	< 180ppm/K
17	Vibration Rectification [g/g^2]		$5\cdot10^{-5}$ (sine)	$2.0\cdot10^{-5}$
18	Operating Temperature [^{o}C]	70±5	-55 to 107	-55
19	Vibration [g] RMS		15	15 (20 to 2000 Hz)
20	Shock [g]	50(11ms)	250 (6ms)	1500 (0.5 ms)
21	Design Feature	Taut Quartz Fibre	Quartz Flexure	Floated Pendulum with Pivot/Jewel Bearings

Table 3.6.1 Data for Some Accelerometers

The balanced capacitance bridge pickoff is formed by the small gaps between the metallized portion of the quartz proof mass and the fixed reference plates in the magnet structure.

The small, precise gas-filled gap between the magnet housings and the proof mass assembly also provides a fairly high damping. Compared to fluid-filled sensors this accelerometer has a small phase shift.

In the Litef B250 accelerometer the pendulum consists of a U-shaped wire suspended on each side of the U by a strained and metallic coated quartz fibre. A magnetic field and the current running through the pendulum generate the forces required to null the output of the optical pickoff.

In the Systron Donner 4310 accelerometer the pendulum is floated and supported by pivot/jewel bearings.

The pendulum rotary axis is called the output axis. The input axis is orthogonal to the output axis and to the pendulum in its zero position. With pendulum accelerometers a so-called "cross-coupling" error or "vibrapendulous rectification" exists, which is similar to the one discussed for the mechanical gyros (s. Table 3.1.2b, Row 4). Correlated accelerations in the input axis and pendulum axis cause this error, which is affected by the stiffness of the servo loop. Pendulous accelerometers also exhibit anisoinertia torques, just as mechanical gyros do, but produce no error from this source if the effective center of mass is properly defined.

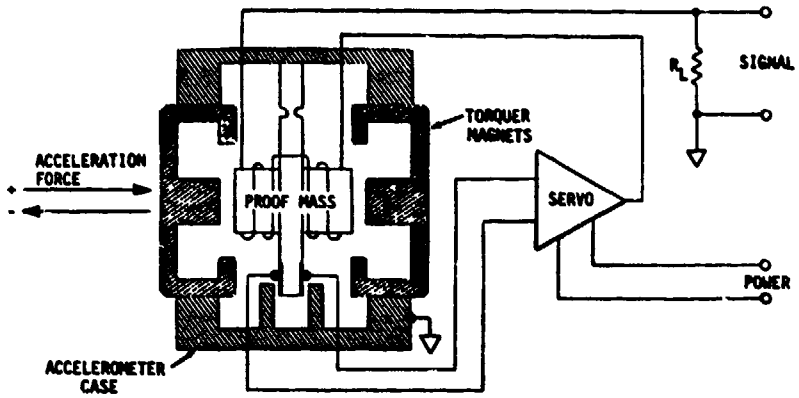

Fig. 3.6.1 The Eystone-Wilson Pendulum Accelerometer in Principle

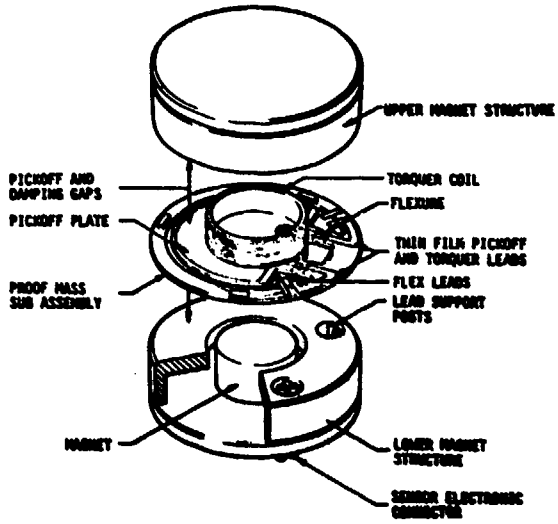

Fig. 3.6.2 The Sundstrand Q-FLEX Pendulum Accelerometer, Exploded View

References for Chapter 3

[3.1] Wrigley, W. Hollister, W. M. Denhard, W. G. — Gyroscopic Theory, Design and Instrumentation. The MIT Press, Cambridge, Mass., (1969).

[3.2] Arnold, R. N. Maunder, L. — Gyrodynamics and its Engineering Applications. Academic Press, New York (1961).

[3.3] — Ball Bearing Yield and System Isoelasticity. The Barden Corporation, Danbury, Connecticut, USA, (1957).

[3.4] Koning, M. G. — High Volume Single-Degree-of-Freedom Gyros for Strapped-Down Use. Proceedings of Symposium on Gyro Technology, held by Deutsche Gesellschaft für Ortung und Navigation e. V., Stuttgart, Germany, September 28 and 29, 1977.

[3.5] Drew, T. A. — Advances in Technology of the Spherical Gas Bearing Gyro. Proceedings of the 25th Meeting of the Institute of Navigation (1969)

[3.6] Schmidt, G. T. L. S. Director — Strap-Down Inertial Systems. Proceedings of the AGARD Lecture-Series-95

[3.7] Rahlfs, D. — On the Accuracy Improvement of Incremental Readout Techniques for Inertial Sensors. ESA-TT-573, Translation of DFVLR report No. DLR-FB 77-70 (1977)

[3.8] — IEEE Standard Specification Formal Guide and Test Procedure for Single-Degree-of-Freedom Rate Integrating Gyros and Supplement for Strapdown Application. The Institute of Electrical and Electronics Engineering, Inc.

[3.9] Denhard, W. G. (Editor) — Inertial Component Testing: Philosophy and Methods. AGARDograph 128

[3.10] Craig, R. J. G. — Theory of Errors of a Multigimbal, Elastically Supported, Tuned Gyroscope. IEEE Transaction on Aerospace and Electronic Systems, Vol. AES-8, No.3, May 1972, page 289 - 297.

[3.11] Ebert, W. — Inertial Measuring Unit for Strapdown Application. Proceedings of the DGON Symposium on Gyro Technology, Stuttgart, Germany, (1979).

[3.12] Donoghue, P. J. — A Strapdown Inertial Reference System for Commercial Airline Use in Navigation and Flight Control. Proceedings of the DGON Symposium on Gyro Technology, Bochum, Germany, (1978).

[3.13] Lübeck, E. — Erprobung und Vergleich von hochgenauen Testverfahren für Lagekreisel. DFVLR Forschungsbericht, DLR FB 69-77 (1969).

[3.14] Vepa, M. — Influence of Damping Associated with the Torsional Flexures and Rotor Drag, on the Performance of a Single Gimbal Dry Tuned Gyro. DGON Journal Ortung und Navigation, 2/1979 (1979).

[3.15] Coffmann, D. E. — Feasibility Study of a Digital Rebalance Loop for a Dry Tuned Gyro. Scientific Report S28 (1974) of the University of Tennessee, USA.

[3.16] Craig, J. G. — Dynamically Tuned Gyros in Strapdown Systems. Proceedings No. 116 of the AGARD Conference on Inertial Navigation, Components and Systems.

[3.17] Wetzig, V. — Analyse des Drift- und Schwingungsverhaltens dynamisch abstimmbarer Kreisel. Proceedings of the Symposium on Gyrotechnology of the Deutsche Gesellschaft für Ortung und Navigation e. V., April 12-14, 1972, Oberlingen, Germany, (1972).

[3.18] Karnick, H. — Effects of Hinge Improvements on Design and Production Cost of a Dynamically Tuned Gyro. Proceedings of the DGON Symposium on Gyro Technology, Stuttgart, Germany, 18-19 Sept., (1978).

[3.19] — Technical Description of the LN 33 Strapdown System. Litton Industries

[3.20] Kornbluth, B. — Derivation of and Test Techniques Used to Investigate Support Mechanism Problems Associated with the Litton Vibrarotor Gyro. Proceedings of the ION/NASA Meeting on Problems in Inertial Guidance, (January 21-22, 1970).

[3.21] Haberland, R. — Some Design Criteria of Elastic Universal Joints for Dry Tuned Gyroscopes. Proceedings of the DGON Symposium on Gyro Technology, Stuttgart, Germany, 28-29 September, (1977).

[3.22] Haberland, R. — Technical Advances through a Novel Gyro Hinge Design. Proceedings of the DGON Symposium on Gyro Technology, Stuttgart, Germany, 18-19 Sept., (1978).

[3.23] Karnick, H. — Experience Based upon Experimental Dry Tuned Gyros. Proceedings of the DGON Symposium on Gyro Technology, Stuttgart, Germany, (1979).

[3.24] Vepa, M. — On the Caging Loops for Dry Tuned Gyros. Proceedings of the DGON Symposium on Gyro Technology, Stuttgart, Germany, (1979).

[3.25] Craig, J. G. — Theory of Operation of Elastically Supported, Tuned Gyroscopes. IEEE Transaction on Aerospace and Electronic Systems, Vol. AES-8, No.3, May 1972.

[3.26] Harress, F. — Die Geschwindigkeit des Lichtes in bewegten Körpern. Dissertation Universität Jena, Erfurt (1912), (no longer available).

[3.27] Sagnac, G. — Comptes Rendus, 157, (1913).

[3.28] Sommerfeld, A. — Optik. Akademische Verlagsgesellschaft Geest & Portig K.-G., Leipzig (1964).

[3.29] Post. E. J. — Sagnac-Effect. Reviews of mod. Physics, Vol. 39, No. 2, (1967), pages 475 to 493.

[3.30] Fredricks, R. J. Carrington, W. A. — Sources of Error in a Discrete Component Sagnac Optical Rate Sensor. Proceedings of the Society of Photooptical Instrumentation Engineers, Vol. 157 Laser Inertial Rotation Sensors, August 30-31, 1978, San Diego, California, pages 50 to 67.

[3.31] Michelson, A. Gale, H. G. — Journal of Astrophysics, 61, (1925), page 137.

[3.32] Vali, V. Shorthill, R. W. — Fiber Laser Gyroscopes. SPIE, Vol. 77, (1976), Fibers and Integrated Optics, page 110-115.

[3.33] Davis, J. L. Ezekiel, S. — Techniques for Shot-Noise-Limited Inertial Rotation Measurement Using a Multiturn Fiber Sagnac Interferometer. Proceedings of the DGON Symposium on Gyro Technology, Stuttgart, Germany, 18-19 Sept., (1978).

[3.34] Cahill, R. F. Udd, E. — Phase Nulling Optical Gyro. Proceedings of the IEEE 1979 National Aerospace and Electronics Conference, page 8-13.

[3.35] Proceedings of the DGON/Uni Stuttgart Symposium on Gyro Technology, Stuttgart, Germany, (1981).

[3.36] Proceedings of the International Conference on Fiberoptic Rotation Sensors and Related Technologies, Massachusetts Institute of Technology, Cambridge, Mass., USA, Nov. 1981.

[3.37] Böhm, K. Russer, P. Weidel, E. Ulrich, R. — Low Noise Fiber-Optic Rotation Sensing. Optic Letters, Vol. 6, No. 2, (1981), pages 61 to 66.

[3.38] Rodloff, R. — Laserkreisel und andere optische Drehgeschwindigkeitssensoren. Bericht über das 105. Wehrtechnische Symposium "Regelungstechnik - Automatisierung", Bundesakademie für Wehrverwaltung und Wehrtechnik, Mannheim (1979).

[3.39] Bergmann-Schaefer (Gobrecht, H. Editor) — Lehrbuch der Experimentalphysik, Band III Optik. Walter de Gruyter, Berlin, New York (1978).

[3.40] Aronowitz, F. — The Laser Gyro. In Laser Applications, Vol. I, Editor M. Ross, Academic Press (1971), page 135-200.

[3.41] Podgorski, T. J. — Langmuir Flow Effects in the Laser Gyro. IEEE Journal of Quantum Electronics, Vol. QE-4, No. 1, Jan. 1968, pages 11-18.

[3.42] Rodloff, R. — Untersuchung zum Lock-in-Problem und zur Signalauslesung an Laserkreiseln. DFVLR Research Report No. DFVLR-FB 81-39 (1981).

[3.43] Hutchings, T. J. Stjern, D. C. — Scale Factor Non-Linearity of a Body Dither Laser Gyro. Proceedings of the IEEE 1978, National Aerospace and Electronics Conference, pages 549-555.

[3.44] Scott, M. L. Elson, J. M. — Multilayer Light Scattering and the Laser Gyro. Applied Physics Letters, Vol. 32, No. 3, February 1978, pages 158-163.

[3.45] Bentlage, H. — Das Rückstreuverhalten von Laserspiegeln. DFVLR Research Report No. DFVLR-FB 81-25 (1981).

[3.46] Smith, I. W. Dorschner, T. A. — Biasing the Raytheon Four-Frequency Ring Laser Gyroscope. Proceedings of the DGON Symposium on Gyro Technology, Stuttgart, Germany, 18-19 Sept., (1978).

[3.47] Voigt, W. — Magneto- und Elektrooptik. Druck und Verlag von B. G. Teubner, Leipzig (1908).

[3.48] McClure, R. E. Vaher, E. — An Improved Ring Laser Bias Element. Proceedings of the IEEE 1978 National Aerospace and Electronics Conference, pages 544-548.

[3.49] Gauert, R. — Untersuchungen zu magnetooptischen Biaselementen für Laserkreisel. DFVLR Research Report No. DFVLR-FB 81-21 (1981).

|3.50| Macek, W. M. (Inventor) — Improvements in or Relating to Ring Lasers. Patent Specification GB-1406730.

[3.51] Matthews, J. B. Gneses, M. J. Berg, D. S. — A High Resolution Laser Gyro. Proceedings of the National Aerospace and Electronics Conference, Dayton, Ohio, USA, May 16-18, 1978.

[3.52] — IEEE Specification Format Guide and Test Procedure for Laser Gyros. The Institute of Electrical and Electronics Engineering, Inc.

[3.53] Lindop, A. J. — A Test Specification for Dithered Ring Laser Gyro. Royal Aircraft Establishment, Technical Report in preparation.

[3.54] Lindop, A. J. — Interaction of Dither and Random Noise in the Testing of Mechanically Dithered Ring Laser Gyros for Inertial Navigation. Proceedings of the DGON/Uni Stuttgart Symposium on Gyro Technology, Stuttgart, Germany (1980).

[3.55] Mc Laren, I. — Open and Closed Loop Accelerometers. AGARDograph No. 160, Vol. 6.

[3.56] — IEEE Standard Specification Format Guide and Test Procedure for Linear, Single-Axis, Pendulous, Analog Torque Balance Accelerometer. The Institute of Electrical and Electronics Engineers, Inc., (1971).

[3.57] — QA-1000 Series, QA-1100 Series, QA-1200 Series and QA-1300 Series Q-FLEX ACCELEROMETERS. Sundstrand Data Control, Inc. Document 012-0293-001.

|3.58| Handrich, E. — Testverfahren für Strapdown Systeme. IABG Report B-TU 2003/00 (1980).

4. ACCURATE DIGITAL READOUT OF INERTIAL SENSORS

4.1 Introduction

In modern flight test systems data handling, storage and evaluation is mostly done in a digital format. With gyros and accelerometers used for this purpose, the output signal is generally an analog signal. Methods of digitizing these signals for the two applications given above will be discussed in this chapter.

If the sensors's output is used for the computation of its time integral, as for example in an inertial navigation system, the digitizing method should be thoroughly selected so that the stochastic as well as the deterministic errors of the integrator's output as caused by the analog to digital conversion are smaller than the sensor's drift. Different digitizing methods are discussed with respect to their accuracy potential.

Signals can be digitized and stored only at sampled intervals nT^S (T^S = sampling time increment) and not continuously like analog signals. This poses problems if their evaluation refers to the continuous time history as in the analysis of their frequency contents or in the computation of their time integral.

Certain well known rules for sampling signals have to be observed for both applications. They are summarized briefly in this chapter.

The following considerations only apply partially to the laser gyro, whose output is a frequency proportional to the angular rate to be measured. The specifics for this sensor will be mentioned separately.

4.2 Methods for Digitizing the Measurements of Inertial Sensors

4.2.1 The Inertial Sensor and the Rebalance Loop

Mechanical gyros and accelerometers and their use as accurate sensors for angular rate and linear acceleration are described in Chapter 3. Fig. 4.2.1a shows the combined block diagram of the sensor plus rebalance loop, which we used in Chapter 3 for the general discussion. The flight test engineer who is looking more deeply into the sensor's readout has to subdivide the two blocks, as shown in Fig. 4.2.1b for the single-degree-of-freedom (SDF) gyro.

This sensor is used as an example in the discussion below. For two-degree-of-freedom (TDF) gyros or accelerometers with force feedback, a similar analysis can be given.

The gyro angular rate (input) ω_I in Fig. 4.2.1b creates a positive torque M_0 about the output axis (s. Fig. 3.2.2) causing a positive pickoff angle θ_0 which is sensed by an inductive, capacitive or optical signal generator. In block $F^{SG}(s)$ (demodulator and filter) this is converted into a voltage u^c as input into the control network $F^c(s)$. The output voltage of this network drives a current i which is converted in the torquer to a torque M^t compensating the torque caused by the input signal and the disturbances M^d ($M_0^I = -M_0 = -H(\omega_I - D)$). The diagram also indicates some of the error sources - the pickoff offset angle $\delta\theta_0$, the control amplifier offset voltage δu^c and the offset current δi - which may cause an input axis misalignment or bias of the sensor.

The torque M^t for compensating the input signal is related to the current through the torquer scale factor S^t or the command rate scale factor S^T ($M^t = S^t i = HS^T i$). It is a true signal of the input angular rate ω_I including the drift rate D, provided the loop gain is high $F(s) \to \infty$. In this case the torquer current for an SDF gyro reads (s. Eq.(3.3.18b)):

$$i = \frac{-H}{S^t}(\omega_I - D) = \frac{-1}{S^T}(\omega_I - D). \tag{4.2.1a}$$

The corresponding voltage u taken over the precision resistor R is converted into an output angular rate $\omega_I^x = -S^x u$ using the nominal gyro scale factor S^x derived from the nominal values of the torquer scale factor S^{tx}, of the angular momentum H^x and of the precision resistor R^x which are in error as compared to the actual parameters:

$$\omega_I^x = -S^x u = -S^x R i = (1 + \kappa)(\omega_I - D) \tag{4.2.1b}$$

with

$$S^x = \frac{S^{tx}}{H^x R^x} = \frac{S^{Tx}}{R^x} \quad \text{and} \quad \kappa = \frac{\delta S}{S} \tag{4.2.2a,b}$$

This indicates the dominant role which the accuracy of the gyro scale factor S^x has upon the accuracy of the input signal's measurement. Comments on it are presented in Section 3.2.2.6.

4.2.2 Analog-to-Digital Conversion (ADC)

For medium accuracy requirements a commercial analog-to-digital converter (ADC) (for instance ADC-16Q with 16 bits, 15 bits resolution and 1 bit for sign, of the manufacturer Analog Devices) may be used for digitizing this signal. The corresponding block diagram including the subsequent sampling and scaling by S', which comprises the gyro scale factor S^x and the ADC scale factor u'/u, is shown in Fig. 4.2.1b. The output signal ω_I' is a whole number presentation of the input signal ω_I but contains ADC errors (for ADC-16Q in the order of 20 ppm nonlinearity, 8 ppm/°C and 3 ppm/day), sensor errors and noise due to the limited resolution. The resolution is limited to the least significant bit (LSB); due to roundoff, information of LSB/2 may get lost. The peak value of this quantization error (uncorrelated noise) is

$$\delta\omega^m = \pm\, \omega^m/(2)^n = \pm\, 6\ ^\circ/h \tag{4.2.3}$$

for $\omega^m = 100\ ^o/s$ and n = 16 bits such as with the ADC 16Q. At certain sampling intervals T^s the ADC is read out for further evaluation.

4.2.3 Voltage-to-Frequency Conversion (VFC)

Fig. 4.2.2 indicates the digitizing of the output voltage u when a voltage-to-frequency generator (VFC) is used (for instance Model 458 with f^p = 100 kHz full scale frequency of the Model 458 of Analog Devices).

The voltage u is integrated. Each time the output voltage of the integrator exceeds a certain threshold an electric charge increment ΔQ of accurately known area is released to reduce the integrator's net charge. A voltage pulse ΔP serves as output. In this digitizing process no information due to roundoff error is lost because the output pulse is fed back to the integrator. Only VFCs with this kind of pulse feedback will be discussed.

One single VFC can handle only positive or negative signals unless it is biased with a voltage above the maximum positive or negative input signals. Of course two VFC's can be used for the two input signals of different sign. The weight of the output pulses ΔP is defined by the maximum frequency f^p = 1/10 of the VFC at the maximum input voltage u^m which again is related to the maximum input angular rate ω^m by the nominal gyro scale factor S^x of Eq. (4.2.2b):

$$\Delta P = u^m/f^p \quad \text{or} \quad \Delta\phi^p = S^x\ \Delta P = \omega^m/f^p = 3.6 \text{ arc sec.} \tag{4.2.4a,b}$$

(The figure quoted is valid for $\omega^m = 100\ ^o/s$ and f^p = 100 kHz as with the VFC Model 458.) The pulse train is fed to a reset counter which sums it; its contents are again transferred for further evaluations at sampling times T^s when the counter is set to zero again. So the output of the reset counter may serve both

- as angular increment measurement

$$\Delta\phi^{sx} = \Delta\phi^s + \varepsilon^s = \sum_{m=1}^{T^s/T^p} \Delta\phi^p(mT^p) = \int_t^{t+T^s} \omega_I\, d\tau + \varepsilon^s \tag{4.2.5}$$

- or as mean angular rate measurement

$$\omega_I^x = \frac{\Delta\phi^{sx}}{T^s} = \frac{1}{T^s}\int_t^{t+T^s} \omega_I\, d\tau + \frac{\varepsilon^s}{T^s} = \bar{\omega}_I + D. \tag{4.2.6}$$

This information is corrupted by noise ε^s or $D = \varepsilon^s/T^s$, respectively, first due to sensor and VFC errors (in the order of 100 ppm nonlinearity, 10 ppm/day and 10 ppm/°C with the VFC Model 458 of Analog Devices) and second due to quantization errors, i.e. when the counter is read out, one increment may just have been missed.

The peak value of the quantization error at sampling intervals is:

$$\varepsilon^m = \pm\,\Delta\phi^p = \pm\,\omega^m/f^p = 3.6 \text{ arc sec}$$
$$D^m = \pm\,\varepsilon^m/T^s = \pm\,\omega^m/(T^s\ f^p) = 360\ ^o/h \tag{4.2.7a,b}$$

for $\omega^m = 100\ ^o/s$, f^p = 100 kHz and T^s = 10 ms. It is reduced by 1/m if ω_I is computed as the mean value over the time $t = mT^s$.

In Section 4.3 we will see that this noise if integrated does not give rise to a random walk type drift.

4.2.4 The Pulse Rebalance Loop (PRL)

A different approach for accurate readout of inertial sensors, the so called "pulse rebalance loop" or "incremental caging loop", is shown in Fig. 4.2.3. A quantizer is placed into the rebalance loop releasing a current i of constant amplitude to flow through the torque generator in positive or negative directions for the pulse time increment TP. The maximum input angular rate is thus defined by the current level i flowing in one direction only

$$\omega^m = S^T\ i \tag{4.2.8}$$

but reduced by the fact that the current is not applied continuously but as a flow of electric charges ΔQ which need time to reach the maximum level. The resulting torquer scale factor S^T is thus reduced by a certain amount, 10 % for instance.

The time increment T^p of one current pulse is

- either a constant time increment, i.e. positive or negative pulses of constant width T^p are applied at a frequency varying with the input signal ("pulse frequency modulation", s. Fig. 4.2.3), or
- a variable time increment, i.e. positive and negative pulses at a constant carrier frequency $1/T^p$ are applied, whereby the width varies with the input rate ("pulse width modulation", s. Fig. 4.2.3).

Due to the inductivity of the torquer coil the frequency of both torquing methods is much lower than the one of the VFC method (s. Section 4.2.3) unless capacitive compensation is provided. A common value is

$$f^p = 1 \text{ kHz.} \tag{4.2.9}$$

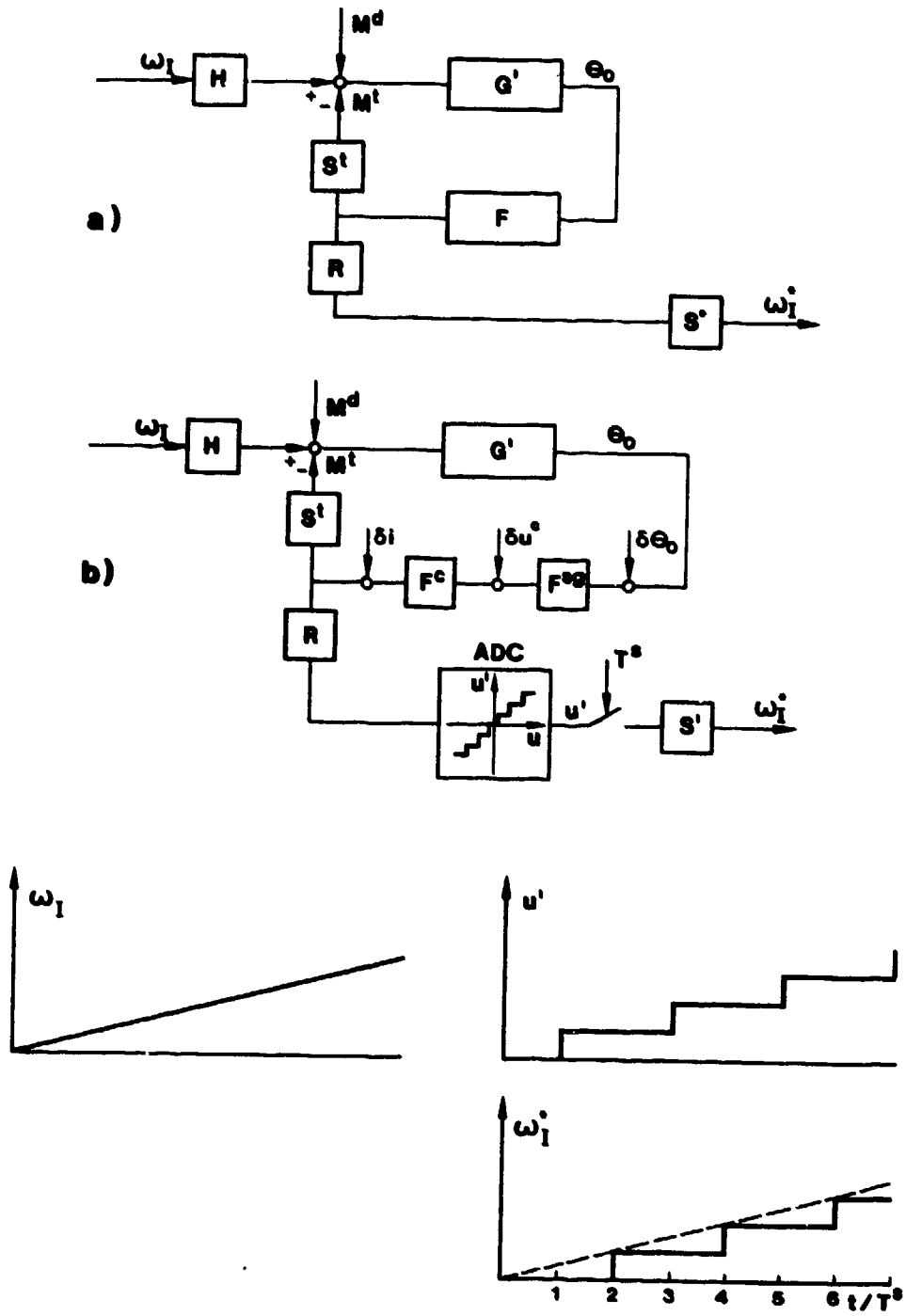

Fig. 4.2.1 Block Diagrams and Signals for Gyro plus Analog Rebalance Loop with Analog Output (a) and Digital Output Using Analog to Digital Converter (b)

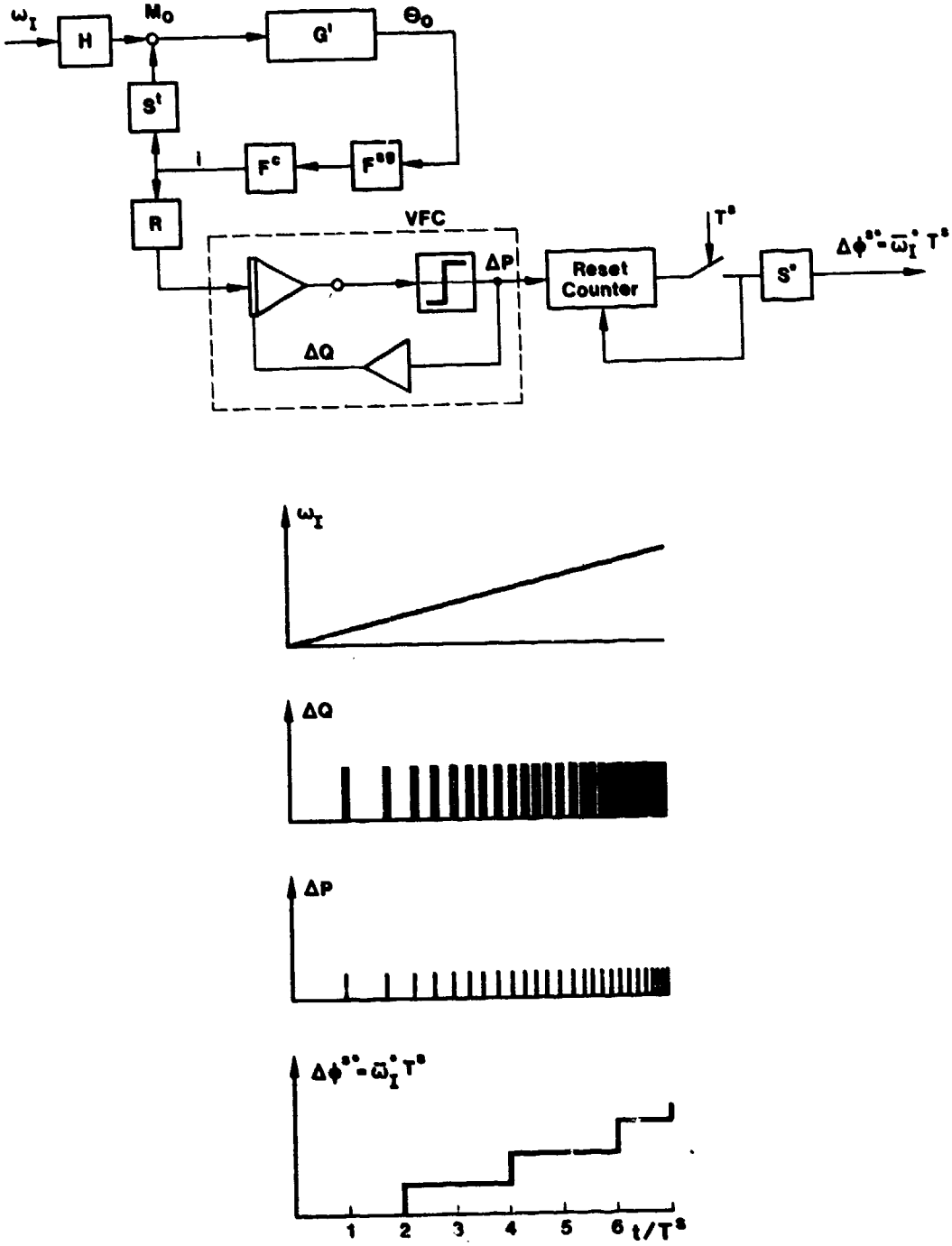

Fig. 4.2.2 Block Diagram and Signals for Gyro plus Analog Rebalance Loop and Voltage to Frequency Converter

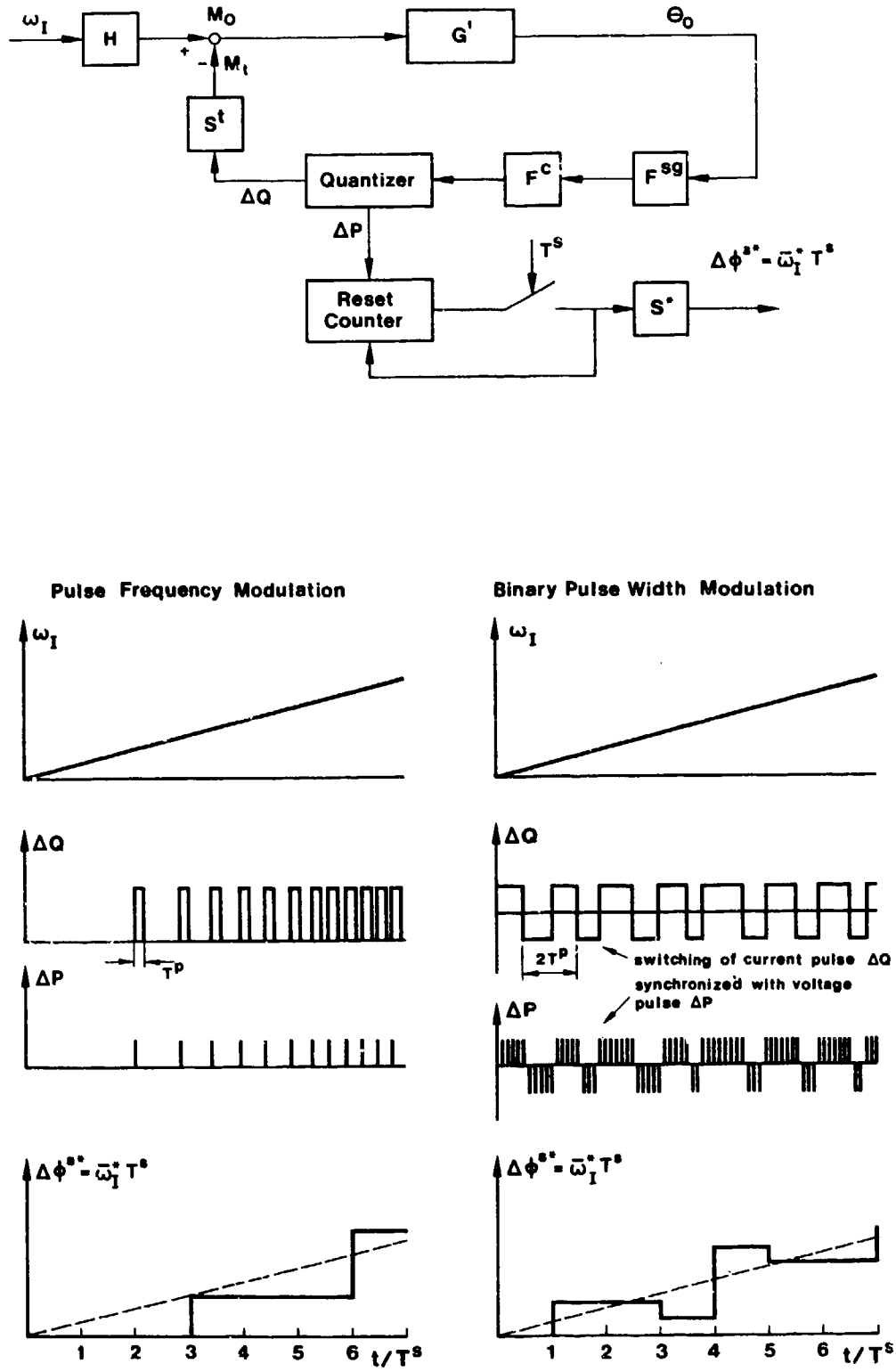

Fig. 4.2.3 Block Diagram and Signals for Gyro plus Incremental Rebalance Loop

With the pulse frequency modulation each current pulse releases a voltage pulse ΔP for the subsequent up down counter whose pulse weight is defined by

$$\Delta\Phi^p = \omega^m/f^p. \tag{4.2.10}$$

The resolution of the pulse frequency modulation is thus limited to 100 times the values mentioned for the VFC digitizing method in Eqs. (4.2.4) and (4.2.7).

With pulse width modulation the width of each pulse is measured with readout counting pulses of much higher frequency

$$f^r = 1/T^r = 256/T^p = 256 \tag{4.2.11}$$

(the figure is taken from [4.1]), thus improving the resolution of one pulse to

$$\Phi^p = \omega^m/f^r. \tag{4.2.12}$$

With the figure quoted above the resolution is 0.4 times the values mentioned for the VFC digitizing method in Eqs. (4.2.4) and (4.2.7).

The pulse evaluation is the same as mentioned in Eqs. (4.2.5) and (4.2.6) for the VFC digitizing method. Since "binary pulse width modulation (BPWM)" is nowadays the preferred method of pulse torquing, its block diagram and its functioning are briefly described based on Fig. 4.2.4 which is taken from [4.1].

The quantizer in this figure contains 3 function blocks:

- the generator for the pulse width signal including the digital modulation limiter,
- the synchronization block with switching bridge of high stability and
- the current control loop with reference voltage of high stability.

The sawtooth voltage u^{st}, added to the input voltage u^i, generates in the comparator the rebalance pulse cycle T^p. It is derived from a quartz-controlled frequency generator. The output of the comparator is positive or negative during each cycle depending upon the sign of the sum $u^i + u^{st}$. The electronics have to inhibit the switching from positive to negative within a minimum time, i.e. within the rise-time of the current (e.g. 0.1 T^p) as mentioned above, and have to enable the switching at integer fractions of T^p. These functions are observed by the digital modulation limiter and the synchronization block.

Compared to the analog rebalance techniques and external digitizing process, BPWM pulse torquing has the following advantages:

- the dissipated rebalance energy within the sensor is constant,
- it works only at two points of the torque-current characteristic of the torquer, and
- the sensor's output signal is not subject to additional error sources (ADC of VFC errors).

Nonlinearities may arise in BPWM-rebalanced sensors from eddy currents varying with the input signal. These effects are minimized by observing certain rules in the design of the torquer [4.1].

Fig. 4.2.5 shows two test results for the stability of an accelerometer (Litef B 250) and an SDF gyro (Ferranti M 2519) plus BPWM rebalance electronics designed at DFVLR.

The accelerometer readings were taken in 1976 during a period when earthquakes in China may have caused movements in the foundation of the laboratory. The digital accelerometer readout, compensated for these movements, has a mean slope of $\approx 3 \cdot 10^{-6}$ g/day.

The gyro measurements were taken with the axes in the optimal orientation (output axis up, s. Table 3.2.1a, Row 2). The readings prove that the stability of the sensor in this position plus rebalance loop is better than 0.001 °/h.

The pulse rebalance method may be used not only with inertial sensors but with all sensors with compensation readout (e.g. flow and pressure sensors).

4.3 Stochastic Errors of the Digitizing Methods for Mechanical Inertial Sensors and Comparison with the Stochastic Errors of Laser Gyros

The quality of the output signal of an Analog-to-Digital Converter (ADC) on the one hand and of a Voltage-to-Frequency Converter (VFC) and a Pulse Rebalance Loop (PRL) on the other hand is quite different as we have seen in Sections 4.2.2 to 4.2.4

- at sampling intervals T^s the ADC delivers a whole number presentation of the input signal (angular rate or acceleration, s. Fig. 4.2.1), and
- the VFC or the PRL delivers a pulse train (angle or velocity increments) which, in connection with a counter, is read out and reset at sampling intervals T^s; these may be interpreted as the integral of the input signal or as mean input signal during T^s (s. Figs. 4.2.2 and 4.2.3 and Eqs. (4.2.5) and (4.2.6)).

For this reason the quantization noise superposed on the useful signal is also of different quality, and has different effects on a control or navigation system when the time integral is of prime interest.

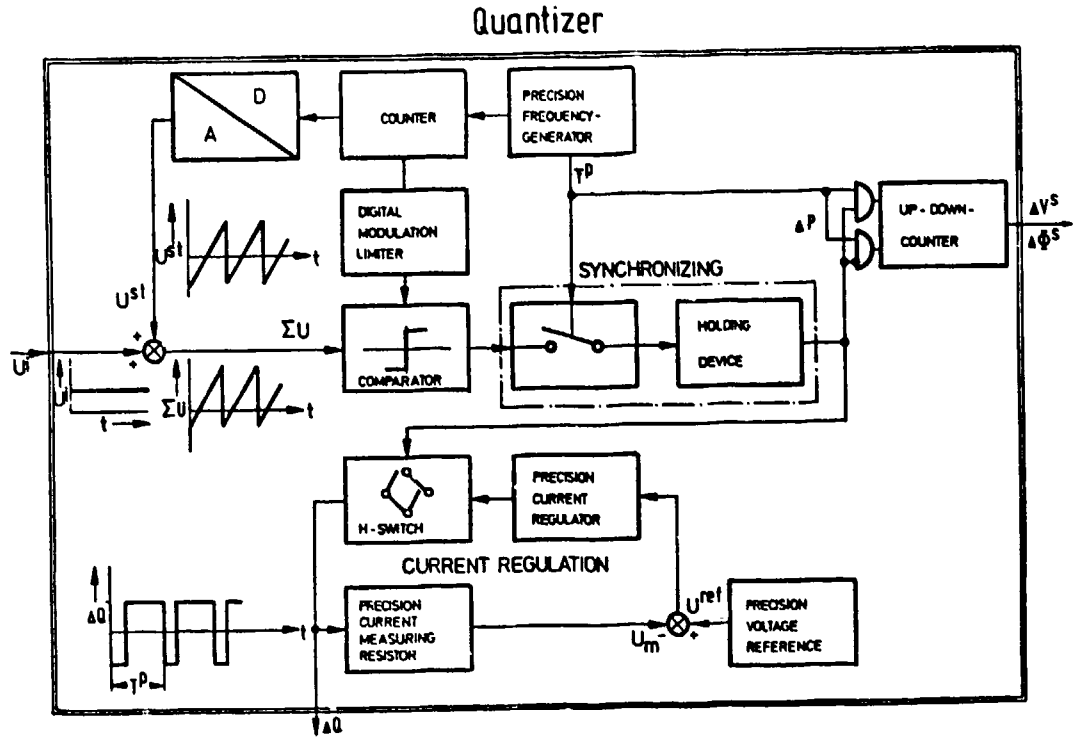

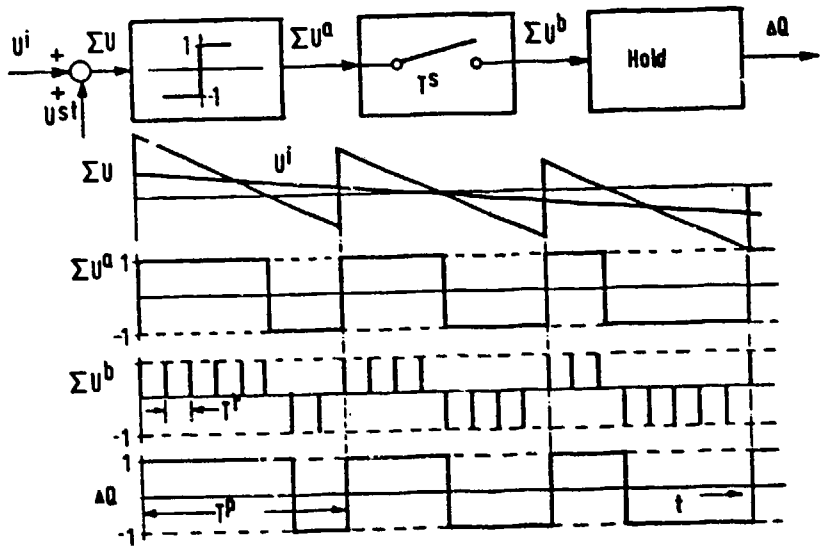

Fig. 4.2.4 Block Diagram and Signal Timing for the Quantizer in the Binary Pulse Width Modulation Rebalance Loop

Fig. 4.2.1 reveals for the ADC that the quantization noise is not fed back in a control loop and causes an uncorrelated noise in the output signal ω_I^*. If this signal is integrated for computing an angle, as for instance in a strapdown system, this noise causes an error, namely a random walk process with a standard deviation growing with $\sqrt{t}$, even if we assume that the sensor measures the input signal correctly.

If we look, with the same assumption, at the VFC and PRL digitizing methods in Figs. 4.2.2 and 4.2.3 we see that the noise due to the quantization process is fed back in a control loop. There is noise superposed on the output signal, but if the corresponding angular increments (s. Eq. (4.2.5)) are summed up for the computation of the time integral of the output signal it will not contain a random walk error due to this quantization process, but only the original uncorrelated noise.

The above mentioned assumption of an ideal sensor is certainly academic. Errors and random noise are contained in all measuring processes as we have seen in Chapter 3. This section will only give an indication that with the use of an ADC for digitizing gyro measurements in the laboratory the parameters of maximum input rate, resolution of the ADC and required accuracy of the measurement should be matched properly. This goal can hardly be achieved in an INS, precluding its use for this purpose.

We have seen in Section 3.5 that the output signal of a ring laser gyro (RLG), rotating with respect to inertial space above the lock-in rate, is a pulse train, each pulse having the dimension of an angle increment in the order of magnitude of several arc seconds. In this respect the RLG is comparable to a mechanical gyro whose output signal is digitized by a voltage to frequency converter (VFC) or which has a pulse rebalance loop (PRL) as discussed in the previous sections.

For circumventing the lock-in effect in the RLG, certain bias techniques have to be provided (mechanical dither, Faraday cell, magnetic mirror) which are of periodic nature, i.e. lead the RLG periodically through the lock-in region. This causes stochastic errors per bias period which are not fed back into the sensor. The RLG theoretically is comparable in this respect with the mechanical gyro with ADC digitizing method in which the quantization error was not fed back either. The resulting error in the subsequent counter is the "random walk" drift discussed above.

It was also shown that the ideal mechanical gyro with VFC or PRL digitizing methods does not produce this random walk error due to quantization and compares advantageously with respect to the RLG. But in general this advantage is only of academic value because it is overshadowed by other, more severe random errors of the mechanical gyros (s. Tables 3.2.1 and 3.2.2).

We have seen in Sections 4.2.2 to 4.2.4 that the quantization noise of the digitized output signal of mechanical sensors depends for all digitizing methods on the maximum input rate ω^m for which the method is designed. The method of "range switching" is a means to adapt the quantization noise to the dynamic environment to which the sensor is exposed. With this method the rebalanced sensor is designed for a low ω^m with low quantization noise. Most of the time the sensor will work in this mode. Only when this low ω^m is exceeded, is the sensor plus readout switched automatically to a higher ω^m by changing the measurement resistor R in the ADC or VFC or the current level in the PRL digitizing methods.

Range switching opens new possibilities in the accurate readout of inertial sensors but also poses new problems. We will not further discuss it here.

4.4 Review of Rules for Sampling Data

The measurements of inertial sensors can be taken and stored digitally at sampled intervals nT^S (T^S = sampling time increment) only, using one of the methods described in the previous sections.

If analog-to-digital conversion (ADC, s. Section 4.2.2) is used and in the process of evaluating the sampled data the continuous time history of the original signal is of significance, as in the analysis of its frequency contents or in the computation of its time integral, certain well known rules have to be observed for the preparation of the signal prior to sampling in order to keep errors in the low frequency domain due to the sampling process to a minimum. They shall be briefly summarized in this section following the course of [4.2].

Voltage to frequency conversion (VFC, s. Section 4.2.3) and the pulse rebalance loop (PRL, s. Section 4.2.4) provide within the described limits an exact information of the increment integral of the measurement or the mean value (s. Eq. (4.2.5) and (4.2.6)) and the preparation of the signal prior to sampling is not necessary.

In all cases the data evaluation is limited in its frequency bandwidth by the sampling process.

Due to the sampling theorem, the maximum frequency f^m contained in the signal x(t) to be sampled may only be half the sampling frequency

$$f^m \leq 1/(2T^S). \tag{4.4.1}$$

Only in that case the original signal x(t) can be recovered from the sampled signal $x(nT^S)$ using the formula (s. [4.2], Eq. (3.5.15)).

$$x(t) = \sum_{n=-\infty}^{\infty} x(nT^S) \frac{\sin \pi(t/T^S-n)}{\pi(t/T^S-n)} . \tag{4.4.2}$$

Since the evaluation of this formula is impracticable, it is proposed in [4.3] to hold the sampled signal constant over the sampling time and pass this through a low-pass filter with a band-pass cutoff frequency of half the sampling frequency.

Whether the signal to be sampled (at intervals T^S, for data evaluation or storage) complies with the

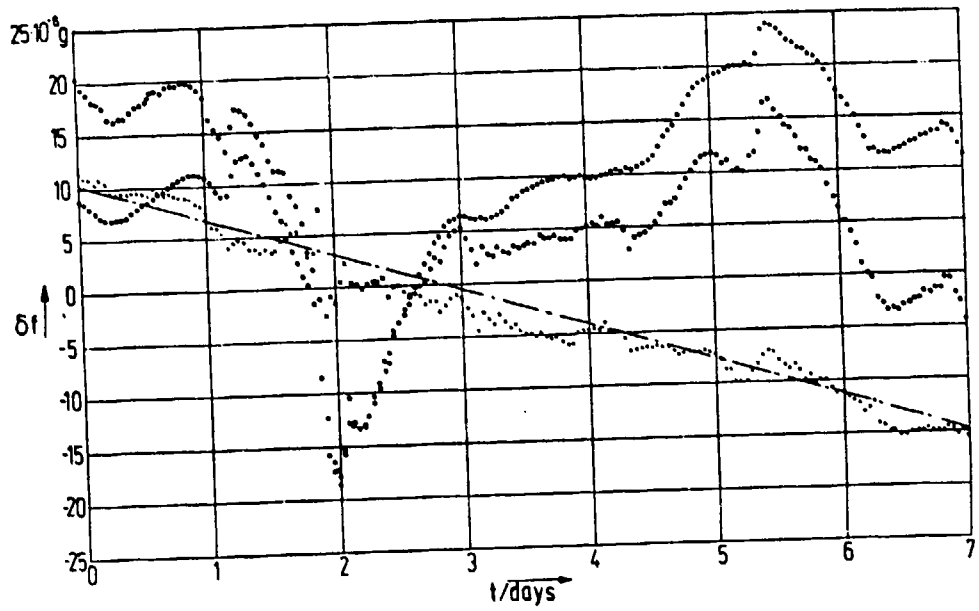

a) Test Results for Litef Accelerometer B 250

ooo uncompensated test result
... error due to inclination of foundation
xxx compensated test result

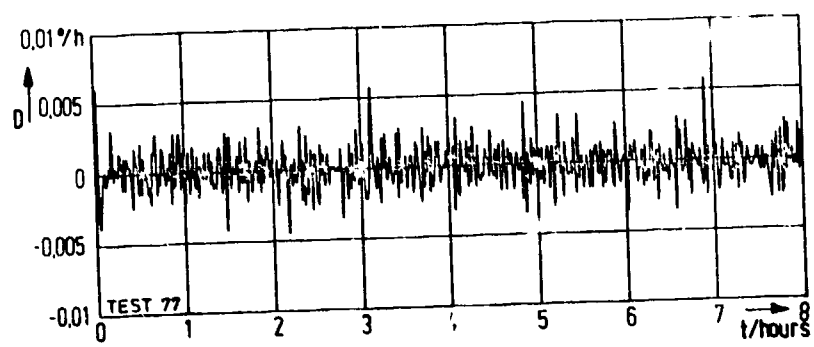

b) Test Results for Ferranti Gyro M 2519 (OA up)

Fig. 4.2.5 Test Results for Two Inertial Sensors Digitally Read Out with BPWM Rebalance Loop

sampling theorem may best be tested by using an analog frequency analyser. If it contains frequencies higher than $1/(2\,T^s)$ the sampling frequency has to be increased or filters have to be implemented. Preferably, these filters should be placed on the analog side (e.g. shock mounts or lag networks), i.e. before the signal is digitized, because any analog-to-digital conversion already contains some kind of sampling at frequencies higher than $1/T^s$. The analog filter tailored to $1/T^s$ includes the sampling-theorem observation for the digitizing process.

Shock mounts have a resonance frequency in the order of magnitude of 10 to 20 Hz, depending on the weight supported. The raise in amplitude is approximately 4 at the resonance frequency, and the transmissibility is below 5 % for frequencies above 35 Hz.

For the analog presampling filtering, so-called Butterworth filters [4.3], [4.4] are often used, because their transfer function is not only maximally flat for frequencies below the break frequency but also decreases rapidly for higher frequencies.

Once the sampling theorem (4.4.1) has been violated the frequency spectrum of the sampled signal is contaminated by the so-called "aliasing error" [4.2 and 4.3]. If a sine wave is sampled at integer fractions of the period, for instance, the aliasing error may have a constant value! It is impossible to deduct the aliasing error from the sampled data.

The aliasing error not only occurs if the input signal into the sampling device is not properly filtered for meeting the sampling theorem, but may also arise if the flight test data are evaluated at a frequency lower than recorded. If the presampling filtering was not sufficient for this data evaluation with sampling intervals mT^s (m>>1), the digital data have to be filtered again. In this procedure the additional filtering has to be done in a digital computer, for which the following results from [4.5] may be used: the analog function

$$F(s) = \frac{x(s)}{y(s)} = \frac{1}{(1+T^a s)(1+T^b s)} \tag{4.4.3}$$

is very well approximated digitally by the following algorithm:

$$\begin{aligned} x(n) = \frac{1}{6T^aT^b+3(T^a+T^b)T^a+(T^a)^2} \{ & (T^a)^2\,[y(n) + 4y(n-1) + y(n-2)] \\ & +[12T^aT^b - 4(T^a)^2]\,x(n-1) \\ & -[6T^aT^b - 3(T^a + T^b)T^a+(T\ )^2]\,x(n-2)\}. \end{aligned} \tag{4.4.4}$$

For a more general review of digital filter design see [4.3]. The whole topic of signal conditioning is discussed more in detail in [4.6] to [4.8].

References for Chapter 4

[4.1] Rahlfs, D. — 'On the Accuracy Improvement of Incremental Readout Techniques for Inertial Sensors'. ESA-TT-573, Translation of DFVLR Report No. DLR-FB 77-70 (1977).

[4.2] Tou, J. T. — 'Digital and Sampled Data Control Systems'. Mc Grow-Hill Book Company, Inc., New York (1959).

[4.3] Chi-Tsong Chen — 'One-Dimensional Digital Signal Processing'. Marcel Dekker Inc., New York and Basel (1979).

[4.4] Glasford, G. M. — 'Linear Analysis of Electronic Circuits'. Addison-Wesley Publishing Comp., Inc., Reading, Massachusetts, USA (1965).

[4.5] Hotop, H.-J. — 'Zur Programmierung eines Tiefpaß- und Bandpaßfilters in einem Digitalrechner - Herleitung und Genauigkeitsbetrachtung zweier Verfahren'. DFVLR Interner Bericht 153 - 77/29 (1977).

[4.6] Pool, A., Bosman, D. — 'Basic Principles of Flight Test Instrumentation Engineering'. AGARD Flight Test Instrumentation Series No. AGARD-AG-160 - Vol. 1.

[4.7] Williams, D. — 'Analysis of Random Data'. AGARD Flight Test Instrumentation Series No. AGARD-AG-160 - Vol. 14.

[4.8] Veach, D. W. — 'Signal Conditioning'. Volume in Preparation for AGARD Flight Test Instrumentation Series (AGARD-AG-160).

5. GYROS AS STABILIZATION DEVICES

5.1 Direct Gyroscopic Stabilization

Direct gyroscopic stabilization has stimulated the minds of the engineers in many fields such as stabilization of monorails, motorcars, ships and most recently satellites. On ships, it has been used since the late 19th century [5.1]. Huge rotors, weighting up to 100 tons or more were installed to damp out rolling and pitching of a vessel. In the Polaris Submarine, for instance, a gyro is still used in this manner.

We will concentrate in this chapter on the direct stabilization of a vertical or heading reference which will be discussed from the operational point of view in Chapter 6.

The gyro in a vertical and heading reference is a gimballed two-degree-of-freedom (TDF) gyro as shown in principle in Fig. 3.1.1b. The gyro case is directly mounted to the vehicle and the gimbals have high angular freedom about the two axes. For measuring the gimbal angle synchros or resolvers are generally used. The angular freedom about one of the gimbal axes is usually limited (approximately $\pm 80^0$ for the inner axis in Fig. 3.1.1b) to prevent the so-called "gimbal lock", i.e. to prevent the spin axis from becoming aligned with the outer gimbal axis. See also Chapter 6 for more details on attitude references.

In order to measure roll and pitch angles with a vertical gyro, the gyro in Fig. 3.1.1b is mounted in the aircraft in such a way that the outer axis is parallel to the longitudinal axis and the inner axis parallel to the lateral axis as indicated in Fig. 5.1.1. The aircraft can then carry out unlimited roll manoeuvres but the pitch angle should not reach $\pm$ 90 degrees.

For describing the performance of a gyro used in this manner as an attitude or heading reference we use Eqs. (3.4.6) and regard:

$$\dot{\underline{\Theta}} = \dot{\underline{\varepsilon}} - \dot{\underline{\phi}}, \tag{5.1.1}$$

the angular rate vector $\dot{\underline{\Theta}}$ of the gimbal angles (Θ corresponds to the pickoff angle in Section 3.4) as being composed of the attitude or heading angular rate vector $\dot{\underline{\phi}}$ of the aircraft (roll, pitch and yaw angular rate) plus the misalignment angular rate vector $\dot{\varepsilon}$ of the gyro's spin vector with respect to the vertical or true north.

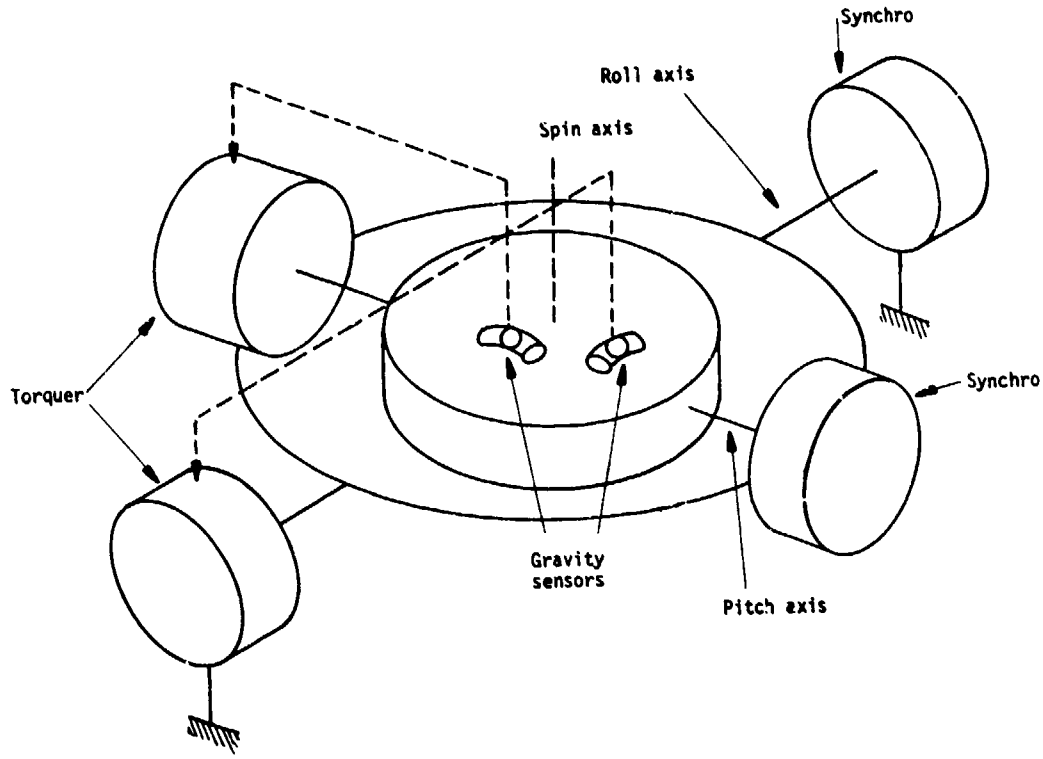

Fig. 5.1.1 Principle of the Vertical Gyro

So we obtain from Eq. (3.4.6):

$$\dot{\underline{\varepsilon}} - \dot{\underline{\phi}} = -\tilde{\underline{\omega}}^i + sH\underline{G}''(s)\,\hat{\underline{I}}\,(\tilde{\underline{\omega}}^t + \tilde{\underline{D}}) \tag{5.1.2}$$

with the transfer function of the undamped gimballed TDF gyro from Eq. (3.4.5):

$$\underline{G}''(s) = \begin{pmatrix} J_I\, s^2 & Hs \\ -Hs & J_O\, s^2 \end{pmatrix}^{-1} \tag{5.1.3}$$

The input angular rate vector $\underline{\omega}^i$ of the gyro case is composed of the angular rate $\dot{\underline{\phi}}$ of the aircraft with respect to the reference and that of the reference with respect to inertial space (ω^{in}).

With this assumption Eq. (5.1.2) becomes:

$$\dot{\underline{\varepsilon}} = -\tilde{\underline{\omega}}^{in} + sH\underline{G}^{*}(s)\,\hat{\underline{I}}\,(\tilde{\underline{\omega}}^{t} + \tilde{\underline{D}}). \tag{5.1.4}$$

For low input frequencies ($s \to 0$) we may neglect the inertia term in the gyro transfer function, when we obtain:

$$\underline{G}^{*}(s)\Big|_{s\to 0} = \frac{-1}{Hs}\hat{\underline{I}} \tag{5.1.5}$$

$$\dot{\underline{\varepsilon}} = -\underline{\omega}^{in} + \underline{\omega}^{t} + \underline{D}. \tag{5.1.6}$$

This relationship shows that the untorqued gyro ($\underline{\omega}^t = 0$) drifts away from the reference direction at the angular rate $\underline{\omega}^{in}$ of the reference direction with respect to inertial space plus the drift rate $\underline{D}$ of the sensor. On a moving vehicle the former is equal to the sum of earth rate plus transport rate (s. Eqs. 2.19 ff.)) i.e. of the order of magnitude of 15 °/h $\pm$ V/R (V = velocity of the vehicle, R = radius of the earth).

The error angle is held within certain limits if control loops from sensors which measure the misalignment $\underline{\varepsilon}$ are implemented to the gyro torquers. Following the discussion of the caging loop of a TDF gyro in Chapter 3.4.4 we write (s. Eq. (3.4.20)):

$$H\,\hat{\underline{I}}\,\underline{\omega}^{t} = \underline{M}^{t} = -\underline{F}(s)\,(\underline{\varepsilon} + \delta\underline{\varepsilon}) \tag{5.1.7}$$

where $\delta\varepsilon$ is the sensor error. In the case of a vertical gyro the ε-sensors for the two axes are, for example, bubble levels or accelerometers and $\delta\varepsilon$ is the error due to sensor bias or horizontal acceleration. The cross axis component of the control loop is used to compensate the input angular rate and, assuming its gain to be

$$\underline{F}(s) = \begin{pmatrix} 0 & K \\ -K & 0 \end{pmatrix} = \hat{\underline{I}}\,K, \tag{5.1.8}$$

we obtain from Eqs. (5.1.4) and (5.1.7):

$$\underline{\varepsilon} = [\underline{G}(s)^{-1} + \underline{F}(s)]^{-1}\,[\tfrac{-1}{s}\underline{G}^{*}(s)^{-1}\,\underline{\omega}^{in} + H\hat{\underline{I}}\,\tilde{\underline{D}} - \underline{F}(s)\,\delta\underline{\varepsilon}] \tag{5.1.9a,b}$$

$$= \frac{1}{sH/K+1}\,[\frac{H}{K}\,(-\tilde{\underline{\omega}}^{in} + \tilde{\underline{D}}) - \delta\underline{\varepsilon}].$$

As compared to the caging loop of a TDF gyro the gain K of the control loop or the inverse of the sensor's time constant are much smaller

$$T = \frac{H}{K} = 1\ \text{min} \tag{5.1.10}$$

because the stabilization gyro serves as a mechanical low-pass filter, similar to an inert mass but with the advantage of

- much lower weight, and
- reacting to command torques with an angular rate and not with an angular acceleration.

For the low input frequencies the performance of the gyro, in holding the reference direction, is limited by:

$$\underline{\varepsilon} = T\,(-\underline{\omega}^{in} + \underline{D}) - \delta\underline{\varepsilon}, \tag{5.1.11}$$

i.e. it is limited by the sensor errors, the drift and the non-compensated earth rate plus transport rate. The non-compensated earth rate causes a constant error angle of

$$\underline{\varepsilon} = 15\ \text{arc min} \tag{5.1.12}$$

if T = 1 min. From this point of view a lower time constant, i.e. a higher gain of the control loop is desirable. But this would decrease the low pass filter effectiveness of the gyro and make it more sensitive to accelerations.

For the high-frequency response of the gyro we may assume that the control loop is open (F(s) = 0) and that $\omega^{in} = 0$, when Eq. (5.1.9a) reduces to

$$\underline{\varepsilon} = \underline{G}^{*}(s)\,\hat{\underline{I}}\,\underline{D} = \frac{1}{H}\,\underline{G}(s)\,\underline{M}^{d}. \tag{5.1.13}$$

For a step function in the disturbance torque about the I-axis the gyro will respond with the undamped nutation and the precession as shown in Fig. 3.4.2.

Nutation may be annoying in the undamped stabilizing TDF gyro especially shortly after power switch-on and switch-off when the spin rate is not yet high enough and the nutation frequency

$$\omega^n = n \frac{I}{J_I J_0} \tag{5.1.14}$$

(s.(Eq. 3.4.8) with n = spin rate, I = moment of inertia of rotor about spin axis, $J_{I,0}$ = moments of inertia of rotor plus gimbal about transverse I, O-axis) is low so that the amplitude of the oscillation may be correspondingly high (s. Eq. (3.4.10)). To prevent nutation during turn-on and turn-off, special brakes may be installed in the gyro. For in-flight operation, electrical damping for the nutation frequency is not feasible because it would degrade the actual task of the gyro - the storage of reference direction. According to [5.2] "inertial dampers" (simple spring-mass-dashpot combination attached to the gimbal) are the only means to suppress this oscillation if required.

Eq. (5.1.14) also shows us that the gimbals of the stabilizing gyro should not be too heavy because they would lower the nutation frequency. Because of this one also will hardly find a platform with direct gyroscopic stabilization. The attitude and heading reference system (AHRS) model SYP 820 discussed in Section 6.3 and shown in Fig. 6.3.3 may serve as an example. The VG in this system has direct stabilization but is decoupled from the platform. The platform follows the VG in the low frequency range by means of a servo loop between the VG pickoffs and the platform torquers, thus preventing the lowering of the nutation frequency into an undesirable range.

In a gyro with direct stabilization the uncertainty torques, and consequently the drifts due to mass unbalance of the rotor and gimbal set and due to friction in the gimbal bearings, increase with their weight. This is another reason why only separate VG's and DG's have direct stabilization. For lowering the effect of friction the gimbal bearings are designed as "rotorace"-bearings, i.e. as ball bearings in which the outer ring is rotated in an alternating sense. In the next sections we will discuss the servo loop stabilization which is superior to direct stabilization in many respects.

5.2 Gyroscopic Stabilization by Means of Servo-Loops

Gyroscopic stabilization of a platform by means of servo loops from the gyro pickoffs to the gimbal servo motors is always applied when

- high stabilization accuracies are required, or
- large masses have to be stabilized.

Combined vertical and directional gyroscopic packages (VG/DG packages) and platforms of inertial navigation systems are stabilized in this way. Since the layout of stabilization loops and the dynamics of the closed loop system differ for single-degree-of freedom (SDF) or two-degree-of-freedom (TDF) gyros, we will discuss them separately.

5.2.1 Servo-Loop Stabilization of a Platform Using Single-Degree-of-Freedom Gyros

Fig. 5.2.1 shows the principle of the platform using SDF gyros. The sensor is mounted on this single axis platform, with its input axis parallel to the axis to be stabilized. The output axis of the gyro is orthogonal to it. The control loop is implemented from the gyro pickoff (PO) to the servo motor (SM) of the platform via the network F(s).

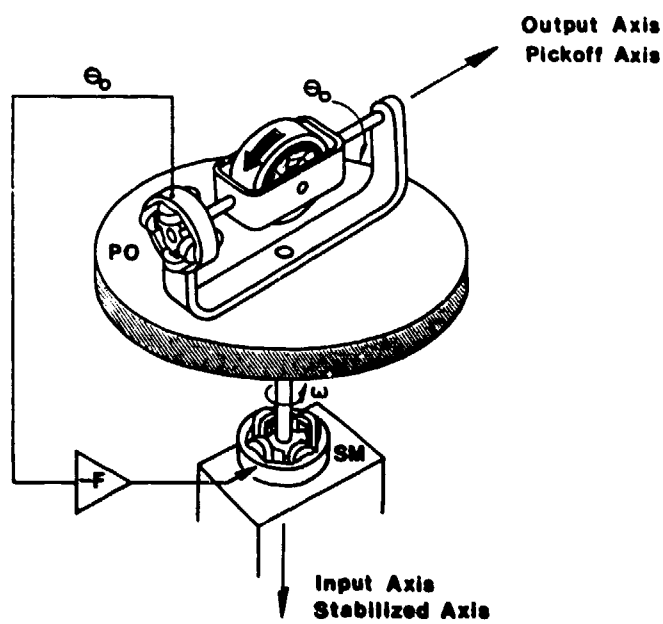

Fig. 5.2.1 Platform Stabilization by Means of a Single-Degree-of-Freedom Gyro

Comparing the open-loop SDF gyro/platform assembly in this figure with the gimballed two-degree-of-freedom-gyro in Fig. 3.1.1b, we immediately see the commonality and we are allowed to use the performance equation (3.4.2) for discussing the dynamics of the stabilized single axis platform (SAP). In Eq. (3.4.2) we recognize in the lower row all the terms of the rate integrating gyro (RIG) performance equation (3.3.11); the other terms describe the dynamics of the platform about the input axis and the reaction torque Hp_{0_0} of the SDF gyro in this axis. Before using Eq. (3.4.2) we will introduce a few assumptions and minor changes in the notation.

In case of the TDF gyro, $\dot{\theta}$ was the rate of the pickoff angle with respect to the case and ω^i the angular rate of the gyro case with respect to inertial space. With the SAP, ω^i is the motion of the base with respect to inertial space, which only affects the SAP dynamics through the friction in the gimbal bearings if the motion about the O-axis is assumed to be zero. The friction torque can be included in the disturbance torque M_I^d/H which also contains unbalance torques and other effects acting on the platform about the I-axis and replaces the drift D_0 in Eq. (3.4.2). This allows us to discard the ω^i-term in this component and regard $\dot{\theta}_I$ as the motion ω_I^{ip} of the platform with respect to inertial space.

It is obvious that we have to introduce in Eq. (3.4.2) the moment of inertia J_I^p of the platform plus gyro about the I-axis and also the viscous torque coefficient C^p of the gimbal bearings.

The servo loop is taken into account by means of the relationship in the Laplace domain (marked with ~):

$$\tilde{\omega}_0^t = \tilde{M}_I^s/H = -F(s)\,\tilde{\theta}_0. \tag{5.2.1}$$

So we find as <u>performance equation of the single axis platform stabilized</u> by a <u>single-degree-of-freedom gyro</u>:

$$\begin{pmatrix} \frac{1}{H}(J_I^p s + C^p) & s + F(s) \\ -1 & \frac{1}{H}(J_0 s + C)s \end{pmatrix} \cdot \begin{pmatrix} \tilde{\omega}_I^{ip} \\ \tilde{\theta}_0 \end{pmatrix} = \begin{pmatrix} \tilde{M}_I^d/H \\ -(\tilde{\omega}_I^t + \tilde{D}_I) \end{pmatrix}. \tag{5.2.2}$$

The open loop SAP ($F(s) = 0$) with zero damping ($C^p = C = 0$) will react to a step function in the input command rate in the same way as the TDF gyro shown in Fig. 3.4.2, i.e. with a precession and superimposed nutation. The natural frequency and the damping ratio for the damped nutation oscillation of the SAP

$$\omega^n = \frac{H}{J_I^p J_0} = n\,\frac{I}{J_I^p J_0}$$

$$\zeta = \frac{C J_I^p + C^p J_0}{2H\,J_I^p J_0} \tag{5.2.3a,b}$$

differ from the ones for the TDF gyro in Eqs. (3.4.8a,b) only in the inertia term J_I^p and the viscous damping coefficients C^p of the gimbal bearings. Assuming $J_I^p = 50\,J_0$, the nutation frequency of the SAP will be lowered by the factor 1/7 as compared to a TDF gyro for which we assume the same moments of inertia and spin rate as the SDF gyro mounted on the SAP. For a rate integrating gyro with $C > C^p$ the damping ratio will be increased by the factor 7. The damping ratio will be very small for a double integrating gyro proving that the layout of the corresponding servo loop requires more attention as with the rate integrating gyro (s. [5.3], Chapter 5.5). (We will see in the next section that the layout of the servo loop of a platform stabilized by a TDF is fairly decoupled from the interior dynamics of the sensor.)

In the layout of the servo loop the closed loop compliance of the SAP

$$\tilde{\phi}_I = \frac{(J_0 s + C)\,\tilde{M}^d}{J_0^p J_I s^3 + (CJ_I^p + C^p J_0)s^2 + (H^2 + C^p C)s + H\,F(s)} \xrightarrow[s \to 0]{} \frac{C\,\tilde{M}^d}{H\,F(0)} \tag{5.2.4}$$

(with $\phi_I = \int \omega_I\,dt$ = input angle) or the inverse of the compliance, the "torque stiffness", plays the dominant role and [5.3 and 5.4] discuss it more in detail.

For low frequencies the compliance tends to zero if an integrating network is implemented ($F(o) \to \infty$). The compliance also tends to zero for high frequencies ($s \to \infty$) when the inertias of the platform and gyro help to counteract the disturbance torque. But this is so only as a first approximation, since angular vibrations of the platform may excite constant drift terms in the gyro corresponding to the ones listed in Table 3.2.1b for strapdown gyros. They are nonlinear and could not be included in this analysis. They confirm the statement given in [5.3], Chapter 3.2 that the amplitudes ϕ_I of the angular vibrations in high quality platforms should be below a few seconds of arc over the whole frequency range.

The two relationships in Eq. (5.2.2) become decoupled

- in the low frequency range of the command rate ω_I^t and the drift D_I acting on the gyro in inertial navigation systems (in this case $s\theta_0 \to 0$), or
- if the servo loop stiffness $F(s)$ is assumed very high (in this case $\tilde{\theta}_0 \to 0$ according to Eq. (5.2.1)).

In both cases we obtain from Eqs. (5.2.1) and (5.2.2):

$$\omega_I^{ip} = \omega_I^t + D_I$$

$$H\omega_0^t = M_I^s = -M_I^d + J_I^p \dot{\omega}_I^{ip} + C^p \omega_I^{ip}. \qquad (5.2.5a,b)$$

These are important relations from which we can deduce the following properties of the SAP:

a) For the stabilization of platforms one can, in principle, use rate gyros as well as integrating gyros or double integrating gyros (s. Eqs. (3.3.8 and 13) for $\theta_0 = 0$). The former are disadvantageous, however, as their accuracy is limited (s. Section 3.3.2) and, in addition, errors in the pickoff cause a platform drift.

b) A constant command torque $M_0^t/H = -\omega_I^t$ about the gyro's output axis causes a constant angular rate of the platform about the gyro's input axis (s. Eq. (5.2.5a)). If for instance in Figure 5.2.1 we attach a small lead weight to one side of the gimbal, the platform starts turning about its vertical axis with respect to the inertial frame, as it was also shown in Figure 3.2.2 for the free gyro. The same is valid for applying a constant voltage to the torquer.

c) The drift-generating disturbance torques $M_0^d/H = -D_I$ cause a drift of the platform about the input axis (s. Eq. (5.2.5a)).

d) Disturbance torques on the platform due to imperfect balancing or to friction torques in the platform bearings when the vehicle is rotating are compensated in the servo motor, i.e. the platform is insensitive to exterior disturbances (s. Eq. (5.2.5b)).

One will, of course, balance the platform as perfectly as possible and keep it free from friction in order to be able to keep the servo motors small and to avoid unnecessary consumption of energy.

Summing up, it can be stated that the servo-loop stabilized platform is comparable with a free gyro whose gimbals and gimbal bearings do not transmit any disturbing moments on to the rotor. In this respect it is by far superior to the direct gyroscopic stabilization discussed in the previous section. It is also superior from the viewpoint of dynamics, since the nutation frequency which is problematic with the direct gyroscopic stabilization of a platform (s. Section 5.1) does not pose a problem with servo-loop stabilization. Damping is achieved by the sensor's viscosity (rate integrating gyro) and the layout of the servo-loop.

The above mentioned properties hold in principle also for the servo-loop stabilization of a platform about more than one axis by means of SDF gyros or two-degree-of-freedom (TDF) gyros. This will be described in the next sections.

5.2.2 Servo-Loop Stabilization of a Platform Using Two-Degree-of-Freedom Gyros

Stabilizing a platform by means of a two-degree-of-freedom gyro (TDF gyro) is, as a matter of principle, considerably easier than by means of a single-degree-of-freedom gyro (SDF gyro).

Only one sensor is required for the stabilization of two axes, as shown in Fig. 5.2.2. The axes to be stabilized and the pickoff axes are parallel to each other and not perpendicular as was the case with the SDF gyro in Fig. 5.2.1.

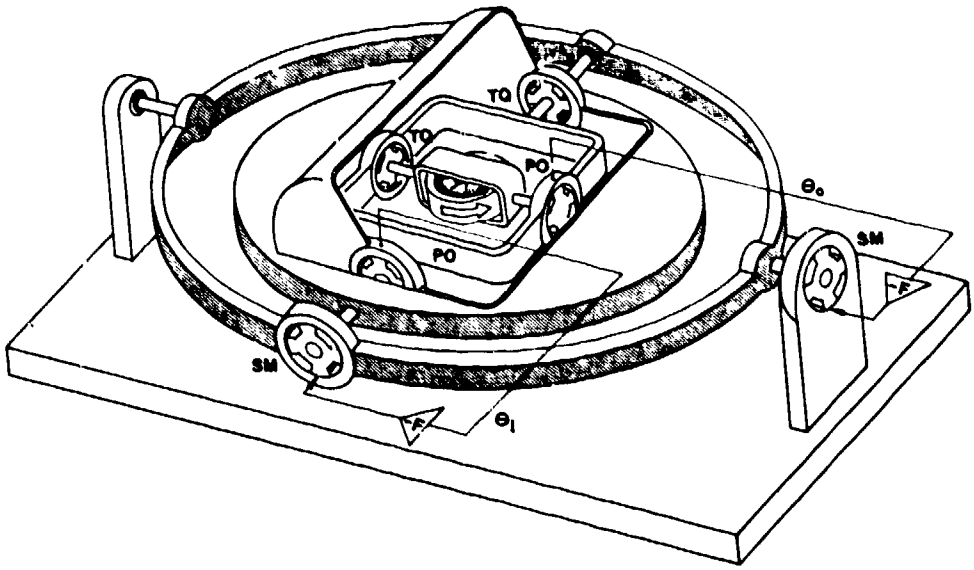

Fig. 5.2.2 Platform Stabilization by Means of a Two-Degree-of-Freedom Gyro

Bases for the discussion of the dynamics of a platform stabilized in this manner are the performance equations (3.4.6a and 14a) of the gimballed and floated TDF gyro, the free-rotor gyro (FRG) and the dynamically tuned gyro (DTG). If $\underline{\underline{G}}(s)$ is the true gyro transfer function including damped nutation for the floated TDF gyro (s. Eq. (3.4.4)) and including the additional coupling drift rates of the FRG and DTG, etc. (s. Eq. (3.4.12)) and $\underline{\underline{G}}''(s)$ includes only the undamped nutation (s. Eq. (3.4.5)), then:

$$\underline{\tilde{\theta}} = \underline{\underline{G}}(s)\,[\frac{-1}{s}\,\underline{\underline{G}}''(s)^{-1}\,\underline{\tilde{\omega}}^{i} + \underline{\underline{H}}\,(\underline{\tilde{\omega}}^{t} + \underline{\tilde{D}})]. \tag{5.2.6}$$

The moments acting on the platform are described by:

$$\underline{\tilde{M}}^{p} = \underline{\tilde{M}}^{s} + \underline{\tilde{M}}^{d} = (\underline{\underline{J}}^{p}\,s + \underline{\underline{C}}^{p})\,\underline{\tilde{\omega}}^{i}, \tag{5.2.7}$$

where we have included in $\underline{M}^{d}$ all disturbance torques acting on the platform due to friction in the gimbal bearings, unbalance of the platform, etc.; the torque $\underline{M}^{s}$ supplied by the servo motor in the closed servo-loop is (s. Fig. 5.2.2)

$$\underline{\tilde{M}}^{s} = -\underline{\underline{F}}(s)\underline{\tilde{\theta}} = -\begin{pmatrix} F_I(s) & 0 \\ 0 & F_O(s) \end{pmatrix}\begin{pmatrix} \tilde{\theta}_I \\ \tilde{\theta}_O \end{pmatrix}; \tag{5.2.8}$$

the moment of inertia tensor of the platform is

$$\underline{\underline{J}}^{p} = \begin{pmatrix} J_I^{p} & 0 \\ 0 & J_I^{p} \end{pmatrix}, \tag{5.2.9}$$

and finally

$$\underline{\underline{C}}^{p} = \begin{pmatrix} C_I^{p} & 0 \\ 0 & C_I^{p} \end{pmatrix} \tag{5.2.10}$$

is the viscous damping tensor of the gimbal bearings.

We will carry out the following discussion making some simplifications. With proper design of the servo loop the pickoff angle in Eq. (5.2.8) will be kept very low (<1 arc sec), so that Eq. (5.2.6) reduces to the <u>performance equation of the platform</u> stabilized by the <u>floated TDF gyro, the FRG and DTG</u>:

$$\underline{\tilde{\omega}}^{i} = sH\underline{\underline{G}}''(s)\,\underline{\underline{I}}\,(\underline{\tilde{\omega}}^{t} + \underline{\tilde{D}}) \approx \underline{\tilde{\omega}}^{t} + \underline{\tilde{D}}. \tag{5.2.11a,b}$$

The approximation in Eq. (5.2.11b) is valid for low frequencies and a high gain network ($\underline{\underline{F}}(0) \to \infty\,\underline{\underline{I}}$), when the platform follows the command rates $\underline{\omega}^{t}$ applied to the gyros and the drift rates $\underline{D}$. The servo motor torques $\underline{M}^{s}$ will then counteract the disturbance torques $\underline{M}^{d}$ applied to the platform (s. Eq. (5.2.7) for $\underline{\omega}^{i} = 0$). This corresponds to the single axis platform (SAP) discussed in Section 5.2.1, and all comments given there apply also here.

The high frequency performance equation (5.2.11a) depends on the transfer function of the undamped TDF gyro $\underline{\underline{G}}''(s)$ (s. Eq. (3.4.5)) and not on the original transfer functions $\underline{\underline{G}}(s)$ in Eqs. (3.4.4 and 3.4.12), which is surprising. If one could accept this result without scepticism it would indicate that the platform stabilized by the floated TDF gyro, the FRG or DTG would respond to a step function in ω^{t}, for instance, with the undamped nutation frequency of the TDF gyro as shown in Fig. 3.4.2. This is a result of our assumption that the servo loop will not allow any relative motion between gyro float and case ($\dot{\theta} \to 0$) so that the viscous damping of the floated TDF gyro and the coupling drift terms in the FRG and DTG remain zero. This interpretation is certainly academic since the platform cannot follow the nutation frequency of several 100 Hz. Once stimulated the gyro float will carry out the damped nutation frequency uncoupled from the platform and $\underline{\theta} \neq 0$.

But Eq. (5.2.11a) is of practical use in the low frequency range as its independence from the FRG transfer function G(s) in Eq. (3.4.12) indicates that the coupling drift of the FRG discussed in Eq. (3.4.11 to 17) including the detuning drift of the DTG discussed in Eq. (3.4.33 to 36) remain insignificant.

But let us again remember that we arrived at this result by assuming that for low frequencies ($s \to 0$) the servo-loop gain and consequently the torque stiffness of the platform are very high ($F(s) \to \infty$ or $M^{d}/\phi \to \infty$, s. Eq. (5.2.4)). If this is not the case, any constant disturbance torque M^{d} will cause a constant pickoff angle and consequently a drift of the platform due to coupling and detuning.

The "torque stiffness" (or its inverse, the compliance of the platform in the high frequency range) may be derived from Eqs. (5.2.6) to (5.2.10). We may assume for the moment $\underline{\omega}^{t} = \underline{D} = 0$ and $\underline{\underline{G}}(s) = \underline{\underline{G}}''(s)$ (s. Eqs. (3.4.4), (3.4.12) and (3.4.5)) when we obtain from Eq. (5.2.6):

$$\underline{\tilde{\theta}} = -\frac{1}{s}\,\underline{\tilde{\omega}}^{i} = -\underline{\tilde{\phi}}, \tag{5.2.12}$$

with ϕ = angular displacement of the platform with respect to inertial space. Introducing this into Eqs. (5.2.8) and (5.2.7) we arrive at the following compliance of the platform in the high frequency range stabilized by TDF gyros:

$$\tilde{\underline{\Phi}} = [\underline{J}^p s^2 + \underline{C}^p s + \underline{F}(s)]^{-1} \tilde{\underline{M}}^d \tag{5.2.13}$$

which for a constant transfer function $\underline{F}(s)$ of the servo-loop describes the oscillation of a spring-mass-dashpot-system. It tends to zero for very high frequencies when the platform inertia counteracts the disturbance torque. As distinguished from the compliance in Eq. (5.2.4) of the platform stabilized by a single-degree-of-freedom gyro, the compliance of the platform stabilized by TDF gyros is independent of the characteristics of the sensor.

The assumption that $\underline{D} = 0$ in the high frequency range is not quite realistic, since we know from Table 3.2.2b that all TDF gyros are sensitive to angular vibrations in a similar way to SDF gyros. The DTG is especially sensitive to angular vibrations at twice the spin frequency (s. Section 3.4.5) and special filters (e.g. comb filters) are implemented in the servo-loop to prevent these frequencies from penetrating from the gyro pickoff to the servo motor and causing a rectified drift of the gyro and platform. As already mentioned in Section 3.4.5 mechanical cross-talk between the gyros cannot be prevented. Those effects are nonlinear and could not be included in this analysis.

5.3 Three-Gimbal Platforms (TGP)

For a platform to stay "base-motion isolated", i.e. decoupled from the angular motion of a vehicle about all three axes, it must be mounted in a set of at least three gimbals as shown in Fig. 5.3.1 and must be equipped with three single-degree-of-freedom (SDF) or two two-degree-of-freedom (TDF) gyros, plus servo-loops from the gyro pickoffs to the servo motors on the gimbals.

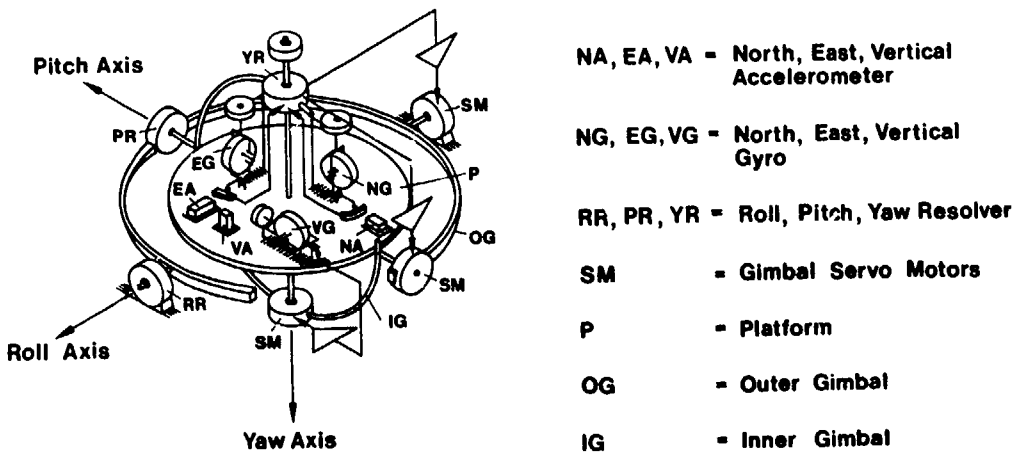

Fig. 5.3.1 Schematic View of Three-Gimbal Platform (TGP)

In Fig. 5.3.1 the three SDF gyros are denoted as north-, east- and azimuth gyro (NG, EG, AG). An important step in the design of the platform and its servo-loop is again to verify the performance equation as derived in the former two sections for the single axis and two axes platforms:

$$\underline{\omega}^{ip} = \underline{\omega}^t + \underline{D} \tag{5.3.1}$$

with the only difference that the angular rate vector $\underline{\omega}^{ip}$ of the platform with respect to inertial space, the slewing rate vector $\underline{\omega}^t$ applied to the gyros' torquer and the gyros's drift rate vector D have three components, for instance in the north, east and down directions. The gyro stabilized TGP will then behave like a free gyro about all three axes, i.e. the non-slewed and driftless TGP will keep its orientation to inertial space ($\underline{\omega}^{ip} = \underline{\omega}^{ie} + \underline{\omega}^{ep} = 0$). On the rotating earth it will move with respect to the ground in a 24h-mode in a sense opposite to earth rate $\underline{\omega}^{ie}$ as indicated in Fig. 5.3.2.

The generation of the slewing rate $\underline{\omega}^t$ for using the TGP in an inertial navigation system will be subject of Chapter 7.

The drift rates are discussed in Sections 3.3 and 3.4 and some error terms are listed in Tables 3.2.1a,b and 3.2.2a,b, where Table 3.2.1a and 3.2.2a contain all the terms under the assumption that the engineers who designed the platform and its servo-loops have met the requirement mentioned in Section 5.2.1, i.e. that the vibratory angular amplitudes of the operating platform are below a few seconds of arc. The error terms in Tables 3.2.1b and 3.2.2b may serve as an expedient to verify these requirements.

We will discuss in this section some of the problems the control engineer faces before he reaches the goal mentioned in Eq. (5.3.1).

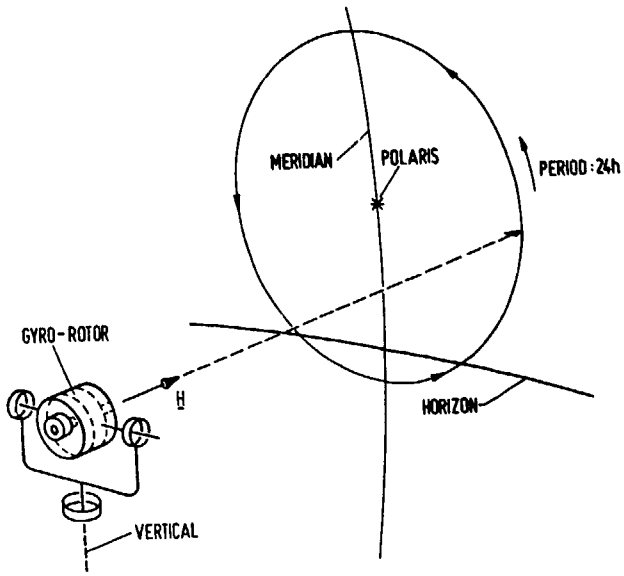

Fig. 5.3.2 The Free Gyro on the Rotating Earth

For moderate pitch angles of the aircraft (theoretically $< \pm 90^0$, in practice $< \pm 60^0$ to 70^0, s. [5.4] and [5.5]) only three gimbals are required for the stabilization of a platform, as shown in Fig. 5.3.1, where the sequence of the gimbals is such that the angular freedom (yaw angle ψ) between platform and inner gimbal is along the down or vertical axis of the aircraft, the angular freedom (pitch angle θ) between the inner and outer gimbals is along the lateral axis and the angular freedom (roll angle ϕ) between the outer gimbal and aircraft is along the longitudinal axis of the aircraft. This enables the synchros mounted on the gimbal axes to indicate yaw, roll and pitch angles (ψ, ϕ, θ) of the aircraft. Other gimbal sequences are also possible, but in these cases the gimbal synchros do not directly indicate the generally used attitude and heading angles and the angle limitation is in another axis.

The control loops for platform stabilization discussed in the previous sections were derived for the torque vector $\underline{M}_p^s$ in the platform coordinate system with the components $M_{N,E,D}^s$ for the north, east and down oriented platform. Since the gimbal servo motor torque vector $\underline{M}_s^s$ with the components $M_{R,P,D}^s$ along the roll axis, the pitch and down axis moves with respect to the platform when the aircraft is maneouvering, a coordinate transformation is required before the torque commands are applied to each servo motor. For the sequence of gimbals mentioned above we obtain the following dependence of the servo motor torques on the platform torques when the aircraft is maneouvering:

$$\underline{M}_s^s = \begin{pmatrix} M_R \\ M_P \\ M_D \end{pmatrix}^s = \underline{\underline{C}}_{sp}\, \underline{M}_p^s = \begin{pmatrix} \sec\theta\cos\psi & -\sec\theta\sin\psi & 0 \\ \sin\psi & \cos\psi & 0 \\ -\tan\theta\cos\psi & \tan\theta\sin\psi & 1 \end{pmatrix} \begin{pmatrix} M_N \\ M_E \\ M_D \end{pmatrix}^s \tag{5.3.2}$$

The platform torques on the right hand side must be related to the gyro pickoff angles in the following way (s. Eqs. (5.2.1) and (5.2.8)).

$$\tilde{\underline{M}}_p^s = -\underline{\underline{F}}(s)\,\tilde{\underline{\theta}} = -F(s)\,\underline{\underline{I}}\,\tilde{\underline{\theta}}, \tag{5.3.3a,b}$$

where Eq. (5.3.3b) is valid for equal servo loop transfer functions in all three axes. We introduce this into Eq. (5.3.2)

$$\underline{M}_s^s = -\,F(s)\,\underline{\underline{C}}_{sp}\,\tilde{\underline{\theta}} \tag{5.3.4}$$

and have now a basis for connecting the pickoff angles $\underline{\theta}$ with the electronic networks F(s) and the servo motors as can be seen on the left side of Fig. 5.3.3. The right side shows the backward coordinate transformation $\underline{\underline{C}}_{ps}$ carried out by the gimbals. Thus we see that the servo motor torques in Eq. (5.3.4) can really supply the torque required in the platform coordinate frame (s. Eq. (5.3.3b)), i.e. independent of the roll, pitch and yaw angle they can address one component on the platform. This zero cross coupling of the torques is only true in the static case. In the dynamic case the following effects cause cross coupling between the axes:

- varying load torques due to angular acceleration of the gimbals and changing moments of inertia and products of inertia (s. [5.4], Chapter 5 and [5.6], Chapter 11.8),
- varying friction torques of the gimbal bearings and sliprings,

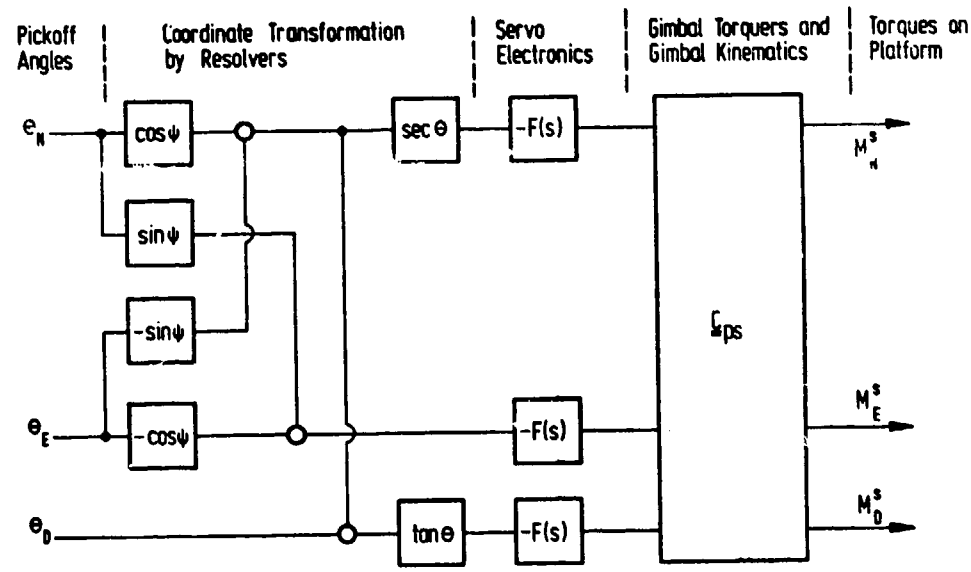

Fig. 5.3.3 Block Diagram for the Three Axis Platform Stabilization

- interaxis sensor coupling (s. [5.3], Chapter 5, 9 and [5.4], Chapter 5), mechanical gyros not only respond to angular rates about the input axis but also to angular acceleration about the output axis, s. Tables 3.2.1b and 3.2.2b; in [5.4] considerations on SDF gyro output axis orientation are presented), and
- sensitivity of the gyro (s. Tables 3.2.1a,b and 3.2.2a,b) and the platform gimbal structure to linear acceleration and angular vibration.

It is the task of the mechanical engineers and the control engineers to reduce these effects to a tolerable level. Their efforts are measured in frequency plots of the dynamic torque stiffness or platform compliance (s. Eqs. (5.2.4) and (5.2.13)) or as ratios of ω^{Pi}/ω^{bJ}, i.e. as ratios of the platform angular rate in the i-axis over base angular rate in the j-axis. For i = j this ratio measures "base motion isolation", otherwise the cross coupling. Fig. 5.3.4 shows a platform frequency plot for the Bodenseewerk Gerätetechnik TNP 627, an inertial navigation platform equipped with two dynamically tuned gyroscopes (Gyroflex of Singer Kearfott, USA). At low frequencies the platform responds to an unbalance of 0.01 Nm with a tilt of 2 arc sec. The platform stiffness decreases by one order of magnitude at high frequencies (5 to 50 Hz) due to the decreasing servo loop response. At very high frequencies it increases again due to the inertia of the platform and the gimbals as we have seen in the discussion of Eq. (5.2.13).

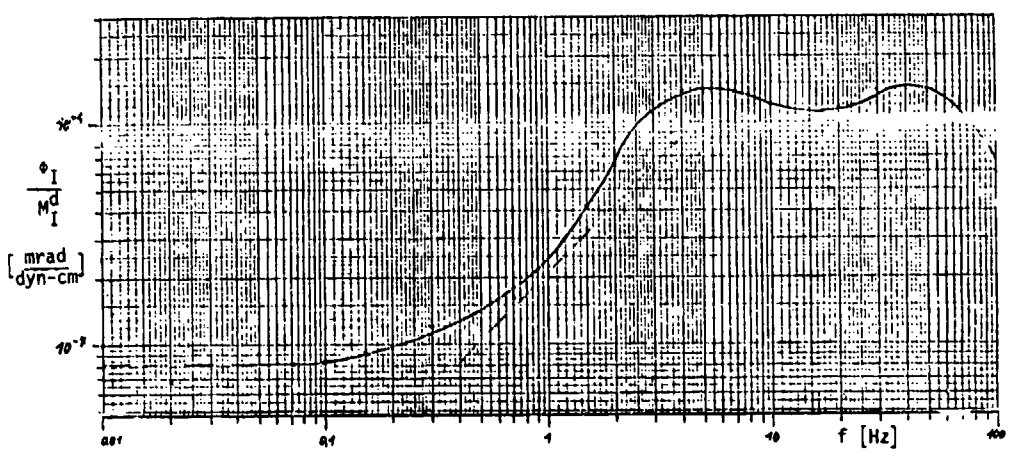

Fig. 5.3.4 Frequency Plot of Closed Inner Roll Platform Compliance (TNP 627)

5.4 Four-Gimbal Platforms (FGP)

In practice the three-gimbal platform (TGP) is limited to pitch angles below +60° to 70° (s. [5.4] and [5.5]). For higher maneouverability the four-gimbal platform (FGP) shown schematically in Fig. 5.4.1 has to be used.

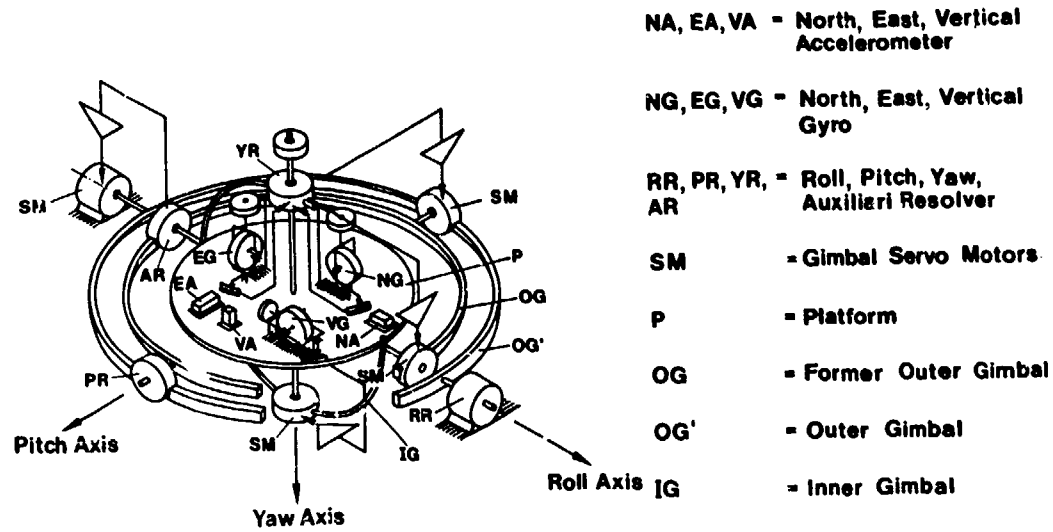

Fig. 5.4.1 Schematic View of Four-Gimbal Platform (FGP)

The FGP is a TGP (s. Fig. 5.3.1) mounted in an additional outer gimbal OG' but with its roll and pitch axes transposed. The three innermost servo motors are controlled as in the TGP but the outer roll servo motor is controlled by the angle between the inner gimbal IG and the former outer gimbal OG. Its task is to keep this angle ϕ' zero in normal flight. With the Litton LN-3 system, for instance [5.7], its freedom is limited to $\pm 20^o$. In the TGP ϕ' was the critical angle θ (the aircraft's pitch angle) and assuming that the angle notation of FGP is ψ, ϕ', θ, ϕ for the synchros from inside to outside (it was ψ, θ and ϕ for the TGP) we see from Eq. (5.3.2) and Fig. 5.3.3 when we replace θ by $\phi' = 0$ that the network from the gyro pickoffs to the servo motors simplifies considerably. In this servo loop only the ψ-resolver is of significance.

If the aircraft passes the critical region where gimbal lock would occur with the TGP (pitch angle vertical, i.e. azimuth axis and roll axis coincide) the control loop from the inner roll angle ϕ' to the outer roll servo motor changes its sign and becomes unstable. This causes the outer gimbal OG' to seek another equilibrium which is 180° away from the initial equilibrium. The FGP thus trades the "gimbal lock" problem for the "gimbal flip" problem which requires a servo loop fast enough so that the gyros do not hit their stops during the maneuver of the aircraft. In the LN-3 system the gimbal flip requires less than 0.3 s to achieve 90° of the required 180° change [5.7].

In an aircraft carrying out a loop maneuver with subsequent roll the gimbal angles for heading and roll will go through 180°-reversals during gimbal flip so that thereafter the platform indicates again roll, pitch and azimuth in the proper way. During gimbal flip an inner roll angle ϕ' develops and reaches its maximum at a time $\Delta T = 0.3$ s in the LN-3 platform [5.7] when the outer roll gimbal has rotated slightly more than 90° of the required 180°. The inner roll angle is then approximately equal to the pitch rate of the maneuver multiplied by ΔT [5.7]. It affects the indication of roll, pitch and azimuth as shown in [5.4], Eqs. (5-73) and (5-74). A detailed analysis of the gimbal flip kinematics is presented in this reference.

References for Chapter 5

[5.1] Sorg, H. — From Serson to Draper, Two Centuries of Gyroscopic Development. Proceedings of the International Navigational Congress 1976, The Institute of Navigation, Washington D. C., page 166 - 172.

[5.2] Wrigley, W., Hollister, W. M., Denhard, W. G. — Gyroscopic Theory, Design, and Instrumentation. The MIT Press, Cambridge, Mass., USA (1969).

[5.3] Pitman, G. R. (Editor) — Inertial Guidance. J. Wiley & Sons, New York (1962).

[5.4] Broxmeyer, Ch. — Inertial Navigation Systems. McGraw-Hill Book Company, New York (1964).

[5.5] Kayton, M., Fried, W. R. (Editors) — Avionics Navigation Systems. J. Wiley & Sons, New York (1969).

[5.6] Arnold, R. N., Maunder, L. — Gyrodynamics. Academic Press, New York (1961).

[5.7] Litton LN-3 Lightweight Inertial Navigation System. Technical Description, Litton Systems, Inc. (1961).

6. ATTITUDE AND HEADING REFERENCES

In many applications for the evaluation of flight tests information about the aircraft attitude and heading is required. In this chapter different sensors for the aircraft roll, pitch and yaw angles are discussed (s. also Chapter 5):

- Vertical Gyro (VG), measuring roll and pitch angles.
- Directional Gyro (DG), measuring the angle between the aircraft roll axis and a reference direction (e. g. true north).
- Attitude and Heading Reference System (AHRS); a combination of a VG and a DG measuring the aircraft roll, pitch and yaw angles with medium accuracy.
- Attitude Platform; a gyro stabilized three- or four-gimbal platform, measuring the aircraft roll, pitch and yaw angles with high accuracy.
- Strapdown attitude and heading reference systems in which the aircraft roll, pitch and yaw angles are computed with high accuracy based on gyro and accelerometer measurements.

6.1 Vertical Gyro (VG)

A vertical gyro is a two-degree-of-freedom gyro with its spin axis vertical. The gimbal angles give the aircraft attitude (roll, pitch) with respect to local vertical (Fig. 6.1.1). In normal operation, the VG outer gimbal is aligned parallel to the aircraft's longitudinal axis, the inner gimbal is parallel to the lateral axis and the spin axis is parallel to the vertical axis. The gyro spin axis is maintained parallel to local vertical by an erection system which uses the signals from a gravity sensing device (two bubble levels in Fig. 6.1.1). A torque proportional to the output of these sensors is applied to the gyro, precessing its spin axis towards the local vertical in unaccelerated flight.

In a first order erection loop (Fig. 6.1.1) the amplified gravity sensor signal, which is proportional to the deviation ε of the spin axis from the apparent vertical, is directly applied to the gyro torquers. The response of this elementary VG in one axis to a horizontal acceleration f can be described by a first order differential equation:

$$\dot{\varepsilon} = -K\,g\,\varepsilon + K\,f + \omega. \qquad (6.1.1)$$

$T = 1/(K\,g)$ is the loop time constant and ω is the sum of the gyro drift rate and the component of the rate of rotation in inertial coordinates of the local vertical along the gyro input axis.

The block diagram in Fig. 6.1.2 illustrates the Equation (6.1.1). Usually a value of K is chosen such that the loop time constant T is of the order of one minute. This compromise value ensures that the error angles due to drift (ω) do not become too large and that, on the other hand, the transient horizontal acceleration (f) during aircraft maneuvers does not have too large an influence. The influence of these ma-

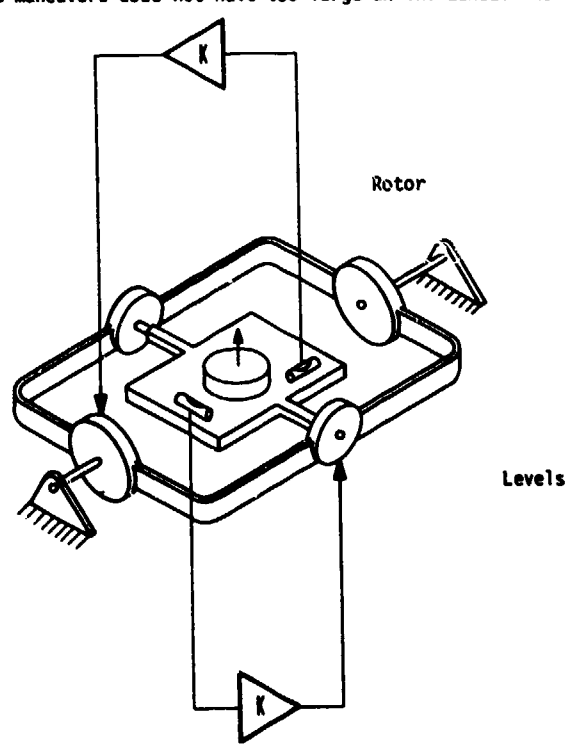

Fig. 6.1.1 Vertical Gyro Principle

neuver accelerations would not be negligible during prolonged turn if no additional measures were taken. In a steady state turn at 20° roll angle at a turn rate of 180 degrees/min the error in the indicated vertical would be about 8 degrees after a 90-degree-turn and about 13 degrees after a 180-degree-turn.

Two types of nonlinearities are usually introduced to reduce these errors (see Fig. 6.1.3)

- erection cut off: The gyro precession signal is cut off when the sensed acceleration is greater than a certain value f^b (typical 0.2 g), and

- precession rate saturation: The precession rate is proportional to the sensed acceleration f until a value f^a is reached. After that the precession rate is constant. A typical value for f^a is 0.01 g.

Fig. 6.1.3 illustrates the application of both nonlinearities at the same time. With these nonlinearities the maximum acceleration-induced errors can be kept smaller than 1°.

Since the direction of the local vertical changes with respect to inertial space as a result of earth rotation (earth rate) and of the aircraft motion around the earth (transport rate), a hang-off angle in the first order VG erection system occurs. This can be explained with the help of Fig. 6.1.2. The sum of the angular rates due to the rotation of the earth and the speed of the aircraft are

$$\omega^{roll} = \Omega \cos\varphi \cos\psi$$
$$\omega^{pitch} = \Omega \cos\varphi \sin\psi + V/R. \qquad (6.1.2)$$

φ = latitude

Ω = 15°/h, earth rate

ψ = aircraft heading

V = aircraft velocity

R = 6400 km, earth radius.

Constant inputs (ω^{roll} + drift) and (ω^{pitch} + drift) are compensated in the first order roll and pitch loops (Fig. 6.1.2) by a static error ε^s, with

$$\varepsilon^{s,roll} = T\,\Omega \cos\varphi \cos\psi \qquad (6.1.3)$$

$$\varepsilon^{s,pitch} = T\,(\Omega \cos\varphi \sin\psi + V/R). \qquad (6.1.4)$$

For a loop time constant of one minute static errors of up to 0.5 degrees can occur.

The static error ε^s can be reduced by using a second order erection loop, as shown in Fig. 6.1.4. The inclusion of an additional integrator in the loop has the effect that (constant) rates such as gyro drift and rotation of the local level are compensated. In stationary conditions, this integrator's output will be equal to these rate inputs with opposite sign, so that their influence is compensated.

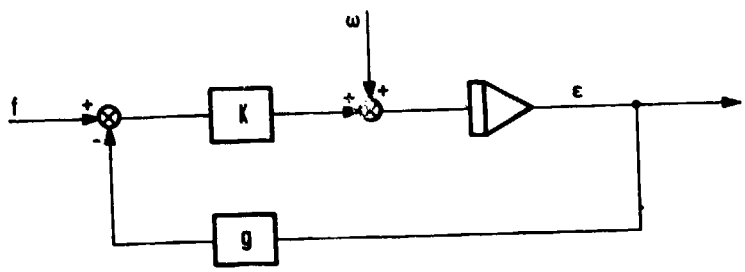

Fig. 6.1.2 Block Diagram of the Vertical Gyro Error Equation (6.1.1)

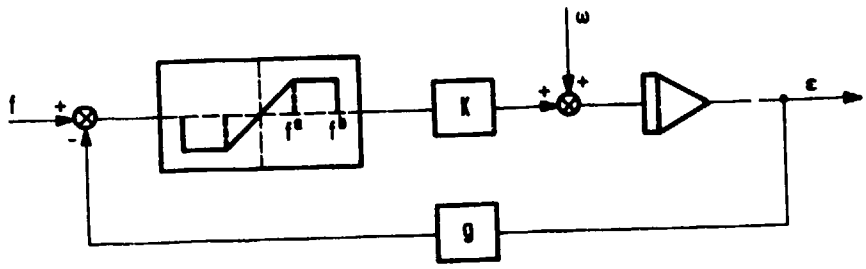

Fig. 6.1.3 Erection Cut Off and Precession Rate Saturation of a Vertical Gyro

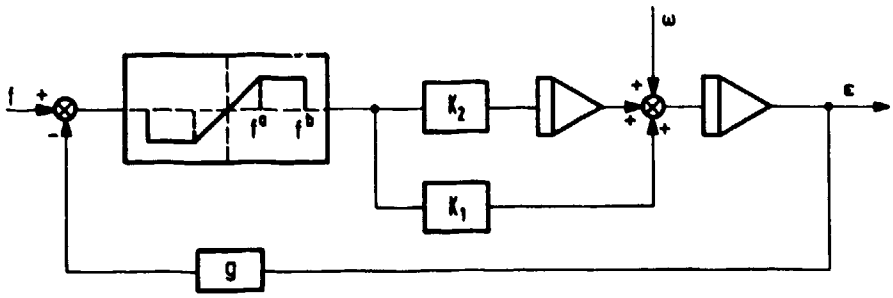

Fig. 6.1.4 Second Order Erection Loop of a Vertical Gyro

HARDWARE EXAMPLE: SPERRY VG-14 Vertical Gyro

Fig. 6.1.5 shows the Vertical Gyro VG-14 which consists of two basic parts: an electronics unit, containing the erection control, torquer drivers, monitors, detectors and power supply control circuitry, and a gyro unit, containing the gyro motor, gimbals, torquer motors, synchros and liquid level switches. Leading particulars for the VG-14 are listed in Table 6.1.1.

A mechanical diagram of the VG-14 is given in Fig. 6.1.6. The gyro erection circuitry uses the signals from two liquid level switches (S1 and S2 in Fig. 6.1.6) to correct the position of the pitch and roll gimbals with respect to the local vertical. These switches consist of glass tubes partially filled with an electrolyte, two end electrodes and a common electrode. When the switch is level, the electrolyte touches both end electrodes and the common electrode, forming two ground paths. Tilting the switch removes one of the end electrodes from the electrolyte, thereby removing a ground path. This signal is used to activate the appropriate torquer motor to correct the position of the gimbal. A torque rate for fast or slow erection can be selected.

Pitch cut-off switches detect the fore-aft accelerations. Pitch erection cut-off occurs when this acceleration is greater than 0.07 g. Roll erection cut-off is initiated by the roll cut-off detector, which monitors the roll angle. At a roll angle of 6°, corresponding to a transverse acceleration of 0.1 g, the roll erection loop is cut off.

Gyro rotor speed	22000 rpm within 5 minutes after power is applied
Gyro angular momentum	3.8 million gm - cm^2 per second
Gyro erection	vertical within 3 minutes after power is applied
Verticality (Alignment of spin axis with true vertical)	0.25 degree (bench)
Erection cut off	0.10 g (Roll); 0.07 g (Pitch)
Erection rate	20 degree/minute (fast) 2.5 degree/minute (slow)
Dimension	18.8 x 16.6 x 26.4 cm^3

Table 6.1.1 Characteristics of the SPERRY VG-14 Vertical Gyro

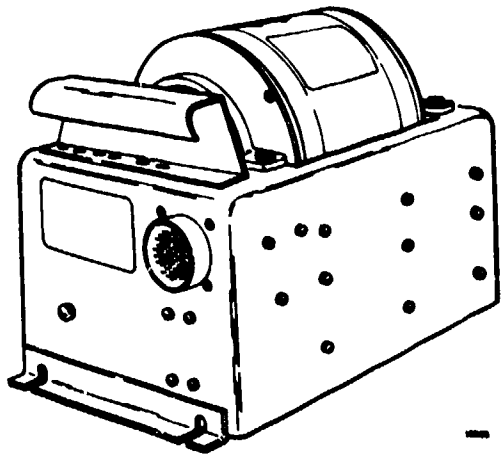

Fig. 6.1.5 SPERRY VG-14 Vertical Gyro (19x17x26cm^3)

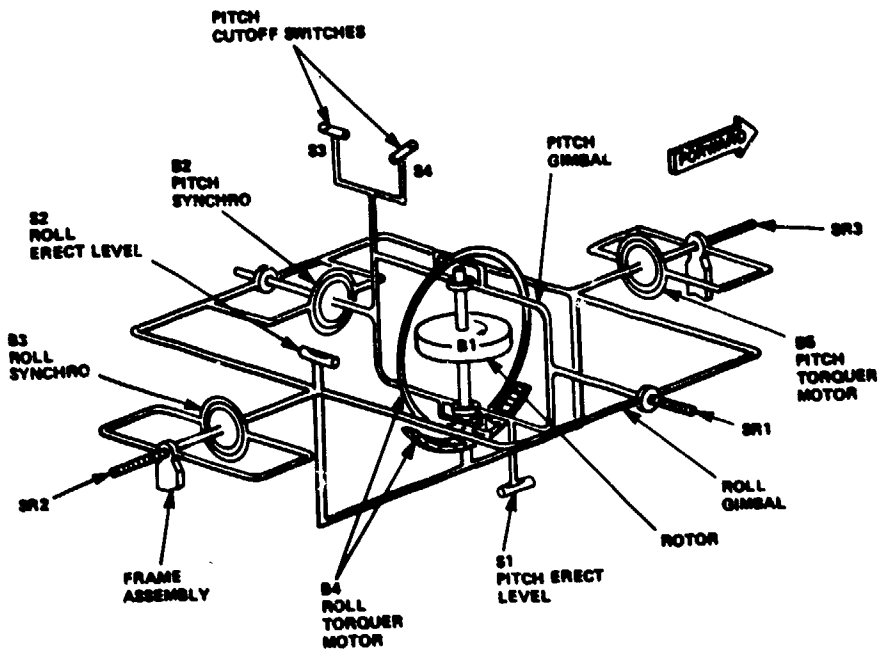

Fig. 6.1.6 Mechanical Diagram of the SPERRY VG-14

6.2 Directional Gyro (DG)

A directional gyro is a two-degree-of-freedom gyro which indicates the motion of an aircraft in azimuth, measured from a certain reference direction (e.g. true north). This reference direction is established by initially aligning the DTG's spin axis to this direction. During the flight, the spin axis is maintained level and it is usually aligned to point to true or magnetic north (Fig. 6.2.1).

Usually the outer gimbal axis is normal to the aircraft floor plane and the inner axis is parallel to the floor plane. Aircraft heading is read from a pick-off on the outer gimbal axis. A level is attached to the gyro housing, sensing a deviation of the spin axis from a horizontal position. Its output is amplified and applied to the outer axis torquer. In this way the spin axis is caged to horizontal with a first order loop (similar to Section 6.1). Usually the DG is used in two modes of operation:

- Free mode. In this mode the gyro conserves the initial alignment as a reference direction.

- Slaved mode. This mode uses an external reference, such as a remote magnetic sensor to provide a continuous azimuth torquing signal. This signal keeps the gyro spin axis aligned with the external reference (Fig. 6.2.2).

Due to the two-gimbal suspension of the DG, a varying error occurs in non-level flight due to kinematic effects - the gimbal error. A mathematical analysis of the gimbal error shows that the indicated heading is a function of the actual heading and also of the roll and pitch angles:

$$\tan\psi^* = \frac{\cos\phi}{\cos\theta}\tan\psi - \tan\theta\sin\psi \qquad (6.2.1)$$

ψ^* indicated heading

ψ actual heading

ϕ roll angle

θ pitch angle.

In most applications of a DG, the pitch angle is only a few degrees, whereas the roll angle frequently may be as high as 40 to 50 degrees, so that the roll angle must be considered as the major contributor to the gimbal error. If the pitch angle is very small ($\theta \approx 0$), the gimbal error equation is a much simpler expression.

$$\tan\psi^* = \tan\psi \cdot \cos\phi.$$

From this equation the gimbal error $\delta\psi = \psi^* - \psi$ can be calculated directly

$$\tan\delta\phi = \frac{\tan\psi(\cos\phi-1)}{1+\tan^2\psi\cos\phi} \qquad (6.2.2)$$

During roll of the aircraft the DG gimbal error results in an apparent change in azimuth which increases as the roll angle increases. The gimbal error reduces to zero only when the roll angle becomes zero. It is less than 2 degrees for roll angles of less than 20 degrees and less than 4.2 degrees for roll angles up to 30 degrees, but can reach a value of 45 degrees at a roll angle of 90 degrees. The DG output can be corrected for this error, if the roll and pitch angles are known.

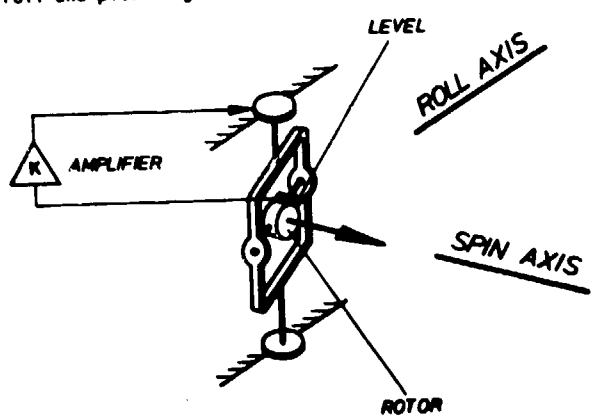

Fig. 6.2.1 Directional Gyro Principle

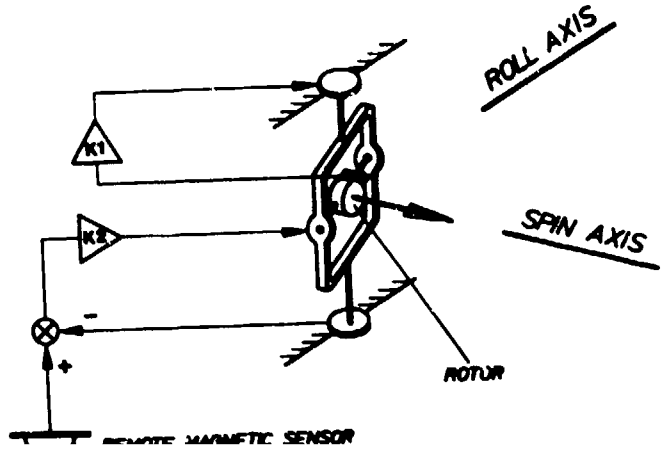

In the free mode, the azimuth error of the DG is equal to the initial misalignment angle plus the integral of the drift rate over the flight time. Apparent drift of the DG due to the meridian convergence and the vertical component of the earth rate can be calculated as follows

Meridian convergence rate $V_E \cdot \frac{\tan\varphi}{R}$

Vertical earth rate $\Omega \cdot \sin\varphi$, (6.2.3)

where

$V_E = V \sin\psi$ east velocity

Ω = earth rate

R = earth radius

φ = latitude

This apparent drift reaches values of twenty and more degrees per hour, so that these effects have to be compensated by a torquing signal.

In the slaved mode, these (uncompensated) drift rates would produce a hang-off angle, similar to that discussed in Section 6.1. Usually the earth rate correction is made with a constant torque signal, corresponding to the mean latitude and the mean velocity. These values have to be set by the pilot before the flight. For a precise correction of the meridian convergence, the aircraft velocity must be known. The major errors of a DG in the slaved mode are introduced by the magnetic sensor. Such errors are caused by the magnetic effects of the aircraft: current-carrying conductors and permanently magnetized portions of the aircraft structure (hard-iron effects, error with one cycle in 360° heading change); high-permeability portions of the structure are magnetized by the earth's field (soft-iron effects, two cycle error); dynamic errors caused by the departure from the horizontal of the pendulous magnetic sensor under acceleration. These errors can be compensated, so that the residual error of the magnetic sensor is in the order of 0.2 - 0.5°.

HARDWARE EXAMPLE: SPERRY Gyroscopic Compass System C-12

This heading reference system consists of the following parts (Fig. 6.2.3)

- directional gyroscope
- induction compass transmitter (flux valve)
- amplifier - power supply
- remote magnetic compensator
- digital controller.

The induction compass transmitter detects the direction of the earth's magnetic field and transmits this information to a synchro that compares magnetic heading with the gyro heading. The error signal then slaves the DG. The system can be operated in this slaved mode or it can operate as an independent directional gyroscope (free mode).

The system has compensation for the errors of the induction compass transmitter (remote magnetic compensator), for the gimbal error (corrector circuit; roll angle required from a VG), for gyro drift and earth rate and for the meridian convergence error. For these corrections, ground speed and latitude are required. The leading particulars are supplied in the Table 6.2.2

Slaved heading accuracy	0.25° rms
Free gyro heading accuracy (latitude corrected)	0.5° rms

Table 6.2.2 Characteristics of a SPERRY C-12 Directional Gyro

6.3 Gimballed Attitude and Heading Reference Systems (AHRS)

The Attitude and Heading Reference System (AHRS) considered in this section is an integrated combination of a VG and a DG. Usually earth-rate and transport-rate compensations are applied and no gimbal error occurs because the DG is mounted on the inner gimbal of the VG (see Fig. 5.3.1). For the transport-rate correction, the aircraft velocity has to be provided by an external source (or a mean value is initially set). With the help of the measured roll, pitch and yaw angles, the transport rate together with the earth rate is resolved to the three axes of the AHRS and the gyros are slaved to the appropriate signals. In modern AHRS a small digital computer is included which controls the measuring unit and provides the required outputs of the system.

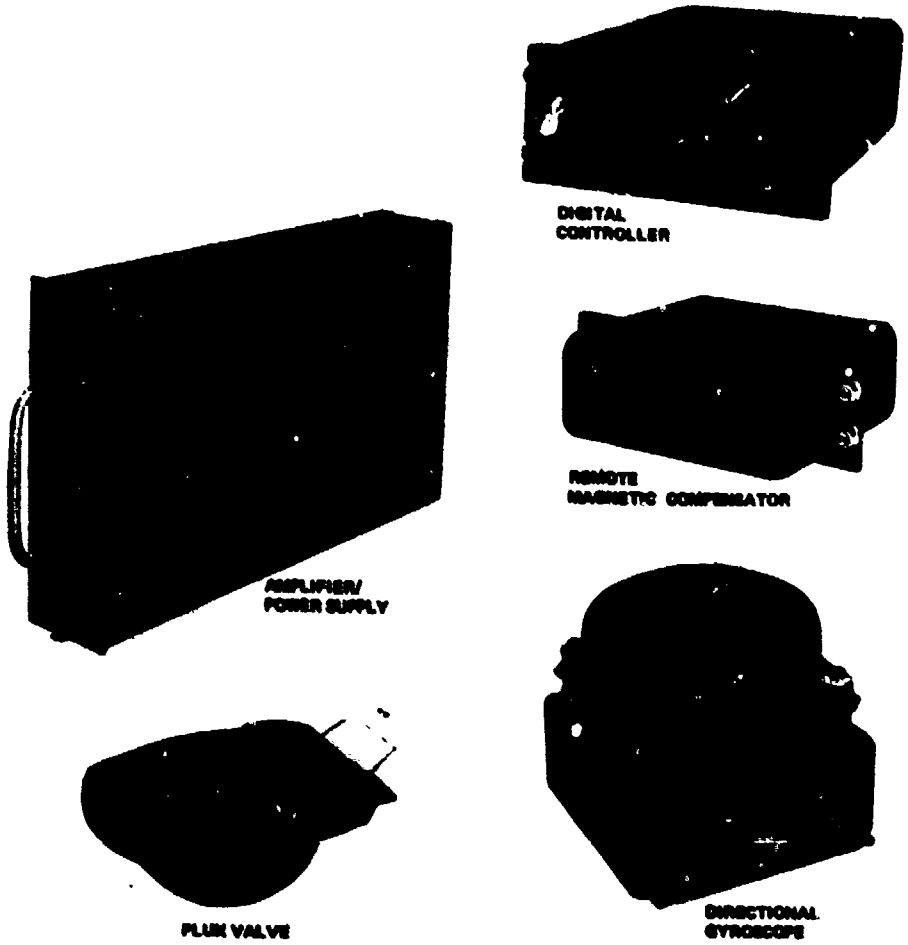

Fig. 6.2.3 SPERRY Directional Gyro C-12

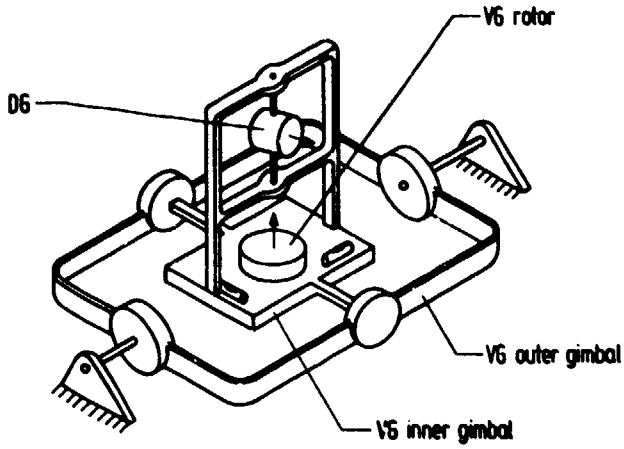

Fig. 6.3.1 Attitude and Heading Reference System Principle

HARDWARE EXAMPLE: SPERRY Attitude and Heading Reference System
SYP 820 (License production by BODENSEEWERK)

The SYP 820 system consists of the following parts (Fig. 6.3.2)

- Gyro reference unit
- Electronics unit
- Controller.

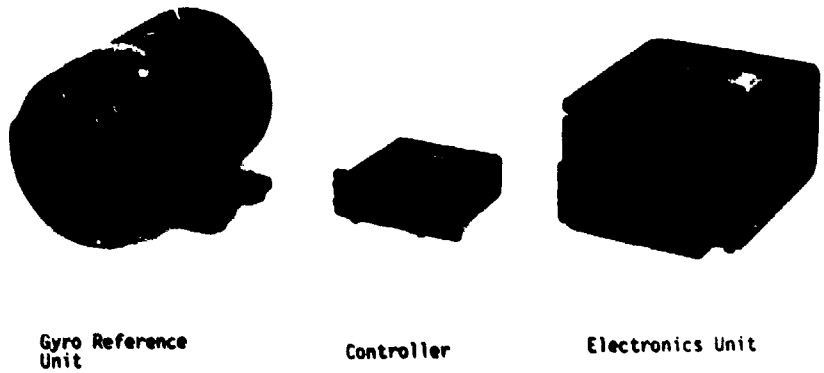

Fig. 6.3.2 SPERRY Attitude and Heading Reference. System SYP 820
(Licence Production by BODENSEEWERK)

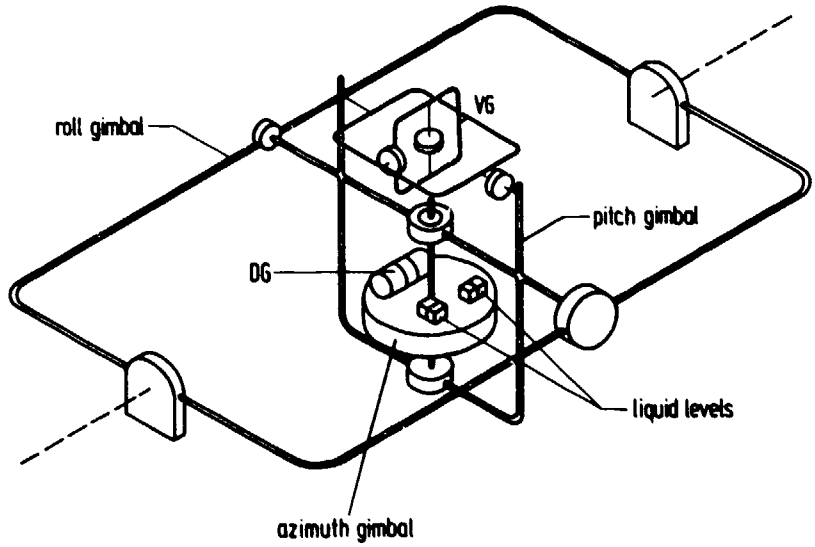

Fig. 6.3.3 Gyro Reference Unit Configuration of the SYP 820

Fig. 6.3.3 shows the gyro reference unit configuration: The directional gyro stabilizes the servoed azimuth gimbal and is mounted in servoed roll and pitch gimbals so that its input axis is in line with the local vertical. The vertical gyro is a two degree of freedom gyro, sensing the aircraft roll and pitch rotations. Transport rate compensation is applied in pitch only, assuming that the aircraft velocity vector is lying along the longitudinal axis of the aircraft, neglecting wind effects. The average velocity is manually set in the controller by the pilot. Earth rate is compensated for a fixed latitude. Two liquid levels are moun-

ted orthogonally on the azimuth gimbal. They indicate changes from the local vertical, caused by gyro drift etc., and control the roll and pitch axes in a first order loop. The directional gyro can be operated in the free mode and slaved to a remote magnetic sensor.

The leading particulars of the system are given in Table 6.3.1.

Heading accuracy	0.6^{o} max in 1 hour
Roll and pitch	0.25^{o} (1σ) unaccelerated flight
First order erection loops	0.8^{o} max in 6 minutes
Erection cut off	0.2 G

Table 6.3.1 Characteristics of the SPERRY SYP 820 Attitude and Heading Reference System

6.4 Attitude and Heading Platforms

The attitude and heading platform discussed in this section is a system with two two degree-of-freedom gyros or three single-degree-of-freedom gyros, mounted on a stable platform. This stable platform is isolated from aircraft rotations by two or three servo-driven gimbals. A three gimbal attitude and heading platform is shown in the schematic diagram Fig. 6.4.1. The azimuth gimbal (the stable platform) is isolated from rotation by a (inner) pitch gimbal and a (outer) roll gimbal. Gimbal lock, which occurs at 90° pitch, does not allow all-attitude operation. By adding a fourth gimbal, an all-attitude platform is obtained. (See also Sections 5.3 and 5.4).

Attitude and heading platforms can be considered as downgraded inertial platforms (see Chapter 7). The angular accuracy of the attitude and heading platform depends on the drift performance of the gyros which are used and on the method of slaving the platform to the vertical. If accelerometers are used to sense the horizontal accelerations on the stable element, the platform can be slaved to the vertical by the well-known second-order Schuler loops (see Chapter 7). The addition of earth rate compensation loops then makes an inertial platform of the attitude and heading platform. The use of liquid levels instead of accelerometers in the levelling loops and of gyros with a lower drift performance and of slaving the azimuth gimbal to magnetic north, derived from a remote magnetic sensor, give the attitude and heading platform an accuracy similar to an attitude and heading reference system.

Modern attitude and heading platforms have digital electronics. This provides the possibility for easy compensation of earth and transport rate and of acceleration effects, if an external velocity signal (such as a Doppler-radar) is available. The digital mechanisation of these compensation loops is similar to those used in inertial platforms (see Chapter 7).

HARDWARE EXAMPLE: SAGEM MGC 10

The MGC 10 attitude and heading platform is shown in the Fig. 6.4.2. It has three miniature floated single-degree-of-freedom gyros, two electrolytic levels and four gimbals. The erection loop is of first order, with additional integrators for the compensation of earth rotation and gyro drift. A compensation signal for the transport rate is resolved along the platform axes by means of the platform heading information and is fed directly to the gyro torquers. Erection cut-off is foreseen if sharp heading changes or roll angles exceeding a given threshold occur. Earth rate compensation is also applied to the azimuth gyro. The leading particulars of the MGC 10 are given in Table 6.4.1.

Heading accuracy	$0.2\ ^{o}$/min
Attitude error (unaccelerated flight)	0.5^{o}
Alignment time	3 min

Table 6.4.1 Characteristics of the SAGEM MGC 10 Attitude and Heading Platform

6.5 Strapdown Attitude and Heading Reference Systems

The philosophy just described for attitude and heading reference by a platform technique can equally be implemented with a strapdown system. In such a system, with sensors attached directly to the vehicle, the task of providing an angular reference is accomplished by a high speed computer rather than by a gyro-stabilized platform. Section 7.4.4 describes this technique in more detail.

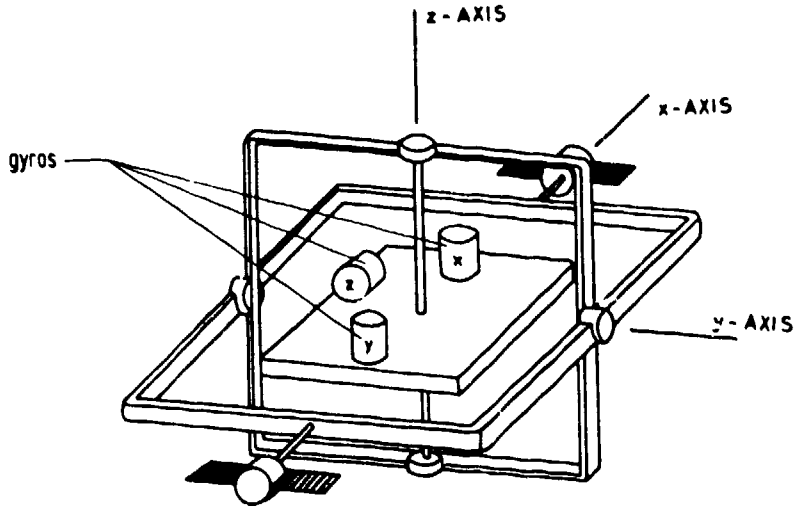

Fig. 6.4.1 Three Gimbal Attitude and Heading Platform

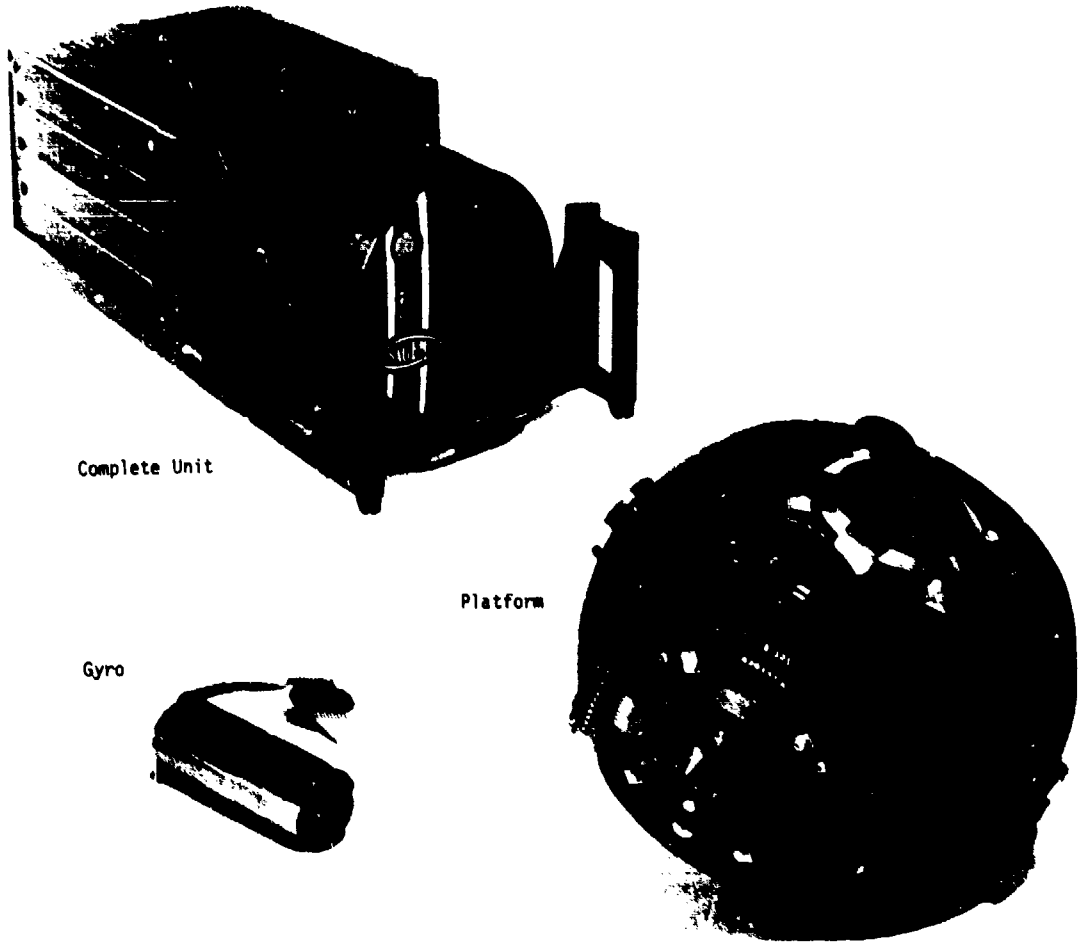

Fig. 6.4.2 SAGEM MGC 10 Attitude and Heading Platform

The strapdown AHRS not only serves as an attitude and heading reference but also delivers information on angular rate and acceleration. This results in a significant overall cost and weight reduction and provides for greater accuracy and higher reliability than heretofore achievable.

The Litton LTR-80, for instance, accepts inputs from the magnetic compass, air data computer and VOR/DME. Its system outputs consist of attitude, heading, ground speed, vertical speed, drift angle, flight path angle as well as linear accelerations and angular rates. It ensures no degradation of accuracy during aircraft maneuvers.

The LTR-80 is equipped with three high accuracy accelerometers of the type A-2 and two dynamically tuned gyroscopes of the type Litef K-273 (s. Fig. 3.4.10). A strapdown system (as shown in Fig. 6.5.1 for the LTR-80, but also offered in a similar configuration by other manufacturers) can allow easier maintenance by ready access to and simple removal of all parts including sensors. Table 6.5.1 summarizes the 95 % performance of the LTR-80.

Heading accuracy	1°
Attitude error	0.25^{o}
Ground speed error (with VOR/DME)	8 kts
Flight path angle	1°
Body rates	0.1^{o}
Body acceleration	0.1 %
	0.01 g

Table 6.5.1 Characteristics of the Litton LTR-80 Strapdown Attitude and Heading Reference System

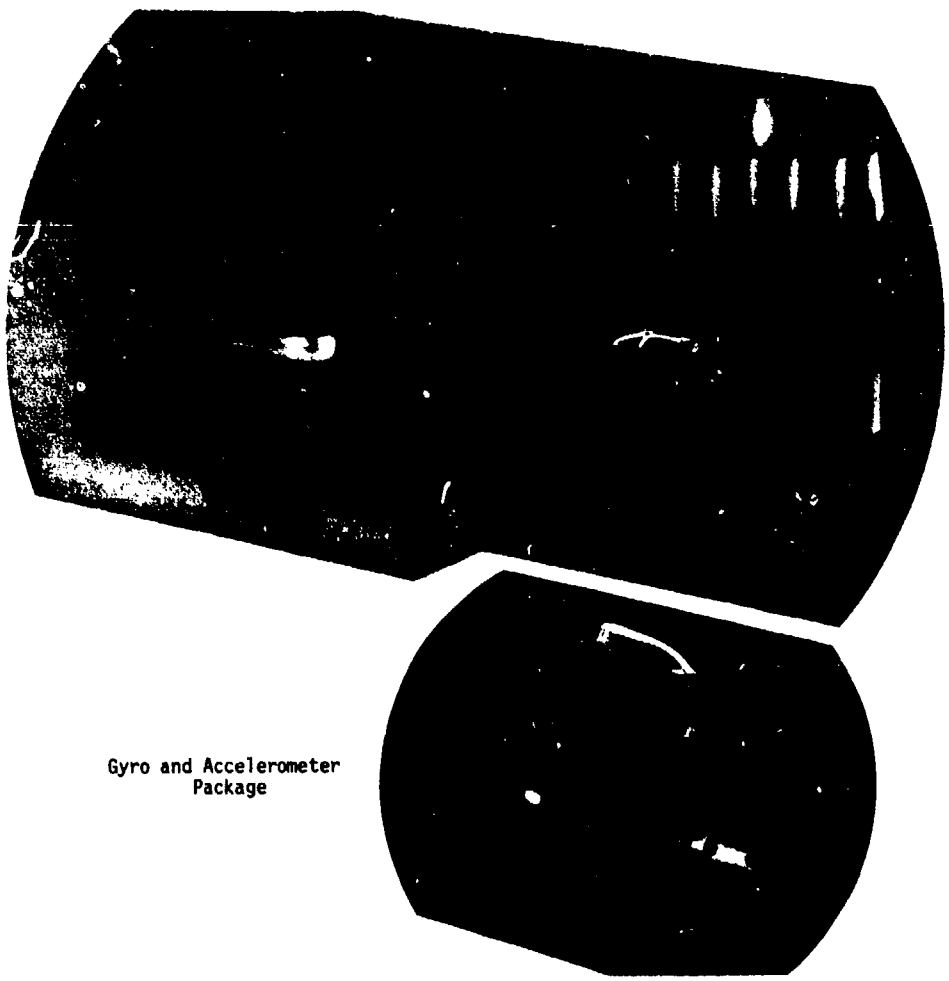

Fig. 6.5.1 Litton LTR-80 Strapdown Attitude and Heading Reference System

7. INERTIAL NAVIGATION

7.1 Introduction

We will start with a brief review of the historical development of inertial navigation, which in the western world primarily took place in Germany and the United States.

The beginning of inertial navigation can be put at the turn of the past century. In 1905 the first patent on a north-seeking gyrocompass was granted to Anschütz, Germany, and in 1913 a passenger ship was for the first time equipped with an Anschütz three-gyro compass. The theoretical outlines for this instrument were laid down by Schuler. His publication [7.1] of 1923 on the principle of the 84-minute tuning, which in technical circles is called the "Schuler tuning", is a frequently cited bibliographical reference in the field of inertial navigation.

The gyrocompass is in principle a damped gyropendulum with a horizontal spin axis and a separation between center of gravity and center of support of about 1 mm. In the geostationary state this is a north-seeking instrument, the input signals being the rotation of the earth and gravity. It has a settling time in the order of 4 hours.

The long settling time of the electromechanical gyrocompass precluded its use on the one-man-submarines developed in Germany towards the end of World War II. In case of emergency these vessels had to switch off all instruments, but the operator had to find true north again within 10 to 20 minutes after the emergency was over. This requirement led to an instrument with short alignment time, the so-called "miniature gyrocompass" (German: "Kleinkreiselkompaß"), for which a patent was granted to Gievers in 1943 [7.2]. It already contained the elements of a modern inertial navigation system, namely an air-supported accelerometer, an air-supported gyro and an electronic "Schuler loop" which could be switched to a shorter period during the alignment mode. The instrument, built by the "Kreiselgeräte GmbH" company, Germany, required only 12 minutes alignment time!

The gyrocompass is appropriate as a vehicle north reference only at low speeds - a velocity component in the north direction results in an error, the so-called "velocity error" of approximately 1 deg. per 10 kn at 45° latitude. Therefore this instrument has been widely used only in sea navigation, and not in aviation.

The idea of a gyrocompass which indicates true north, independent of the speed, goes back to Boykow and was pushed forward by Gievers, who developed the concept of an "over-ground compass" (German: "Obergrundkompaß") in 1940 and 1942 [7.2]. The latter corresponds in principle to an inertial navigation system with analog computer, which is still in use today!

The work on another idea of Boykow, the so-called "track-meter" (German: "Wegemesser" patent granted in 1935), became more widely known in the literature shortly after World War II. The work was carried out by the company "Siemens-Luftfahrtgerätewerk" and the name Reisch is closely connected with it [7.2 to 7.5]. Independent of Gievers, Reisch also developed the concept of an INS by the end of World War II.

After the war the lead in the development of this technology was taken over by the United States, especially Draper in the Massachusetts Institute of Technology. The first successful flight of an INS was carried out in 1953 between Massachusetts and California [7.4].

We will now discuss the role of an INS as a navigation and flight test reference system.

It will be shown in this chapter that an inertial platform indicates true north with highest accuracy only if it is at the same time also aligned most accurately to the vertical and if, in addition, the north-south and the east-west velocities as well as the geographical latitude are known. Therefore in an autonomous inertial navigational system a closed loop of information on

the north direction,
the vertical,
the ground velocities in north-south and east-west directions, and
the position in geographical latitude and longitude

is implemented.

As an inertial navigational system (INS) has this essential information for flight guidance available in the form of a closed loop, it is undoubtedly the most attractive among the various navigational systems.

For this reason inertial systems are not only used in civil and military aviation, in space flight, in sea navigation and for missiles, but also as measuring instruments in flight tests and in other cases where moving base measurements have to be carried out with respect to the vertical (e.g. geodesy).

The achievements in space flight are still in our minds. The high accuracy achieved in flight guidance was based on outputs from inertial systems which, together with outputs from other sensors, were combined into optimal information on attitude, velocity and position.

This draws attention to one aspect which, among others, should be one of the conclusions from this chapter and Chapter 8. Like all technical instruments an INS has its specific error sources, which are, however, of a different nature compared to those of radio navigation aids (e.g. VOR/DME, TACAN, Doppler radar, ILS). An optimum of information can be obtained by using information from different sources. In this respect mathematicians have provided technicians with a fairly efficient tool in the form of the Kalman filter algorithms [7.6 to 7.9]. The above-mentioned achievements in space flight have been obtained through the contribution of engineers in the form of hardware and of mathematicians in the form of software.

As an inertial system comprises information levels in a closed loop as mentioned above, i.e. north direction, direction of gravity, ground speed and position, aiding the system by means of external references on the velocity level (e.g. Doppler radar) or position level (e.g. VOR/DME), also increases the accuracy for the other levels. Therefore systems for high-accuracy simultaneous measurements of velocity and position or attitude and velocity, or even the three states together, are always centered around an INS. It is also advantageous to use an INS in those cases when the high-accuracy measurement of position is a main purpose of the test [7.10].

Chapter 8 notes that the best available hardware in the form of an INS, and the best software of the optimal filter algorithms are the basis for an accurate reference system during flight tests.

We will first discuss the functioning of a conventional platform inertial navigation system and its error dynamics. This is followed by a description of other inertial navigation system mechanizations, especially the strapdown systems. The commonality of the error dynamics of all inertial navigation systems is the topic of the next section. The chapter concludes with a review of the self-alignment method for platform and strapdown systems and an overview of existing inertial navigation systems.

7.2 Mechanization of an Inertial Navigation System with its Sensors Pointing North, East and Down - the North Indicating System (NIS)

7.2.1 The Platform and the Command Rates

Fig. 7.2.1 shows the diagram of an INS which we use to obtain an understanding of its functioning. The wind vane on the platform symbolizes that it is indicating true north. This is called a "north indicating system (NIS)".

The platform represented as a round disc in Fig. 7.2.1 is suspended in the vehicle (airplane, missile, ship) with three degrees of rotational freedom. For simplification this figure shows only the vertical axis. The rotational freedom as well as the other indicated signals are understood to have 2 or 3 orthogonal components; 2 components for horizontal acceleration, velocity and position, 3 components for the angular rate. It will be shown in Section 7.3.5 that the vertical velocity and position (altitude) cannot be obtained alone from inertial measurements.

On the platform one gyro can be seen - in place of the three gyros - which, with the control loop from gyro pickoff (P) via the electronics to the servo-motors at the gimbals, ensures the stabilization of the platform.

As we have seen in Section 5.3 stabilization means that the platform does not follow the vehicle's angular motion, but tends to maintain its position with regard to the inertial space which is "stored" in the gyros.

The rotation vector $\underline{\omega}^{ip}$ of the platform with respect to inertial space will be zero if no command rate $\underline{\omega}^{t}$ is applied to the gyro torquers and if the gyro drift vector $\underline{D}$ is zero. Otherwise the platform orientation changes according to Eq. (5.3.1):

$$\underline{\omega}^{ip} = \underline{\omega}^{t} + \underline{D}. \tag{7.2.1}$$

In case of the NIS, the platform always has to be aligned with its axes parallel to north, east and down, i.e. parallel to the axes of the "navigational coordinate frame" (subscript n), defined in Section 2.1 and Fig. 2.1. The total angular motion of the platform with respect to inertial space is

$$\underline{\omega}^{ip} = \underline{\omega}^{ie} + \underline{\omega}^{en} + \underline{\omega}^{np}, \tag{7.2.2}$$

with $\underline{\omega}^{ie}$ = earth rate and $\underline{\omega}^{en}$ = transport rate (s. Eqs. (2.20) to (2.24)). The angular rate $\underline{\omega}^{np}$ of the platform with respect to the navigational frame must vanish. The condition for meeting this requirement is

$$\underline{\omega}^{t} = \underline{\omega}^{ie} + \underline{\omega}^{en} - D = \underline{\omega}^{in} - D \tag{7.2.3}$$

i.e. the gyros on the platform have to be fed with a command rate equal to the sum of earth rate, transport rate and drift as indicated in Fig. 7.2.1.

If the flight is towards the west, $\underline{\omega}^{t}$ decreases with increasing velocity, vanishing completely when $\underline{\omega}^{en} = \underline{\omega}^{ie}$ (1200 km/h for $\varphi = 45^{o}$). The effect of scale factor errors of the torquers in the gyros thus decreases as westerly velocity increases.

Since with the NIS the geographic coordinate frame is stored in the platform, the aircraft attitude and azimuth can directly be measured at the gimbal axes (s. Fig. 7.2.1).

7.2.2 The Navigation Computer

The navigation computer receives the specific force vector $\underline{f}$ as input signal from the accelerometers on the platform and generates the command rate vector $\underline{\omega}^{t}$ for the gyros as feedback signal to the platform. According to Eq. (7.2.3) $\underline{\omega}^{t}$ depends on earth rate and transport rate, i.e. on groundspeed and position.

Eq. (2.29) is the basis for the integration of groundspeed and position from the accelerometer measurements $\underline{f}$. In the NIS it is evaluated in the navigational coordinate frame and reads:

$$\dot{\underline{v}}_n = \underline{f}_n - (2\underline{\omega}^{ie} + \underline{\omega}^{en})_n \times \underline{v}_n + \underline{g}_n \tag{7.2.4a}$$

or in components:

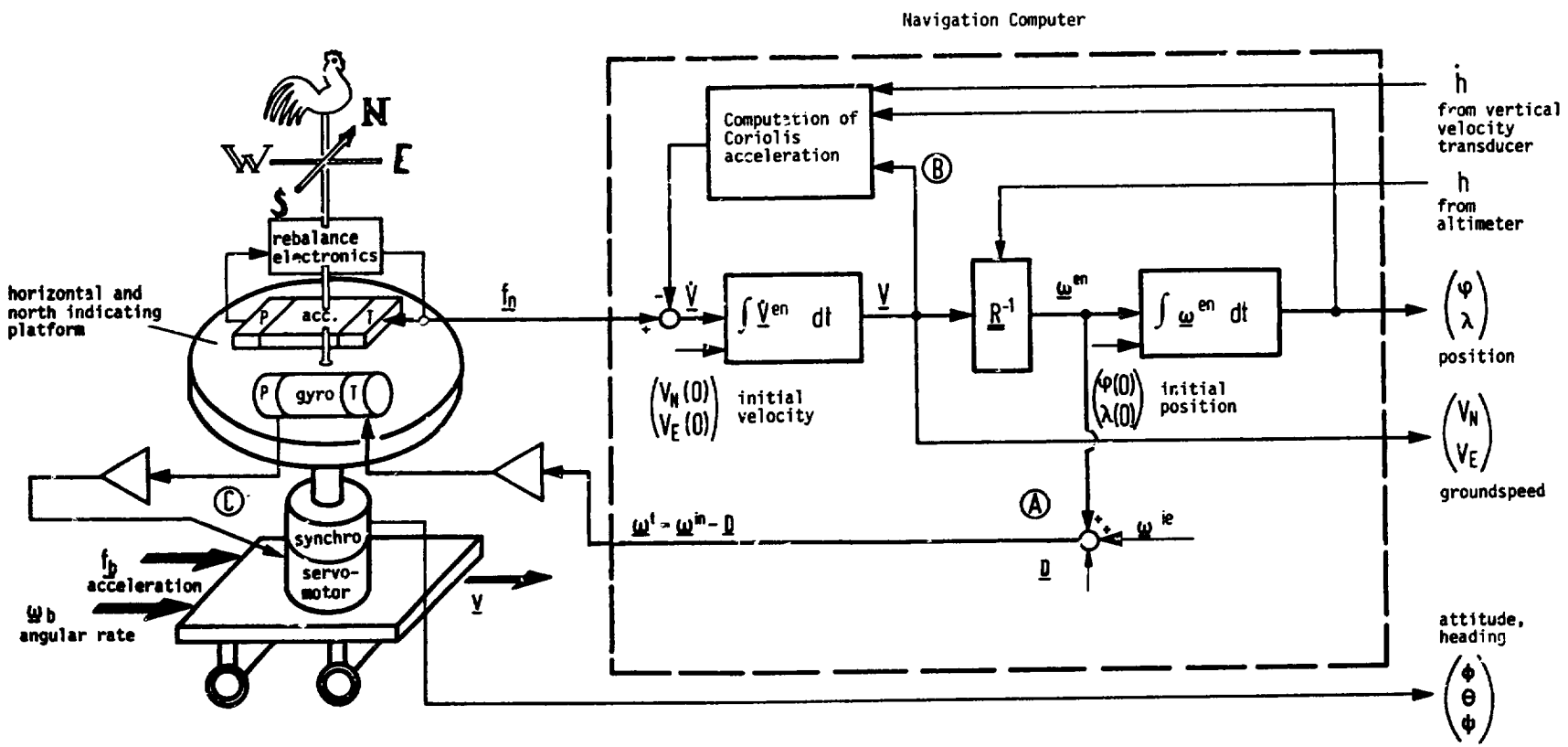

Effects of Feedback Loops:

Ⓐ + Ⓑ Foucault modulated Schuler oscillation, T ≈ 84 min

Ⓒ 24 hour oscillation

Fig. 7.2.1 Simplified Functional Diagram of an Inertial Navigation System (Platform System)

$$\begin{pmatrix} \dot{V}_N \\ \dot{V}_E \\ -\ddot{h} \end{pmatrix} = \begin{pmatrix} f_N \\ f_E \\ f_D \end{pmatrix} + \underbrace{\begin{pmatrix} -2V_E\ \Omega'\sin\varphi + \dot{h}\dot{\varphi} \\ 2V_N\ \Omega'\sin\varphi - 2\ \dot{h}\ \Omega'\cos\varphi \\ -2V_E\ \Omega'\cos\varphi - V_N\ \dot{\varphi} \end{pmatrix}}_{\text{these terms have to be compensated in the computer.}} + \begin{pmatrix} \xi g \\ -\eta g \\ g \end{pmatrix} \tag{7.2.4b}$$

The following relationships have to be observed (s. Section 2.1):

$$\Omega' = \Omega + \dot{\lambda}/2 \tag{7.2.5}$$

$$\Omega = \frac{2\pi}{86{,}164.1}\ \frac{\text{rad}}{\text{s}} = 7.292\ 115 \cdot 10^{-5}\ \frac{\text{rad}}{\text{s}} = 15.041\ 067\ \frac{\text{arc sec}}{\text{s}} \tag{7.2.6}$$

= earth rate magnitude

$$\dot{\lambda} = \frac{V_E}{(R_E+h)\cos\varphi} \quad = \text{rate of change of geographic longitude} \tag{7.2.7}$$

$$\dot{\Lambda} = \Omega + \dot{\lambda} \quad = \text{rate of change of celestial longitude} \tag{7.2.8}$$

$$\dot{\varphi} = \frac{V_N}{(R_N+h)} \quad = \text{rate of change of geographic latitude} \tag{7.2.9}$$

$$R_N = R[1 + e^2(\tfrac{3}{2}\sin^2\varphi - 1)] \quad = \text{radius of curvature in the meridian plane} \tag{7.2.10}$$

$$R_E = R[1 + \tfrac{1}{2}e^2\sin^2\varphi] \quad = \text{radius of curvature in the transverse plane of the ellipsoid} \tag{7.2.11}$$

$$R = 6{,}378.160\ \text{km} \quad = \text{semimajor axis of the ellipsoid} \tag{7.2.12}$$

$$e^2 = f(2 - f) \quad = \text{numerical eccentricity} \tag{7.2.13}$$

$$f = \frac{1}{298.247} \quad = \text{flattening of the ellipsoid.} \tag{7.2.14}$$

The components of the feedback signal $\underline{\omega}_n^t = \underline{\omega}_n^{ie} + \underline{\omega}_n^{en}$ from the computer to the gyros on the platform are:

$$\underline{\omega}_n^{ie} = \Omega \begin{pmatrix} \cos\varphi \\ 0 \\ -\sin\varphi \end{pmatrix} \quad = \text{earth rate vector} \tag{7.2.15}$$

$$\underline{\omega}_n^{en} = \begin{pmatrix} \dot{\lambda}\cos\varphi \\ -\dot{\varphi} \\ -\dot{\lambda}\sin\varphi \end{pmatrix} = \begin{pmatrix} V_E/(R_E + h) \\ -V_N/(R_N + h) \\ -[V_E/(R_E + h)]\tan\varphi \end{pmatrix} \quad = \text{transport rate vector.} \tag{7.2.16}$$

As already mentioned above, pure inertial navigation can only be carried out in the horizontal plane and Fig. 7.2.1 is only valid for this case. For the navigation in the vertical plane a setup according to Fig. 8.2.1 is recommended, in which the vertical acceleration and velocity are corrected by the difference of the inertial and barometric altitudes via the gains $1/T^2$ and $2/T$ with $T = 30$s. In this setup the Coriolis acceleration and the modelling of gravity as function of altitude and latitude (s. Eqs. (2.32) and (2.33)) can be neglected without severe effects on accuracy. For further details s. Sections 7.3.5 and 8.2.1.

The deflection of the vertical with components ξ and η (s. Fig. 2.4) is the point where geophysics affects inertial navigation (s. Eq.(7.2.4b). For the INM/h class INS it remains uncompensated in the computer and the navigation in the horizontal plane becomes independent of gravity. The modelling of gravity is therefore not required in the horizontal computer of Fig. 7.2.1. Yet gravity has an influence on the dynamics of the system, which will be dealt with in the next section.

In modern INS's the signal format of the accelerometer output $\underline{f}$ is a pulse train, where each pulse is a velocity increment of 0.5 mm/s, for instance. This is fed into an up/down counter, sampled at a rather low rate of approximately 5 Hz for the evaluation of Eq. (7.2.4).

7.3 The Error Dynamics of the North Indicating System

7.3.1 The Error Dynamics of a Single Axis Inertial Navigation System

The signal flow of Fig. 7.2.1 for the two horizontal channels from the accelerometers, via the integrators and the division by the representative radius of curvature of the earth, to the torquers of the gyros are called Schuler loops. They are the electronic implementation of a two-axes mathematical pendulum whose length is equal to the radius R of the earth, having the frequency and period of:

$$\omega^S = (g/R)^{1/2} = 1.235 \cdot 10^{-3}\ s^{-1} \qquad T^S = \frac{2\pi}{(g/R)^{1/2}} = 84.4\ \text{min}, \tag{7.3.1}$$

which are called "Schuler frequency" and "Schuler period".

A pendulum tuned to this frequency always indicates the vertical on a moving vehicle, once it has been aligned to it prior to the start. Also a gyrocompass, tuned to this frequency, will not be excited to disturbance oscillations by the horizontal acceleration. These rules were revealed by Schuler in his publication of 1923 [7.1]. The Schuler period also governs the motion of a satellite surrounding the earth or the motion of a stone traversing a hole drilled through the earth [7.11].

A conventional physical pendulum can hardly be Schuler-tuned. For a physical pendulum, the following relationship would have to be satisfied:

$$\frac{i^2}{r} = R \tag{7.3.2}$$

(i = radius of inertia = 2,5 m for r = pivot-to-center-of-mass separation = 1 μm).

In practice the Schuler tuning condition can only be met with the aid of a gyroscope - as in a gyrocompass or the INS. The simplified single axis INS shown in Fig. 7.3.1, may serve as a basis for the following discussion.

The platform (P) is mounted on a vehicle heading north and gyro-stabilized about its east-west axis (perpendicular to the plane of the drawing) by means of the servo loop from the gyro (G) signal generator (S) to the servomotor (SM) of the platform. The accelerometer (A) has its sensitive axis in the direction of motion and its output signal f is coupled to the torquer (T) of the gyro via the integrator and the amplifier $-\frac{1}{R}$. V_N is the velocity and ε_E the angular deviation with respect to the vertical.

The system's error dynamics are described by the linearized state space equations:

$$\begin{pmatrix} \dot{\varepsilon}_E \\ \delta\dot{V}_N \\ \delta\dot{\varphi} \\ \dot{D}_E \\ \dot{B}_N \end{pmatrix} = \begin{pmatrix} 0 & -1/R & 0 & 1 & 0 \\ g & 0 & 0 & 0 & 1 \\ 0 & 1/R & 0 & 0 & 0 \\ 0 & 0 & 0 & 0 & 0 \\ 0 & 0 & 0 & 0 & 0 \end{pmatrix} \cdot \begin{pmatrix} \varepsilon_E \\ \delta V_N \\ \delta\varphi \\ D_E \\ B_N \end{pmatrix} \tag{7.3.3a to e}$$

with D_E = gyro drift and B_N = accelerometer error assumed to be constant.

This equation is of the following form:

$$\underline{x} = \underline{F}\,\underline{x} + \underline{G}\,\underline{u} \tag{7.3.4}$$

with $\underline{G}\,\underline{u} = \underline{0}$. It has the following solution as shown in [7.7], Chapter 3

$$\underline{x}(t) = \underline{\Phi}(t, t_0)\,\underline{x}(t_0) + \int_{t_0}^{t} \underline{\Phi}(t,\tau)\,\underline{G}(\tau)\,\underline{u}(\tau)\,d\tau. \tag{7.3.5}$$

The transition matrix $\underline{\Phi}$ is the solution to the differential equation:

$$\frac{d}{dt}\underline{\Phi}(t,\tau) = \underline{F}\,\underline{\Phi}(t,\tau) \quad \text{with} \quad \underline{\Phi}(t,t) = \underline{I}. \tag{7.3.6}$$

For constant coefficients in $\underline{F}$ the transition matrix $\underline{\Phi}$ depends only on the time difference $t-\tau$, i.e.

$$\underline{\Phi}(t,\tau) = \underline{\Phi}(t-\tau). \tag{7.3.7}$$

If we set $\tau = t_0$ and $\Delta t = t - t_0$ in Equation (7.3.6), its solution will read:

$$\underline{\Phi}(\Delta t) = e^{\underline{F}\cdot\Delta t} \simeq \underline{I} + \underline{F}\cdot\Delta t + \frac{1}{2}\underline{F}^2\,\Delta t^2 + \ldots\ldots, \tag{7.3.8}$$

which is the basis for numerically solving Eq. (7.3.5). For a closed solution based on Laplace transformation we use the following relationship (s. [7.12], Chapter 7):

$$\hat{\underline{\Phi}}(s) = [s\underline{I} - \underline{F}]^{-1} \qquad \underline{\Phi}(t) = \mathcal{L}^{-1}\{[s\underline{I} - \underline{F}]^{-1}\}. \tag{7.3.9a,b}$$

So we obtain:

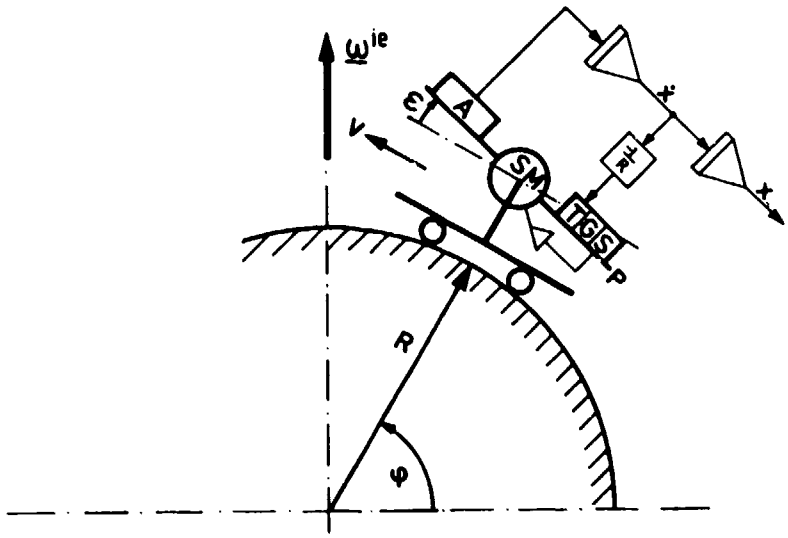

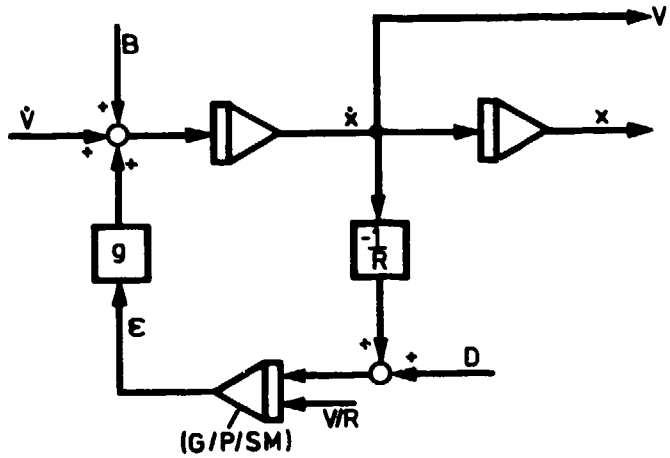

Fig. 7.3.1 Signal Flow Diagram and Block Diagram for a Single Axis Inertial Navigation System

$$\begin{pmatrix} \varepsilon_E(t) \\ \delta V_N(t) \\ \delta\varphi(t) \\ D_E \\ B_N \end{pmatrix} = \begin{pmatrix} \cos\omega^s\Delta t & -\frac{1}{R\omega^s}\sin\omega^s\Delta t & 0 & \frac{1}{\omega^s}\sin\omega^s\Delta t & -\frac{1}{g}(1-\cos\omega^s\Delta t) \\ R\omega^s\sin\omega^s\Delta t & \cos\omega^s\Delta t & 0 & R(1-\cos\omega^s\Delta t) & \frac{1}{\omega^s}\sin\omega^s\Delta t \\ 1-\cos\omega^s\Delta t & \frac{1}{R\omega^s}\sin\omega^s\Delta t & 1 & \Delta t-\frac{1}{\omega^s}\sin\omega^s\Delta t & \frac{1}{g}(1-\cos\omega^s\Delta t) \\ 0 & 0 & 0 & 1 & 0 \\ 0 & 0 & 0 & 0 & 1 \end{pmatrix} \begin{pmatrix} \varepsilon_E(t_o) \\ \delta V_N(t_o) \\ \delta\varphi(t_o) \\ D_E \\ B_N \end{pmatrix}$$

(7.3.10a to e)

The single axis INS errors due to east-west gyro drift D_E and north-south accelerometer bias B_N are plotted in Fig. 7.3.2.

All INS errors are bounded, except for the effect of gyro drift D_E on position error $\delta\varphi$, confirming the importance of these sensors on long-term system accuracy. The slope, i.e. the mean velocity error provides the "rule of thumb for inertial navigation":

$$\overline{\delta V} = R \cdot D \rightarrow \frac{1\text{km}}{\text{h}} \text{ navigational error per } \frac{1}{100}\,\frac{\text{degree}}{\text{h}} \text{ gyro drift.} \tag{7.3.11}$$

Physically this rule becomes understandable if we consider that the gyros keep stored in the platform the reference coordinate system for navigation, and that the gyro drift causes an analogous drifting of the reference coordinate system. (As a reminder: 1 degree of longitude = 111 km at the equator).

It is interesting to note that the effect of accelerometer bias B_N on INS errors is not as severe as one would expect. The misalignment error ε_E and the position error are alike. The mean error is limited to

$$\overline{\varepsilon_E} = \overline{\delta\varphi} = B_N/g. \tag{7.3.12}$$

This means that the accelerometer bias is compensated by a component of gravity due to the mean platform tilt.

For periods that are short with respect to the Schuler period, one can introduce in Eqs. (7.3.10) the approximations:

$$\sin\omega^s t \approx \omega^s t - \frac{1}{6}(\omega^s t)^3 \tag{7.3.13}$$

$$\cos\omega^s t \approx 1 - \frac{1}{2}(\omega^s t)^2. \tag{7.3.14}$$

This leads to the curves marked in dotted lines in Figure 7.3.2, which for a longer time period are al so valid for the set-up of Figure 7.3.1 without Schuler loop or for inertial navigation on a flat earth. The respective approximations read as follows:

$$\varepsilon_E(t) \approx \varepsilon_E(o) + D_E \cdot t,$$

$$\delta V_N(t) \approx (g\,\varepsilon_E(o) + B_N)\,t + D_E\,\frac{g}{2}\,t^2$$

$$\delta\varphi(t) \approx \delta\varphi(o) + (\varepsilon_E(o) + \frac{B_N}{g}\frac{g}{R})\,\frac{t^2}{2} + D_E\,\frac{g}{R}\,\frac{t^3}{6}\,. \tag{7.3.15a,b,c}$$

In summary we may conclude that inertial navigation would not be possible for extended periods if the earth were flat.

7.3.2 The Error Dynamics in the Horizontal Channels of a Three-Axis North Indicating System (NIS) for a Short Period of Time

Fig. 7.3.3 shows in simplified form the block diagrams of the error models for a three-axis NIS in the lower half and the barometric aided altitude channel in the upper half. On the left side the sensor errors are listed, on the right side the system errors, and in the middle the error models of the NIS and altitude channel dynamics are represented.

As compared to the complete error model of an NIS [7.13], which will be discussed later (s. Fig. 7.3.4), the so-called 24-hour oscillation caused by the coupling of the platform angles $\varepsilon_{N,E,D}$ via the components of the earth rate plus the transport rate $\dot{\lambda}$ (with $\dot{\lambda} = \Omega + \dot{\lambda}$) or $\dot{\varphi}$, respectively, has been cut down to the coupling of the azimuth misalignment ε_D into the rotation about the east-west axis ε_E. For the purpose of discussion this is justified because on the one hand ε_D is in general one order of magnitude higher than the horizontal misalignment $\varepsilon_{N,E}$. On the other hand for flight periods of up to 2 hours we can assume with good accuracy: $\sin\dot{\lambda}t = \dot{\lambda}t$ and $\cos\dot{\lambda}t = 1$ (error in this approximation < 10 %).

For an estimation of the errors in the NIS channels we assume that the slewing of the vertical gyro as well as the compensation of the Coriolis acceleration can occur without errors and there remain two Schuler loops as in Fig. 7.3.1. In addition to these Schuler loops Fig. 7.3.3 shows the influence of the azimuth error ε_D as well as of the vertical gyro drift D_D.

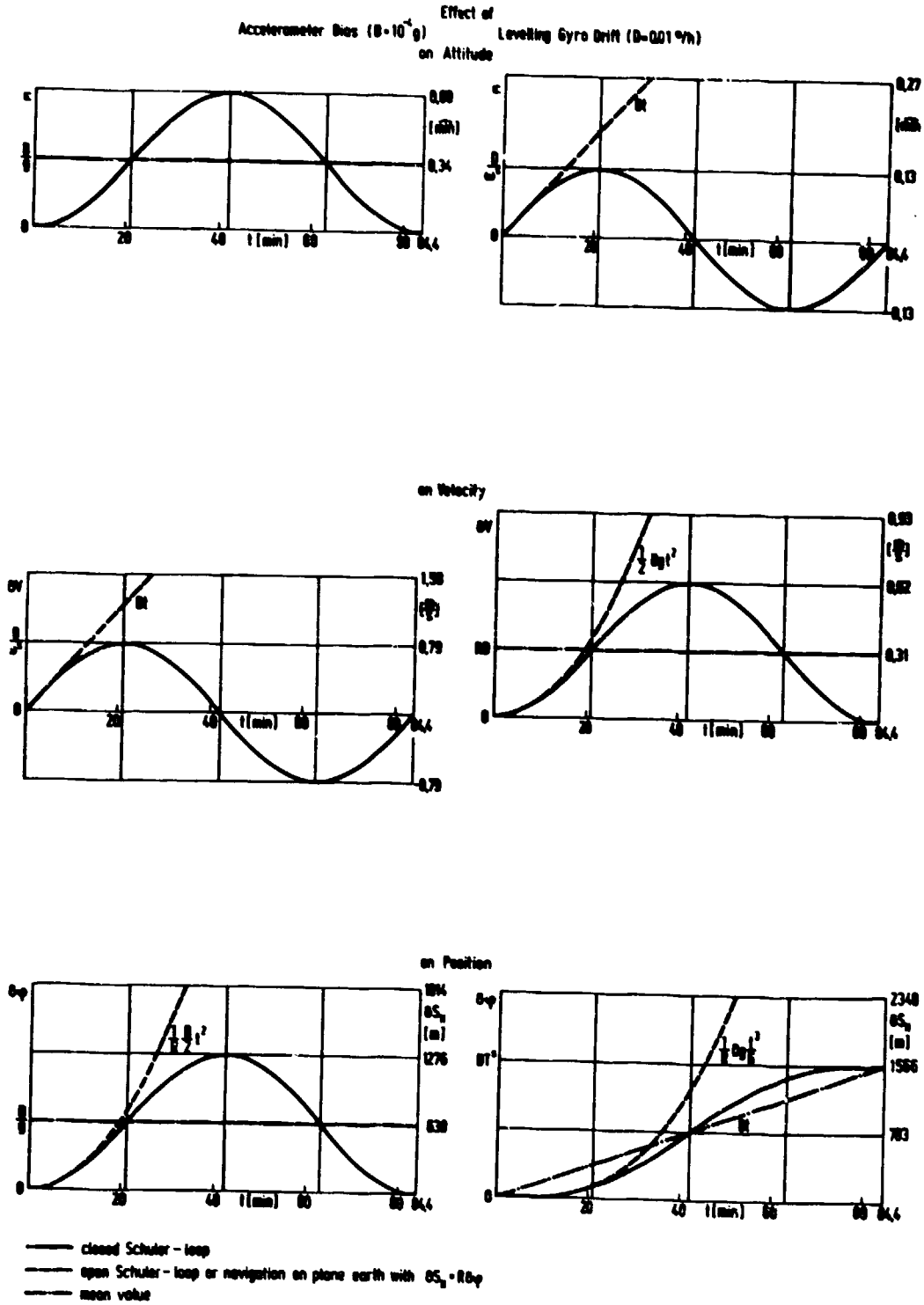

Fig. 7.3.2 Errors of a Single-Axis Inertial Navigation System

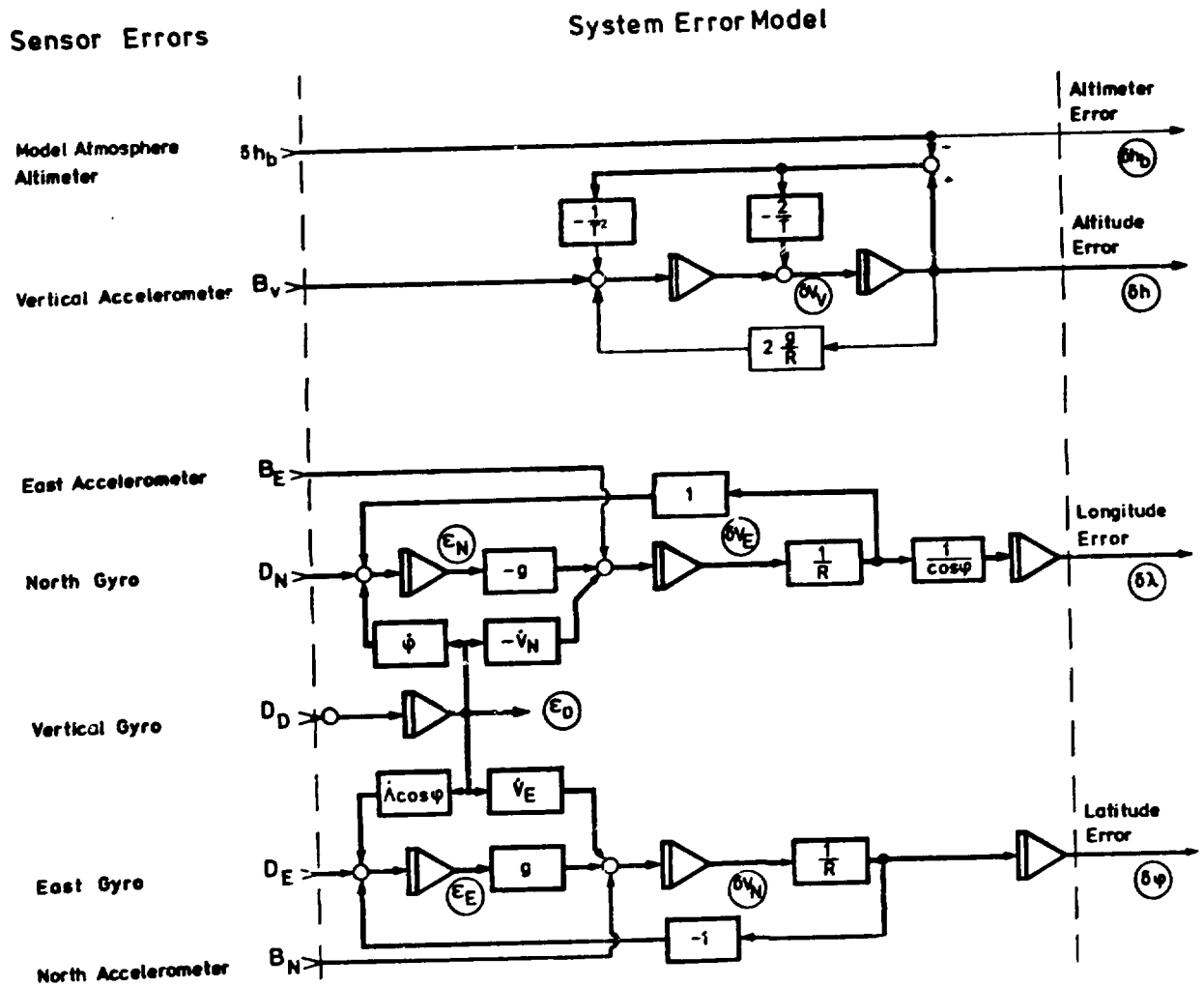

Fig. 7.3.3 Simplified Block Diagram for the Error Model of a North Indicating INS

On one hand the azimuth deviation ε_D causes an acceleration error in the horizontal channel which is orthogonal to the respective horizontal acceleration $\dot{V}_{N,E}$ of the vehicle. We assume that the acceleration of the vehicle from start to the constant cruise velocity is short compared to the Schuler period, which means that this cross-track acceleration error is integrated in an initial velocity error:

$$\delta V_N'(o) = \delta V_N(o) + \varepsilon_D(o)\, V_E \qquad \delta V_E'(o) = \delta V_E(o) - \varepsilon_D V_N. \tag{7.3.16a,b}$$

On the other hand, the azimuth error has an effect comparable to a north-south or east-west gyro drift through the coupling of the rates $\dot{\varphi}$ and $\dot{\lambda}\cos\varphi$ into the respective orthogonal platform axes:

$$D_N' = D_N - (\varepsilon_D + D_D t)\dot{\varphi} \qquad D_E' = D_E + (\varepsilon_D + D_D\, t)\dot{\lambda}\cos\varphi. \tag{7.3.17a,b}$$

The relationships compiled on the following page (Eqs. (7.3.18 a to g)) were obtained in a way similar to the one for the single axis inertial navigation system in Section 7.3.1; the state space equations of the two uncoupled horizontal channels were supplemented by Eqs. (7.3.16 and 17) and $\cos\varphi$ was assumed to be constant.

Of the results we want to discuss only the position equations and cast a glance at the main error sources. The initial position error ($\delta\varphi(o)$ and $\delta\lambda(o)$) can be assumed to be zero, as on any major aerodrome the geographic longitude and latitude are indicated at the aircraft parking positions. The initial error velocity can also be neglected; if the switching of the NIS into the navigational phase takes place on a stationary aircraft, V(o) is then accurately known.

In comparison to Eq. (7.3.10) essentially only the effects of the azimuth alignment error $\varepsilon_D(o)$ and of the vertical gyro drift D_D have been added. It is interesting to note that the deviation with time of the "cross-track-error" is equal to that of a common dead reckoning navigational system in the east-west channel ($\delta\lambda(t)\cos\varphi = -\varepsilon_D(o)\ \Delta\varphi$). In the north-south channel this is true only for short times when $\delta\varphi(t) = \varepsilon_D[\Delta\Lambda - (\Omega/\omega^S)\sin\omega^S\Delta t]\cos\varphi \approx \varepsilon_D\ \Delta\lambda\ \cos\varphi$. After approximately 10 minutes, earth rate coupling becomes effective.

It is this difference in the error characteristics that allows in-flight gyrocompassing of a misaligned NIS based on a Doppler radar for measuring the body-fixed ground speed components and the misaligned platform as heading reference. We will come back to this topic in Section 8.2.1.2.

If we start from the assumption that before the start the platform has aligned itself in the north direction and in the horizontal plane as a result of a gyrocompassing procedure, we shall under ideal conditions have the following relationships between the alignment and sensor errors (s. Eqs. (7.5.2a to c)):

$$\varepsilon_N(o) \approx B_E/g \quad (\approx 0.1 \text{ m rad} = 20 \text{ arc sec}) \qquad \varepsilon_E(o) \approx -B_N/g \ (\approx 0.1 \text{ m rad} = 20 \text{ arc sec})$$

$$\varepsilon_D(o) \approx -D_E/(\Omega\cos\varphi) \quad (\approx 1 \text{ m rad} = 3{,}4 \text{ arc min}), \tag{7.3.19a,b,c}$$

the numbers being valid for $B = 10^{-4}$ g and $D_E = 1/100\ ^{o}/h$ as well as $\varphi = 45^{o}$. Eqs. (7.3.18f,g) reduce in this case to:

$$\delta\varphi(t) \approx \varepsilon_D(o)\frac{S_E}{R} + D_D\ \{\Delta\Lambda\frac{t}{2} - \frac{\dot{\lambda}\cos\varphi}{(\omega^S)^2}(1 - \cos\omega^S t)\}$$

$$\delta\lambda(t)\cos\varphi \approx -\varepsilon_D(o)\frac{S_N}{R} - D_N(t - \frac{\sin\omega^S t}{\omega^S}), \tag{7.3.20a,b}$$

$S_{N,E}$ being the distance flown. For periods that are short in comparison with the Schuler period (6 min approximately for a 10 % error) these relationships will reduce to:

$$\delta\varphi(t) \approx \varepsilon_D(o)\frac{S_E}{R}$$

$$\delta\lambda(t)\cos\ \ \approx -\varepsilon_D(o)\frac{S_N}{R} \tag{7.3.21a,b}$$

which means, that after fully completing self-alignment, the navigation error of the NIS under ideal conditions initially consists exclusively of the cross-track error, and is identical with that of a normal dead reckoning navigational system with ideal velocity indicators!

7.3.3 The 1σ-Errors in the Horizontal Channels of a Three-Axis North Indicating System (NIS) for a long Period of Time

Fig. 7.3.4 shows without simplifications the block diagram for the erroneous signal flow in an NIS. The lower feedback for slewing the vertical platform axis is proportional to $\tan\varphi$, indicating that inertial navigation with this kind of mechanization is impossible for polar flights. In the discussion of this section we will stay in the allowable latitude ranges (for the Ferranti FE 500 system $\varphi < \pm 88.5^{o}$).

For flight times above 6 minutes, the drifts of the horizontal gyros become significant. The Coriolis acceleration errors and the earth rate couplings become significant after approximately 2 hours.

If the NIS is standing on the ground, the dynamics of its errors for long periods are described by the following frequencies (s. [7.13], Eq. (7-49)):

$$\omega_{1,2} = \omega^S \pm \Omega\sin\varphi \quad \text{see Fig. 7.2.1 and 7.3.4 feedback } \text{Ⓐ} + \text{Ⓑ}$$

$$\omega_3 = \Omega \quad \text{see Fig. 7.2.1 and 7.3.4 feedback } \text{Ⓒ}. \tag{7.3.22a,b}$$

	$\varepsilon_N(t_o)$	$\varepsilon_E(t_o)$	$\varepsilon_D(t_o)$	$\delta V_N(t_o)$	$\delta V_E(t_o)$	$\delta\varphi(t_o)$	$\delta\lambda(t_o)$	B_N	B_E	D_N	D_E	D_D
$\varepsilon_N(t) =$	$\cos\omega^s\Delta t$	$+0$	$+0$	$+0$	$+\frac{\sin\omega^s\Delta t}{R\omega^s}$	$+0$	$+0$	$+0$	$\frac{-\cos\omega^s\Delta t}{g}$	$+\frac{\sin\omega^s\Delta t}{\omega^s}$	-0	$-\frac{\dot\varphi}{(\omega^s)^2}(1-\cos\omega^s\Delta t)$
$\varepsilon_E(t) =$	0	$+\cos\omega^s\Delta t$	$+\frac{\Omega}{\omega^s}\cos\varphi\sin\omega^s\Delta t$	$\frac{\sin\omega^s\Delta t}{R\omega^s}$	$+0$	$+0$	$+0$	$-\frac{(1-\cos\omega^s\Delta t)}{g}$	$+0$	$+0$	$+\frac{\sin\omega^s\Delta t}{\omega^s}$	$+\frac{\dot\Lambda\cos\varphi}{(\omega^s)^2}(1-\cos\omega^s\Delta t)$
$\varepsilon_D(t) =$	0	$+0$	$+1$	$+0$	$+0$	$+0$	$+0$	$+0$	$+0$	$+0$	$+0$	$+\Delta t$
$\delta V_N(t) =$	0	$+R\omega^s\sin\omega^s\Delta t$	$+R[\dot\Lambda-\Omega\cos\omega^s\Delta t]\cos\varphi$	$+\cos\omega^s\Delta t$	$+0$	$+0$	$+0$	$+\frac{\sin\omega^s\Delta t}{\omega^s}$	$+0$	$+0$	$+R(1-\cos\omega^s\Delta t)$	$+R\dot\Lambda\cos\varphi(\Delta t-\frac{\sin\omega^s\Delta t}{\omega^s})$
$\delta V_E(t) =$	$-R\omega^s\sin\omega^s\Delta t$	$+0$	$-R\dot\varphi$	$+0$	$+\cos\omega^s\Delta t$	$+0$	$+0$	$+0$	$+\frac{\sin\omega^s\Delta t}{\omega^s}$	$-R(1-\cos\omega^s\Delta t)$	$+0$	$-R\dot\varphi(\Delta t-\frac{\sin\omega^s\Delta t}{\omega^s})$
$\delta\varphi(t) =$	0	$+(1-\cos\omega^s\Delta t)$	$+(\Delta\Lambda-\frac{\Omega}{\omega^s}\sin\omega^s\Delta t)\cos\varphi$	$+\frac{\sin\omega^s\Delta t}{R\omega^s}$	$+0$	$+1$	$+0$	$+\frac{(1-\cos\omega^s\Delta t)}{g}$	$+0$	$+0$	$+\Delta t-\frac{\sin\omega^s\Delta t}{\omega^s}$	$+\Delta\Lambda\cos\varphi\frac{\Delta t}{2}-\frac{\dot\Lambda\cos\varphi}{(\omega^s)^2}(1-\cos\omega^s\Delta t)$
$\delta\lambda(t)\cos\varphi =$	$-(1-\cos\omega^s\Delta t)$	$+0$	$-\Delta\varphi$	$+0$	$+\frac{\sin\omega^s\Delta t}{R\omega^s}$	$+0$	$+\cos\varphi$	$+0$	$+\frac{1-\cos\omega^s\Delta t}{g}$	$-\Delta t+\frac{\sin\omega^s\Delta t}{\omega^s}$	$+0$	$-\Delta\varphi\frac{\Delta t}{2}+\frac{\dot\varphi}{(\omega^s)^2}(1-\cos\omega^s\Delta t)$

(7.3.18a to g)

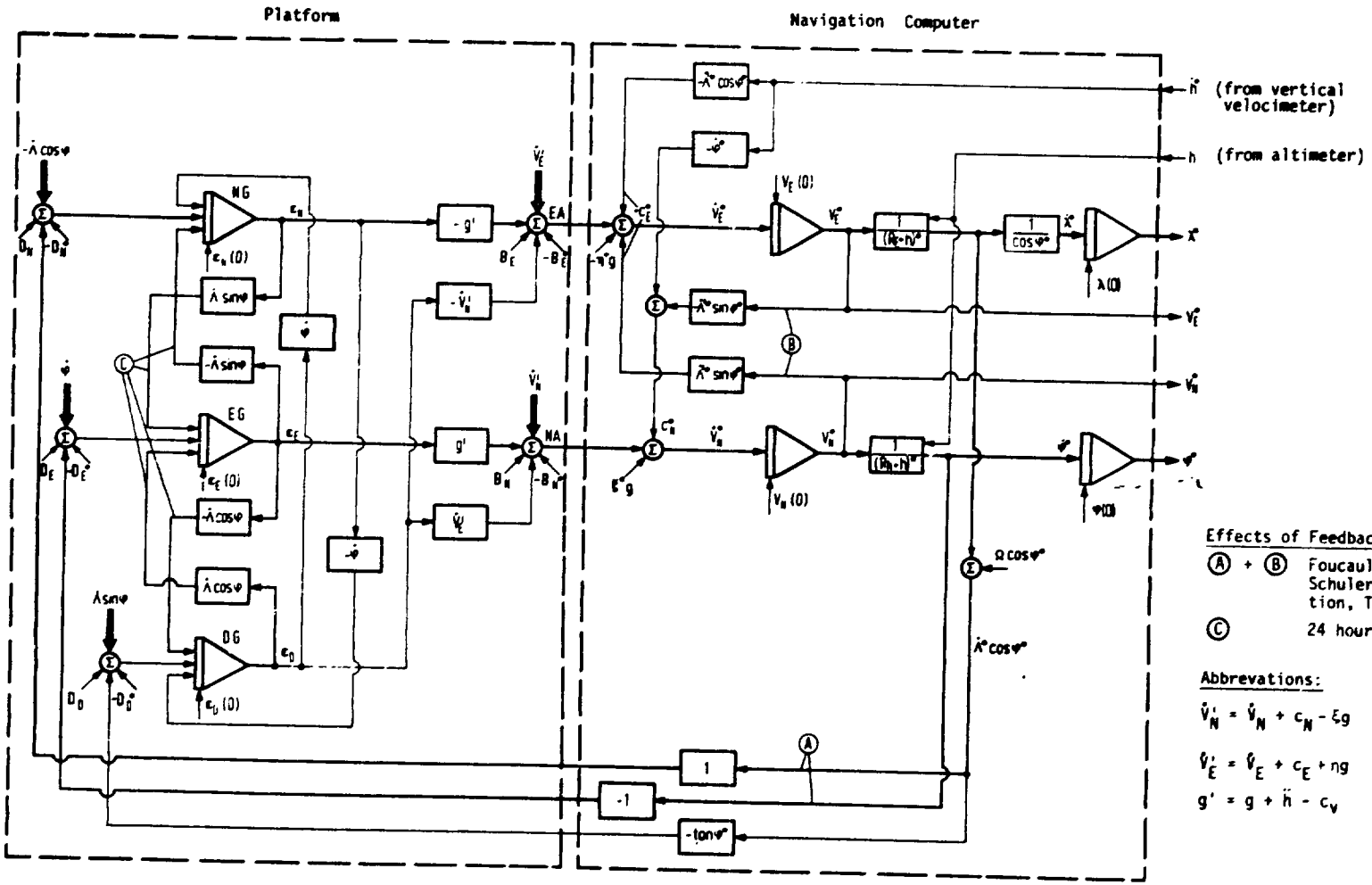

Effects of Feedback Loops:

Ⓐ + Ⓑ Foucault modulated Schuler oscillation, T ≈ 84 min

Ⓒ 24 hour oscillation

Abbrevations:

$\dot{V}_N' = \dot{V}_N + c_N - \xi g$

$\dot{V}_E' = \dot{V}_E + c_E + \eta g$

$g' = g + \ddot{h} - c_V$

Fig. 7.3.4 Block Diagram for the Erroneous Signal Flow in an Inertial Navigation System with North Indicating Platform

* for computed or measured value

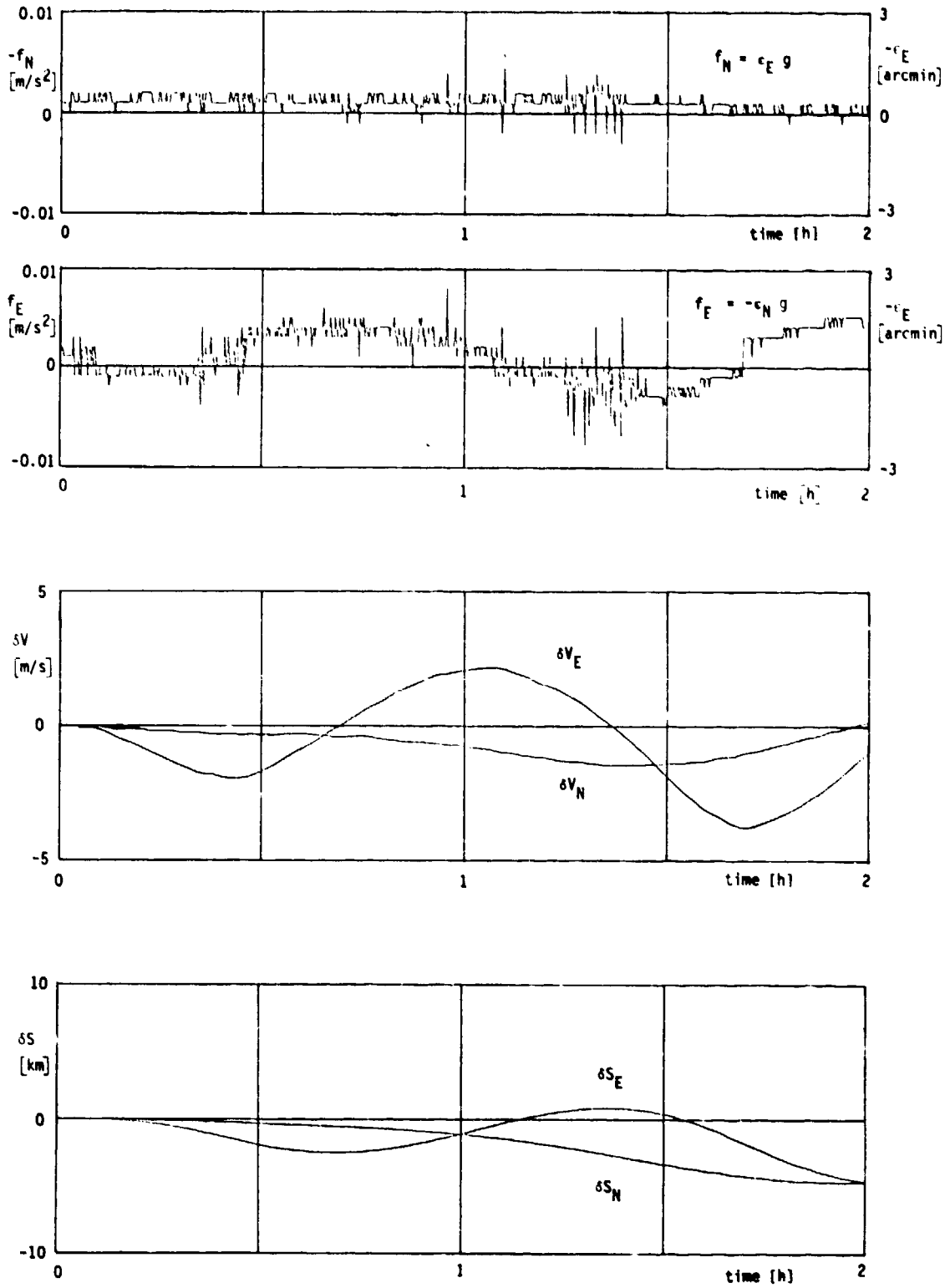

Fig. 7.3.5 Errors in Acceleration, Velocity and Position of a Stationary Litton LN-3A INS

The first two frequencies characterize the Foucault-modulated Schuler oscillation, i.e. the oscillation of a freely swinging pendulum of length R on the rotating earth. The oscillation plane of this pendulum stays, as it is well known, inertially fixed, i.e. it rotates with the negative vertical component of the earth rate $\Omega \sin\varphi$ with respect to the earth.

The third frequency characterizes the 24-hour oscillation, i.e. the motion as indicated in Fig. 5.3.2, which is carried out by a misaligned gyro-stabilized platform without a Schuler loop on the rotating earth.

The linearized error equations of the NIS including the altitude channel aided by a barometric altimeter are summarized on the next page (Eqs. (7.3.23 to 7.3.29)). The error dynamics of the altitude channel will be discussed in Sections 7.3.5 and 8.2.1.1.

The theory discussed above is confirmed in the measurements of a modified uncalibrated LN-3 system taken over 2 hours in the laboratory of DFVLR and plotted in Fig. 7.3.5. These plots show the acceleration, velocity and position errors: large Schuler oscillations as well as the initial part of a 24-hour oscillation are excited by the bias errors of the uncalibrated gyros and accelerometers.

The LN-3 (s. Fig. 7.4.5) system was modified in the following way: the Schuler loop was not closed via the analog computer which is part of the original system, but via a Honeywell DDP 527 computer. In doing so the accelerometer signals were tapped and converted into digital format by a 16 bit analog to digital converter (DFVLR design) and the platform slewing rate was again converted from digital to analog format by a digital to analog converter.

The NIS in-flight system errors differ from the stationary system errors by the manoeuvre-dependent cross-track velocity errors ($\delta V_{N,E} = \pm \varepsilon_D V_{E,N}$) and position errors ($\delta S_{N,E} = \pm \varepsilon_D S_{E,N}$, s. Eqs. (7.3.21a,b) and (7.3.18 d to g)). They are superposed to the Schuler oscillations shown in Fig. 7.3.5.

We will now come back to the discussion and evaluation of the state space error equations (7.3.23) of the NIS, which are of the type (7.3.4) where for a system in flight the matrix $\underline{F}$ has time varying coefficients. A general solution of this set of equations cannot be obtained without considerable simplifications. In most references the horizontal acceleration is put to zero, but in this case the cross-track error of the system is not taken into account properly.

In order to be able to judge the NIS accuracy over more than 2 hours flight time, the Eqs. (7.3.23) are solved on the digital computer following the course of Eqs. (7.3.4 to 8) and under the assumption that the coefficients of $\underline{F}$ do not change during the computation cycle increment Δt.

The NIS errors resulting from this numerical integration are valid for one set of initial conditions, sensor errors and one aircraft flight profile only. Even if we assume in a simulation that the flight profile does not change from day to day we may still not predict exactly the performance of the system since the sensor errors and the initial misalignment angles of the platform will change.

The specification of sensors on the manufacturer's data sheet always defines an accuracy class which is obtained from the test results of a great number of different samples. Plotting a histogram of the gyro test results after bias compensation, the test engineer will certainly obtain a distribution similar to Fig. 7.3.6a, which can be approximated by a Gaussian-distribution with zero mean shown in Fig. 7.3.6b. The same will hold for the accelerometers and for the system alignment errors which are related to the sensor errors as we have seen above (s. Eqs. (7.3.19a to c)).

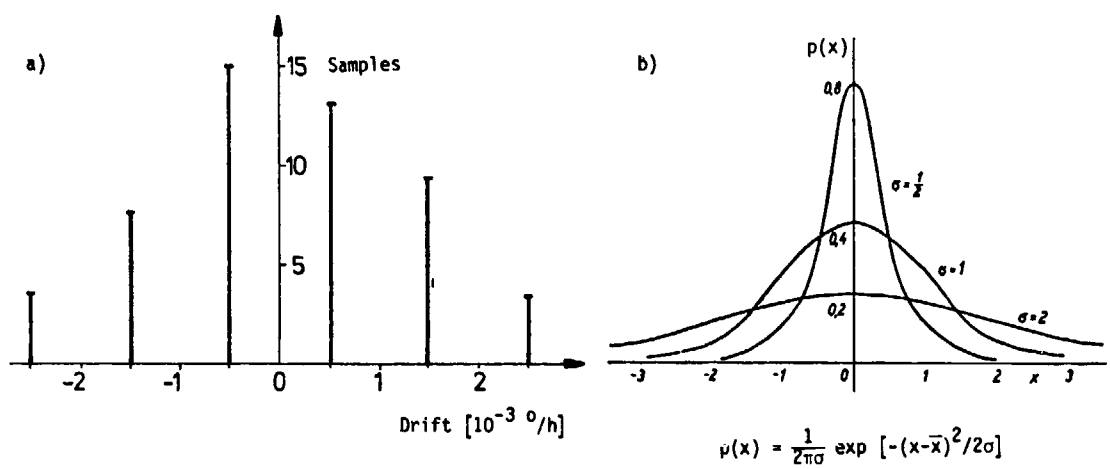

Fig. 7.3.6 Histogram for the Drift Measurement of a Certain Type of Gyro (a) and Approximation by Gaussian Probability Density Function with Zero Mean (b)

Based on these assumptions a more general statement can be obtained for the accuracy of systems of one class, all in the same dynamic environment, by applying the error covariance propagation equation [7.7]:

$$\underline{P}(t) = \underline{\Phi}(t, t_0)\, \underline{P}(t_0)\, \underline{\Phi}^T(t, t_0) + \underline{Q}(\Delta t), \qquad (7.3.30)$$

where the first term on the right hand side describes the covariance propagation within the time increment $\Delta t = t - t_0$ and the second term the covariance increase due to white noise. This relationship is also

$$
\begin{pmatrix} \dot{\varepsilon}_N \\ \dot{\varepsilon}_E \\ \dot{\varepsilon}_D \\ \delta\dot{V}_N \\ \delta\dot{V}_E \\ \delta\dot{\varphi} \\ \delta\dot{\lambda} \end{pmatrix}
=
\left(\begin{array}{ccc|cc|cc}
0 & -\dot{\lambda}\sin\varphi & \dot{\varphi} & 0 & 1/R & -\Omega\sin\varphi & 0 \\
\dot{\lambda}\sin\varphi & 0 & \dot{\lambda}\cos\varphi & -1/R & 0 & 0 & 0 \\
-\dot{\varphi} & -\dot{\lambda}\cos\varphi & 0 & 0 & -\tan\varphi/R & -(\Omega\cos\varphi + \dot{\lambda}/\cos\varphi) & 0 \\
\hline
0 & g' & \dot{V}_E' & -\dot{h}/R & -2\dot{\lambda}\sin\varphi & -V_E(2\Omega\cos\varphi + \dot{\lambda}/\cos\varphi) & 0 \\
-g' & 0 & -\dot{V}_N & 2\Omega'\sin\varphi & (V_N\tan\varphi - \dot{h})/R & V_N(2\Omega\cos\varphi + \dot{\lambda}/\cos\varphi) + 2\dot{h}\Omega\sin\varphi & 0 \\
\hline
0 & 0 & 0 & 1/R & 0 & 0 & 0 \\
0 & 0 & 0 & 0 & 1/(R\cos\varphi) & \dot{\lambda}\tan\varphi & 0
\end{array}\right)
\times
\begin{pmatrix} \varepsilon_N \\ \varepsilon_E \\ \varepsilon_D \\ \delta V_N \\ \delta V_E \\ \delta\varphi \\ \delta\lambda \end{pmatrix}
+
\begin{pmatrix} D_N - \dot{\lambda}\cos\varphi\ \delta h/R \\ D_E + \dot{\varphi}\ \delta h/R \\ D_D + \dot{\lambda}\sin\varphi\ \delta h/R \\ B_N - \dot{\varphi}\ \delta\dot{h} + (V_E\dot{\lambda}\sin\varphi + \dot{h}\dot{\varphi})\ \delta h/R \\ B_E - 2\Omega'\cos\varphi\,\delta\dot{h} - 2\dot{\lambda}(V_N\sin\varphi - \dot{h}\cos\varphi)\delta h/R \\ -\dot{\varphi}\ \delta h/R \\ -\dot{\lambda}\ \delta h/R \end{pmatrix}
$$

(7.3.23a to g)

The abbrevations used are:

(7.3.24a to d)

$\dot{\varphi} = V_N/R \qquad \dot{\lambda} = \Omega + \dot{\lambda} \qquad \dot{V}_N' = \dot{V}_N + 2\,\Omega' V_E \sin\varphi + \dot{h}\,\dot{\varphi} \qquad g' = g + \ddot{h} - 2\Omega' V_E \cos\varphi - \dot{\varphi} V_N$

(7.3.25a to d)

$\dot{\lambda} = V_E/(R\cos\varphi) \qquad \Omega' = \Omega + \dot{\lambda}/2 \qquad \dot{V}_E' = \dot{V}_E - 2\,\Omega'(V_N \sin\varphi - \dot{h}\cos\varphi) \qquad R = R_o + h$

The error-generating terms on the right-hand side show that an altitude measurement error δh causes an erroneous platform slewing and an erroneous Coriolis computation corresponding to a gyro drift D and accelerometer error B. For $\dot{\lambda} = \dot{\varphi} = \Omega$ or $V = 1000$ km/h at $\varphi = 45^o$ we obtain:

(7.3.26a,b)

$D \simeq 3 \cdot 10^{-3}\ {}^o/h$ per ($\delta h = 1000$ m); $\qquad B \simeq 3 \cdot 10^{-7}$ g per ($\delta h = 1000$ m).

The corresponding maximum accelerometer error B due to an error $\delta\dot{h}$ in the measurement of the vertical velocity is:

(7.3.27)

$B \simeq 3 \cdot 10^{-3}$ g per ($\delta\dot{h} = 10$ m/s).

This is a later proof for the acceptability of separating the horizontal and vertical channels in Fig. 7.3.3 and 7.3.4.
The state space equations for the barometrically aided vertical channel in Fig. 7.3.3 are:

$$
\begin{pmatrix} \delta\ddot{h}_1 \\ \delta\dot{h} \end{pmatrix}
=
\begin{pmatrix} 0 & 2\,Kg/R - \underline{1/T^2} \\ \underline{1} & \underline{-2/T} \end{pmatrix}
\begin{pmatrix} \delta\dot{h}_1 \\ \delta h \end{pmatrix}
+
\begin{pmatrix} B_v + 2h\,(K-1)\,g_o/R + \delta h_b/T^2 \\ 2\delta h_b/T \end{pmatrix},
$$

(7.3.28a,b)

whereby δh_1 is the output of the first integrator, B_v the vertical accelerometer error and δh_b the barometric altimeter error.

Put $K = 1$ if $g(h) = g_o/(1+h/R)^2$ is programmed in the computer and $K = 0$ if $g(h) = g(0)$. The latter corresponds to an accelerometer error of:

(7.3.29)

$\frac{B_v}{g} = \frac{-2h}{R} = -3 \cdot 10^{-4}$ per ($h = 1000$ m).

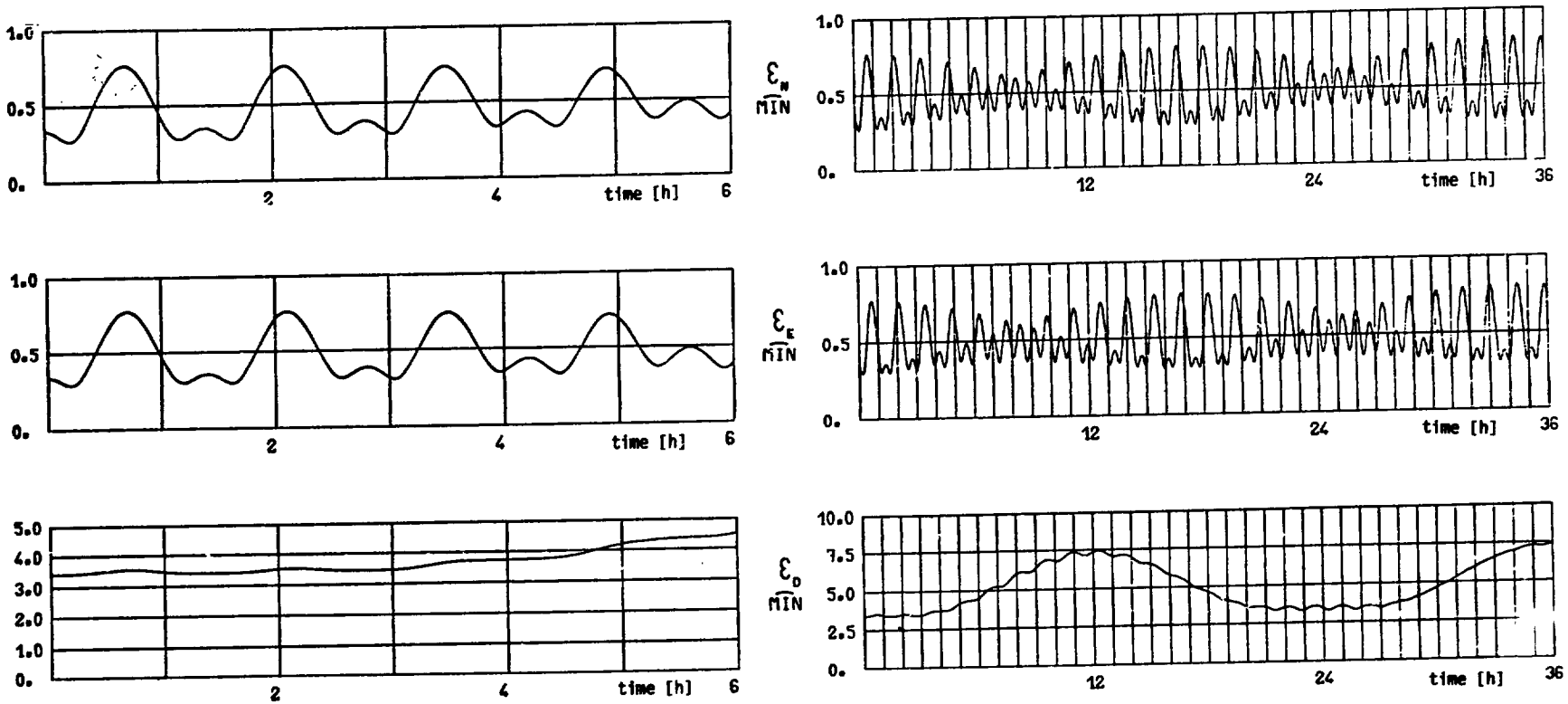

Velocity: $V = 0$

Initial misalignment angles: $\varepsilon_N = \varepsilon_E = 0.1$ mrad = 0.34 arc min; $\varepsilon_D = 1$ mrad = 3.4 arc min

Gyro drift: $D_N = D_E = D_D = 0.01\ ^{o}/h$

Accelerometer bias: $B_N = B_E = 0.0001$ g

Fig. 7.3.7a 1σ-Horizontal Misalignment and Heading Error of an Inertial Navigation System with North Indicating Platform

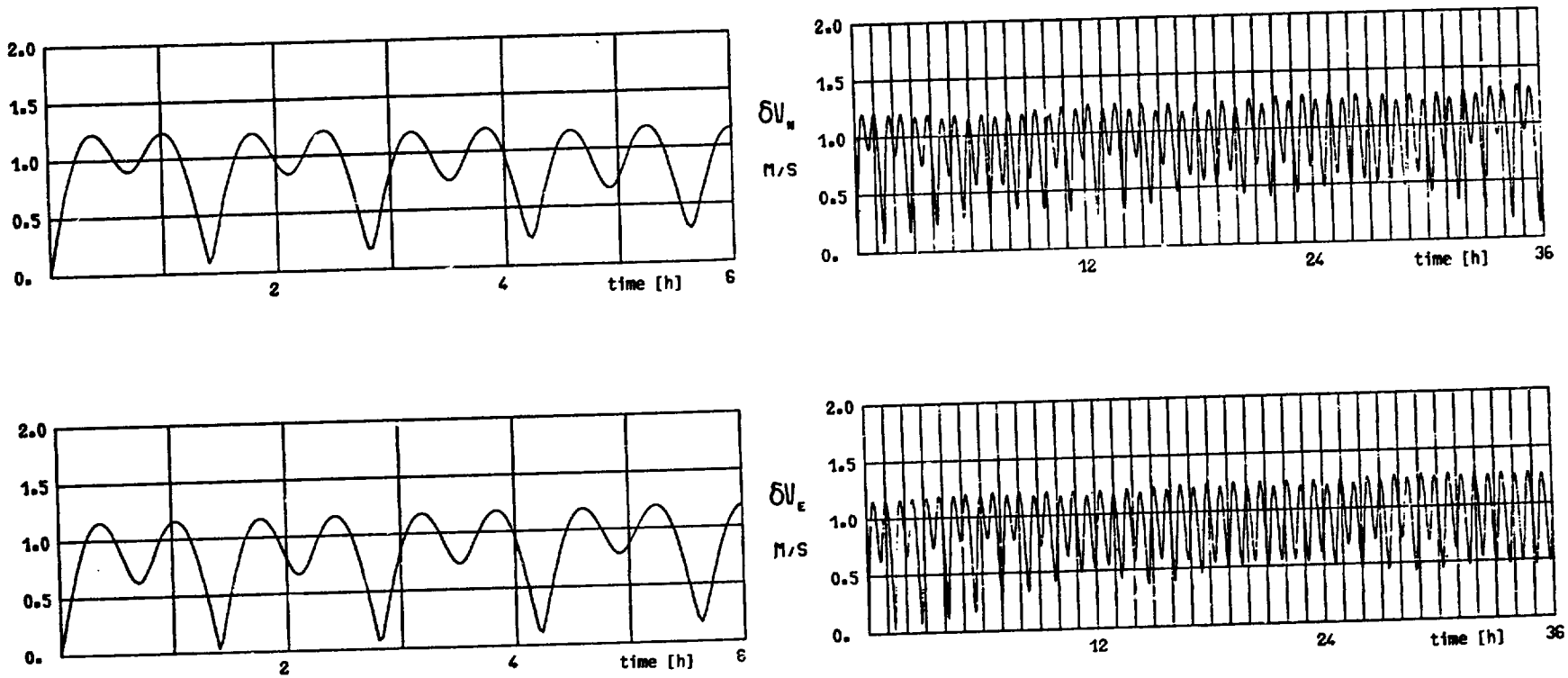

Velocity: $V = 0$

Initial misalignment angles: $\varepsilon_N = \varepsilon_E = 0.1$ mrad $= 0.34$ arc min; $\varepsilon_D = 1$ mrad $= 3.4$ arc min

Gyro drift: $D_N = D_E = D_D = 0.01\ ^{o}/h$

Accelerometer bias: $B_N = B_E = 0.0001$ g

Fig. 7.3.7b 1σ-Velocity Error of an Inertial Navigation System with North Indicating Platform

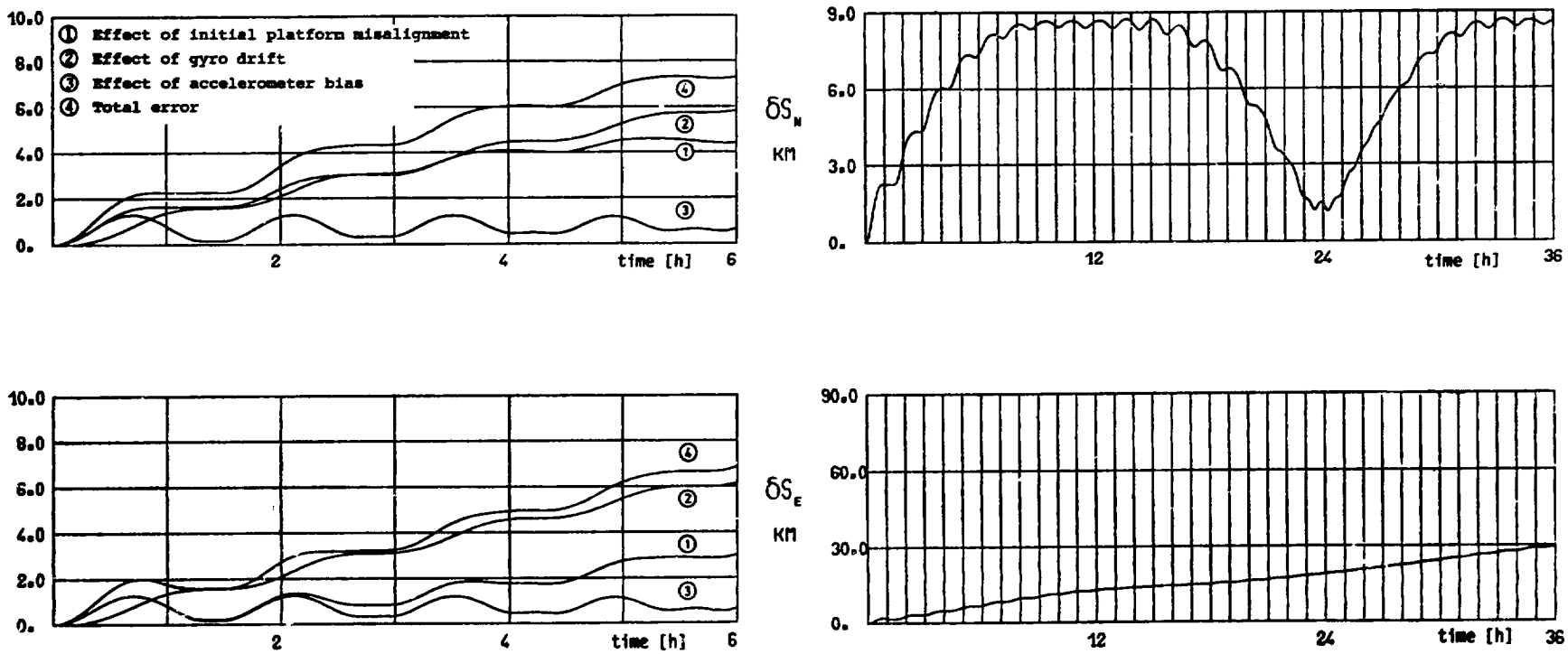

Velocity: $V = 0$

Initial misalignment angles: $\varepsilon_N = \varepsilon_E = 0.1$ mrad $= 0.34$ arc min; $\varepsilon_D = 1$ mrad $= 3.4$ arc min

Gyro drift: $D_N = D_E = D_D = 0.01\ ^{o}/h$

Accelerometer bias: $B_N = B_E = 0.0001$ g

Fig. 7.3.7c 1σ-Position Error of an Inertial Navigation System with North Indicating Platform

used in the Kalman filter algorithms for describing the systems accuracy during the optimal estimation process [7.6 to 7.9].

Day-to-day changes in sensor bias have to be included in the state vector $\underline{x}$ as is done in Eq. (7.3.3) for the single axis inertial navigation system.

In the case where no sensor errors and no noise affect the single axis inertial navigation system ($D_E = B_N = Q_i(\Delta t) = 0$) we obtain the following time dependent covariance matrix with the initial uncertainties $\sigma_{\varepsilon 0}$ and σ_{V0} for platform misalignment and velocity.

$$\underline{P}(t) = \begin{pmatrix} \sigma_{\varepsilon 0}^2 \cos^2 \omega^s \Delta t + (\frac{\sigma_{V0}}{R\omega^s})^2 \sin^2 \omega^s \Delta t & (\sigma_{\varepsilon 0}^2 R\omega^s - \frac{\sigma_{V0}^2}{R\omega^s}) \cos \omega^s \Delta t \sin \omega^s \Delta t \\ (\sigma_{\varepsilon 0}^2 R\omega^s - \frac{\sigma_{V0}^2}{R\omega^s}) \cos \omega^s \Delta t \sin \omega^s \Delta t & \sigma_{V0}^2 \cos^2 \omega^s \Delta t + (\sigma_{\varepsilon 0} R\omega^s)^2 \sin^2 \omega^s \Delta t \end{pmatrix} \tag{7.3.31}$$

On the main diagonal we find the quadratic sums of the errors in Eqs. (7.3.10a,b). The 1σ-values of the errors with Gaussian distribution are the square roots of the elements on the main diagonal:

$$\sigma_{ii} = \sqrt{P_{ii}}. \tag{7.3.32}$$

In Fig. 7.3.7a to c the 1σ errors of an NIS are plotted over a 6-hour and a 36-hour period. They describe the Gaussian distribution of the system error (s. Fig. 7.3.6), i.e. with a probability of 68 per cent the respective system error is within the limits indicated, under the condition that the NIS is within the class of accuracy marked by the given 1σ alignment and sensor errors.

From the effect of the various uncorrelated error sources on the position error in Fig. 7.3.7c the following can be stated:

- As V = 0, the cross-track error does not become significant.
- For short periods of up to 1/2 h in the north-south channel or 2 h in the east-west channel the influences of the initial misalignment and of the accelerometer bias are identical, which can be explained by the fact that initially the azimuth misalignment does not become significant.
- In the north-south channel the initial misalignment causes a mean position error increasing linearly with time - according to Eq. (7.3.17b) the azimuth misalignment has the effect of an east-west gyro drift.
- The gyro drifts cause a mean position error increasing linearly with time, which is due mainly to the horizontal gyros. According to Eq. (7.3.18f) the vertical gyro drift of a stationary NIS after a time

$$\Delta t = 4/(\Omega \cos\varphi) \gg 2h, \tag{7.3.33}$$

causes the same mean position error as that produced by an east-west gyro drift of the same amount. However at longer times the effect of this vertical gyro drift becomes dominant.

7.3.4 The Circular Error Probable (CEP) in the Horizontal Channels of a North Indicating System (NIS)

The covariance matrix describe the multidimensional Gaussian distribution for the states of the NIS errors.

For the two components of the horizontal velocity error or position error this distribution is similar to Fig. 7.3.8. Horizontal sections through this distribution are error ellipses as described by the exponent of p(x) in Fig. 7.3.8 and as shown in Fig. 7.3.9 for the position error similar to Fig. 7.3.7c at a time between 3 to 4 hours.

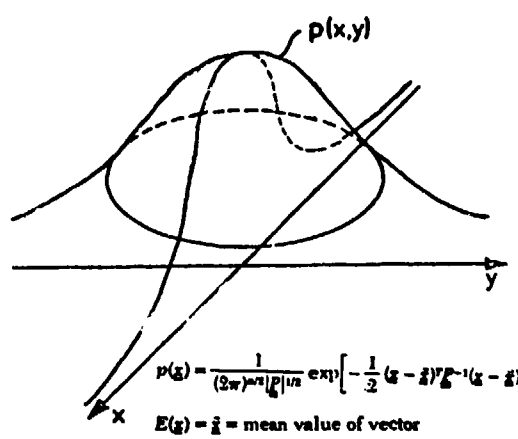

$$p(\underline{x}) = \frac{1}{(2\pi)^{n/2}|\underline{P}|^{1/2}} \exp\left[-\frac{1}{2}(\underline{x}-\underline{\bar{x}})^T \underline{P}^{-1}(\underline{x}-\underline{\bar{x}})\right]$$

$E(\underline{x}) = \underline{\bar{x}}$ = mean value of vector

$E[(\underline{x}-\underline{\bar{x}})(\underline{x}-\underline{\bar{x}})^T] = \underline{P}$ = covariance matrix of vector

Fig. 7.3.8 Two Dimensional Gaussian Distribution

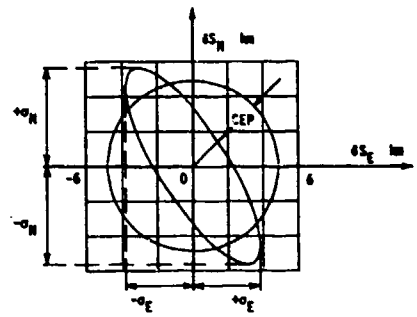

$$\underline{P} = \begin{pmatrix} \sigma_N^2 & \rho\sigma_N\sigma_E \\ \rho\sigma_N\sigma_E & \sigma_E^2 \end{pmatrix} = \begin{pmatrix} 5{,}62^2 & -0{,}9\cdot 3{,}81\cdot 5{,}62 \\ -0{,}8\cdot 3{,}81\cdot 5{,}62 & 3{,}81^2 \end{pmatrix}$$

Fig. 7.3.9 Covariance Matrix, Error Ellipses and Circular Error Probable (CEP)

The projection of the ellipses on the north-south and east-west axes are the 1σ values obtained from Eq. (7.3.32) for $\delta S_{N,E}$.

For system specification these 1σ values in the two axes are not so convenient; the manufacturer gives the overall specification in form of the CEP (circular error probable) value which in a two-dimensional case is the radius of a circle around the mean value comprising the errors with 50 % probability unless otherwise mentioned (e.g. CEP_{90} corresponds to 90 % probability).

The covariance analysis shows that the CEP in the one-dimensional case is:

$$CEP = 0.675\ \sigma. \tag{7.3.34}$$

In the two dimensional case the CEP value can be obtained from Fig. 7.3.10, once the uncorrelated σ-values on the elliptic main axes are known, which can be found by rotating the coordinate frame. One may show that the covariance matrix in a rotated coordinate system $\underline{x} = \underline{C}\ \underline{x}'$ is defined by

$$\underline{P} = \underline{C}^T\ \underline{P}'\underline{C}. \tag{7.3.35}$$

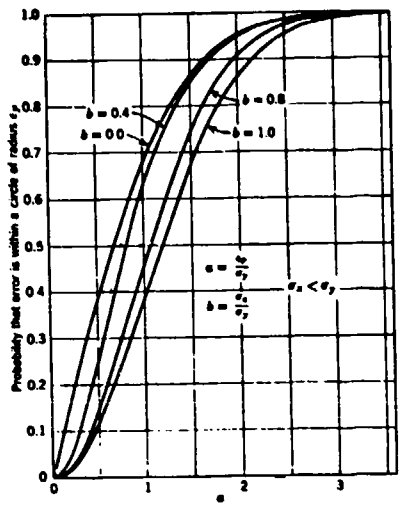

Fig. 7.3.10 Probability of an Error Lying within a Circle of Radius εp ($\sigma_{x,y}$ are the uncorrelated standard deviations in x,y). From [7.33] and [7.14, Fig. 2.13].

Requiring that its components are uncorrelated, i.e. that $\underline{P}'$ has components on the main diagonal only, we find for the angle of rotation

$$\alpha = \frac{1}{2} \arctan \frac{2\rho\ \sigma_{x'}\ \sigma_{y'}}{\sigma_{x'}^2 - \sigma_{y'}^2} \tag{7.3.36}$$

and the uncorrelated σ-values:

$$\sigma_{x,y}^2 = \frac{1}{2}\{\sigma_{x'}^2 + \sigma_{y'}^2 \pm [(\sigma_{x'}^2 - \sigma_{y'}^2)^2 + (2\rho\ \sigma_{x'}\ \sigma_{y'})^2]^{1/2}\} \tag{7.3.37}$$

In the example of Fig. 7.3.9 we obtain, with $\sigma_{x'} = \sigma_N = 5.62$ km and $\sigma_{y'} = \sigma_E = 3.81$ km, the uncorrelated σ-values $\sigma_x = 6.58$ km, $\sigma_y = 1.98$ km and the 50 % and 90 % probability circles CEP = 5.0 km and CEP_{90} = 11.1 km.

The CEP contains the random NIS errors, which up to now we have obtained as a result of an analysis by assuming random sensor errors (s. Fig. 7.3.6) and random initial misalignment errors. As a result of flight tests the CEP has to be understood as

- for a single system, the system day-to-day error variation about a mean error for a certain flight profile due to the day-to-day sensor error variation about the mean error;
- for a whole class of systems, the performance to be expected from this system series for a certain flight profile.

In the latter case it is assumed that the manufacturer has compensated the mean error of the sensors to a minimum before delivering the systems. When judging the system performance the customer should bear in mind the randomness of the CEP and the effect of the flight profile on it. This randomness also means that the system performance during testing may have been better on a "Sunday flight" than on a "Monday flight" and the manufacturer may tend to forget the latter one. As to the effect of the flight profile one should

realize that system performance may also be better on a flight where the aircraft returns to the starting point when the cross-track error, for instance, vanishes (s. Eq. (7.3.18)).

7.3.5 Justification of the Decoupling Between the Vertical and Horizontal Channels in an INS - the Error Dynamics in the Vertical Channel

So far we have discussed the errors in the horizontal channels of an INS only. But the decoupling between the vertical and horizontal channels is justified as may be seen from Eqs. (7.3.23) to (7.3.29).

The last column of Eq. (7.3.23) indicates that an altitude error δh causes an erroneous platform slewing, an acceleration error and a position error slope. The altitude rate error $\delta\dot{h}$ again causes an acceleration error. But the estimations in Eqs. (7.3.26) and (7.3.27) show us that both have a negligible effect on the horizontal channels.

As to the effect of the horizontal channels on the vertical channel we have to consider that the exclusively inertially derived altitude is unstable, which can be deduced from Figs. 8.2.1 and 7.3.3 or Eq. (7.3.28) by cutting off the barometric aiding (put $T \to \infty$). If, for the computation of g(h), Eq. (2.36) is expressed as $(g(h) = g_0/(1+h/R)^2)$, for which the altitude is fed back from the system output, the eigenvalues

$$\varkappa = \pm (2g/R)^{1/2} \tag{7.3.38}$$

escribe the unstable error growth of

$$\delta h(t) = \delta h(o) \cosh \varkappa t - \frac{B_v}{K^2} (1 - \cosh \varkappa t) \tag{7.3.39}$$

This is plotted as a function of time in Fig. 7.3.11.

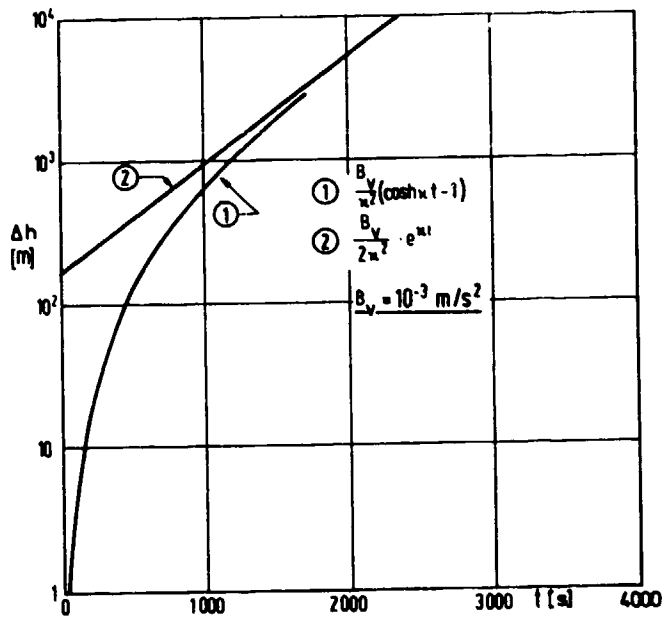

Fig. 7.3.11 Error in the Vertical Channel of an INS Due to an Accelerometer Bias

The vertical channel has to be aided by external measurements as discussed in Section 8.2.1.1.

7.4 Other Mechanizations of Inertial Systems

In the NIS the geographical coordinate frame is mechanized with the accelerometers measuring the vehicle's horizontal motion in north-south and east-west directions from which the computer derives velocity and position in the same directions. Other mechanizations are possible where the acceleration is measured in other directions (wander azimuth platform, strapdown inertial measuring unit, inertial stabilized platform). [illegible] se on earth all, in common with the NIS, derive by means of the computer the velocity and positi[illegible] north-south and east-west directions.

Th[illegible] systems and their advantages will be described briefly below. Differences and commonalities of the error propagation of all systems as compared to the NIS are discussed in the next section.

7.4.1 Navigation Based on Inertial Measurements in the Wander Azimuth Coordinate Frame

7.4.1.1 The Platform and the Command Rates

The wander azimuth coordinate frame (subscript "a", s. Fig. 7.4.1) is defined by a rotation α (the wander angle) of the platform about the vertical axis with respect to the navigational frame, so that:

$$\underline{\omega}_a^{na} = \underline{\omega}_n^{na} = (0 \quad 0 \quad \dot{\alpha})^T, \tag{7.4.1}$$

i.e. the wander azimuth angular rate $\dot{\alpha}$ is just the difference between the actual vertical platform slewing and the vertical rate of change of the navigational frame with respect to inertial space.

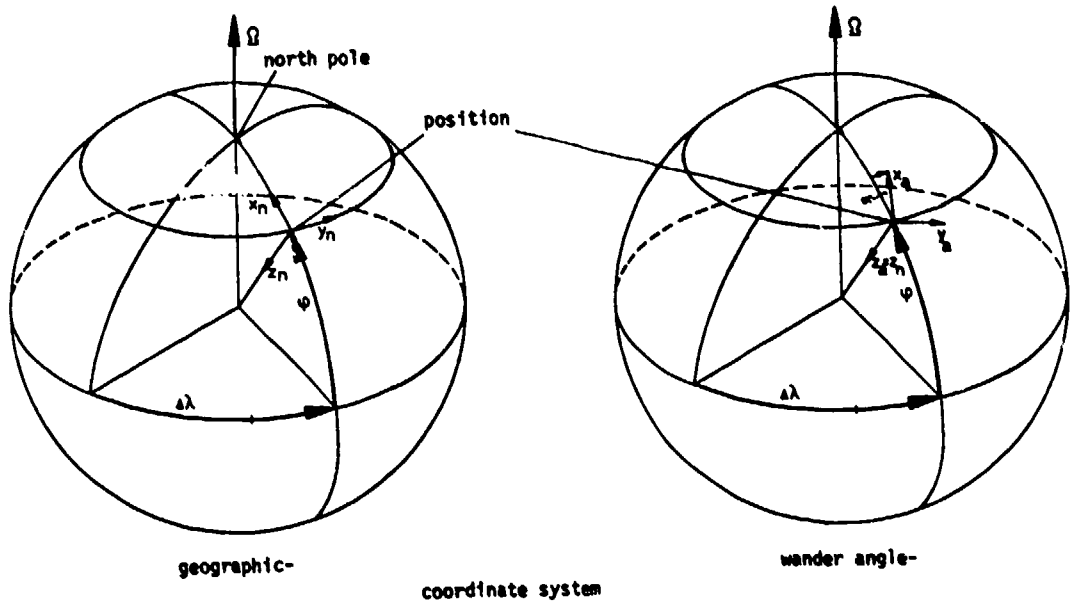

Fig. 7.4.1 The Wander Angle Coordinate Frame

By selecting different relationships for α, certain advantages may be obtained:

- by-pass of Coriolis acceleration $(2\underline{\omega}^{ie} + \underline{\omega}^{ea})_a \times \underline{V}_a$ (s. Eq. (7.2.4a)) in the horizontal channels which may be advantageous in analog computers, by choosing:

$$\dot{\alpha} = -(2\underline{\omega}^{ie} + \underline{\omega}^{ea})_{za}; \tag{7.4.2}$$

- by-pass of vertical platform slewing by choosing

$$\dot{\alpha} = (\underline{\omega}^{ie} + \underline{\omega}^{ea})_{za}; \tag{7.4.3}$$

- worldwide inertial navigation, including navigation over the poles, by not slewing the platform about the vertical axis with the vehicle's transport rate (s. Eq. (7.2.16)

$$\dot{\alpha} = -\omega_z^{en} = -[V_E/(R_E + h)] \tan\varphi \; ; \tag{7.4.4}$$

  Fig. 7.4.2 shows a block diagram of this kind of navigation and a picture of the Litton LTN-72 in which this is implemented;

- worldwide inertial navigation plus reduction of gyro drift effects on system performance by slewing the horizontal sensors on the platform with the rate of, for instance, 1 revolution per minute about the vertical axis with respect to the vertical gyro, which remains unslewed; the Delco Carousel IV INS is mechanized in this way as indicated in Fig. 7.4.3.

In the Carousel IV INS the output signals of the horizontal accelerometers rotating with $\dot{\beta}$ = 1 RPM with respect to the unslewed vertical gyro are first transformed into the axes of the vertical gyro using the angle β as measured by a synchro between the two halves of the platform (s. Fig. 7.4.3). The wander azimuth, i.e. the angle between the computer and the navigational coordinate frames, can be derived from the following relationship:

$$\dot{\alpha} = -\omega_z^{in} = -\Omega \cos\varphi - \frac{V_E}{R+h} \tan\varphi \; . \tag{7.4.5}$$

7.4.1.2 The Navigation Computer

The navigation computer of the wander azimuth INS (s. Fig. 7.4.2 and 7.4.3) works internally with the velocity vector:

$$\underline{V}_a = (V_x \quad V_y \quad -\dot{h})^T, \tag{7.4.6}$$

which is obtained from the accelerometer outputs by implementing Eq. (2.29) with the subscript "n" replaced by "a".

The velocities in the geographic coordinate frame may be computed via

$$\underline{V}_n = \underline{C}_{na} \underline{V}_a \tag{7.4.7}$$

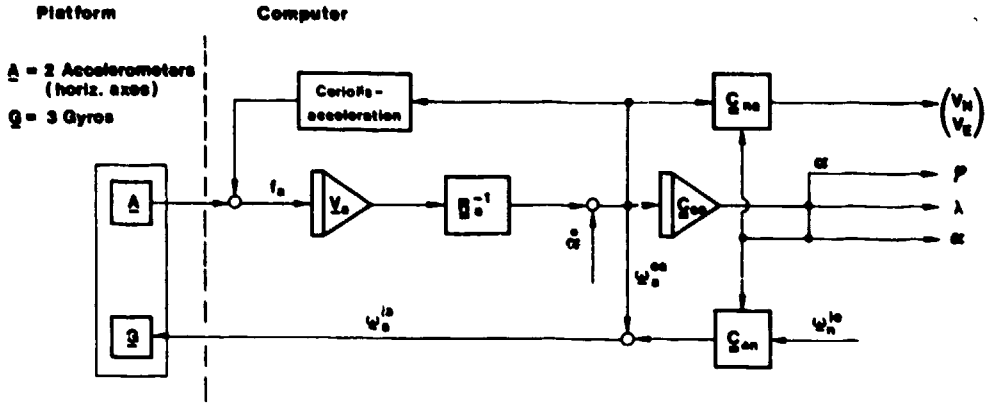

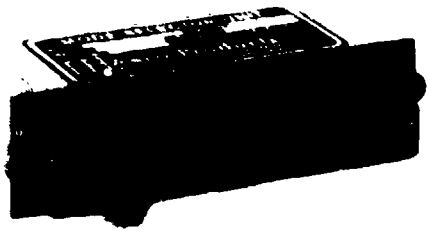

mode selector unit

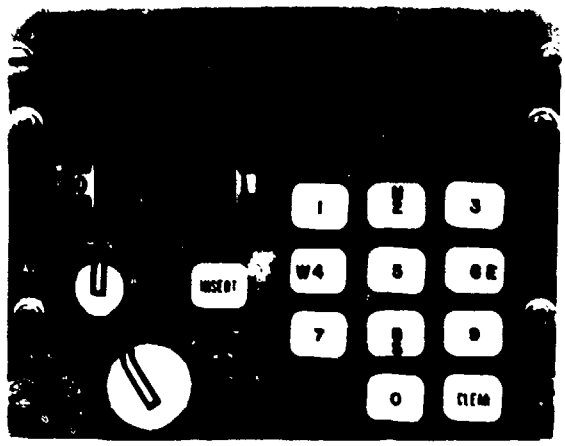

control and display unit

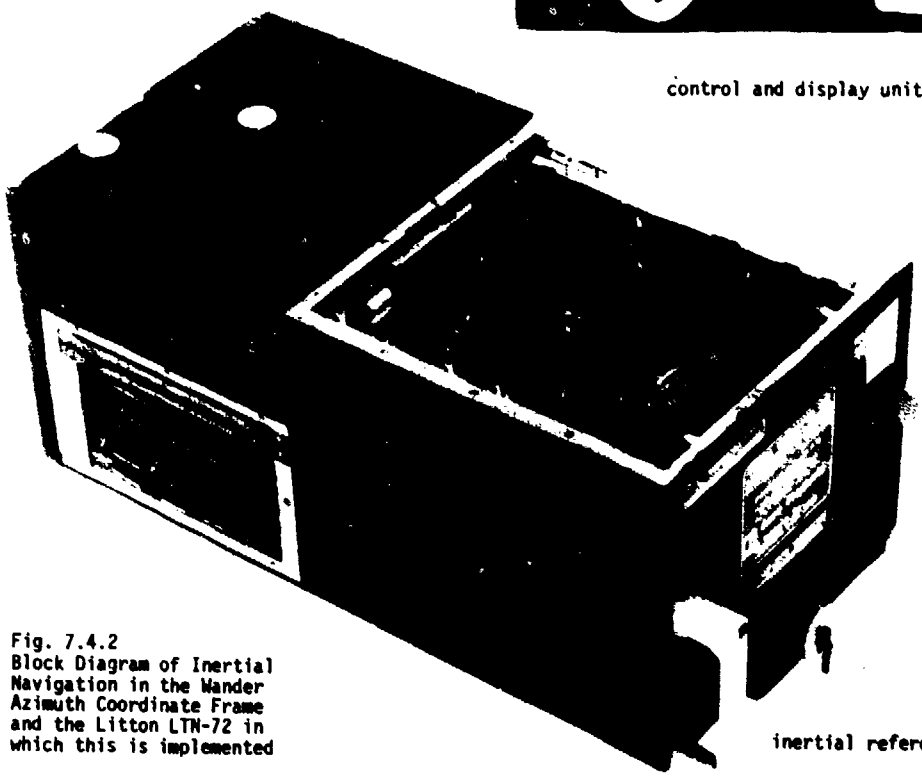

inertial reference unit

Fig. 7.4.2
Block Diagram of Inertial Navigation in the Wander Azimuth Coordinate Frame and the Litton LTN-72 in which this is implemented

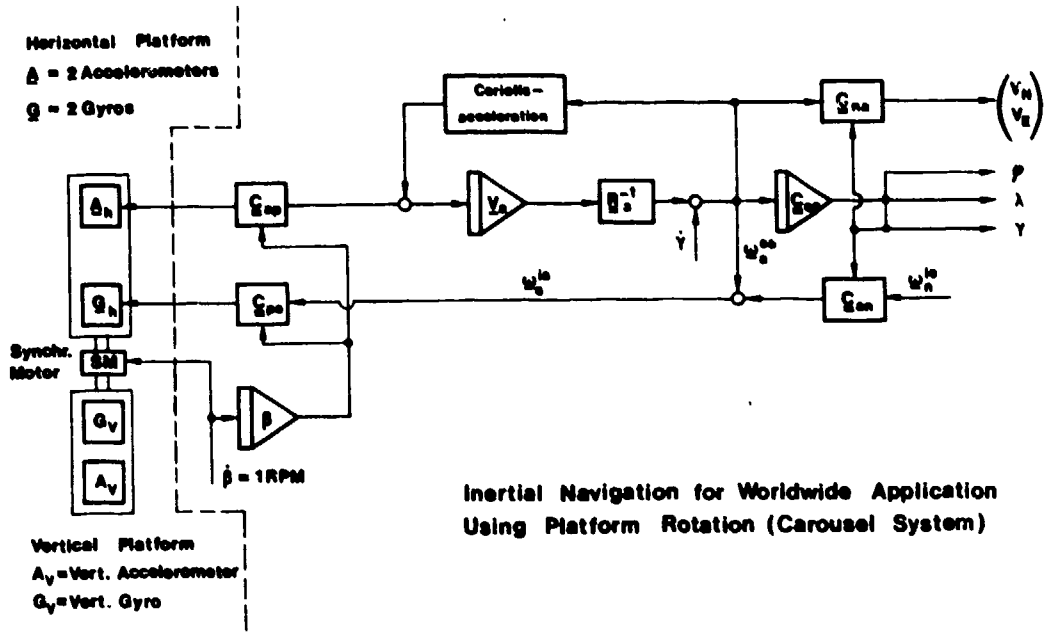

CAROUSEL IV-A
INERTIAL NAVIGATION SYSTEM

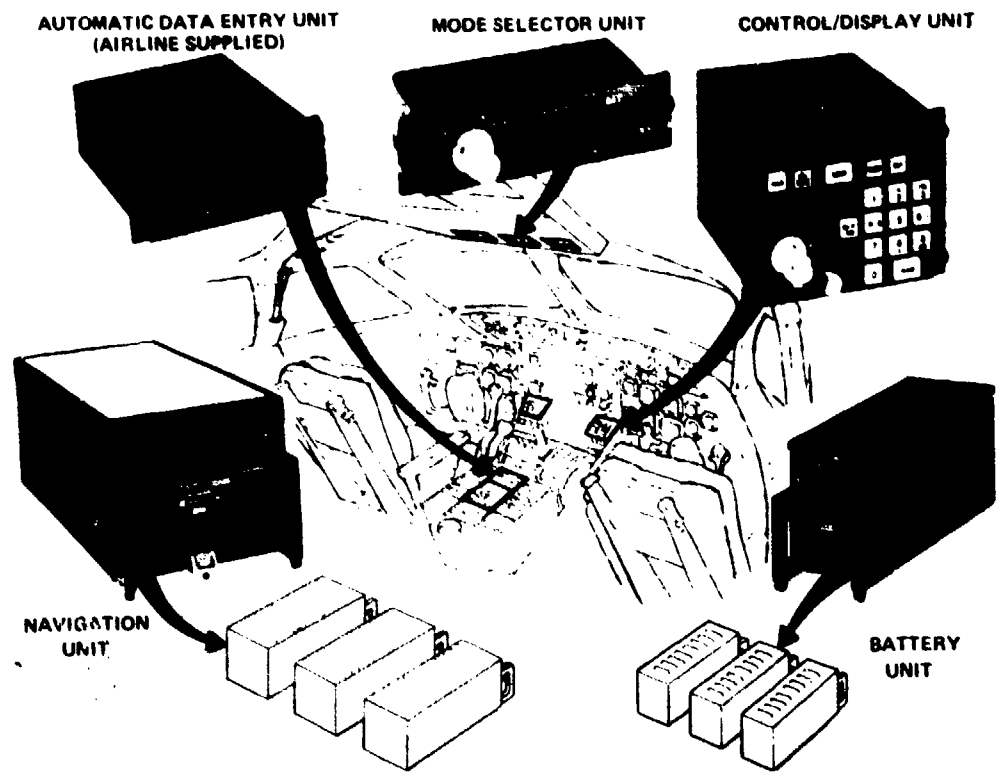

Fig. 7.4.3 Block Diagram of Inertial Navigation using Platform Rotation Implemented in the DELCO CAROUSEL IV Systems; Typical Installation of the Systems

where

$$\underline{C}_{na} = \begin{pmatrix} \cos\alpha & -\sin\alpha & 0 \\ \sin\alpha & \cos\alpha & 0 \\ 0 & 0 & 1 \end{pmatrix}. \tag{7.4.8}$$

The earth rate in the wander azimuth frame:

$$\underline{\omega}_a^{ie} = \underline{C}_{an}\, \omega_n^{ie} = (\Omega\cos\varphi\cos\alpha \quad -\Omega\cos\varphi\sin\alpha \quad -\Omega\sin\varphi)^T \tag{7.4.9}$$

and the wander azimuth rate with respect to the earth

$$\underline{\omega}_a^{ea} = \underline{\omega}_a^{en} + \underline{\omega}_a^{na} = \underline{C}_{an}\, \underline{\omega}_n^{en} + (0 \quad 0 \quad \dot{\alpha})^T$$

$$= \begin{pmatrix} V_y\left(\frac{\cos^2\alpha}{R_E} + \frac{\sin^2\alpha}{R_N}\right) + V_x \frac{\sin 2\alpha}{2}\left(\frac{R_N - R_E}{R_N R_E}\right) \\ -V_x\left(\frac{\cos^2\alpha}{R_N} + \frac{\sin^2\alpha}{R_E}\right) - V_y \frac{\sin 2\alpha}{2}\left(\frac{R_N - R_E}{R_N R_E}\right) \\ \frac{-1}{R_E}(V_y \cos\alpha + V_x \sin\alpha)\tan\varphi + \dot{\alpha} \end{pmatrix} \tag{7.4.10}$$

are added up for slewing the platform.

Position computation is based on the following integral equation

$$\underline{C}_{ea}(t) = \underline{C}_{ea}(o) + \int_o^t \underline{C}_{ea}\, \underline{\Omega}^{ea}\, d\tau = \begin{pmatrix} C_{11} & C_{12} & C_{13} \\ C_{21} & C_{22} & C_{23} \\ C_{31} & C_{32} & C_{33} \end{pmatrix}, \tag{7.4.11}$$

where

$$\underline{\Omega}_a^{ea} = \begin{pmatrix} 0 & -\omega_z & \omega_y \\ \omega_z & 0 & -\omega_x \\ -\omega_y & \omega_x & 0 \end{pmatrix}_a^{ea}. \tag{7.4.12}$$

The matrix $\underline{C}_{ea}$ can also be interpreted as being obtained from the rotations of the wander azimuth with respect to the earth-fixed frame via the angles $\Delta\lambda, \varphi$, α (s. Fig. 7.4.1):

$$\underline{C}_{ea} = \underline{C}_{en}\, \underline{C}_{na} = \begin{pmatrix} \cos\varphi\cos\alpha & -\cos\varphi\sin\alpha & -\sin\varphi \\ -\sin\varphi\sin\Delta\lambda\cos\alpha + \cos\Delta\lambda\sin\alpha & \sin\varphi\sin\Delta\lambda\sin\alpha + \cos\Delta\lambda\cos\alpha & -\cos\varphi\sin\Delta\lambda \\ \sin\varphi\cos\Delta\lambda\cos\alpha + \sin\Delta\lambda\sin\alpha & -\sin\varphi\cos\Delta\lambda\sin\alpha + \sin\Delta\lambda\cos\alpha & \cos\varphi\cos\Delta\lambda \end{pmatrix} \tag{7.4.13}$$

Equalizing the elements of (7.4.11 and 13), the geographic position and true north can be computed using:

$$\sin\varphi = -C_{13} \qquad \tan\Delta\lambda = -C_{23}/C_{33} \qquad \tan\alpha = -C_{12}/C_{11}. \tag{7.4.14a,b,c}$$

Although singularities do exist in the computation of the latitude φ and the wander azimuth α at the geographic poles, the computation of the matrix $\underline{C}_{ea}(t)$ does not have singularities so that the continuity of inertial navigation is assured on a polar flight and φ and α are again correctly computed shortly after passage of a pole.

According to [7.14] the integration of Eq. (7.4.11) has to be executed with 26 bit words and the integration of the acceleration with 17 bit words if the corresponding drift is to be kept below 1/1000 °/h.

7.4.2 Navigation Based on Inertial Measurements in the Pseudo-Pole Coordinate Frame

Worldwide inertial navigation in the wander azimuth coordinate frame just discussed requires a digital computer. For an INS equipped with an analog computer the pseudo-pole coordinate frame opens the way for inertial navigation in the polar region. The Litton LN-3 and LN-12 systems operate in this fashion.

The pseudo-pole frame (subscript "m", s. Fig. 7.4.4) can be looked upon as a special case of the wander azimuth frame. Its z_m-axis is also aligned with the normal to the reference ellipsoid and its x-, y-axes are rotated with the convergence angle α with respect to true north.

The pseudo-pole of this coordinate frame is located at the geographic equator as shown in Fig. 7.4.4, which as compared to the navigational coordinate frame ("n") is achieved by rotating its axes in a reversed sequence of rotation with respect to the earth fixed coordinate frame ("e"): a first rotation about the east-west axis through the angle μ and a second rotation about the initial north-south axis through the angle σ. The corresponding transformation matrix from "m" to "e" is thus

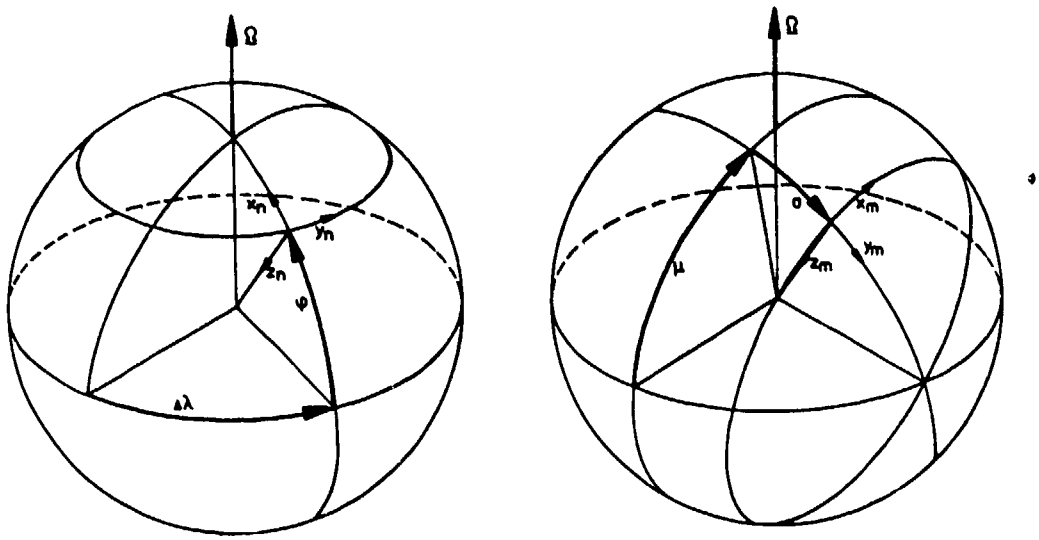

Fig. 7.4.4 The Navigational and the Pseudo-Pole Coordinate Frames

$$\underline{C}_{em} = \begin{pmatrix} \cos\mu & -\sin\sigma\sin\mu & -\cos\sigma\sin\mu \\ 0 & \cos\sigma & -\sin\sigma \\ \sin\mu & \sin\sigma\cos\mu & \cos\sigma\cos\mu \end{pmatrix}. \tag{7.4.15}$$

The rate of change of σ and μ is related to the velocities $V_{x,y}$ in the following way:

$$\dot{\sigma} = \frac{V_y}{R_y} \qquad \dot{\mu}\cos\sigma = \frac{V_x}{R_x}, \tag{7.4.16a,b}$$

whereby $R_{x,y}$ theoretically have to be computed with the aid of Eq. (2.16) for ψ replaced by α; in the LN-3 they are kept constant.

The sum of earth rate

$$\underline{\omega}_m^{ie} = \underline{C}_{me}\,\underline{\omega}_e^{ie} = \begin{pmatrix} \Omega\cos\mu \\ -\Omega\sin\sigma\sin\mu \\ \Omega\cos\sigma\sin\mu \end{pmatrix} \tag{7.4.17}$$

and transport rate

$$\underline{\omega}_m^{em} = \begin{pmatrix} \dot{\sigma} \\ -\dot{\mu}\cos\sigma \\ \dot{\mu}\sin\sigma \end{pmatrix} = \begin{pmatrix} V_y/R_y \\ -V_x/R_x \\ -(V_x/R_x)\tan\sigma \end{pmatrix} \tag{7.4.18}$$

is used for slewing the platform. How this is accomplished with only analog hardware is indicated in the simplified block diagram of the LN-3 Schuler loops in Fig. 7.4.5.

The LN-3 system does not navigate in absolute coordinates (longitude and latitude) but in heading and distance to preselected waypoints, whereby the heading is referenced to the so-called "grid heading", differing from the north-referenced heading by the wander azimuth angle α. The corresponding computation is carried out in a separate analog computer, the so-called "position and homing indicator (PHI)" based on the position increments Δσ and Δμ from the LN-3 analog computer and the grid heading from the platform.

From Fig. 7.4.4 and Eqs. (7.4.17 and 18) it is obvious that the vertical slew rate is infinite at the pseudo-pole. Since the initial meridian (pseudo equator) can be chosen freely, any crossing of the pseudo-pole can be circumvented. For fighter aircraft this problem does not arise in general since their range of operation is limited. Thus the LN-3 INS is designed for ± 25° in σ only, corresponding to a range of ± 3000 km.

If the LN-3 system is used as a flight test reference system it is of interest to know the relationships between the system velocity ($V_{x,y}$) and position (σ,μ) and the geographic velocity ($V_{N,E}$) and latitude and longitude (φ,λ). They may be derived from the fact that the pseudo-pole coordinate frame is a special wander azimuth frame and we set equal the elements of $\underline{C}_{em}$ and $\underline{C}_{ea}$ in Eqs. (7.4.15) and (7.4.13). So we find

$$\sin\varphi = \cos\sigma\sin\mu \qquad \sin\sigma = \cos\varphi\,\sin\Delta\lambda \qquad \cos\sigma\cos\mu = \cos\varphi\,\cos\Delta\lambda \tag{7.4.19}$$

$$\sin\alpha = \sin\sigma\sin\mu/\cos\varphi.$$

Knowing α we obtain $V_{N,E}$ with Eqs. (7.4.8) and (7.4.7).

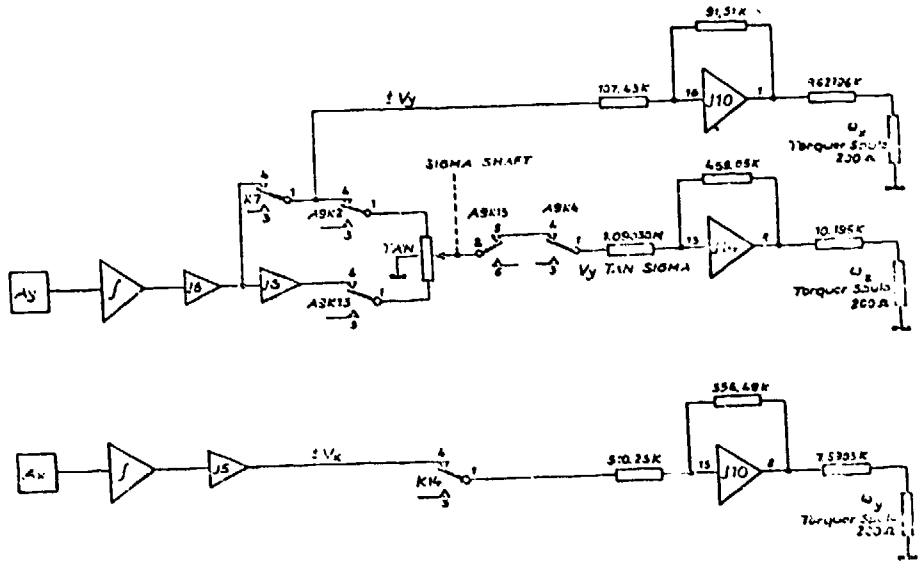

Fig. 7.4.5 The Litton LN-3A Inertial Navigation System and Functional Diagram of its Analog Schuler Loops for Navigating in the Pseudo-Pole Coordinate Frame (x,y pointing east, north)

7.4.3 Navigation Based on Inertial Measurements in the Space-Stabilized Coordinate Frame

Inertial navigation systems with space-stabilized platforms are used for:

- space navigation
- terrestrial navigation when the platform is equipped with electrostatically supported gyros which are not torqued in the navigation mode.

Figs. 7.4.6a,b show two possible configurations for inertial navigation with a space-stabilized system.

The first configuration in Fig. 7.4.6a seems very simple on first sight. It is implemented in the Honeywell ESGN (electrically suspended gyro navigator) for marine application and the Honeywell GEANS (gimballed ESG aircraft navigation system) [7.15]. The navigation is carried out in the inertial frame by the double integration in the computer of:

$$\left.\frac{d^2\underline{R}_i}{dt^2}\right|_i = \underline{f}_i + \underline{G}_i\,(\underline{R}_i). \tag{7.4.20}$$

Once $\underline{R}_i$ is known it can be converted into the geodetic latitude φ_c and celestial longitude Λ. For deriving the corresponding relationships we transform the radius vector $\underline{R}_n$ in the navigational frame into the inertial frame $\underline{R}_i = \underline{\underline{C}}_{in}\,\underline{R}_n$ with

$$\underline{\underline{C}}_{in} = \begin{pmatrix} \cos\varphi_c & 0 & -\sin\varphi_c \\ -\sin\varphi_c \sin\Delta\Lambda & \cos\Delta\Lambda & -\cos\varphi_c \sin\Delta\Lambda \\ \sin\varphi_c \cos\Delta\Lambda & \sin\Delta\Lambda & \cos\varphi_c \cos\Delta\Lambda \end{pmatrix}. \tag{7.4.21}$$

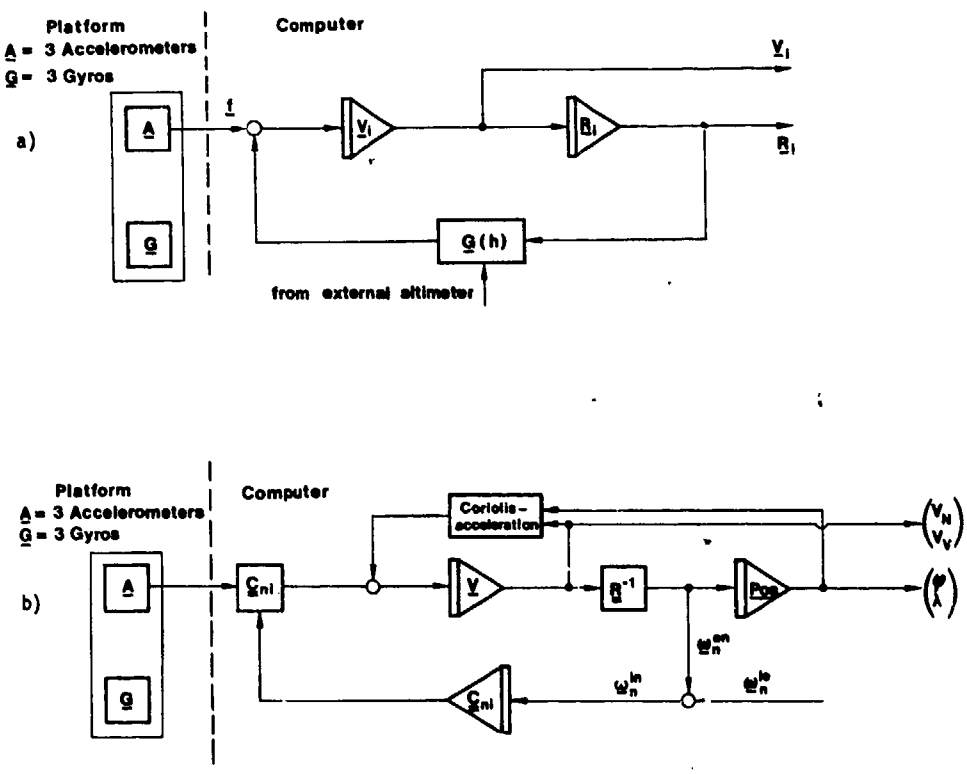

Fig. 7.4.6 Two Kinds of Inertial Navigation Using Space-Stabilized Platforms

So we find the relationships for computing φ_c and $\Delta\Lambda$ as:

$$\underline{R}_i = \begin{pmatrix} R_x \\ R_y \\ R_z \end{pmatrix} = R \begin{pmatrix} -\sin\varphi_c \\ -\cos\varphi_c \sin\Delta\Lambda \\ \cos\varphi_c \cos\Delta\Lambda \end{pmatrix} . \tag{7.4.22}$$

The geographic latitude is derived from Eq. (2.11) and the geographic longitude from Eq. (7.2.8).

The difficulty of this first implementation lies in the exact modelling of the earth's mass attraction $\underline{G}(R_i)$ in Eq. (7.4.20) for which we find assumptions in [7.13], Chapter 4. Because of the instability of the vertical channel, treated in Section 7.3.5 and Chapter 8, the computation of $\underline{G}(\underline{R}_i)$ is based on external altitude measurements as indicated in Fig. 7.4.6.

In the second implementation of Fig. 7.4.6b the acceleration vector $\underline{f}_i$ measured in the inertial frame is transformed into the navigational frame via the transposition of Eq. (7.4.21).

Inertial navigation is then carried out in the conventional way (s. Fig. 7.3.4). This relationship does not require the modelling of $\underline{G}_i$ $(\underline{R}_i)$.

The Autonetics ESGM (electrostatically suspended gyro monitor) for marine application works in this way [7.16].

7.4.4 Navigation Based on Inertial Measurements in the Body-Fixed Coordinate Frame (Strapdown Systems SDS)

7.4.4.1 The Functioning of Strapdown Systems

In the preceding sections the functioning of inertial navigational systems with a gimbal-suspension gyro-stabilized platform as an inertial measurement unit has been dealt with. There are also inertial navigational systems available in which gyros and accelerometers are directly mounted to the vehicle, literally strapped down to it.

Fig. 7.4.7 shows an inertial platform in comparison to a strapdown sensor block. The former is a design of the sixties - showing the platform of the Litton LN-3A system suspended in four gimbal frames. The figure provides an idea of the complex mechanical set-up required for such a system. The mechanics of the strapdown measurement unit (Steinheil Lear Siegler LBFK) are considerably simpler.

By comparing Fig. 7.4.8 with Fig. 7.2.1 we will try to come to an understanding of some characteristics of strapdown systems. In Fig. 7.4.8 one can see that the wind vane is now transfered into the computer, i.e., the information of the north direction and the vertical is now no longer physically given in the platform as in Fig. 7.2.1, but analytically stored in a transformation matrix $\underline{C}_{nb}$ for the transformation of a vector from the body-fixed "b" coordinate system into the "n" or navigational coordinate system. The part on the right of $\underline{C}_{nb}$ presents the structure of the navigational computation and in this case is identical with that of the platform system. The part left of it is different. We see the sensors directly mounted to the vehicle. The gyros are used for the direct measurement of the vehicle's rotation $\underline{\omega}_b^{ib}$ of the body-fixed coordinate system with respect to the inertial coordinate system. Contrary to the platform system where they had to provide for its stabilization as null sensors, they are here equipped with signal readout electronics similar to accelerometers. Their output signal is fed to the computer for the integration of the transformation matrix based on the formula:

$$\underline{C}_{nb}(t) = \underline{C}_{nb}(t_o) + \int_{t_o}^{t} \underline{C}_{nb}(\tau)\, \underline{\Omega}_b^{nb}(\tau)\, d\tau \tag{7.4.23}$$

with (s. [7.26])

$$\underline{C}_{nb} = \begin{pmatrix} C_{11} & C_{12} & C_{13} \\ C_{21} & C_{22} & C_{23} \\ C_{31} & C_{32} & C_{33} \end{pmatrix} = \begin{pmatrix} \cos\theta\cos\psi & \sin\phi\sin\theta\cos\psi - \cos\phi\sin\psi & \cos\phi\sin\theta\cos\psi + \sin\phi\sin\psi \\ \cos\theta\sin\psi & \sin\phi\sin\theta\sin\psi + \cos\phi\cos\psi & \cos\phi\sin\theta\sin\psi - \sin\phi\cos\psi \\ -\sin\theta & \sin\phi\cos\theta & \cos\phi\cos\theta \end{pmatrix} \tag{7.4.24a,b}$$

where ϕ, θ and ψ are the roll, pitch and yaw angles of the aircraft and

$$\underline{\Omega}^{nb} = \begin{pmatrix} 0 & -\omega_z & \omega_y \\ \omega_z & 0 & -\omega_x \\ -\omega_y & \omega_x & 0 \end{pmatrix}_b^{nb} . \tag{7.4.25}$$

The components of the $\underline{\Omega}$-matrix are derived from the body-fixed gyro output $\underline{\omega}^{ib}$ and the Schuler feedback $\underline{\omega}^{in}$ in the computer (s. Fig. 7.4.8) according to:

$$\underline{\omega}_b^{nb} = \underline{\omega}_b^{ib} - \underline{\omega}_b^{in} = \underline{\omega}_b^{ib} - \underline{C}_{bn}\, \underline{\omega}_n^{in} \tag{7.4.26}$$

where $\underline{\omega}_n^{in}$ is the sum of Eqs. (7.2.15) and (7.2.16).

Because of the similarity of the navigational computation including the Schuler feedback loops in Figs. 7.4.8 and 7.2.1 we may conclude that in a stationary strapdown system the navigational errors will also be subject to oscillations of the Schuler period of 84.4 minutes and of a superposed 24-hour period as discussed in Section 7.3 for the platform system. We may also deduce from this similarity between platform and strapdown systems that the same physical rules will hold for the latter one, i.e. especially the rule

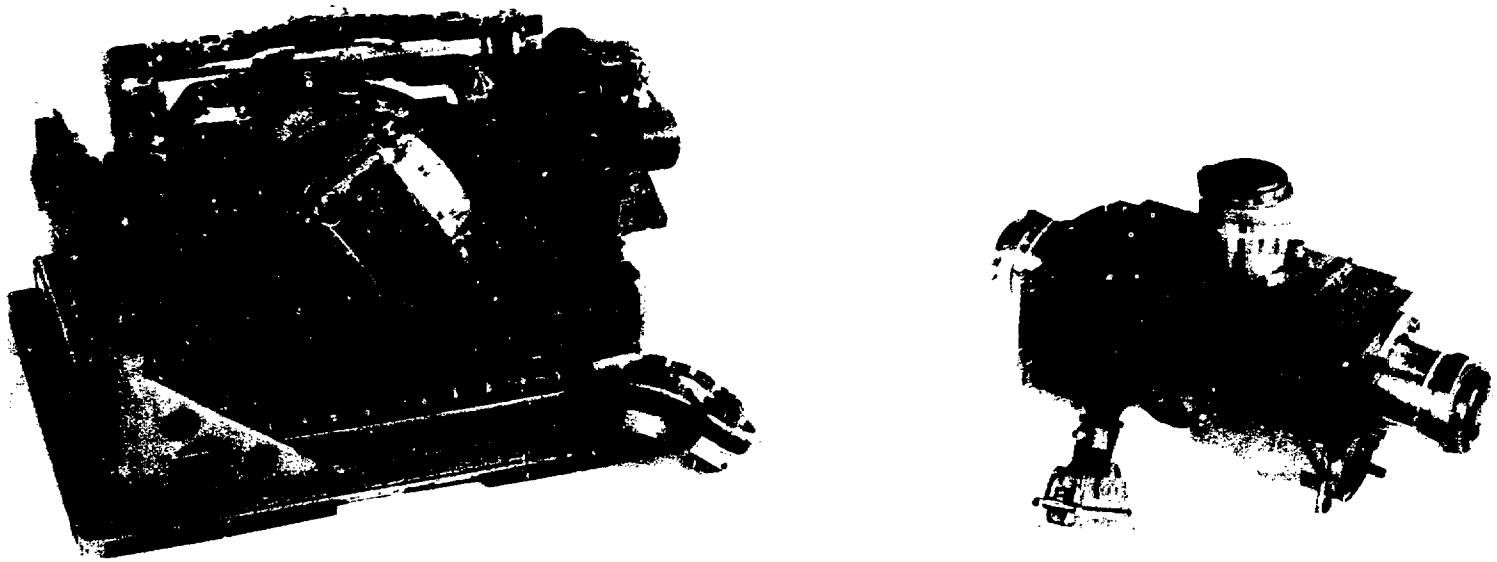

Fig. 7.4.7 The Inertial Measurement Unit in Platform and Strapdown Technique
(Litton LN-3A platform and Steinheil-Lear Siegler Strapdown Package LBFK)

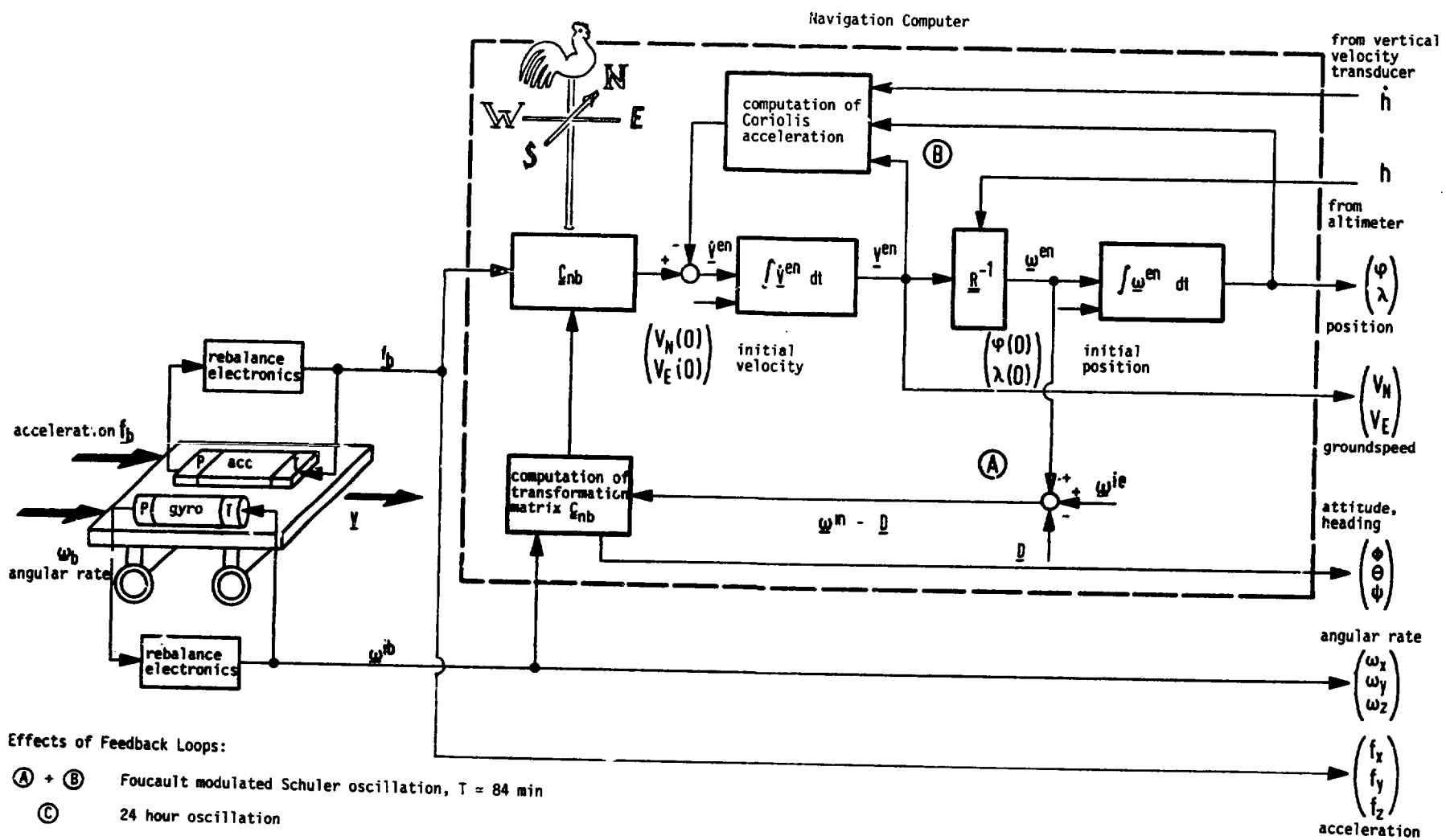

Effects of Feedback Loops:

Ⓐ + Ⓑ Foucault modulated Schuler oscillation, T ≈ 84 min

Ⓒ 24 hour oscillation

Fig. 7.4.8 Functional Diagram of an Inertial Navigation System (Strapdown System)

of thumb that a navigation accuracy of 1 km/h requires an angular rate measurement error in the order of $<0.01^{0}/h$ (s. Eq. (7.3.11)) which also includes the "drift" of the signal processing in the computer. This leaves an impression of the tight requirements put on the gyros and their readout.

In summary we may state that the transformation matrix C_{ib} in a strapdown system without Schuler feedback plays the same role as the gyro-stabilized platform. Thus all mechanizations discussed in the previous sections for platform systems (inertial navigation and attitude and heading reference systems) are in principle also possible in strapdown technique. The methods for the initial alignment of platform and strapdown systems are equally very similar as will be shown in Section 7.6.

A literature survey on strapdown navigation technology covering the aspects of concepts, components, analysis, error generation and propagation, data processing and reliability is presented in [7.17]. A comprehensive overview on strapdown theory and application is given in [7.18].

7.4.4.2 Advantages of Strapdown Systems

Figure 7.4.8 reveals one essential advantage of the strapdown system as compared to the gimballed platform system: the inertial measurement unit provides additional measurement signals which are essential for flight guidance, instrumentation, and especially for flight tests. Those are the body-fixed measured accelerations and angular rates. The above mentioned information on the flight attitude, heading, the acceleration and velocity relative to the earth as well as the position is provided, as it is in platform systems.

In the platform system the information on the reference coordinate frame stored in the gyros is mechanically transferred to the accelerometers. In the strapdown system the gyros provide output signals on the rate of change of the vehicle's attitude with respect to the inertial frame, which is used in the computer for the calculation of the reference coordinate frame. This has disadvantages as regards the overall navigation accuracy, but also essential advantages as regards the resolution of the attitude and attitude rate information, the implementation of reliability and the flexibility of the use of strapdown systems.

Let us first have a look at the reliability of inertial navigation in plattform and strapdown usage. Platform systems now available on the market can, for instance, no longer be operated if there is failure of one gyro. The sensors still functioning on the platform can no longer be used for the navigation.

For a reliable inertial navigation three complete platform systems inclusive of computers are used. This method is applied, for instance, by the airlines for meeting the requirements for Category III landing (s. Fig. 7.4.3). The resulting increase in system reliability R, i.e. the probability of mission success, can be estimated from Fig. 7.4.9.

In this diagram R is plotted over the ratio of mission time τ divided by the MTBF (mean time between failure) T of one sensor for different set-ups of redundant configurations. According to experience the MTBF of mechanical gyros is in the order of magnitude of:

$$10{,}000\ h \leq T \leq 20{,}000\ h. \tag{7.4.27}$$

Fig. 7.4.9 is taken from [7.19] and is derived for the reliability of angular rate measurements with a strapdown system. For a rough estimate we may use it also for reliability aspects of gyro stabilization.

Although the reliability of a system having three independent platforms with failure identification through comparison is better than that of a single platform (e.g. a doubling of mission time for R = 90 %), it is less than that of a platform with three sensors on each axis where the defective gyro can be found by comparison and the remaining functioning gyros can be still be used. Note that the same number of gyros is used in each case (three systems side by side or one system with three sensors on each axis), confirming the general rule of system layout for reliability by which it is more advantageous to implement redundancy at the sensor level rather than at the system level.

In platform techniques one does not triple the number of sensors per measurement axis. The system would become very complex and there are specific construction "bottlenecks" such as sliprings and torque motors making this design impracticable.

This redundant sensor arrangement and their use for the increase in reliability can be implemented in strapdown systems without loss in efficiency from the bottlenecks jsut mentioned.

Fig. 7.4.9 shows, however, another solution for strapdown systems which is still more advantageous and cheaper - sensors are oriented with their measurement axes normal to the planes of a dodecahedron. The included angle between any adjacent pair of measurement axes is approximately 63°. In the Strapdown Inertial Reference Unit (SIRU) system described in [7.19] failure identification is still possible when two sensors have failed, and failure discovery when three sensors have failed. The accuracy of SIRU is of course affected if a sensor has failed; in comparison with that of a conventional system with three gyros in an orthogonal arrangement, SIRU however still has the same system error if two sensors have failed; for all sensors operating, the system error is 30 per cent smaller.

The other advantage of strapdown as compared to platform techniques indicated above is illustrated by the fact that one single strapdown inertial measurement unit mounted, for instance, on the turret of a tank can be used not only for precision pointing of a weapon but also for navigation. Corresponding concepts are discussed in [7.20 and 7.21].

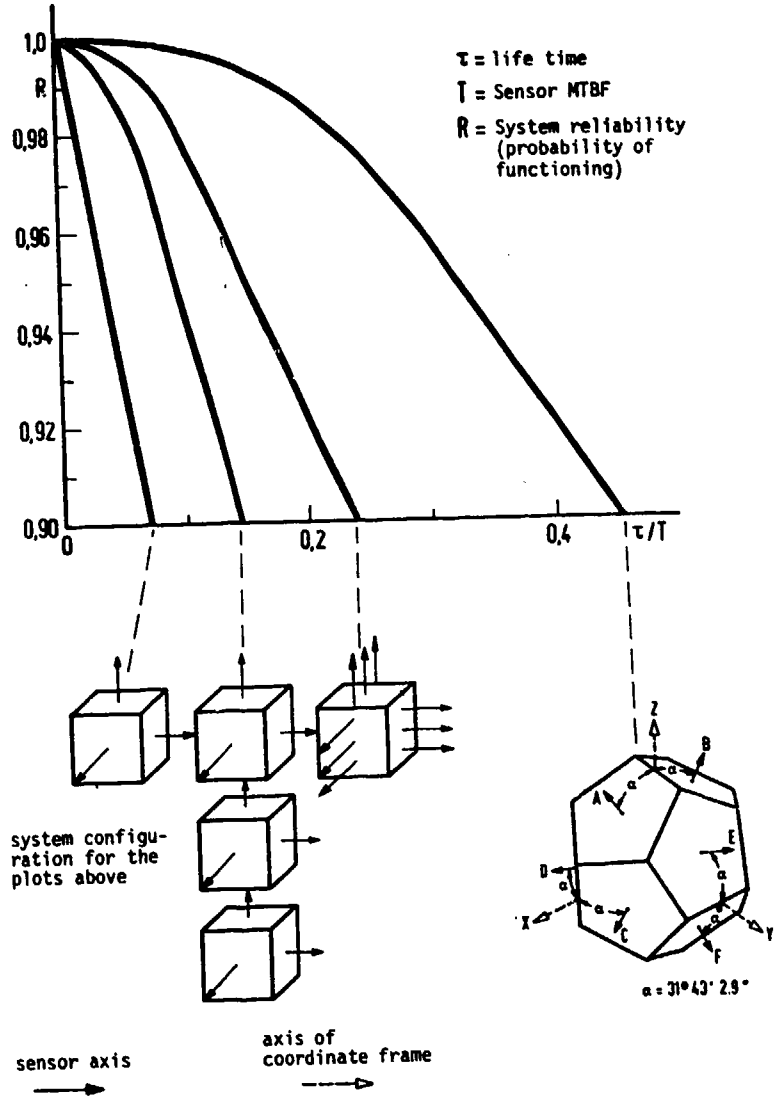

Fig. 7.4.9 System Reliability as a Function of Operating Hours for Different Configurations |7.19|

Summarizing we can state:

- In the field of avionics and flight test instrumentation one can predict as a future trend that one strapdown measurement unit will be used for taking over the functions of the totality of gyro instruments that are on board an aircraft today (rate gyro, vertical and heading references and inertial platforms).
- The high reliability required for flight guidance and navigation can be implemented in a more elegant way in strapdown techniques than in platform techniques.
- Modular strapdown sensor units can easily be adapted to specific applications facilitating the record-keeping for the ground instruments and the spare parts as well as the maintanance of the systems.
- In terms of cost of acquisition and maintanance, strapdown systems will certainly be superior to the platform systems.

This will not mean that inertial platforms will no longer be used. In the near future they will certainly remain superior to strapdown systems as far as their accuracy is concerned. Problems affecting the strapdown system accuracy are discussed in Chapter 3 with regard to sensors and will be discussed in the next few sections with regard to the computer.

7.4.4.3 The Strapdown Computer

In the discussion of strapdown computer algorithms we have to concentrate on the computation of the transformation matrix $\underline{C}_{nb}$ only and on the transformation of the acceleration vector from the body-fixed frame to the navigational frame

$$\underline{f}_n = \underline{C}_{nb}\,\underline{f}_b. \tag{7.4.28}$$

For the remaining computation in an inertial navigation or attitude and heading reference system (AHRS) the reader is referred to the previous sections describing the same problems for platform application.

The highly accurate sensor readout is done in increments as described in Chapter 4, with each pulse coming from the reset counters of the accelerometers as a velocity increment Δv ($\leq$ 1 mm/s) and coming from the reset counters of the gyros as an angle increment $\Delta\phi$($\leq$ 3 arc sec).

The transformation matrix $\underline{C}_{nb}$ is updated from the gyro measurements and the Schuler feedback (s. Eqs. (7.4.24) to (7.4.26) and Fig. 7.4.8) and the corresponding accuracy requirements are described by the following facts:

- the unit vectors of the n-coordinate frame after transformation from the b coordinate frame must remain orthogonal
- the unit vectors must keep their unity length, i.e. $\underline{C}_{nb}$ must remain normal
- the drift of $\underline{C}_{nb}$ must be lower than the gyro drift.

There are several choices for the $\underline{C}_{nb}$-updating, described more in detail in [7.18] and [7.22] to [7.25] and briefly summarized below.

7.4.4.3.1 The Direction Cosine Update

The direction cosine update is carried out according to the numerical integration of Eqs. (7.4.23) to (7.4.26). Only three of the nine elements C_{ij} (i,j = 1,2,3) of the $\underline{C}_{nb}$ matrix can be computed independently from the three measurements. The remaining six equations are derived from the condition of normality:

$$C_{i1}^2 + C_{i2}^2 + C_{i3}^2 = 1 \tag{7.4.29a}$$

or

$$C_{1i}^2 + C_{2i}^2 + C_{3i}^2 = 1 \tag{7.4.29b}$$

with i = 1,2,3

and the condition of orthogonality, when the product of two unit vectors vanishes:

$$C_{i1}\,C_{j1} + C_{i2}\,C_{j2} + C_{i3}\,C_{j3} = 0 \tag{7.4.30a}$$

or

$$C_{1i}\,C_{1j} + C_{2i}\,C_{2j} + C_{3i}\,C_{3j} = 0 \tag{7.4.30b}$$

with i = 1,2,3 and j = 1,2,3 but $i \neq j$.

The following relationship is equivalent with Eq. (7.4.30):

$$C_{ij} = -A_{ij} \tag{7.4.30c}$$

with A_{ij} = cofactor.

The direction cosine update thus always gives an orthogonal and normal matrix, briefly called an orthonormal matrix. The computational burden is higher as compared to the quaternions mentioned below (s. [7.18] and [7.22] to [7.25]).

7.4.4.3.2 The Euler Angle Update

The relationships between the rate of change of the vehicle's roll (ϕ), pitch (θ) and yaw (ψ) angles and the body fixed angular rates $\omega_{x,y,z}$ are (s. [7.26]):

$$\begin{pmatrix} \dot{\phi} \\ \dot{\theta} \\ \dot{\psi} \end{pmatrix} = \begin{pmatrix} 1 & \sin\phi\tan\theta & \cos\phi\tan\theta \\ 0 & \cos\phi & -\sin\phi \\ 0 & \sin\phi/\cos\theta & \cos\phi/\cos\theta \end{pmatrix} \begin{pmatrix} \omega_x \\ \omega_y \\ \omega_z \end{pmatrix} . \tag{7.4.31a,b,c}$$

These differential equations can be integrated at high speed in the computer and the transformation matrix $\underline{C}_{nb}$ assembled according to Eq. (7.4.24b) just prior to the transformation of the acceleration.

This three parameter transformation matrix update always results in an orthogonal matrix but has a singularity at $\theta = \pm 90^0$ (s. Eq. (7.4.31)) comparable to "gimbal lock" of a three-gimbal platform (s. Section 5.4). It requires the computation of trigonometric functions and is only of advantage in special cases [7.27].

7.4.4.3.3 The Quaternion Update Algorithms

This procedure is most widely used in present strapdown systems and will be discussed more in detail based on [7.18] and [7.22] to [7.25].

The orientation of a coordinate frame (subscript n) with respect to a reference frame (subscript b) can be uniquely described by one rotation through an angle δ about one axis defined with respect to the reference frame through the three direction cosines, i.e. through the coordinates of its three unit vectors (s. Fig. 7.4.10).

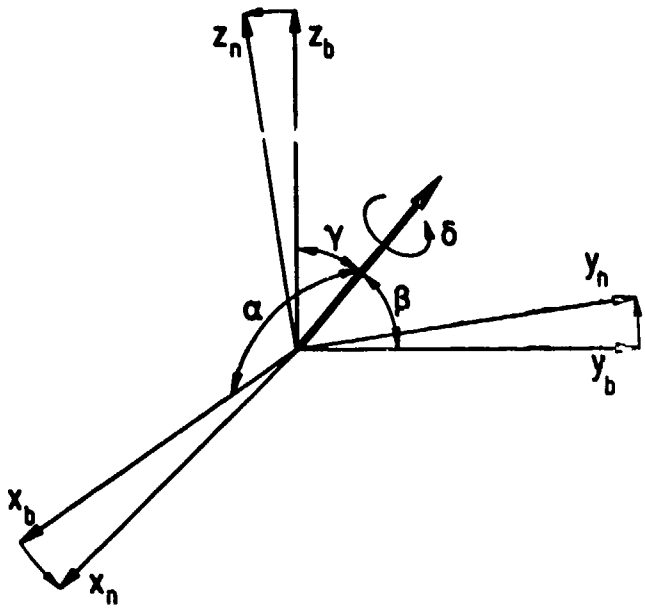

Fig. 7.4.10 Illustration of The Parameters Describing Quaternions

These four parameters are comprised in the four quaternion elements

$$q_0 = \cos \delta/2$$

$$q_1 = \cos \alpha \sin \delta/2$$

$$q_2 = \cos \beta \sin \delta/2$$

$$q_3 = \cos \gamma \sin \delta/2. \qquad (7.4.32a \text{ to } d)$$

The quaternion $\underline{q}'$ is written as a one dimensional matrix

$$\underline{q}' = (q_0 \quad \underline{q})^T = (q_0 \quad q_1 \quad q_2 \quad q_3)^T, \qquad (7.4.33)$$

i.e., as a combination of a scalar q_0 and a vector $\underline{q}$ with the orthogonal components $q_{1,2,3}$. Such a combination will be marked also in the following by a prime.

From Eq. (7.4.32) it is obvious that a meaningful set of quaternion elements has to satisfy the condition of normality, the so-called norm $N(\underline{q})$ being:

$$N(\underline{q}) = \sum_{i=0}^{3} q_i^2 = 1. \qquad (7.4.34)$$

The transformation matrix $\underline{C}_{nb}$ is composed of the quaternion elements in the following way

$$\underline{C}_{nb} = \begin{pmatrix} (q_0^2 + q_1^2 - q_2^2 - q_3^2) & 2(q_1 \cdot q_2 - q_0 \cdot q_3) & 2(q_1 \cdot q_3 + q_0 \cdot q_2) \\ 2(q_1 \cdot q_2 + q_0 \cdot q_3) & (q_0^2 + q_2^2 - q_1^2 - q_3^2) & 2(q_2 \cdot q_3 - q_0 \cdot q_1) \\ 2(q_1 \cdot q_3 - q_0 \cdot q_2) & 2(q_0 \cdot q_1 + q_2 \cdot q_3) & (q_0^2 + q_3^2 - q_1^2 - q_2^2) \end{pmatrix}. \qquad (7.4.35)$$

The quaternion update is based on the differential equation:

$$\dot{\underline{q}}'(t) = \underline{\Omega}(t)\, \underline{\omega}'(t)/2, \qquad (7.4.36)$$

which is programmed in the computer as:

$$\underline{q}'(t) = \underline{\Omega}(t-T^s)\, \underline{X}'(t)., \qquad (7.4.37)$$

where

$$\underline{Q} = \begin{pmatrix} q_o & -q_1 & -q_2 & -q_3 \\ q_1 & -q_o & -q_3 & -q_2 \\ q_2 & -q_3 & q_o & -q_1 \\ q_3 & -q_2 & q_1 & q_o \end{pmatrix} \tag{7.4.38}$$

$$\underline{\omega}' = (0 \quad \underline{\omega})^T = (0 \quad \omega_x \quad \omega_y \quad \omega_z)^T \tag{7.4.39}$$

and

$$\underline{\chi}'(t) = (\chi_o(t) \quad \underline{\chi}(t))^T = (\chi_o(t) \quad \chi_1(t) \quad \chi_2(t) \quad \chi_3(t))^T. \tag{7.4.40}$$

The components of χ' are derived from the angular increments $\underline{\Delta\Phi}(t)$ delivered by the gyros and the Schuler-feedback (s. Eq. (7.4.26)) for the time increment from $t-T^S$ to t.

$$\underline{\Delta\Phi}(t) = \int_{t-Ts}^{t} \underline{\omega}(t)\, d\tau = (\Delta\Phi_x \quad \Delta\Phi_y \quad \Delta\Phi_z)^T. \tag{7.4.41}$$

Different approximations for χ are derived in [7.22] to [7.25]:

$$\begin{aligned} \underline{\chi}'(t) &= (\chi_o(t) && \underline{\chi}(t) &&)^T \\ &= (1 && \tfrac{1}{2}\,\underline{\Delta\Phi}(t) &&)^T \ 1^{st} \text{ approximation} \\ &+ (\tfrac{1}{8}|\underline{\Delta\Phi}^2(t)| && 0 &&)^T \ 2^{nd} \text{ approximation} \\ &+ (0 && -\tfrac{1}{48}|\underline{\Delta\Phi}^2(t)|\underline{\Delta\Phi}(t) && \\ & && +\tfrac{1}{24}\,\underline{\Delta\Phi}(t-T^S)\times\underline{\Delta\Phi}(t))^T && 3^{rd} \text{ approximation.} \end{aligned} \tag{7.4.42}$$

The first approximation needs no further comment, the second approximation gives a correction to the scalar part of $\underline{\chi}'$ and the third approximation to the vector part including the angle increment of the previous cycle.

The quaternion always results in an orthogonal transformation matrix but requires normalization due to numerical errors. This can be carried out at a much lower rate, for instance every 10th update cycle based on the following equations (s. [7.22] to [7.25]):

$$q'_{new} = q'_{old}/(N(q))^{1/2}. \tag{7.4.43}$$

Based on Eqs. (7.4.24a,b) and (7.4.35) the Euler angles are computed as follows:

$$\phi = \tan^{-1}\frac{C_{32}}{C_{33}} = \tan^{-1}\frac{2(q_o\, q_1 + q_2\, q_3)}{q_o^2 - q_1^2 - q_2^2 + q_3^2}$$

$$\theta = \tan^{-1}\frac{-C_{31}}{(1-C_{31}^2)^{1/2}} = \tan^{-1}\frac{2(q_1\, q_3 - q_o\, q_2)}{[1-4(q_1\, q_3 - q_o\, q_2)^2]^{1/2}}$$

$$\psi = \tan^{-1}\frac{C_{21}}{C_{11}} = \tan^{-1}\frac{2(q_o\, q_3 + q_1\, q_2)}{q_o^2 + q_1^2 - q_2^2 - q_3^2} \tag{7.4.44a,b,c}$$

For the initialization of Eq. (7.4.37) based on known elements of C_{nb} or known Euler angles the following relationships can be used:

$$q_o = \tfrac{1}{2}\,(1 + C_{11} + C_{22} + C_{33})^{1/2}$$

$$q_1 = (C_{32} - C_{23})/(4\, q_o)$$

$$q_2 = (C_{13} - C_{31})/(4\, q_o)$$

$$q_3 = (C_{21} - C_{12})/(4\, q_o) \tag{7.4.45a+d}$$

These equations have a singularity for $q_o = 0$, i.e. for the strapdown system pointing south ($\psi = 180^o$). A more general strategy for initialization without constraints is presented in [7.28].

7.4.4.3.4 Errors in the Computation of the Transformation Matrix

Errors in the computation of the transformation matrix are caused

- by the drift of the gyros or the errors in the Schuler feedback signals
- by the so-called pseudoconing error
- by computational errors in the computer.

Since in a strapdown system the gyro axes are body-fixed, the effects of gyro drift differ considerably as compared to platform systems. When the aircraft changes its heading the gyro drift builds up an error angle in a different direction and its overall effect on system performance is reduced.

We will see in a following section that the requirements for the strapdown accelerometers as compared to platform accelerometers are more stringent in a manouvering aircraft.

For understanding the pseudoconing error let us first have a look at the kinematics of the coning motion shown in Fig. 7.4.11. We assume the x and y axes of the strapdown inertial measurement unit (IMU) to be horizontal and to carry out angular vibrations of

$$\omega_x = \alpha\,\Omega \sin \Omega t \approx \dot{\phi}$$

$$\omega_y = \beta\,\Omega \sin (\Omega\, t + \varphi) \approx \dot{\theta} \qquad (7.4.46a,b)$$

with $\dot{\phi}$ and $\dot{\theta}$ being the roll and pitch angular rates (s. Eqs. (7.4.31a,b)). If the yaw rate $\dot{\psi}$ of the IMU remains zero in the mean

$$\bar{\dot{\psi}} = 0, \qquad (7.4.47)$$

the vertical gyro will measure a mean angular rate of

$$\bar{\omega}_z = \frac{1}{2}\,\alpha\beta\,\Omega \sin \varphi. \qquad (7.4.48)$$

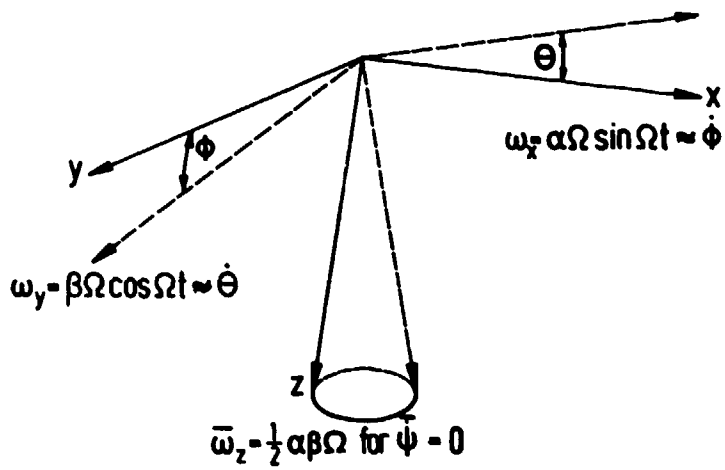

Fig. 7.4.11 The Coning Motion

From this we may deduce that a pseudoconing drift can arise:

- if the phase of a two-axes angular vibration is not correctly detected, e.g. due to bandwidth limitation of the sensors, of the signal readout or of the quaternion update process
- if a single-axis angular vibration is erronously measured as a two-axes measurement, e.g. due to the angular acceleration sensitive drift of mechanical gyros (s. Tables 3.2.1b and 3.2.2b)
- if the sequence of processing of a two axis angular vibration in the computer is not correct, thus causing a phase shift.

The first may be present in inertial navigation systems employing laser gyros with mechanical dither lock-in compensation. In the Honeywell laser INS this is taken care of by a special coning electronics.

The latter is called "commutation error" which gives us a keyword for the computational errors in the computer, mentioned above. They are caused by the fact that the transformation matrix update algorithms are solved in the digital computer sequentially and in quantized increments. This approximation to a continuous process results in the following errors (s. [7.18] and [7.22] to [7.25]):

- the commutation errors (s. above)
- the numerical integration errors
- the round-off errors
- the quantization errors.

The numerical integration errors arise from the fact that the differential equation (7.4.36) for the quaternions, for instance, having time varying $\underline{\Omega}$ (t) and $\underline{\omega}'$(t) is approximated by a difference equation

with $\underline{Q}$ (t-ΔT) taken at the beginning of the interval and $\underline{X}'$ the angular increments provided by the gyros and the Schuler feedback. The algorithms mentioned in Eq. (7.4.42) for the quaternions are based on a truncated power series and the corresponding integration errors per step are derived analytically in [7.22] to [7.25], for instance. Table 7.4.1 summarizes the results for algorithm drift and computer load, which indicate that it is advantageous to use the 3rd order algorithms. To further increase the order of numerical integration algorithms does not bring about any reward because the improvements get lost in in the roundoff errors.

Quaternion update approximation (s. Eq. (7.4.42))	1st	2nd	3rd
Drift for constant input rate ω and update frequency f	$\frac{1}{12}\frac{\omega^3}{f^2}$	$\frac{1}{24}\frac{\omega^3}{f^2}$	$\frac{1}{480}\frac{\omega^5}{f^4}$
Required update frequency [Hz] for 0.1 °/h drift and 1 rad/s input rate	415	293	8
Number of additions and subtractions	24	30	45
Number of multiplications	24	31	52
Program memory (15 bit words)	415	447	540
Computing time [ms] per update[1)]	0.55	0.64	0.88
Computer load [%] including velocity transformation at 50 Hz[1,2)]	26	22	4

1) Honeywell DDP-516 computer

2) Conversion of quaternion to transformation matrix requires 0.42 ms and the velocity increments transformation 0.27 ms.

Table 7.4.1 Algorithm Drift and Computer Load for Quaternion Update[2)] (s. [7.22] to [7.24])

Since the quaternion update does not yet include the computation of the transformation matrix and the transformation of the velocity increments, additional computer time has to be added as mentioned in the footnote of Table 7.4.1. It is taken into account in the last row of the table.

The roundoff errors are similar to the errors arising in analog-to-digital (ADC) conversion plus subsequent integration (s. Section 4.3). There is only one difference. The ADC output has to be multiplied with the sampling interval T^s for proper scaling so that the adder's output Δφ corresponds to the integral of ω_I. In the present case the integration process is already carried out within the gyros and the transformation update is a mere summation in principle. The roundoff error standard deviation σ(Cij) of the transformation matrix elements obeys the following relationship:

$$\sigma(C_{ij}) \sim \text{LSB}\ (t/T^s)^{1/2}. \tag{7.4.49}$$

The quantization errors have already been discussed in Section 4.3. They are the stochastic errors in an integrator fed by the output of a voltage-to-frequency converter (VFC) or pulse-rebalance-loop (PRL) as shown in Figs. 4.2.2 and 4.2.3. The errors are due to the fact that the angular increments Δφ for updating the transformation matrix are processed in the computer in integer fractions of one pulse $\Delta\phi^p$ (s. Eq. (4.2.4)). In the angular increment Δφ the information on this pulse $\Delta\phi^p$ is not lost, but delayed by one sampling time increment. The corresponding noise is independent of time and sampling interval. It depends only on the layout of the VFC or PRL of mechanical gyros or on the scale factor (i.e. the perimeter) of the laser gyro, respectively.

The errors just discussed, their dependence on certain system parameters and countermeasures for their minimization are summarized in Fig. 7.4.12.

All errors depend on the angular increment Δφ, i.e., for a given dynamic environment of the vehicle, on the update cycle T^s as indicated in Fig. 7.4.12. The update frequency $1/T^s$ is 50 to 100 Hz in the strapdown systems available at present. In addition to the update cycle, the wordlength in the computer - double precision required in general in a 16 bit [illegible] [7.18] - and the choice of the update algorithm (s. Eq. (7.4.42)) also affect the update accuracy.

7.4.4.3.5 The Transformation of the Velocity Increments

Exact inertial navigation requires the continous transformation of the body-fixed acceleration signal $\underline{f}_b$ into the navigational frame and the continuous correction of Coriolis acceleration prior to the first integration indicated in Fig. 7.4.8.

In the strapdown computer $\underline{f}_b$ is integrated during the sampling interval T^s

$$\Delta v_b(t) = \int_{t-T^s}^{t} \underline{f}_b(\tau)\, d\tau \tag{7.4.50}$$

and the velocity increments only are transformed into the navigational frame:

$$\Delta \underline{v}_n(t) = \underline{C}_{nb}(t)\ \Delta \underline{v}_b(t). \tag{7.4.51}$$

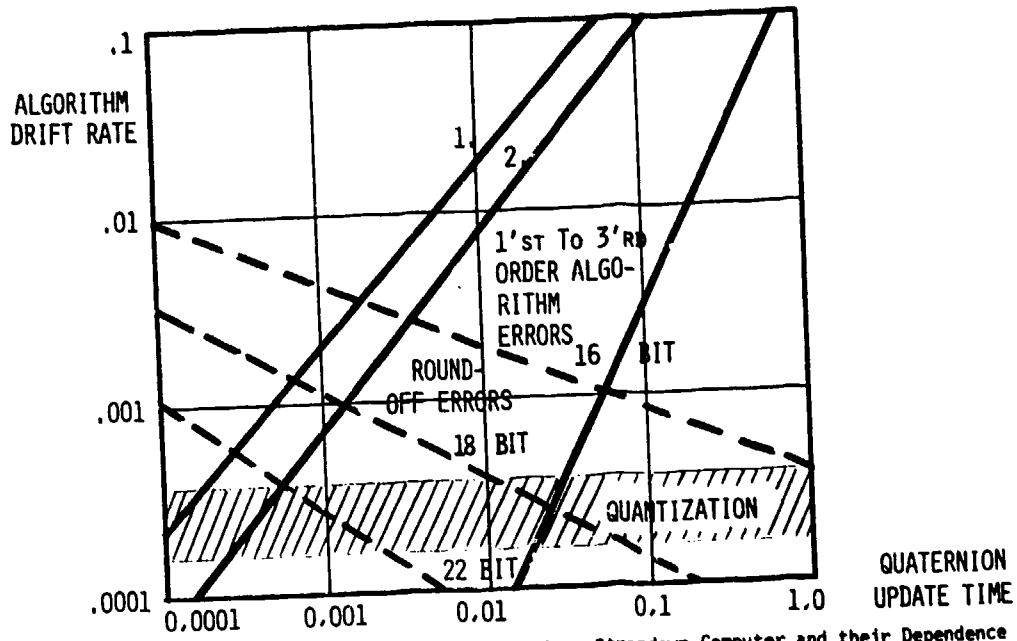

Fig. 7.4.12 Qualitative Plot of the Computational Errors in a Strapdown Computer and their Dependence on the Integration Algorithms and Computer Parameters (note: absolute values on scales are function of input dynamics)

take into account that the continuous integration of $\Delta \underline{v}_n(t)$ when solved by partial integration

$$\Delta \underline{v}_n(t) = \int_{t-T^s}^{t} f_n(\tau)\, d\tau = \int_{t-T^s}^{t} \underline{C}_{nb}(\tau)\, \underline{f}_b(\tau)\, d\tau = \underline{C}_{nb}(t)\, \Delta \underline{v}_b(t) - \int_{t-T^s}^{t} \underline{C}_{nb}\, \underline{\Omega}^{nb}\, d\tau' \int_{t-T^s}^{\tau'} f_b(\tau)\, d\tau \tag{7.4.52}$$

contains also the changes of $\underline{C}_{nb}$ and $\underline{f}_b$ during the sampling interval T^s. The second approximation of the velocity increments reads accordingly:

$$\Delta \underline{v}_n(t) = \underline{C}_{nb}(t)\, (\underline{I} - \tfrac{1}{2}\, \Delta \underline{\Theta})\, \Delta \underline{v}_b, \tag{7.4.53}$$

where $\Delta \underline{\Theta} = \underline{\Omega}\, T^s$ is the skew symmetric angle increment matrix according to Eq. (7.4.25). The second approximation gives thus an improvement of 10^{-2} g if the angular rate is 1 rad/s the acceleration is 1 g and the sampling frequency is 50 Hz. It is shown in [7.23] that this approximation meets the accuracy requirements of strapdown systems.

7.4.4.3.6 Acceleration and Angular Rate Extraction for the Purpose of Aircraft Control and Flight Tests

If the inertial sensor is equipped with an analog rebalance loop with subsequent voltage-to-frequency conversion for generating the velocity or angle increments, the acceleration and angular rate can be taken from the analog signal. Before digitizing and sampling this signal, the high bandwidth has to be limited according to the sampling theorem, preferably by using Butterworth filters (s. Section 4.4). If the inertial sensor is equipped with a pulse-rebalance loop or if laser gyros are used, which both deliver the measurement in pulses, the rate extraction has to be done digitally. The simple computation

$$\dot{V}(nT^s) = \frac{1}{T^s}\, \Delta V(nT^s) \quad \text{or} \quad \omega(nT^s) = \frac{1}{T^s}\, \Delta \Phi(nT^s) \tag{7.4.54}$$

may be very noisy (s. Sections 4.2.3 and 4.2.4). For noise suppression Eq. (4.4.16) may be used, which is equivalent to a series of two first order lags (s. Eq. (4.4.15)).

In the Honeywell laser inertial reference system the acceleration is tapped before the voltage-to-frequency conversion and subsequently filtered with a Butterworth filter of

$$F(s) = \frac{1}{1 + 0.028s + 0.0004s^2}, \tag{7.4.55}$$

limiting the bandwidth (-3dB) to 8 Hz. The laser gyro pulses are filtered with a digitally mechanized first order lag so that the bandwidth is 5 Hz.

7.4.4.4 Practical Aspects of Strapdown System Integration - the Experimental Strapdown System of DFVLR (MOSY)

The functional diagram of a strapdown system including information on the various requirements for sensor readout, error compensation and computation as discussed in the different sections of this book is presented in Fig. 7.4.13. The ranges of the frequencies mentioned there are taken from existing strapdown systems, for example, the Honeywell and the Litton strapdown inertial reference systems employing ring laser gyros as shown in Fig. 7.4.14. Tables 7.4.2 and 7.7.1b summarize more details on these systems.

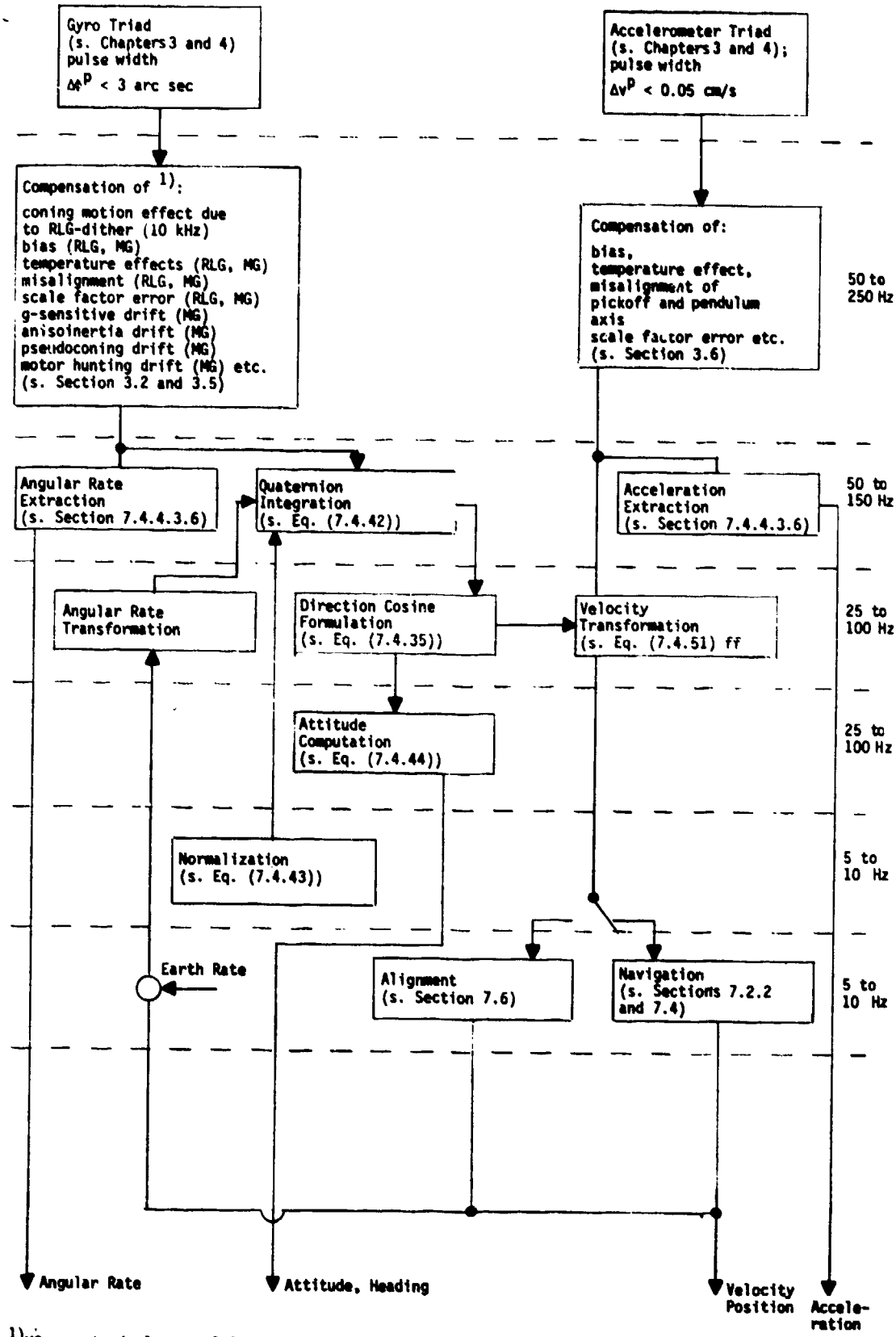

1) MG = mechanical gyro; RLG = ring laser gyro

Fig. 7.4.13 Functional Diagram of a Strapdown Inertial Reference System

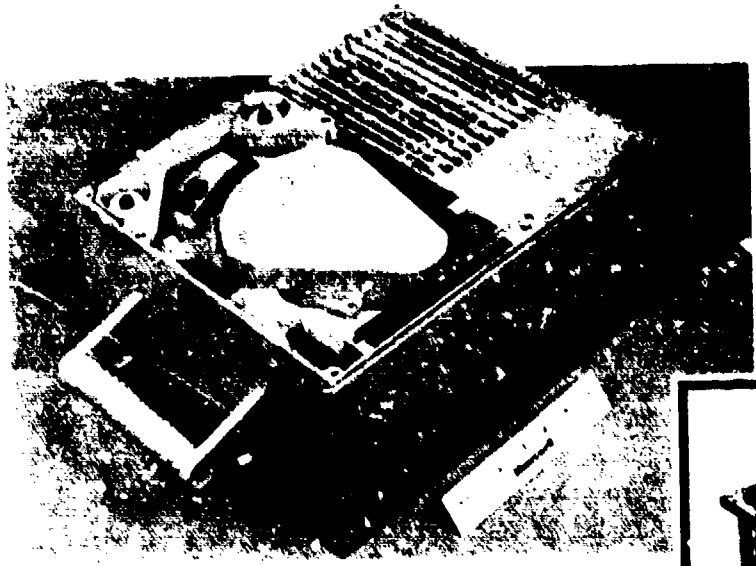

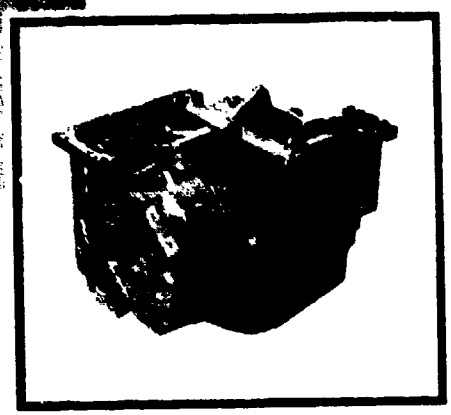

a) Honeywell Laser Inertial System

b) Litton Laser Inertial System

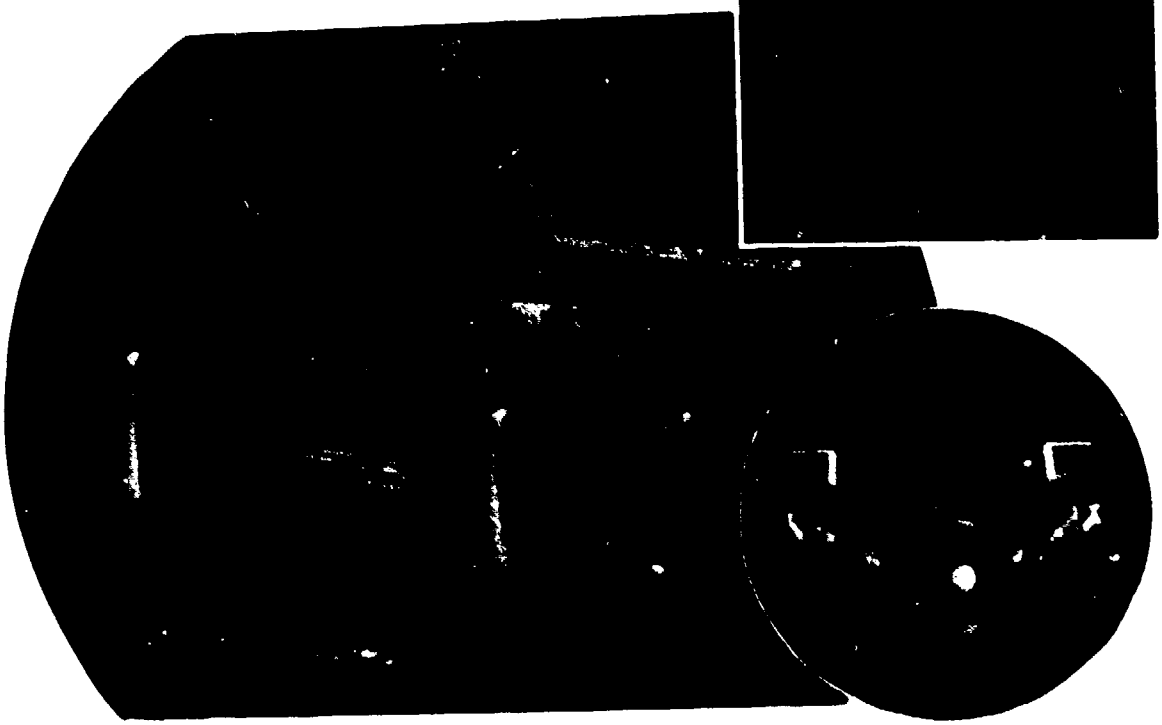

Fig. 7.4.14 The Honeywell and the Litton Inertial Reference Systems

Task	Execution Rate (Hz)	Words Required	% Duty Cycle
Executive	256	400	2
Fast Instrument Compensation	256	150	14
Medium Instrument Compensation	128	200	6
Quaternion Integration	128	300	15
Direction Cosines	64	300	5
Attitude/Velocity Transform	64	350	5.5
Dits	128	400	3
Vehicle Rates	16	550	5
Navigation (Fast)	8	100	2
Navigation (Medium)	2	600	0.5
Navigation (Slow)	1	350	0.5
Mode Controller	1	1650	1
Self Test	2	1050	2
Math Library	-	400	-
Data Base	-	1500	-
TOTALS		6800 ROM *) 1500 RAM	61.5

Table 7.4.2 Operational Software Task Budgets in the Litton LTN-80 Strapdown System Computer

The coning motion effect compensation due to the mechanical dither of the ring laser gyros as mentioned in Fig. 7.4.13 is taken care of by means of special microprocessor circuits in the Honeywell system. They sum up and down, at very high frequency, the cross product of corresponding gyro readings and release the net results for compensation.

The motor hunting drift compensation is not based on the modelling of Fig. 3.2.8; if the rotor spin speed with respect to the case can be measured, any deviation from a nominal value can be corrected with a corresponding correction of the gyro scale factor.

The computation of the other error terms is straightforward, once the coefficients of the error models (s. Tables 3.2.1 and 3.2.2) are known.

For future research in the field of inertial strapdown technology DFVLR has developed in cooperation with the Technical University of Braunschweig an Experimental Strapdown System (MOSY), shown in Fig. 7.4.15 and described more in detail in [7.29]. It consists of an inertial measurement (IMU) employing interchangeable sensor modules each including temperature control and binary pulse width modulation readout electronics (s. Section 4.2.4). The accelerometers are of the type Litef B-250 and the gyros Hamilton Standard RI-1010.

The strapdown computer consists of multiple LSI-11/2 micro computers. A very flexible laboratory interface system - CAMAC developed by European Atomic Research Centers - assures the communication between the microcomputers, the IMU and external sensors.

The supervision of the proper function of the sensor modules is shared by the micro computer system and the sensor control and alarm unit (SCA). A plausibility and bit-error check is made in the first computer which interfaces the sensor modules via up-down counters. After detecting a hardware error an alarm can be messaged to the computer control and display unit (CCD) and from there to the SCA which generates an automatic gyro motor power supply shut off. This control loop covers the most important failures within the sensor itself and the electronic rebalance circuitry.

All frequencies in the MOSY system are generated in a Central Time Base (CTB) Unit from a temperature-controlled 10 MHz quartz-generator with a frequency stability of 10^{-8}.

For command and display purposes a Computer Control Display (CCD) was developed. It not only allows for the quicklook of information from MOSY but also for feeding information into the computer via a keyboard.

Test results of the system are presented in Chapter 9.

7.4.4.5 Simulation Results of a Strapdown System in a Benign and in a Highly Dynamic Environment

Programs for simulating a strapdown system are very effective tools for obtaining an insight into the contribution of different sensor and algorithm errors to system performance. Such complex programs have been developed during the past few years at DFVLR. This section gives the summary of some simulation re-

*) ROM = Read Only Memory
RAM = Random Access Memory

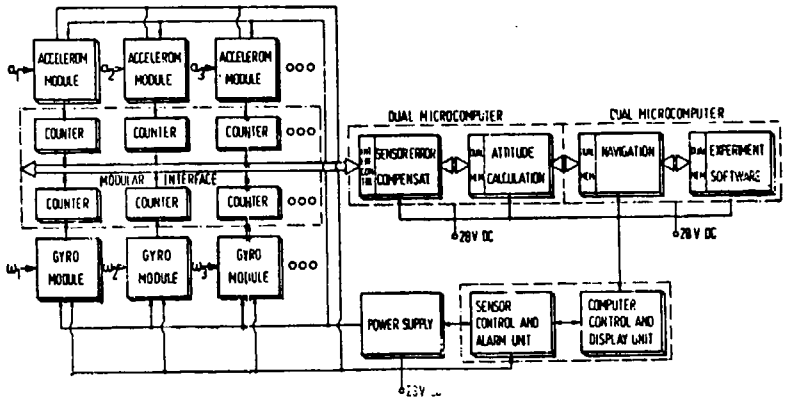

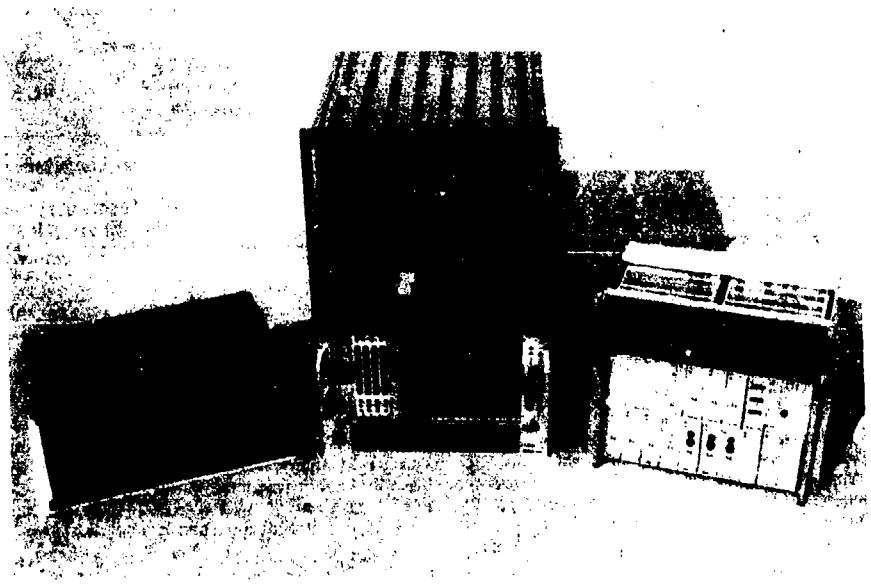

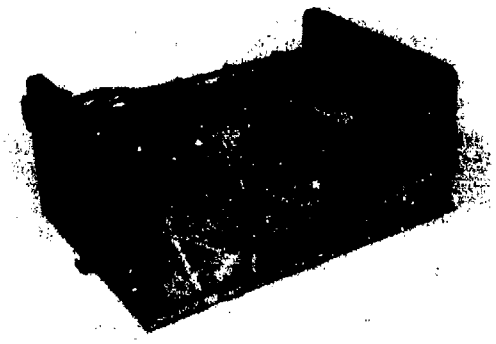

Fig. 7.4.15 The DFVLR Modular Experimental Strapdown System (MOSY)

sults [7.30] of the strapdown system position errors developed during a simulated flight time of 2600 s:

- on a straight flight of a transport aircraft (TA) flying at 540 km/h towards the west including take-off and a 360° turn after 1500 s (maximum take-off acceleration 3 m/s^2, maximum yaw rate 2 °/s and roll rate 6 °/s, maximum roll acceleration 6 $°/s^2$) and

- on a highly dynamic flight of a remotely piloted vehicle (RPV) flying at 990 km/h towards the east for a distance of 280 km including take-off and landing at the starting point and several maneuvers in yaw, pitch, roll and terrain following (maximum take-off acceleration 50 m/s^2, maximum yaw rate 4 °/s and roll rate 200 °/s, maximum roll acceleration 660 $°/s^2$).

Table 7.4.3 gives a summary of all error contributors, whereby several errors were combined in groups. The numerical values are fairly small and they should be understood as 1σ-residual errors after compensation.

Table 7.4.4 summarizes some characteristics of the strapdown system and Fig. 7.4.16 the simulation results.

Number	Error Source	Numerical Value
1	algorithm	
2	azimuth misalignment	3.4 arc min
3	gyro fixed drift	0.01 °/h
4	gyro g-dependent drifts	
	unbalance	0.02 °/h/g
	anisoelasticity	0.03 °/h/g^2
5	gyro ω-dependent drifts	
	axes misalignment	6 arc sec
	fixed scale factor error	$3 \cdot 10^{-5}$
	asymmetry scale factor error	$3 \cdot 10^{-6}$
	quadratic nonlinearity scale factor error	$6 \cdot 10^{-4}$ °/h/(°/s)^2
	angular acceleration drift	0.04 °/h/(°/s^2)
	anisoinertia drift	0.4 °/h/(°/s)^2
6	accelerometer bias	10^{-4} g
7	additional accelerometer errors	
	misalignment	6 arc sec
	fixed scale factor error	10^{-5}
	asymmetry scale factor error	10^{-5}
	quadratic nonlinearity scale factor error	10^{-5} g^{-1}
	cubic nonlinearity scale factor error	10^{-6} g^{-2}
	cross coupling	10^{-5} g^{-1}

Table 7.4.3 Summary of the Residual Sensor Errors of Strapdown System Simulation

Transformation matrix computation	
algorithm	quaternion 3rd order
update frequency	100 Hz
normalization frequency	5 Hz
velocity transformation	
algorithm	3rd order
frequency	20 Hz
angular pulse weight	0.9 arc sec
velocity pulse weight	$1.85 \cdot 10^{-3}$ mm/s
navigation computation frequency	20 Hz

Table 7.4.4 Characteristics of the Simulated Strapdown System

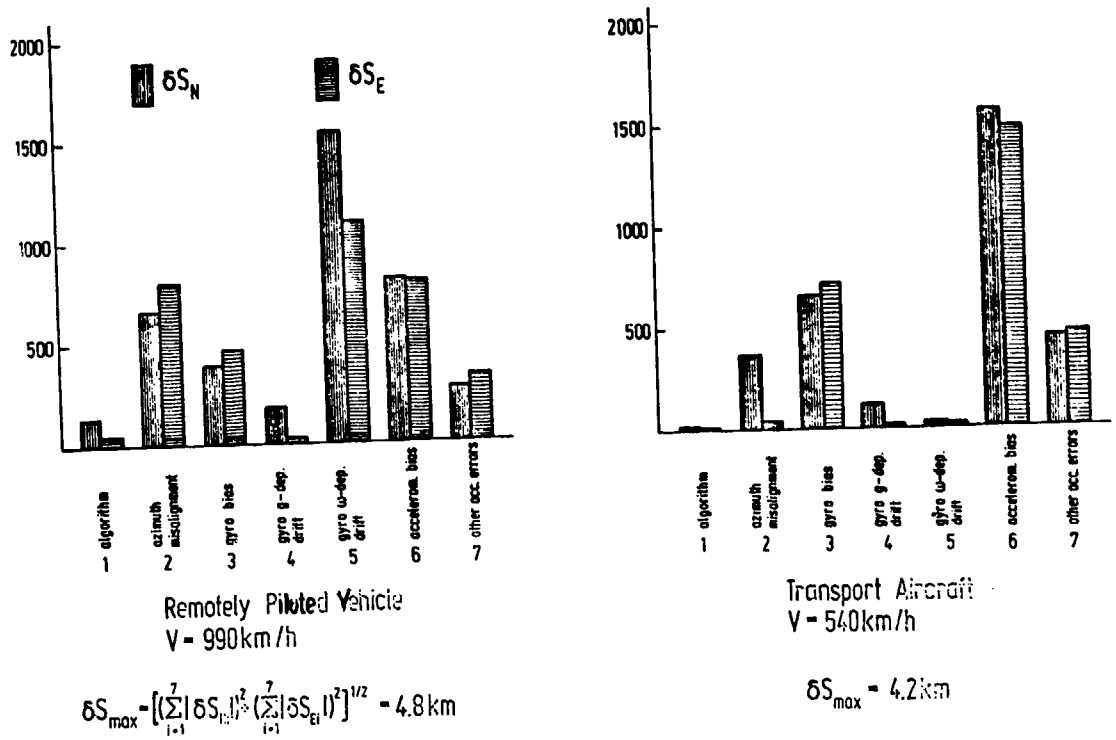

Fig. 7.4.16 Simulation Results for a Strapdown System in Two Different Types of Aircraft

In the benign environment of the transport plane the accelerometer biases are the main error contributors. If the aircraft heading during the self alignment mode differs from the heading during the subsequent flight, which in general is the case, the equilibrium at the end of the alignment mode is disturbed leaving a constant acceleration error of up to twice the amount of the bias (s. Section 7.5). In this respect the error growth of the strapdown system differs considerably from that of the platform system. This is not the case for the effect of constant gyro drift in straight flight; the strapdown and platform system performances are alike in this respect.

The azimuth misalignment primarily causes the cross-track error (s. Section 7.3.2), i.e., for the westerly flying transport plane a position error in the north-west channel. The algorithm error is negligible.

In the highly dynamic environment of the remotely piloted vehicle (RPV) the pseudoconing error, i.e. the gyro drift due to angular acceleration (s. Section 7.4.4.3.4 and Tables 3.2.1 and 3.2.2), is dominant. Because of the RPV's return to the starting point other errors are smaller than in the first case, such as the errors due to accelerometer bias and due to gyro drift. The algorithm errors are still negligible as compared to the sensor errors, but are approximately 8 times the amount in the benign environment of the transport case.

7.5 The Linearized Error Dynamics of Inertial Navigation Systems

In the previous sections we have become familiar with several inertial navigation systems, differing in the mechanization of the reference coordinate frames in which the accelerometers carry out their measurements. They all have in common the generation of information on the aircraft's, attitude and heading, ground speed and position with respect to the geographic coordinate frame.

In this section we will briefly discuss the linearized error dynamics of all systems, which is the basis for modelling it in a Kalman filter.

The two vector equations for the error dynamics are derived in [7.13] and [7.31], for instance. They describe firstly the rate of change $\underline{\varepsilon}_n$ of the computed navigational coordinate frame's misalignment with respect to the true coordinate frame about the north, east and down axes (s. Eqs. (7.3.23a,b,c) for the north indicating system):

$$\dot{\underline{\varepsilon}}_n = \underline{\varepsilon}_n \times \underline{\omega}^{in} + \delta\underline{\omega}^{in} + \delta\underline{\omega}^{nr} + \underline{C}_{nr}\,\underline{D} \qquad (7.5.1)$$

with the effects of:

- $\underline{\omega}^{in}$: earth rate plus transport rate on misaligned system or platform (feedback Ⓒ in Figs. 7.2.1 and 7.3.4)
- $\delta\underline{\omega}^{in}$: erroneous Schuler feedback (feedback Ⓐ in Figs. 7.2.1 and 7.3.4)
- $\delta\underline{\omega}^{nr}$: erroneous slewing about vertical axis in wander azimuth mechanization
- $\underline{D}$: gyro drift

Secondly they describe the acceleration error $\delta\dot{\underline{v}}_n$ in the north and east axes (s. Eqs. (7.3.23d,e) for the north indicating system):

$$\delta\dot{\underline{v}} = -\underline{\varepsilon}_n \times \underline{f}_n - \delta\underline{c}_n + \delta\underline{g}_n + (\underline{\underline{I}} - \underline{\varepsilon}_n \times)\, \underline{\underline{C}}_{nr}\, \underline{B}$$

with the effects of

- $-\underline{\varepsilon}_n \times \underline{f}_n$: acceleration measured in misaligned system or platform
- $\delta\underline{c}_n$: erroneous Coriolis acceleration compensation (feedback Ⓑ in Figs. 7.2.1 and 7.3.4)
- $\delta\underline{g}_n$: deflection of the vertical (s. Fig. 2.4)
- $(\underline{\underline{I}} - \underline{\varepsilon}_n \times)\, \underline{\underline{C}}_{nr}\, \underline{B}$: accelerometer error including the effect of correlated misalignment and accelerometer error (sculling in strapdown systems)

(7.5.2)

This confirms that Eq. (7.4.23) may serve as a basis for modelling the error dynamics of any inertial navigation system in a Kalman filter, the only difference lying in the modelling of the sensor errors, which act in the north, east and down axes via the transformation matrix $\underline{\underline{C}}_{nr}$.

For the north indicating systems (NIS):

$$\underline{\underline{C}}_{nr} = \underline{\underline{I}}, \tag{7.5.3}$$

as can be seen from Eq. (7.4.23).

For the wander azimuth inertial navigation systems

$$\underline{\underline{C}}_{nr} = \underline{\underline{C}}_{na}, \tag{7.5.4}$$

(s. Eq. (7.4.8)) with the wander azimuth angle α derived from Eq. (7.4.4) for the Litton systems and from Eq. (7.4.5) plus $\dot{\beta}$ = 1 RPM for the Delco Carousel IV systems.

For the pseudo-pole inertial navigation systems, Eq. (7.5.4) is also valid. The wander azimuth α has to be computed from Eq. (7.4.19), which can be simplified for small angles μ.

For the inertial navigation systems with space-stabilized platform

$$\underline{\underline{C}}_{nr} = \underline{\underline{C}}_{ni} \tag{7.5.5}$$

(s. Eq. (7.4.21)).

And finally for the strapdown systems we have the effect of the sensor errors in the north, east and down directions changing with the aircraft manouvers

$$\underline{\underline{C}}_{nr} = \underline{\underline{C}}_{nb} \tag{7.5.6}$$

(s. Eq. (7.4.24)). The strapdown system errors are thus comparable to the errors of a north indicating platform system in a straight flight and benign environment, but they differ considerably from it if the aircraft is manouvering (s. Section 7.4.4.5). It is an advantage that in the latter case the gyro drift also changes its direction, but it is a disadvantage that the equilibrium at the end of the self-alignment mode (s. Eqs. (7.6.2a to c)) between east-west gyro drift and azimuth misalignment as well as between horizontal misalignments and accelerometer biases is disturbed. After a change of 180° in yaw angle these sensor biases drive the system error with twice their steady state amount. This indicates that very tight requirements need to be set up for not only the strapdown gyros but also the accelerometer.

7.6 Self-Alignment of Platform and Strapdown Systems

7.6.1 Introduction

The initial self-alignment loop or gyrocompassing loop of a stationary inertial platform is in principle the electronic equivalent of a mechanical gyrocompass mentioned in Section 7.1.

In the following we will briefly review the principles of the gyrocompassing loop of an inertial platform and the accuracy achievable for the initial alignment.

A second method for the alignment and calibration of platform and strapdown system will also be described - an open loop estimation procedure for azimuth misalignment and north gyro drift - which has the advantage of

- resulting in simple formulas for the covariance and the estimation gain of the two state vector elements,
- being easily programmable,
- speeding up the alignment time - becoming increasingly insensitive to vehicle sway with estimation time.

7.6.2 The Gyrocompassing Loop of an Inertial Platform

Fig. 7.6.1 shows in principle the mechanical gyrocompass consisting of a pendulous two-degree-of-freedom gyro with nearly horizontal spin axis. The sensor can move freely with respect to the base. Once disturbed from its equilibrium, namely true north, it will oscillate in an elliptic cone about this equilibrium or will align itself with true north if it is damped as indicated in this figure.

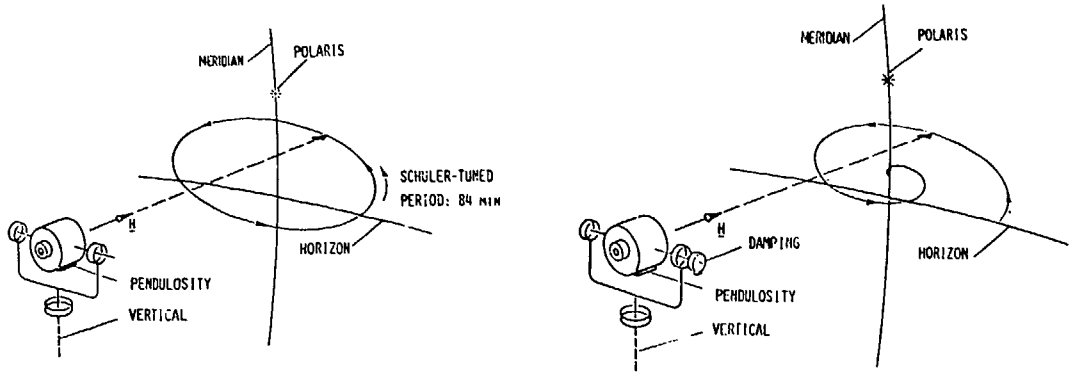

Fig. 7.6.1 The Motion of the Undamped and the Damped Gyrocompass

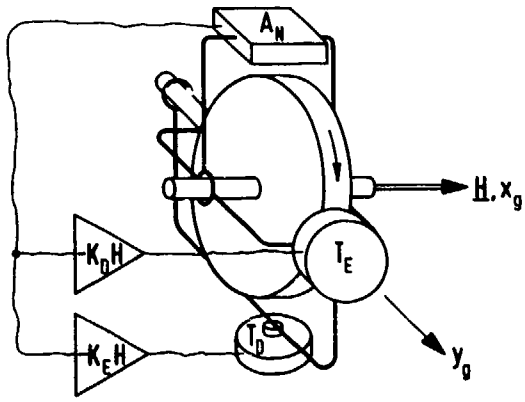

Fig. 7.6.2 The Gyrocompass Mechanized with a Free Gyro, an Accelerometer and Two Feedback Loops

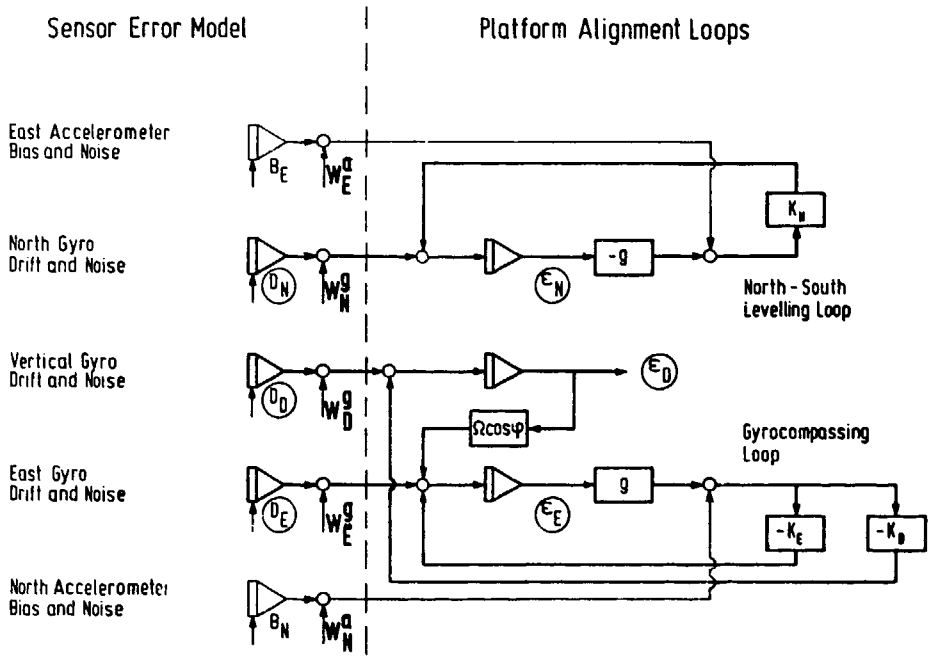

Fig. 7.6.3 Simplified Block Diagram of the Gyrocompassing and the North Levelling Loops for an Inertial Platform

Fig. 7.6.2 indicates how the mechanical gyrocompass is implemented electronically. The pendulosity of Fig. 7.6.1 is replaced by an accelerometer whose input axis is aligned with the spin axis and whose output signal is fed via the gain $-K_D H$ to the horizontal torquer for raising the frequency and via he gain $-K_E H$ to the vertical torquer for raising the damping of the sensor's oscillation.

We find the same interconnections in the simplified gyrocompassing loop of an inertial platform whose block diagram is shown in the lower half of Fig. 7.6.3. The output of the north-south accelerometer NA causes a platform rotation $\omega_{E,D}$ about the east-west and down axes via the gains $-K_E$ and $-K_D$. The upper half of the block diagram shows the levelling loop for the north-south axis.

One of the simplifications in this diagram concerns the model of the free platform (s. Fig. 7.3.4) which has been reduced to the coupling of the vertical misalignments ε_D into the east-west axis via the horizontal component of earth rate $\Omega^C = \Omega\cos\varphi$. The coupling between the horizontal axes via the vertical component $\Omega^S = \Omega\sin\varphi$ of earth rate has been neglected, which is acceptable since the horizontal misalignment angles $\varepsilon_{N,E}$ are smaller than the azimuthal misalignment ε_D.

7.6.3 Platform Equilibrium and Sensor Calibration at the End of the Alignment Process

From the block diagram in Fig. 7.6.3 one can easily derive the following relationships for the equilibrium of the platform at the end of the alignment process when the inputs to the integrators are zero:

- for ideally compensated sensors, i.e. no accelerometer biases ($B_{N,E} = 0$) and no gyro drifts ($D_{N,E,D} = 0$) the platform will be ideally aligned with the vertical and true north:

$$\bar{\varepsilon}_{N,E,D} = 0; \tag{7.6.1}$$

- for non-ideally compensated accelerometer biases ($B_{N,E} \neq 0$) no distinction can be made in the output signals of the accelerometer between bias and corresponding constant horizontal misalignment angles of the platform, i.e. the accelerometer bias cannot be measured during or at the end of the alignment process, but is compensated by the horizontal platform tilt:

$$\bar{\varepsilon}_{N,E} = \pm B_{E,N}/g \quad (= \pm 0.1 \text{ m rad} = 20 \text{ arc sec for } B_{N,E} = 10^{-4}\ g); \tag{7.6.2a,b}$$

- for non-ideally compensated east-west gyro drift ($D_E \neq 0$) no distinction can be made at the input of the east-west gyro between its drift and the effect of vertical misalignment ε_D, i.e. the east-west gyro drift cannot be measured either during or at the end of the alignment process, but is compensated by the azimuth misalignment:

$$\bar{\varepsilon}_D = -D_E/\Omega^C \quad (= 1 \text{ m rad} = 3.4 \text{ arc min for } D_E = 1/100\ ^{\circ}/h \text{ and } \varphi = 45^{\circ})$$

where $\Omega^C = \Omega\cos\varphi$; (7.6.2c)

- if in addition the north-south and the vertical gyros are corrupted by the drift $D_{N,D}$, the horizontal accelerometers furnish additional control offset signals at the end of the alignment process:

$$\bar{\varepsilon}_N = \frac{1}{g}(B_E + D_N/K_N) \tag{7.6.2d}$$

$$\bar{\varepsilon}_E = \frac{1}{g}(B_N + D_D/K_D). \tag{7.6.2e}$$

Whilst the accelerometer biases $B_{N,E}$ cannot be measured, the north-south and the vertical gyro drift $D_{N,D}$ cause an output voltage of the horizontal accelerometers and thus can be measured.

The additional tilt due to $D_{N,D}$, and thus the control offset voltage, can be reduced by setting the loop gains $K_{N,D}$ high or preferably by shunting the amplifiers of the levelling loops with an integrator as indicated in Fig. 7.6.4 for the north-south gyro drift. In practice only this sensor error is compensated in the manner shown. The vertical gyro drift can only be measured by means of the synchro mounted on the vertical gimbal axis, which requires the absence of any platform motion.

Eq. (7.6.2c) is applicable to all north-seeking methods with gyroscopic sensors. These methods are limited to 80° latitude, approximately ($\varphi < \pm 76.5^{\circ}$ for Delco Carousel IV platform system). Note that only the initial self-alignment of the INS is limited to this latitude; the actual navigation function can be performed at all latitudes (s. Section 7.4).

If we choose the following gains in the gyrocompassing loop of Fig. 7.6.4:

$$K_N = 1/(2gT)$$

$$K_E = K_N$$

$$K_D = 1/(16gT^2\ \Omega^C) \tag{7.6.3a,b,c}$$

and the gain of the shunt integrator in the levelling loop

$$K_N' = K_D\ \Omega^C, \tag{7.6.3d}$$

both loops - the north-south levelling loop and the gyrocompassing loop - have the same dynamics, namely four equal roots with the time constant

$$\tau = 2T = 60 \text{ s} \tag{7.6.4}$$

(the figure was selected in laboratory tests [7.32]) and the problems of compensating the north-south gyro drift and of vertical platform alignment are alike.

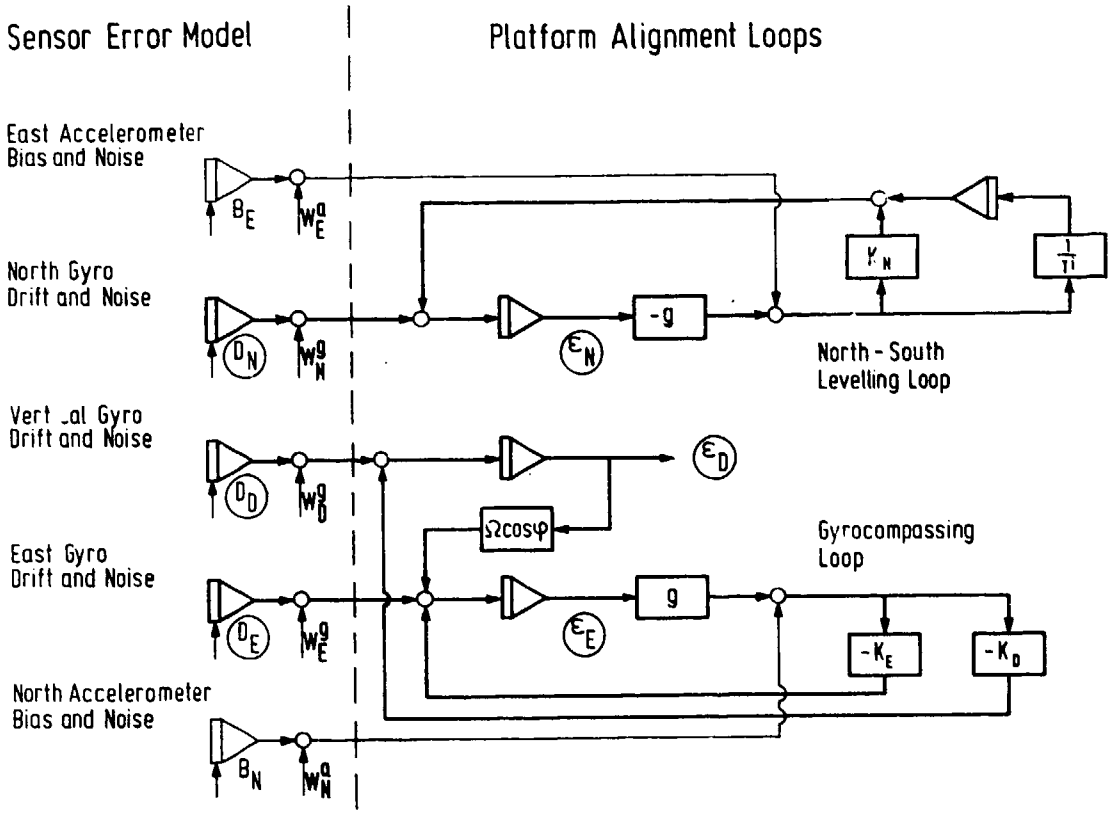

Fig. 7.6.4 Simplified Block Diagram of the Gyrocompassing and North Levelling Loops Including Integrating Networks for a Stationary Platform

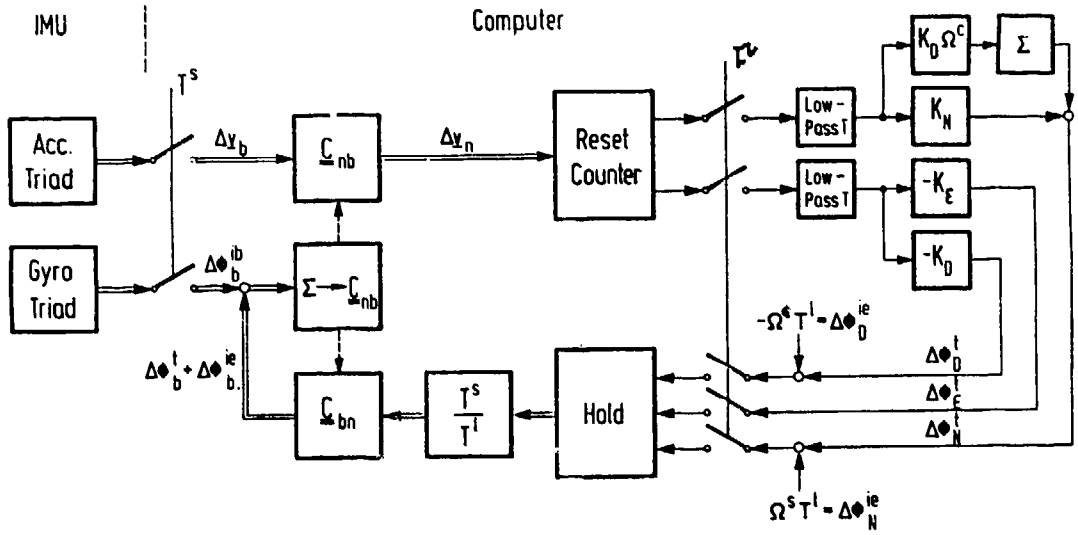

Fig. 7.6.5 Block Diagram for the Gyrocompassing and North Levelling Loops for a Strapdown System

We have not yet mentioned the vertical accelerometer. Its output signal, which should be gravity, can certainly be used for calibration. For the field-calibration of all sensor biases ($D_{N,E,D}$ and $B_{N,E,D}$) and scale factors ($S^g_{N,E,D}$ for the gyros $S^a_{N,E,D}$ for the accelerometers) the gyrocompassing mode is carried out several times with the input axes of each gyro once in the north and once in the south directions and the input axes of each accelerometer once in the up and once in the down directions, which requires 9 orientations of the platform. The sum and differences of the currents into the north or south gyro $i_{N,S}$ and into the up or down accelerometer $i_{U,D}$ are evaluated in the following way:

$$D = -S^g(i_N + i_S)/2 \qquad S^g = (i_N - i_S)/(2\Omega^c)$$

$$B = -S^a(i_D + i_U)/2 \qquad S^a = (i_D - i_U)/(2g). \qquad (7.6.5a,b,c,d)$$

7.6.4 The Gyrocompassing Loop in a Strapdown System

We now apply gyrocompassing to the initial alignment and sensor calibration of a strapdown system. "Alignment" means initialization of the transformation matrix $\underline{\underline{C}}_{nb}$ for transforming the body-fixed measured acceleration vector, i.e. the vector of the velocity increments $\Delta\underline{v}_b$ into the navigational frame $\Delta\underline{v}_n$. The corresponding block diagram is shown in Fig. 7.6.5.

The underlined signals in this block diagram have to be interpreted as vectors - as pulse train vectors of the vehicle's velocity increments in the body frame ($\Delta\underline{v}_b$) and in the navigational frame ($\Delta\underline{v}_n$) and similarly as angular increments of the vehicle's motion with respect to inertial space ($\Delta\underline{\phi}^{ib}_b$) measured in the body frame and as angular increments due to the sum of earth rate ($\Delta\underline{\phi}^{ie}_b$) and gyrocompassing plus north levelling feedback ($\Delta\underline{\phi}^{c}_b$) transformed into the body frame. The sum of all angular increments just mentioned updates the transformation matrix $\underline{\underline{C}}_{nb}$.

It is quite obvious that in the strapdown system all sensor errors limiting the platform alignment accuracy (s. Eqs. (7.6.2a,b,c)) and the north gyro drift calibration accuracy are composed of all body-fixed sensor components according to

$$\underline{D}_n = \underline{\underline{C}}_{nb}\,\underline{D}_b \qquad \underline{B}_n = \underline{\underline{C}}_{nb}\,\underline{B}_b. \qquad (7.6.6)$$

7.6.5 Coarse Alignment of the Strapdown System - Interplay of the Sensor Signals During the Alignment Process

Before starting gyrocompassing, the platform is in general levelled and magnetically aligned to true north in order to speed up the procedure. With strapdown systems another coarse alignment procedure may be utilized if the base is stationary. This coarse alignment procedure is based on the fact that the strapdown IMU measures earth rate $\underline{\omega}^{ie}_b$ and gravity $\underline{g}_b$ in the body frame which theoretically could be instantly used to initialize the transformation matrix $\underline{\underline{C}}_{nb}$ by means of the following equations for the elements of the transformation matrix $\underline{\underline{C}}_{nb}$

$$C_{31} = -f_x/g \qquad C_{11} = \omega_x/\Omega^c + C_{31}\tan\varphi$$

$$C_{32} = -f_y/g \qquad C_{12} = \omega_y/\Omega^c + C_{32}\tan\varphi$$

$$C_{33} = -f_z/g \qquad C_{13} = \omega_z/\Omega^c + C_{33}\tan\varphi\ . \qquad (7.6.7a \text{ to } f)$$

The remaining equations for the missing three elements are found from the condition of orthogonality:

$$C_{21} = -C_{12}\,C_{33} + C_{13}\,C_{32}$$

$$C_{22} = C_{11}\,C_{33} - C_{13}\,C_{31}$$

$$C_{23} = -C_{11}\,C_{32} + C_{12}\,C_{31}. \qquad (7.6.7g,h,i)$$

This alignment procedure is recommended only for the "levelling" of strapdown systems using the accelerometer output signals $\Delta\underline{v}_b$. The derivation of azimuth misalignment on a moving vehicle must be based on the acceleration values $\Delta\underline{v}_n$, which are "base motion isolated" via the $\underline{\underline{C}}_{nb}$ matrix as shown in Fig. 7.6.5, where the signals from the gyros and the computer serve to update this matrix. The gyro signals alone, even if averaged over a certain length of time, can hardly be used for the direct measurement of azimuth misalignment because earth rate and vehicle angular rate cannot be separated. Their use would be comparable to the derivation of true north from the change of time of the synchro signals of a gyro stabilized platform. For the sensitivity of this method to vehicle motions we can use the relationship between azimuth misalignment and corresponding east-west gyro drift in Eq. (7.6.2c). Therefore it can be deduced that even if the synchro signals of the platform or the gyro signals of a strapdown system were to be evaluated over 1 hour, for instance, a 1° steady state change of the vehicle's attitude in that time would be interpreted as a 5° change in azimuth!

For fast coarse azimuth alignment external measurements (magnetic or optic) should be used, and the procedure just described should be utilized for levelling only.

7.6.6 Considerations on the Alignment Time

The alignment time depends on the accuracy with which the horizontal misalignment angles and their slope can be measured with the aid of the horizontal accelerometers. We have to remember in this connection that the vertical misalignment is based on the slope of the north-south accelerometer output signal according to

$$\Delta\dot{v}_N/g = \varepsilon_D\,\Omega\cos\varphi = 10^{-6}/s \text{ for } \varphi = 45^o \text{ and } \varepsilon_D = 1^o. \qquad (7.6.8)$$

This is a very small signal, especially if we bear in mind that ε_D should be less than 1 mrad!

The measurement of the horizontal misalignment angles by means of the accelerometer output signals $\Delta v_{N,E}$ is corrupted by

- the quantization noise Δv^p
- the bias and its stability
- the vehicle sway.

It is shown in [7.32] that the alignment with the gyrocompassing loop of Fig. 7.6.5 is fairly insensitive to the errors just mentioned as long as their autocorrelation time is much smaller than the integration time of the gyrocompassing loop:

$$T^i = \frac{K_E}{K_D\ \Omega\cos\varphi}\ . \tag{7.6.9}$$

With a quantization noise of

$$\Delta v^p = 0.8\ \text{mm/s} \tag{7.6.10}$$

approximately 10 minutes were required in a strapdown system to drive the azimuth misalignment from 3° to 0.2^o when the gyrocompassing procedure was used [7.32].

Speeding up the alignment requires a smaller integration time and makes the loop more sensitive to the errors mentioned above, especially to vehicle sway. We will see in the next section that it is advisable to use an open loop misalignment estimation procedure, which becomes fairly insensitive to vehicle sway with elapsed time.

7.6.7 The Open-Loop Azimuth Misalignment and North-South Gyro Drift Estimation Procedures

As preparation for the application of this procedure to the alignment of platform and strapdown systems we simply open in Figs. 7.6.4 and 7.6.5 the loop of the shunt integrator in the north-south channel and the loop for the vertical alignment. At the same time we reduce the time constant of the levelling loops to, for example, 0.1 of the value in the gyrocompassing mode. The torque signals for levelling the platform (or the transformation matrix) are used as measurements for the estimation procedure after they have been integrated up and divided by the elapsed time. The corresponding block diagram is shown in Fig. 7.6.6. This measurement will be a signal for the mean torque rate.

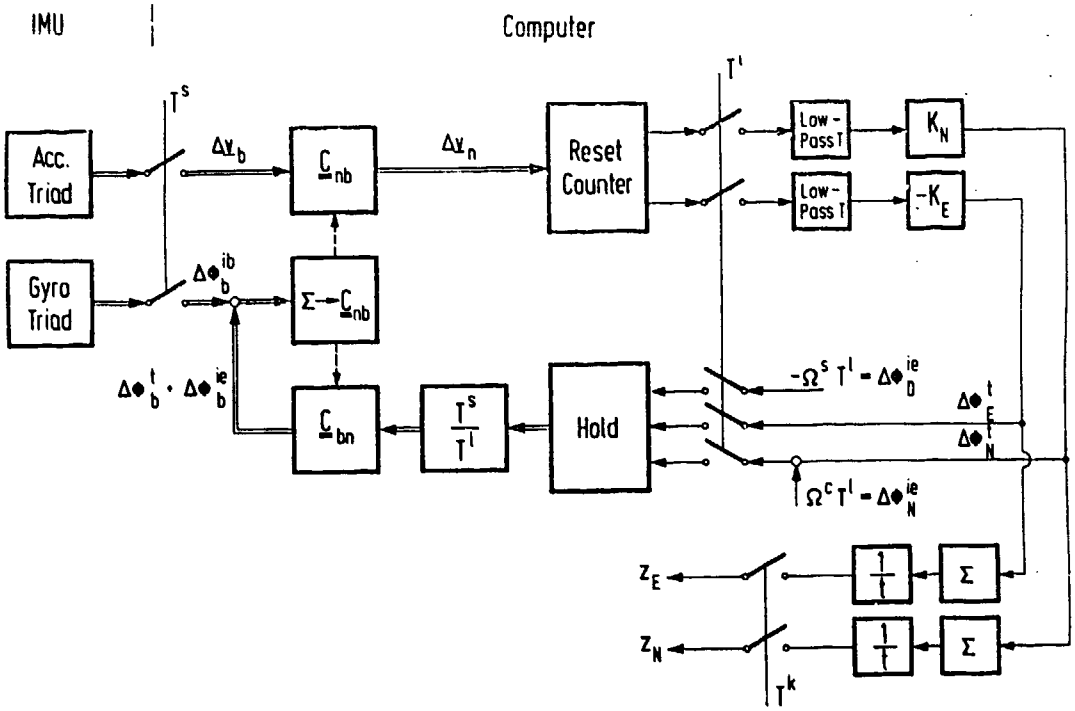

Fig. 7.6.6 Block Diagram for the Levelling Loops of a Strapdown System Delivering Measurements for the Estimation of Azimuth Misalignment and North Drift

If measurements for the estimation procedure are taken in time increments greater than the longest period of the base motion, we may neglect the modelling of the base motion as required in a Kalman filter and assume that each measurement is a signal for the north-south gyro drift D_N or the azimuth misalignment $\varepsilon_D' \Omega \cos\varphi$, contaminated by noise dependent on sensor and readout quality and base motion dynamics.

In a fine levelling mode at the beginning of the procedure no measurement is taken, since for a step function as input the loop reaches its stationary output at $t/\tau = 5$, i.e. after approximately 30 s. The measuring is then initiated and an estimation is carried out every $T^K = 30$ s, for instance.

The formulas for the estimation procedure with stationary measurements are easily derived from the Kalman filter algorithms. They are listed in Table 7.6.1.

State to be estimated:	$x = D_N$ or $\varepsilon_D \Omega \cos\varphi$
Measurement at time $t = kT^K$	$z(k) = \frac{1}{kT^K}\int_0^{kT^K} (x + v)\, d\tau = \frac{1}{kT^K}\int_0^{kT^K} x \; d\tau + v(k)$
Measurement noise: (with σ_z = quantization noise covariance and T^1 = levelling loop sampling time)	$v(k) \sim N(o, \sigma_z^2(k))$; $\sigma_z(k) = \sigma_z \frac{T^1}{kT^K}$
Covariance of estimate before measurement: (with q = noise covariance of north and east drifts)	$\sigma_x^{2'}(k) = \sigma_x^2(k-1) + q$
after measurement:	$\sigma_x^2(k) = \frac{\sigma_x^{2'}(k) \cdot \sigma_z^2(k)}{\sigma_x^{2'}(k) + \sigma_z^2(k)}$
Estimation gain:	$K(k) = \frac{\sigma_x^2(k)}{\sigma_z^2(k)}$
Estimates before measurement:	$\hat{x}'(k) = \hat{x}(k-1)$
after measurement:	$\hat{x}(k) = \hat{x}'(k) + K(k)\,[z(k) - \hat{x}'(k)]$
Theoretical estimation accuracy limitations:	$\sigma_{D_N,\infty} \to 0$
	$\sigma_{\varepsilon_D,\infty} \to \sigma_{D_E}/(\Omega \cos\varphi)$

Table 7.6.1 Recursive Formulas for the Estimation Procedure of Azimuth Misalignment and North Drift

The states to be estimated (ε_D and D_N) are comprised in x. The measurement z is the output of the integrators in Fig. 7.6.6 divided by the elapsed time, and the measurement noise, assumed to be quantization noise, decreases correspondingly. The estimate covariance is represented by a very simple formula as is the estimation gain which decreases with elepsed time as expected. In Table 7.6.1 the theoretical estimation accuracy limitations are mentioned, showing again that the physical limitations of any inertial north seeking method cannot be surpassed by the estimation procedure (s. Eq. 7.6.2).

As compared to the gyrocompassing alignment discussed in the Section 7.6.6 the alignment with the open-loop estimation procedure was approximately twice as fast when the following parameters were used [7.32]:

$$\sigma_x(o) = 0.1 \text{ [rad]} \qquad \sigma_z = 3.2 \cdot 10^{-4} \text{ [rad/s]} \qquad q = 3.0 \cdot 10^{-4} \text{ [rad}^2\text{/s]}$$
$$T^K = 30 \text{ [s]} \qquad T^S = T^1 = 0.02 \text{ [s]}$$

(7.6.11a to d)

With increasing estimation time it also became more and more insensitive to accelerometer noise, bias instabilities and vehicle vibrations. This was not so much the merit of the optimal estimation algorithms but of signal conditioning in Fig. 7.6.6, i.e. the integration of the torquing signal and division by the elapsed time. An analogy for this measurement improvement over elapsed time is the accelerometer readout on a platform with no levelling loop and with earth rate compensation but having north gyro drift or azimuth misalignment. Both will drive the platform about the horizontal axes and the output of the accelerometers increases with time (s. Eq. (7.6.8)). The relative share of sensor disturbances and acceleration noise will decrease with elapsed time also. The gyrocompassing loop remains constantly sensitive to accelerometer bias instabilities and vehicle motions whose autocorrelation time is greater than the integration time T^1 (s. Eq. (7.6.9)) of the corresponding loops in Figs. 7.6.4 and 7.6.5.

7.7 Summary and Overview of Existing Inertial Navigation Systems

Inertial navigation systems (INS) render information on position, velocity, attitude and heading. They are used not only for navigation but also for flight guidance and for flight testing (Section 7.1).

The functioning of platform systems with their accelerometers pointing north, east and down (north indicating system NIS) and their error dynamics have been discussed (Sections 7.2 and 7.3).

The use of the NIS is limited to geographic latitudes below 90°. Other inertial navigation system mechanizations, especially with wander-azimuth platforms, allow worldwide navigation (Litton systems, Delco systems) and offer additional advantages (Section 7.4.1 and 7.4.2).

Inertial navigation systems employing electrostatically supported gyros have space-stabilized platforms (Section 7.4.3). Strapdown systems represent the new development in the field of inertial navigation and flight testing (Section 7.4.4). Again the functioning and the advantages of all these systems are discussed.

The linearized error dynamics of all inertial navigation systems regardless of internal mechanization but whose output signals are attitude and heading, ground speed and position with respect to north, east and down can be modelled in a Kalman filter in the same way, the only difference being in the driving function of the sensor errors (Section 7.5).

The initial self-alignment mode of platform and strapdown systems, including the accuracy achievable is discussed (Section 7.6).

Tables 7.7.1a and b summarize the characteristics of existing platform and strapdown systems.

No.	Parameter	Manufacture Model No.			
		Delco Carousel IV	Ferranti FIN 1000	Litton LTN-72	SAGEM ULISS
	Volume [litres]/ Mass [kg]				
1	inertial navig. unit	28.0/24.5	31.2/20.4	28.6/26.8	14.3/15
2	control display unit	2.3/ 1.77	2.7/ 1.8	2.6/ 2.3	2.9/ 3
3	mode selector unit	0.3/ 0.32	-	0.3/ 0.5	0.6/ 0.9
4	automatic data entry unit	0.8/ 1.6	0.13/0.15	-	-
5	battery unit	7.6/12.2	-	7.5/12.3	-
6	total	39.0/40.39	34.03/22.35	39.0/41.9	17.8/18.9
7	Power dissipation [Watts]	405	285	460	260
	Sensors				
8	gyro type	RIG	RIG	DTG	DTG
9	day to day [°/h]		0.05/0.0026	< 0.01	< 0.01
10	accelerometer type	floated, flexure support	fluid damped flexure support	dry, flexure support	dry
11	acc. bias stability [g]		10^{-4}	10^{-4}	$5 \cdot 10^{-5}$
	Some Output Signals and their Accuracy				
12	attitude [°]	0.2	0.15 RMS	0.2	0.05(1σ)
13	heading [°]	0.4	0.15 RMS	0.4	0.08(1σ)
14	ground speed [m/s]		1.0		1 (50 %)
15	position [n m/h]	< 1.7 (95 %), < 0.7 (50 %)	< 0.6 (50 %)		1 (50 %)
16	vertical acceleration [g]	0.02		0.01	0.06(1σ)
17	wind speed [kn]	yes	yes	yes	yes
18	wind angle [°]	yes	yes	yes	yes
19	Remarks on System Mechanization	wander azimuth, platform rotation, DME update	north indicating platform or wander azimuth (option)	wander azimuth, DME update	wander azimuth

Table 7.7.1a Summary of Some Characteristics for Existing Platform Inertial Navigation Systems

No.	Parameter	Manufacture Model No.			
		Litton LTN-90	Honeywell HG 1050	SAGEM MSD	Teledyne TDY-740A
	Volume [litres]/Weight [kp]				
1	inertial reference unit	/20.0	/20.9	8/7.5	28/20
2	inertial sensor display unit	/ 0.6	/ 2.2		2.8/2.0
3	mode selector unit	/ 2.3			
4	total	/22.9	/23.1	8/7.5	30.8/22
5	Power dissipation [Watts]	90	131	70	200
	Sensors				
6	gyro type	RLG, LG-8028A	RLG,GG 1342	DTG,GSD	DTG,SDG-5
7	day to day drift [^{o}/h]			<0.05	
8	accelerometer type	A2	Sundstrand QA2000 or Systron Donner 4851	A 310	Sundstrand QA1200 or Systron Donner 4841
9	acc. bias stability [g]		$8 \cdot 10^{-5}$	$5 \cdot 10^{-5}$	
	Some Output Signals and their Accuracy				
10	attitude [^{o}]	0.1	0.1	0.3	0.03
11	heading [^{o}]	0.4	0.4	0.3	0.3
12	ground speed [m/s]	4.0	4.9		4.1
13	position [n mi/h]	2	2	3	1.5
14	angular rate resolution ^{o}/s / band width [Hz]	$4.9 \cdot 10^{-4}$/8	0.01/5		0.01/100[a)]
15	acceleration resolution [g]/ band width [Hz]	$2.3 \cdot 10^{-5}$/8	0.001/8		0.123/100[a)]
16	wind speed resolution [m/s]/ band width [Hz]	0.5/3	0.3/2		-
17	wind angle resolution [^{o}]/ band width [Hz]	1/3	1.0/2		-
18	Remarks on System Mechanization	wander azimuth	wander azimuth		wander azimuth

[a)] pulse weight and update frequency of angle increments in degrees and velocity increments in m/s

Table 7.7.1b Summary of Some Characteristics for Existing Strapdown Inertial Navigation Systems

References for Chapter 7

[7.1] Schuler, H. — Die Störung eines Pendels und eines Kreiselgerätes infolge Beschleunigung des Fahrzeugs. Physikalische Zeitschrift, Band 24, Kiel (1923).

[7.2] Gievers, J. — Erinnerungen an Kreiselgeräte. Jahrbuch 1971 der DGLR, page 263 - 291.

[7.3] Sorg, H. — From Serson to Draper, Two Centuries of Gyroscopic Development. Proceedings of the International Navigational Congress 1976, August 3 - 6, Boston Museum of Science, page 166 - 172.

[7.4] Wrigley, W. — History of Inertial Navigation. Proceedings of the International Navigational Congress 1976, August 3 - 6, Boston Museum of Science, page 92 - 95.

[7.5] Stieler, B. Klein, G. — Contributions of Late Dr. Johannes Gievers to Inertial Technology - Some Aspects on the History of Inertial Navigation. Proceedings of the DGON Symposium on Gyro Technology, Stuttgart, Germany (1979).

[7.6] Leondes, T. (Editor) — Theory and Applications of Kalman Filtering. AGARDograph 139 (1970).

[7.7] Gelb, A. (Editor) — Applied Optimal Estimation. The MIT Press (1974).

[7.8] Bryson, Jr., A.E. Ho, Y.C. — Applied Optimal Control. Blaisdell Publishing Company (1969).

[7.9] Schrick, K.W. (Editor) — Anwendung der Kalman-Filter-Technik - Anleitung und Beispiele. R. Oldenbourg-Verlag, München - Wien (1977).

[7.10] Stieler, B. Winter, H. — Advanced Instrumentation and Data Evaluation Techniques for Flight Tests. Proceedings of the XI Congress of the International Council of the Aeronautical Sciences, Lisboa, Portugal, September 10 - 16, 1978.

[7.11] Magnus, K. — Kreisel als vielseitige Hilfsmittel in Luft- und Raumfahrt. Zeitschrift für Flugwissenschaften und Weltraumforschung 1978, Vol. 2, page 217 - 227.

[7.12] Chen, C.F. Haas, I.J. — Elements of Control System Analysis. Prentice-Hall (1968).

[7.13] Britting, K. — Inertial Navigation System Analysis. Wiley Interscience (1971).

[7.14] Kayton, M. Fried, W.R. — Avionics Navigation Systems. J. Wiley and Sons, Inc., New York (1969).

[7.15] Hall, P.E. — ESGN Development Performance Improvement through Modification. Proceedings of the Institute of Navigation, National Marine Meeting, 23 and 24 Oct 1973, US Merchant Marine Academy, Kings Point, N.Y.

[7.16] Moore, J.P. — Trident Electrostatically Suspended Gyro Monitor. Proceedings of the SAE Aerospace Control and Guidance Systems Committee, 17 May 1974, Phoenix, Arizona.

[7.17] Garg, S.C. Morrow, L.D. Mamen, R. — Strapdown Navigation Technology: a Literature Survey. AIAA Journal of Guidance and Control, Vol. 1, No. 3, May - June 1978, page 161 - 172.

[7.18] Schmidt, G.T. (Lecture Series Director) — Strapdown Inertial Systems. AGARD Lecture Series No. 95, May 1978.

[7.19] Gilmore, J.P. McKern, R.A. — A Redundant Strapdown Inertial System Mechanization SIRU. The Charles Stark Draper Laboratory, Cambridge, Mass., USA, Rep. No. E-2527 (s. also Journal of Spacecraft and Rockets, Vol. 9, No. 1, January 1972).

[7.20] Donoghue, P.J. Napjus, G.A. — The Application of Strapdown Inertial Systems to Land Vehicle Positioning, Navigation and Pointing. Proceedings of the DGON Symposium Gyro Technology 1980, Stuttgart, Germany.

[7.21] Stieler, B. — System mit einer Plattform mit kardanischer Aufhängung als Geräteträger in Verbindung mit einem Fahrzeug und einem Inertialsystem. Patentanmeldung P 30 19 743.4 beim Deutschen Patentamt (1980).

[7.22] McKern, R.A. — A Study of Transformation Algorithms for Use in a Digital Computer. MIT Master Thesis, No. T-493 (1968) under the auspices of the Charles Stark Draper Laboratory, Inc., Cambridge, Mass., USA.

[7.23] Wetzig, V. — Methoden zur Ermittlung der Richtungsreferenz und deren Fehlerverhalten in Strapdown-Systemen. DFVLR Interner Bericht No. IB 153 - 76/31 (1976).

[7.24] Wetzig, V. — Computation of Attitude and Heading in a Strapdown Computer. DFVLR Interner Bericht No. IB 153 - 78/32 (1978).

[7.25] Baumann, H. — Fehleranalyse und Simulation eines Trägheitsnavigationssystems mit fahrzeugfesten Sensoren. Dissertation Technische Universität Braunschweig (1976).

[7.26] — Flugmechanik, Begriffe, Benennungen, Zeichen, Grundlagen. Normenstelle Luftfahrt LN 9300.

[7.27] van Bronkhorst, A. — The Euler Angle Strapped-Down Computer. Proceedings of the DGON Symposium Gyro Technology, 1971, Kiel, Germany.

[7.28] Shepperd, S.W. — Quaternion from Rotation Matrix. AIAA Journal of Guidance and Control, Vol. 1, No. 3, May-June 1978, page 223 and 224.

[7.29] Rahlfs, D. — The Experimental Strapdown System of DFVLR. Proceedings of the DGON Symposium Gyro Technology, 1979, Stuttgart, Germany.

[7.30] Wetzig, V. Hellerdieck, E. — Simulation für zwei Flugbahnen verschiedener Dynamik ohne überlagerte Vibrationen. Proceedings of the Course BF 5.05 "Inertial Navigation, Methods of Aiding, Strapdown Systems" of the Carl-Cranz-Gesellschaft, Heidelberg, Germany (1980).

[7.31] Stieler, B. — Die Navigationsgleichungen und das Fehlerverhalten von Trägheitsnavigationssystemen. DFVLR Interner Bericht No. IB 153 - 76/26 (1976).

[7.32] Stieler, B. Zenz, H.P. — On the Alignment of Platform and Strapdown Systems. Proceedings of the DGON Symposium on Gyro Technology 1978, Stuttgart, Germany.

[7.33] Bacon, R.H. Sonberg, D.F. Swanson, R.A. — Probability Circles for Elliptical Distribution. Internal Report of GPL Division, General Precision Systems, Inc., Pleasantville, New York, July 1957.

8. HYBRID INSTRUMENTATION SYSTEMS AND THEIR APPLICATION TO FLIGHT TESTING OF ON-BOARD AND GROUND EQUIPMENT

In the preceding chapters gyroscopic and inertial measuring equipment which is used for flight tests has been discussed. The deterministic errors of these sensors and systems have been described and calibration methods which are used to measure and compensate these errors have been considered. The accuracy of the sensors is then basically limited by the stochastic errors, which change from switch-on to switch-on. More or less sophisticated pre-flight alignment and calibration procedures are applied to measure and compensate these errors. These procedures are usually successful in the case of random bias type errors which have different but constant values for each flight. The time varying random errors - especially the medium and high frequency errors - can be reduced in part only by direct filtering (for example low-pass filtering). Here the engineer is confronted with the problem that direct filtering not only affects the errors but also destroys the high frequency signal information.

A way out of this problem consists f using redundant integrated instrumentation and of applying filters to the difference between the redundant sensor signals. The principles of this method will be explained in this chapter and examples will be given.

The basic principle of error reduction in a hybrid sensor system is explained with the help of Fig. 8.0.1. The sensors A and B measure the same physical quantity, e.g. the aircraft velocity. They have been selected so that they have different error characteristics. For example the sensor A may have low frequency errors (e.g., INS) and the sensor B high frequency errors (e.g. Doppler radar, which is discussed later in this chapter). The difference between the velocity outputs of these two sensors contains only information about the errors of these sensors and not about the true velocity. This fact has to be explained. The indicated velocities v^A and v^B are the sum of the true velocity v and the sensor errors δv^A and δv^B

$$v^A = v + \delta v^A$$

$$v^B = v + \delta v^B$$

The difference is

$$\Delta v = v^A - v^B = \delta v^A - \delta v^B.$$

So if filtering is applied to the difference between both sensor outputs, the true signal v, is not affected. This is the first great advantage of filtering in a hybrid sensor system in comparison with direct filtering of the sensor output. The second advantage is that the use of detailed models of the sensor errors allows the identification of the deterministic and stochastic errors with high accuracy, so that these errors can be compensated with similar accuracy. If recursive filters are used (e.g. Kalman Filters) one obtains continuous estimates of these errors, which can be compensated on-line. An important condition for the success of this hybrid filtering is that the sensor errors are complementary, for instance when they have different frequency spectra (e.g. low and high frequency errors). These types of hybrid filters will be discussed in the following text:

- Conventional (analog) filtering.
- Kalman filtering.
- Optimal smoothing.

The mathematical theory of these methods will not be explained in this text - only the principles will be discussed. The reader who wants to apply these methods is referred to excellent text books existing on these subjects [8.1, 8.2].

As an example, Fig. 8.0.2 shows a hybrid autonomous measuring system for the aircraft attitude, acceleration, velocity and trajectory, which uses a Kalman filter. The measurements of the INS are compared with those of an additional sensor, such as a Doppler radar or TACAN. The difference between the measurements, which in the Kalman filtering theory is called the "measurement", is fed into a Kalman filter which estimates the errors of the INS and the additional sensor. These errors can then be corrected on-line with the help of a suitable controller.

Another example is shown in Fig. 8.0.3, describing a hybrid system for reference trajectory measurement. This system uses an optimal smoothing technique and the figure summarizes the basic principles of this technique. The low frequency aircraft motions are measured with high precision by a tracking radar, by a long distance radar, by TACAN or by cinetheodolites. Only low frequency sampling is required (e.g. once every 10 seconds). The high frequency motions of the aircraft are measured by the on-board INS or by the Doppler navigation system. These navigation systems have the necessary short term stability to provide an accurate measurement of the high frequency aircraft motions. The smoothing technique is applied in the following manner. The differences between the position measurements of the on-board and the ground-based sensors are fed into an optimal smoothing algorithm, which estimates the (low frequency) errors of the on-board sensors with high precision. The measurements of the on-board sensors are then corrected for the estimated errors to obtain the reference trajectory, velocity, attitude and heading. Thus the optimal smoothing is applied only to the difference between measurements of two sensors and this difference is equal to the difference of the errors of both sensors, and the true trajectory is not affected by the smoothing process. We shall see later on that smoothing can be applied only off-line, because the smoothing algorithm uses all the measurements taken during the flight test in order to estimate the sensor errors. But this is no restriction in most cases, when the reference data are required with high precision after the flight test.

8.1 Models for the Sensor Errors

As examples of the sensor error modelling, an inertial navigation system and a Doppler radar system are considered. The former is described in Chapter 7. Laboratory measurements for the horizontal channels of an INS of the type Litton LN3 are shown in Fig. 7.3.5. The error model describing these measurements is

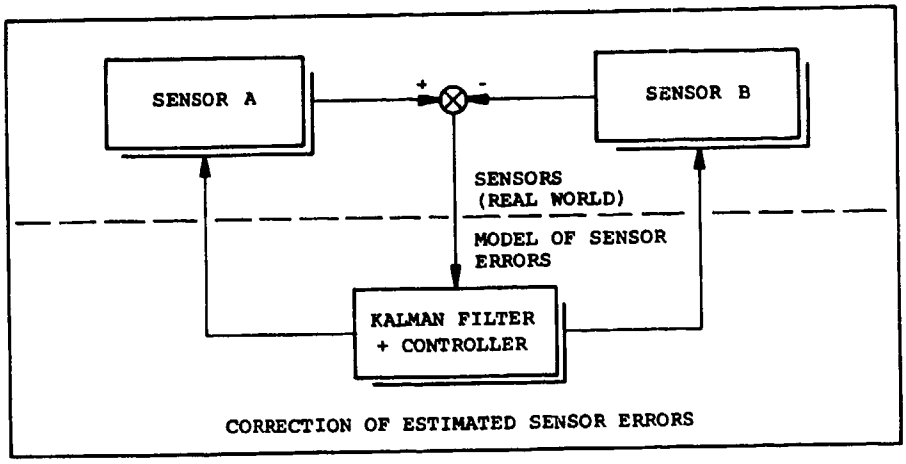

Fig. 8.0.1 Basic Principle of Error Reduction in a Hybrid System

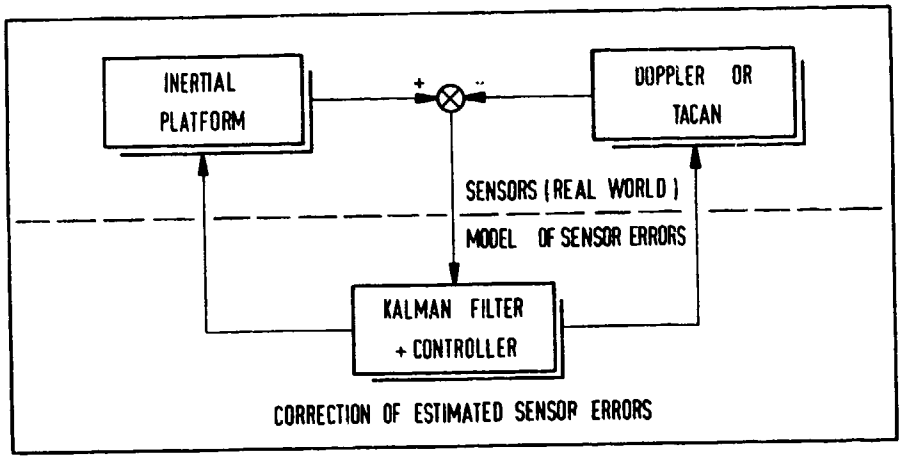

Fig. 8.0.2 Hybrid Measuring System for Attitude, Acceleration, Velocity and Position

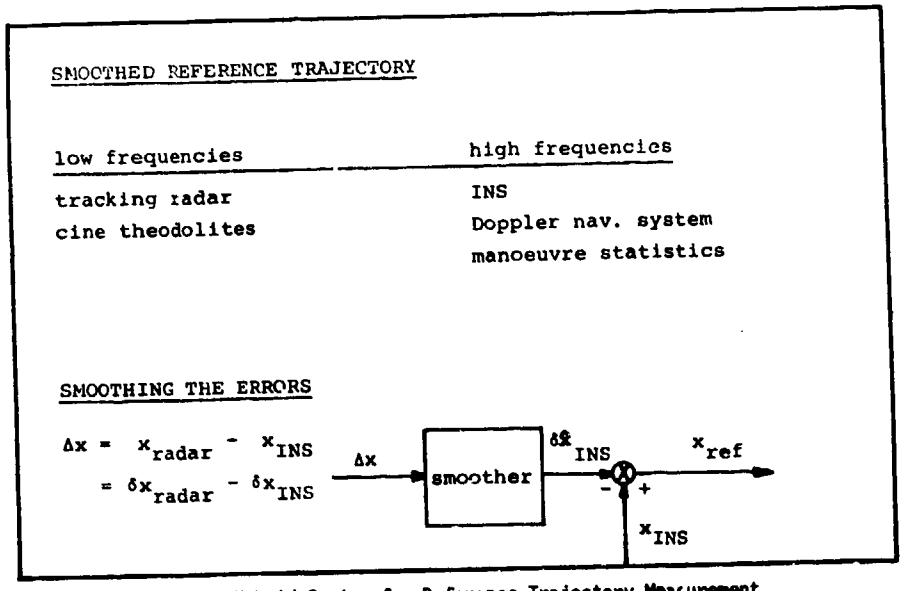

Fig. 8.0.3 Hybrid System for Reference Trajectory Measurement

summarized in Eqs.(7.3.23a to g). The corresponding block diagrams are shown in Figs. 7.3.3 and 7.3.4.

Sections 7.3.5 and 8.2.1.1 deal with the error model of the vertical channel which is augmented by the barometric altimeter. The error growth of the unaided inertial altitude is plotted in Fig. 7.3.11. The block diagram including the augmentation is shown in Fig. 7.3.3. The measurements and the theoretical error models prove the statement that the INS has excellent short term stability but that its error increases with time.

We will now discuss the error of a Doppler radar. Fig. 8.1.1 shows a comparison of the horizontal aircraft velocities of the DFVLR HFB 320 test aircraft measured by the well-calibrated and aligned LN3, and by the Doppler radar: the correlation time of the Doppler radar errors is of the order of a few seconds, so that the assumption of an uncorrelated Doppler error seems to be justified for the most applications.

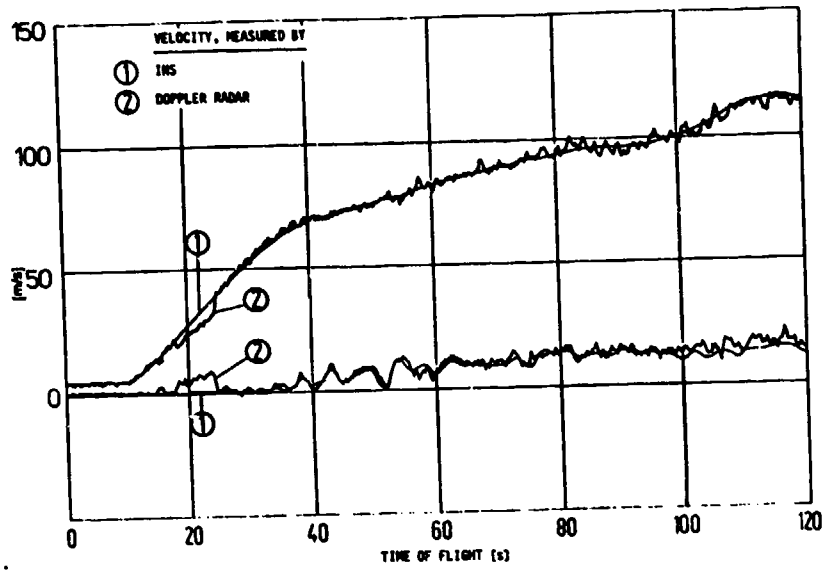

Fig. 8.1.1 Measured Velocity of the Test Aircaft

The accuracy of the filtered estimates of the sensor errors depends strongly on the short term stability of the on-board sensors. For the calibrated INS, the short term position error is primarily caused by the noise in the acceleration measurements. This noise is twice integrated to give the INS position error. In the Doppler system the short term position error is caused by the fluctuation (velocity) error. This velocity noise is integrated to give the Doppler position error. (These statements are only valid if all the constant errors in the INS and the Doppler system are perfectly estimated and compensated.)

Fig. 8.1.2 shows the time variation of these short term position errors for a Doppler and an inertial navigation system; in this example a Doppler fluctuation error of 2 m/s (1σ) and an acceleration noise of 10^{-3}g (1σ) sampled with 5 Hz have been assumed.

- The Doppler position error (random walk) increases rapidly in the first hundred seconds (3 m in 2 s; 7 m in 10 s).
- The INS position error (integrated random walk) remains very small in the first hundred seconds (1cm in 2 s; 8 cm in 10 s).

Fig. 8.1.2 demonstrates that this INS with very noisy acceleration measurements has by far the better short term stability compared with the Doppler system. If the measurements of the radar, which are used to aid the on-board sensors are sampled once per 10 seconds, the position error due to the INS can be neglected between the successive measurements. But in the Doppler system a random error of the order of 10 metres builds up between these measurements, thus basically limiting the obtainable accuracy of the hybrid system.

8.2 Filtering Procedures

In this section, conventional (analog) filtering, Kalman filtering and optimal smoothing are discussed, as examples for the filtering techniques which are in use for flight tests.

8.2.1 Conventional (analog) Filtering

As examples for this technique, the conventional baro-INS and the conventional Doppler-INS mechanizations are considered.

8.2.1.1 Conventional Baro-INS

The conventional augmentation of the vertical channel of the platform is shown in Fig. 8.2.1. The difference between the hybrid height h and the barometric height h_b is fed back through the gain factors, K_1 and K_2, for the correction of the vertical velocity and height. The factors K_1 and K_2 are chosen so that the control system (second order) shows a reasonable transient behaviour and that the hybrid height follows the

barometric height well. For the test flights, K_1 and K_2 were chosen such that $K_1 = 2/T$ and $K_2 = 1/T^2$ with $T = 30$ seconds; that is, the two poles of the control system were identical. As a result of this soft coupling, the hybrid height follows long-term alterations of the barometric height, but smoothes out its short-term fluctuations (see Fig. 8.2.2).

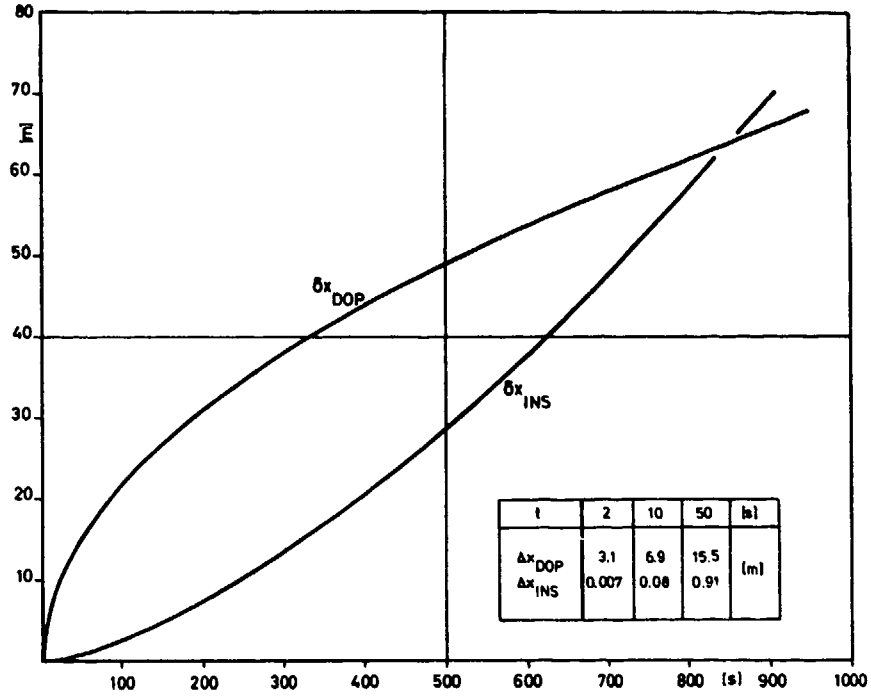

Fig. 8.1.2 Short Term Position Errors of an INS and a Doppler Radar

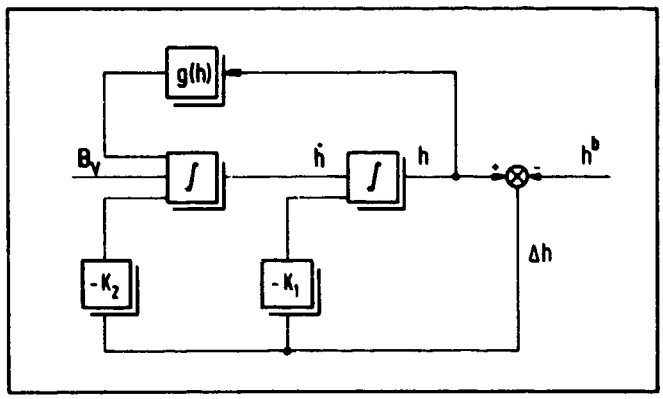

Fig. 8.2.1 Conventional Barometric Aiding of the Vertical Channel of an INS

In this process an accelerometer bias B_V produces steady velocity and height errors such as

$$\delta\dot{h} = 2TB_V$$

$$\delta h = T^2 B_V.$$

For $B_V = 10^{-4}$ g, the errors for $T = 30$ seconds are $\delta h = 1$ meter and $\delta\dot{h} = 0.06$ meter per second. The mixing process has the drawback that the indicated height (baro-inertial height) still has the same low frequency errors as the barometric height, especially those dependent upon weather and sensor position.

8.2.1.2 Conventional Doppler-INS

The conventional Doppler aiding of the INS consists of feeding the differences between the INS velocities and the Doppler velocities back into the INS to correct the platform attitude and velocity.

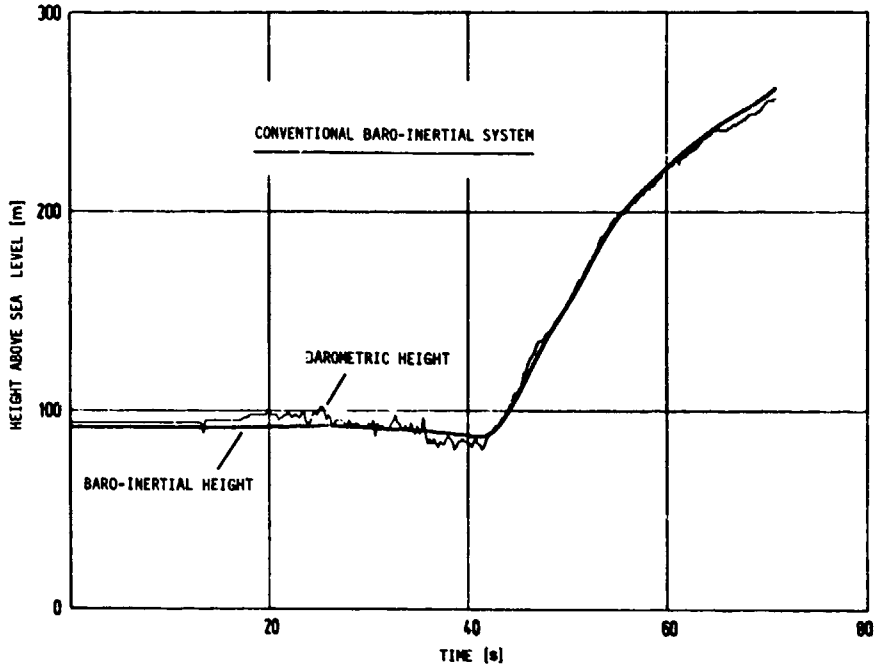

Fig. 8.2.2 Comparison of Baro-Inertial and Barometric Height of the Test Aircraft

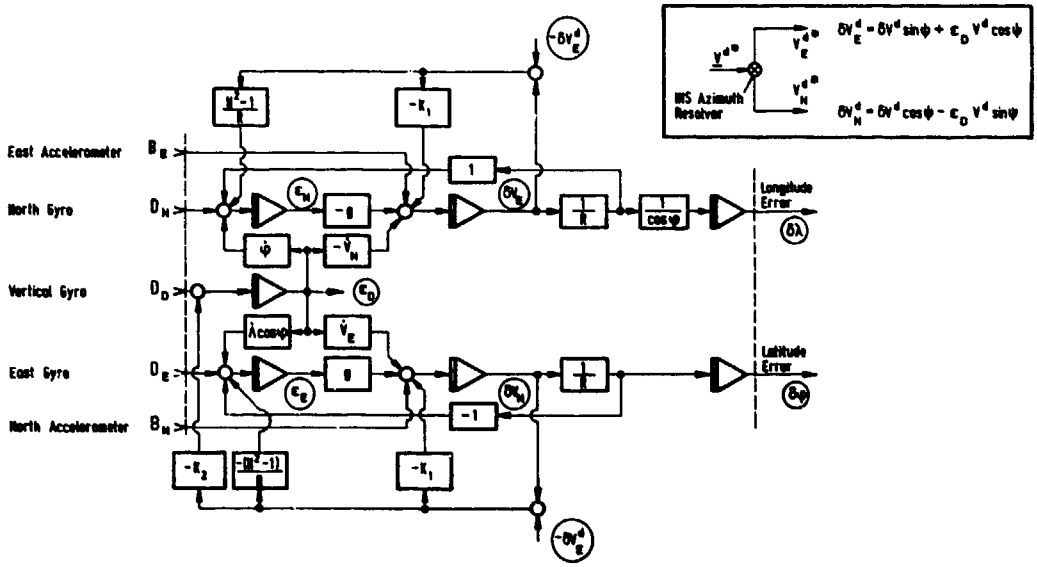

Fig. 8.2.3 Third-Order Levelling and Gyrocompassing Loop of a Doppler/Inertial System

Fig. 8.2.3 shows the error block diagram of a third-order in-flight gyrocompassing loop, whereby the Doppler velocities measured in the body-fixed coordinate frame are resolved into the north and east directions by the attitude and heading angles as measured by the INS. This is indicated in the upper right corner of Fig. 8.2.3. Due to the feedback in the horizontal channels the Schuler oscillations of the autonomous INS are damped and the frequency is augmented: the loops are N-times Schuler tuned and often critically damped. Analog aiding of this kind has the effect that this hybrid system

- has a very accurate non-delayed short term velocity output, but

- follows the low frequency Doppler errors.

Fig. 8.2.3 also shows that the north velocity difference between INS and Doppler is fed back to the vertical gyro torquer to correct the azimuth INS misalignment. This alignment procedure in the vertical channel becomes feasible since the errors of the INS due to the azimuth misalignment differ in the north-south channel from those of a dead reckoning system, i.e. the Doppler system (see Section 7.3.2 and Eq. (7.3.18)). In the east-west channel the INS error due to azimuth misalignment equals the Doppler crosstrack error and feedback of the corresponding velocity difference is of no use.

Eq. (7.3.21) finally reveals that also in the north-south channel the INS error is equal to that of the dead reckoning system, if it was aligned initially using the stationary gyrocompassing procedure. From this we may deduce that Eq. (7.3.19c) also limits the in-flight gyrocompassing accuracy under the presumption that the Doppler velocities are measured accurately in the body-fixed coordinate frame. Any azimuth misalignment of the Doppler antenna, for instance, causes a corresponding INS misalignment.

8.2.2 Kalman Filtering

Kalman filtering is extensively used in integrated navigation systems. The underlaying theory has been described in many excellent text-books [8.2, 8.3] and also the equations which have to be solved are given there. In this chapter only the basic principles will be discussed, so that the flight test engineer can understand how such filters work.

These basic principles are explained using Fig. 8.0.1. At the beginning of this chapter it has been shown that, in hybrid systems, filtering is applied to the differences of the sensor errors. Thus the Kalman filter in Fig. 8.0.1 is operating on the sensor errors only. The heart of the Kalman filter is a mathematical model of these sensor errors, such as those considered in Sections 7.3 and 8.1. With these models, starting with rather arbitrary initial values which have to be set by the filter designer, the filter computes the values for the sensor errors which are to be expected from the next measurement under the assumption that the initial values are correct. The actually observed sensor errors are of course different from those which have been forecast by the model. The Kalman filter is now able to correct the values of the errors in the model in such a manner that, with increasing number of measurements taken, the errors in the model approach more and more to the actual sensor errors. So the sensor errors are identified in the model by the Kalman filter and can be corrected in the process. It has become obvious in looking at the Kalman filter operation that the success of filtering greatly depends on the quality of the mathematical models on which these filters are based.

8.2.3 Optimal Smoothing

In hybrid reference systems, high precision information on the aircraft trajectory, velocity, attitude and heading can be obtained by smoothing the radar with the help of an INS or Doppler system. Direct smoothing of radar data is very common in flight test evaluation, for example by least square curve fitting techniques. The disadvantage of direct smoothing is that not only the high frequency errors of the tracking radar but also the high frequency movements of the aircraft are smoothed out. This disadvantage is avoided when the hybrid technique described in this section is used.

The smoothing algorithm used for the evaluation of DFVLR flight tests is that given by Rauch/Tung/Striebel [8.4], which consists of a Kalman forward- and a backward-filter.

8.2.3.1 Forward-Filtering

The Kalman filter equations are solved for the flight time under consideration. The results are the estimates of the sensor errors just as in the case of the usual Kalman filtering.

8.2.3.2 Backward-Smoothing

The backward-smoother equations are solved backwards in time, utilizing and improving the error estimates of the forward-filter.

The improved accuracy, which is obtained by smoothing the data, in comparison with normal Kalman filtering can be explained with the help of Fig. 8.2.4. This figure shows the optimal smoother in a somewhat diferent mathematical formulation, the two-filter-form. In this formulation the optimal estimate of the state vector at the time t is obtained by combining two Kalman filter estimates in an optimal manner: A Kalman forward-filter gives an estimate of the sensor errors at the time t, based on all the measurements before the time t. This estimate has the accuracy of ordinary Kalman filtering. The second estimate is obtained from a backward Kalman filter and gives an estimate of the sensor errors at the time t, based on all the measurements collected after the time t. The smoothed estimate is the weighted mean of these two estimates. It can be shown that the smoothed estimate is always at least as accurate as the Kalman filtered one. In most cases it is considerably more accurate.

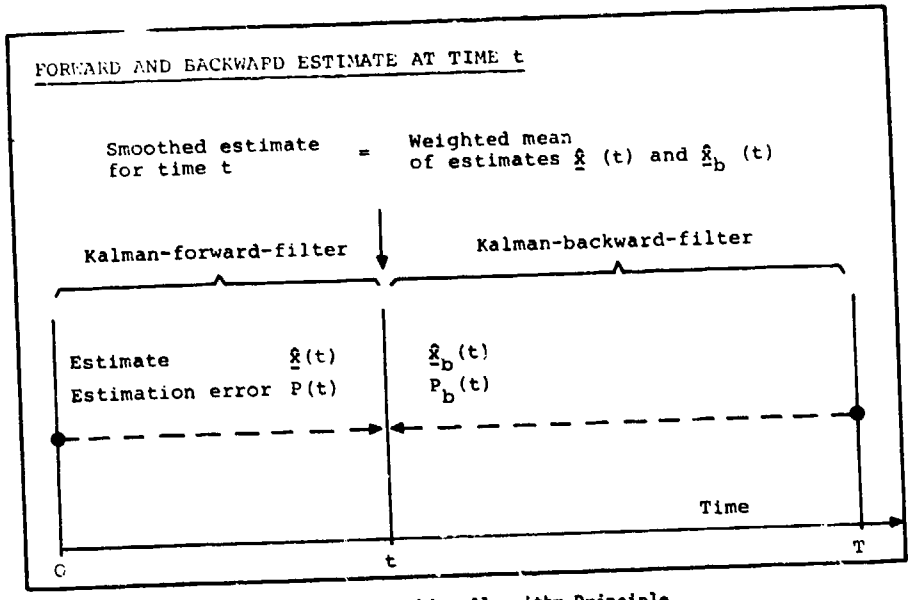

Fig. 8.2.4 Smoothing Algorithm Principle

8.3 Examples of Hybrid Systems

Inertial Navigation Systems are widely used for the flight testing and calibration of navigation equipment (e.g. [8.5], [8.6]). The two examples of hybrid systems described in the Sections 8.3.1 and 8.3.2 are used to illustrate the methods and to demonstrate the accuracy potential of these instrumentation systems.

8.3.1 Hybrid Reference System for the Testing of a Microwave Landing System

The DME-based Landing System (DLS) has been the German candidate in the ICAO competition for the next generation landing systems. The DLS has been tested by DFVLR at the Braunschweig airport. Hybrid measuring techniques have been applied during these tests.

The DLS landing system had to be tested mainly in-flight, when the exact position of the aircraft was measured by the tracking system, so that the outputs of the DLS on-board sensors could be compared with this reference flight path. According to a rule of thumb, the accuracy requirements for the tracking system should be better than the accuracy expected from the DLS system by one order of magnitude, which could be met only if at least for short ranges the measurements were based on cinetheodolites. They are the most accurate tracking sensors. The cinetheodolites have one drawback: the data evaluation is cumbersome. In order to alleviate this problem the DFVLR had decided to pursue the following proposal (s. Fig. 8.3.1).

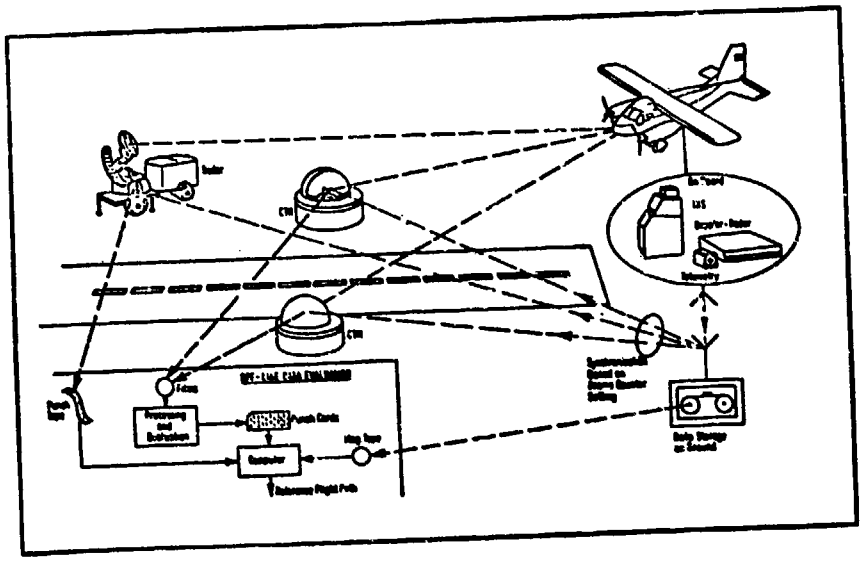

Fig. 8.3.1 Hybrid Measuring System for the Test Aircraft Trajectory

The ground based sensors

3 cinetheodolites
1 tracking radar

giving intermittent tracking data with high accuracy were supplemented by on-board sensors

1 inertial platform
1 barometric altimeter

giving continuous tracking data. The inertial system is aided in the vertical channel by a barometric altimeter and has a high short-time but a relatively low long-time accuracy. Thus the characteristics of ground-based and on-board sensors are complementary Because of the special data evaluation process for the cinetheodolites (processing of the films, manual evaluation of each picture and storing the information on punched card), all data can only be combined off-line for reference flight path computation.

The major purpose of the on-board sensors was to "interpolate" between 2 position fixes. For a quasi continuous reference flight path of 1 point every 1/30 s, one position fix was then required only every 8 s.

The data flow in Fig. 8.3.1 is as follows. The time base of the system was a digital counter (frame counter) on board the aircraft. By means of a PCM telemetry system the following data required for the computation of the flight path were transmitted to the ground by telemetry:

- frame count,
- 3 accelerations as measured by the inertial platform,
- 2 velocities as computed by the analog computer of the inertial system,
- roll-, pitch- and yaw angle of the aircraft as measured by the platform,
- 2 Doppler velocities, and
- barometric altitude.

The frame counts received on the ground controlled the radar and cinetheodolites measurements. This guaranteed a high accuracy for the synchronization of all data measured on the ground and on board. The time between 2 fixes was in general 8.388 s. The radar measurements were stored on punched tape. The weighted combination of all ground based measurements and mixing with the on-board measurements was done in a Kalman filter. In carrying out the measurements it was necessary to define a rectangular coordinate system. The origin of this system was centered in the azimuth antenna of the DLS system (DLS-A Station). The x-axis was aligned with the runway and pointed nearly east (84, 782°), the y-axis nearly north and the z-axis upwards.

The cinetheodolites are Bodenseewerk KTH 59. Here the tracking is done manually by handwheels and by means of telescopes. During the DLS trial, the registrations were made synchronously with the radar. The tracking radar was the Hollandse Signaalapparaten L4/3. This radar follows the target automatically during the measuring process, and gives the angles of elevation and azimuth of the antenna system and the slant range to the target. Automatic tracking is achieved by rotation of the radar beam (conical scan). The distance to the target is determined by the interval between transmission and reception of every individual radar pulse.

The test aircraft, a Dornier Do 28, is shown in Fig. 8.3.2 and part of the on-board electronics can be seen in Fig. 8.3.3: the inertial system (Litton LN3-2A) and the CAMAC interface for digitizing the signals. Not included in the figure are the Doppler radar and the barometric altimeter. The inertial system consists of the inertial platform, the analog computer, the flux valve for coarse alignment of the platform and the align control plus switch-on unit. This unit also contains the preamplifier and analog readout for the signals.

Fig. 8.3.2 DO 28 Test Aircraft

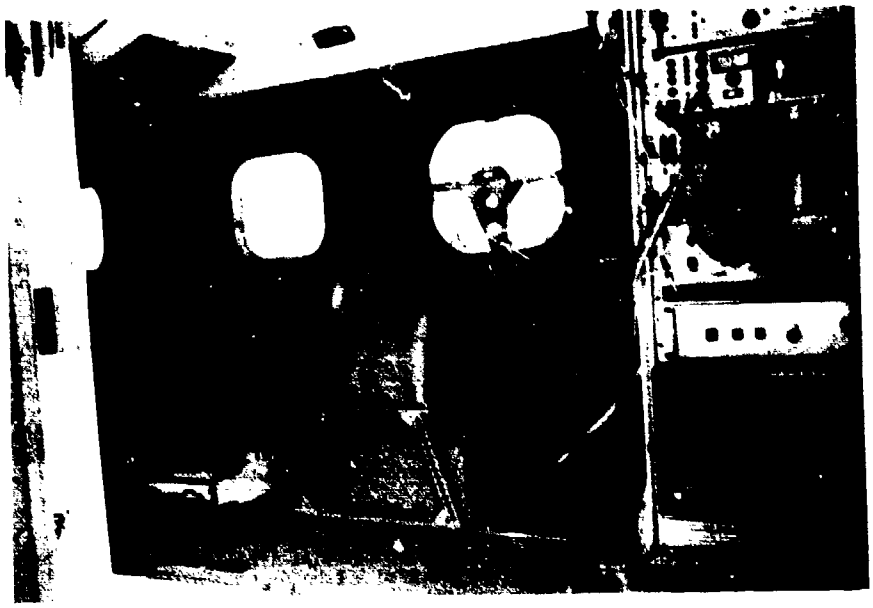

Fig. 8.3.3 On-Board Equipment of the DO 28 Test Aircraft

As mentioned above, all on-board signals - the accelerations, velocities, the attitude and heading angles, the Doppler velocity, the barometric altitude - were digitized in the CAMAC interface and fed to the PCM telemetry.

The Doppler radar was the General Precision Laboratory ANP-153 (V). Its radio energy is transmitted incoherently and as impulses. The antenna is pitch and track stabilized. The barometric altimeter was the Rosemount Engineering Company, Model 840E.

In general, only three measurements are necessary to determine the position of a target. From the three cinetheodolites and the tracking radar nine measurements are available and the position of the target is overdetermined. Therefore the calculation of the various position fixes was achieved by means of an optimum fitting using the least mean square method. The evaluation program for the computer was set up in such a way as to permit working with less than nine data points. For further processing, the coordinates of the position fixes were stored on magnetic tape. The accuracy of the various points can be expressed by the error covariance matrix which was determined for each position fix based on the radar specifications (range-, elevation-, azimuth accuracy). The ground-derived data from the cinetheodolites and the radar including the covariance matrix describing the accuracy of the information were recorded on magnetic tape.

The data measured on board - 3 components of the acceleration from the INS, 2 components of the velocity from the INS, 2 components of the velocity from the Doppler radar, barometric altitude - were transmitted from on-board to ground and stored on magnetic disc. The synchronization of the data on magnetic tape and on magnetic disc was based on the frame counter setting transmitted from on-board to ground and recorded on tape and disc as the first word of each data frame.

Based on the INS velocity outputs the computation of the raw flight path was carried out with a frequency of 5 Hz. By comparing the frame counter setting on the magnetic disc and on the magnetic tape a position fix was recognized by the computer, which started the Kalman filter algorithm for estimating the INS error state vector. The state vector, state transition matrix and covariance matrices before and after the measurement were temporarily stored on magnetic disc. When the last position fix had been processed, the smoothing of the INS errors (using the Rauch-Tung-Striebel algorithms) backwards in time was started based on the forward filter state vector, transition matrix and covariance matrices stored temporarily on the disc.

Since the final smoothed error state vector estimates for correcting the INS flight path were 8 seconds or sometimes more apart (if no position fix was at hand) while the flight path had to be corrected at a frequency of 5 Hz, the errors during the 8 seconds had to be calculated by interpolation. Then the final reference flight path could be calculated. An interesting figure for the reference flight path is the self-diagnosis of the estimation. This 1σ-band for the reference flight path is simply the square root of the corresponding value on the main diagonal of the covariance matrix. Since the optimal estimation was not tied down to fixed time intervals, the reference flight path computation could also be carried out when the aircraft was out of the range of the tracking radar and the cinetheodolites. The reference flight path was then based solely on the INS with position errors growing according to its error dynamics.

The data flow during the final reference flight path computation is illustrated in this flow-diagram:

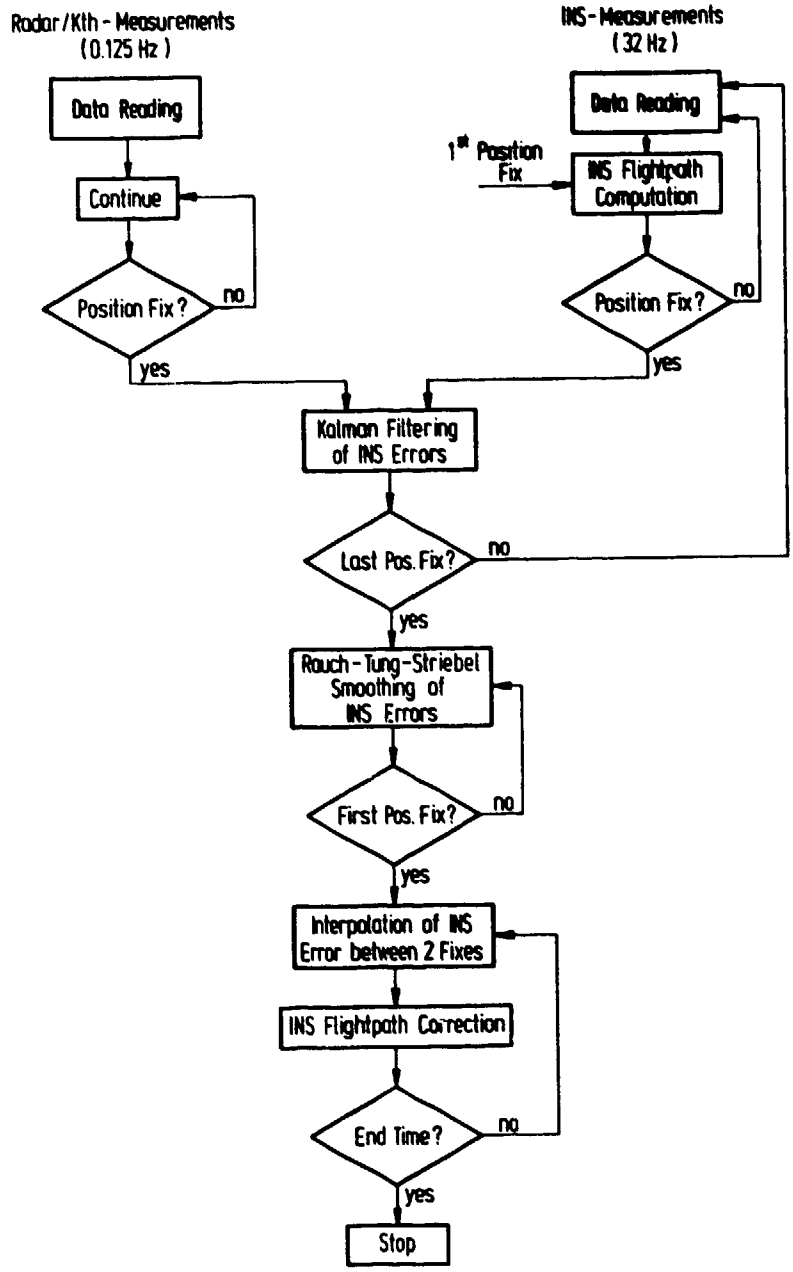

Fig. 8.3.3a Flight Path Computation Diagram

The ground and the on-board data are read from the magnetic tapes. The INS flight path is computed using the measured velocity. Every 8 seconds - if a position fix is available - the INS errors are estimated with the help of the forward Kalman filter. After the last position fix the INS error data are processed in the backward filter. Finally the INS flightpath is corrected for the interpolated INS errors which have been estimated.

In the following discussion the accuracy of the reference trajectory is described, as achieved in three typical flight tests by smoothing the tracking radar and cinetheodolites data using the information of the on-board sensor system. The errors in these cases have been computed with respect to the DLS-coordinates, azimuth, elevation and slant range. As reference point for the cinetheodolite measurements, a flash lamp which was mounted between the main landing gears was used. Because of the location the flash light was not visible on every cinetheodolite picture. The measuring accuracy of the cinetheodolites was therefore limited to 0.3 m for the error analysis.

Figs. 8.3.4 to 8.3.8 show the accuracy of the reference trajectory (2σ) for three typical flights.

Figs. 8.3.4 to 8.3.6: The aircraft was flying at 10.000 ft from 32 nm to 2 nm on a radial towards the DLS-A station. Because of insufficient visibility, no cinetheodolite measurements were possible. The reference trajectory was computed using the tracking radar and INS data. The maximum range of the radar is 28 nm; therefore beyond 28 nm, only INS was available, which leads to an increasing error of the trajectory with increasing distance. This is clearly seen in the plot for the DME error. This effect is almost not visible in the plots for the angular errors, because with increasing x, y, z-errors the distance to the DLS stations is also increasing. The angular errors increase when the aircraft approaches the DLS stations due to the following geometric effect: for constant x, y, z-errors, the angular error becomes very great if the slant range to the DLS stations becomes very small.

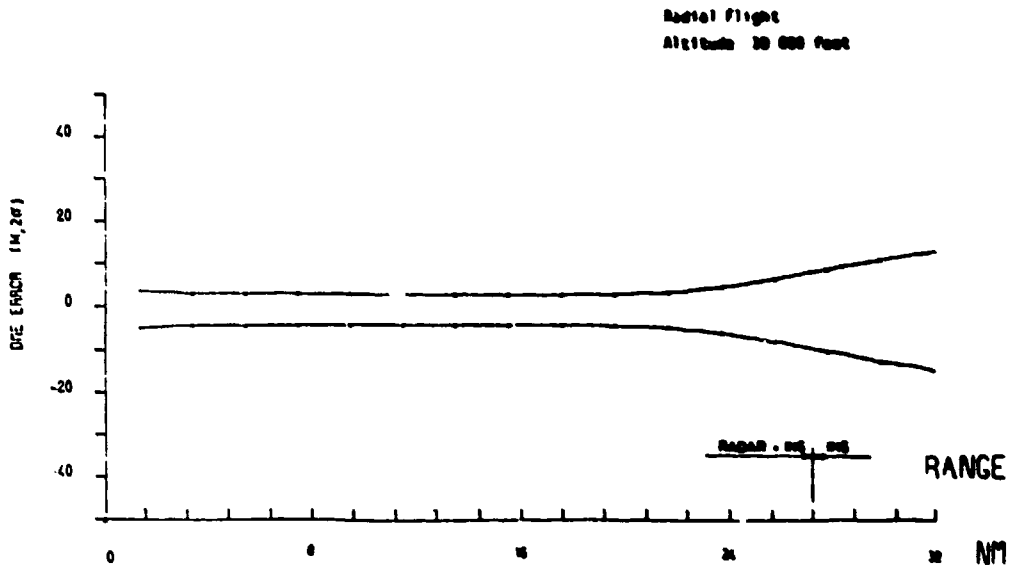

Fig. 8.3.4 Accuracy of the Reference System for the Distance to the Test Aircraft

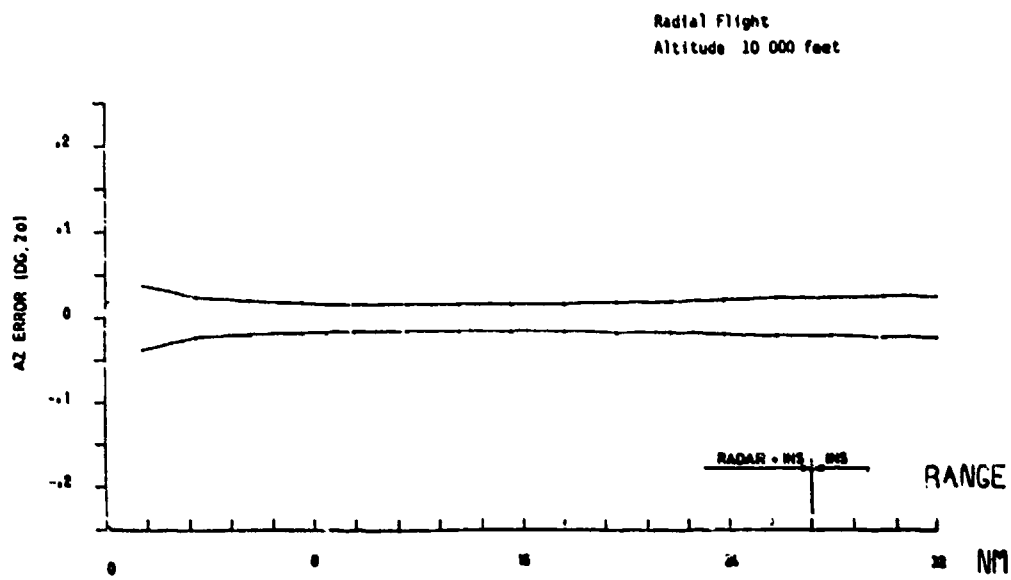

Fig. 8.3.5 Accuracy of the Reference System for the Azimuth to the Test Aircraft

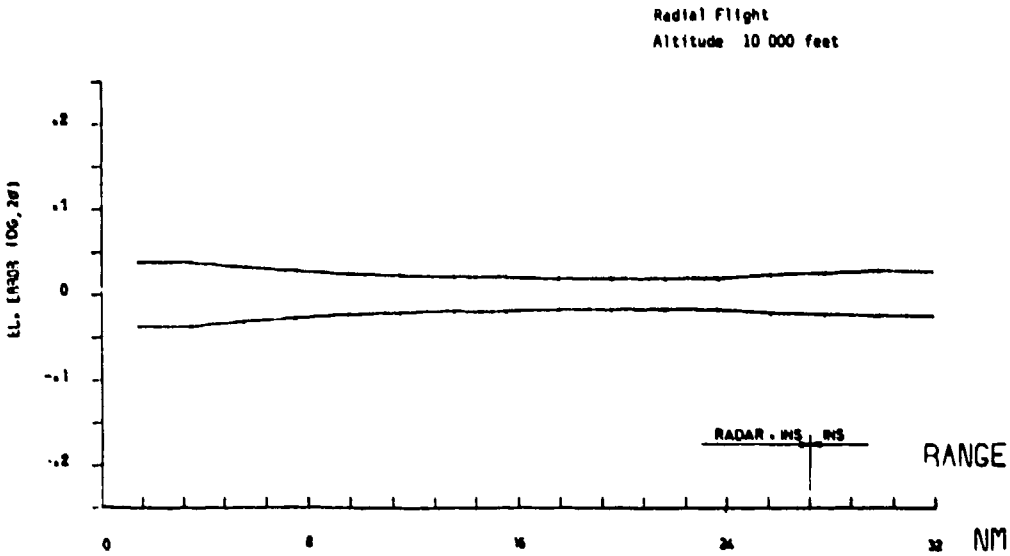

Fig. 8.3.6 Accuracy of the Reference System for the Elevation Angle to the Test Aircraft

Fig. 8.3.7: The aircraft was flying at 3000 ft on a radial to the DLS-A station. This flight illustrates the reference trajectory accuracy when different combinations of the sensors are used: Beyond 9 nm tracking radar and INS are available. For a short period of time the radar had lost the target. Between 9 and 5 nm, only one cinetheodolite could track the aircraft. At a distance of 1 nm from the DLS-A station - i.e. close by the DLS-E station - a telemetry break-down occured, because the aircraft was flying over the telemetry station. So the synchronization was cut off and no on-board data were available for the evaluation.

Fig. 8.3.8: This figure displays the errors during final approach. In this case all the sensors were in operation (3 cinetheodolites, tracking radar and INS). The geometric effects due to a small distance between the aircraft and the DLS stations are clearly visible.

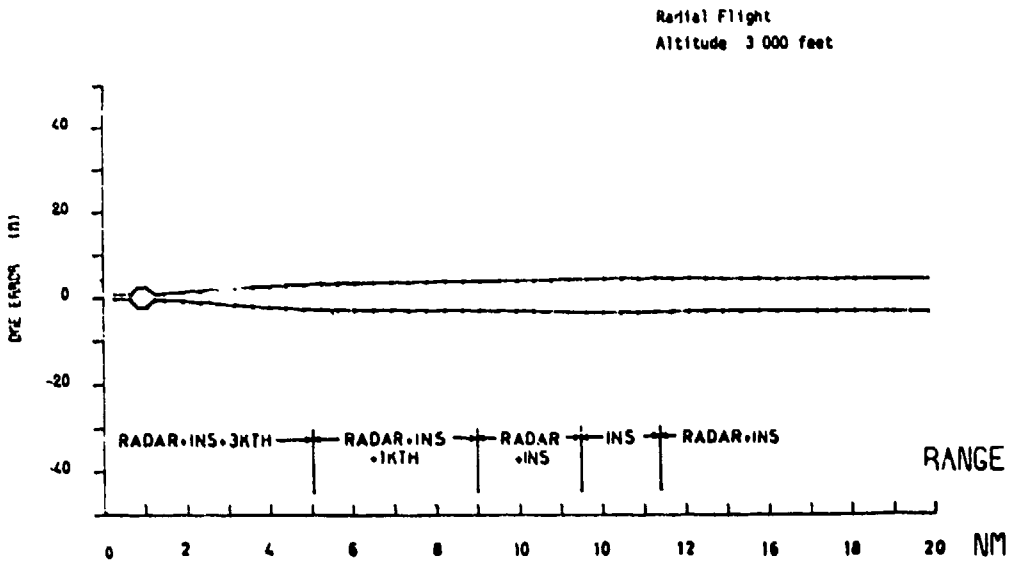

Fig. 8.3.7 Accuracy for the Distance to the Test Aircraft

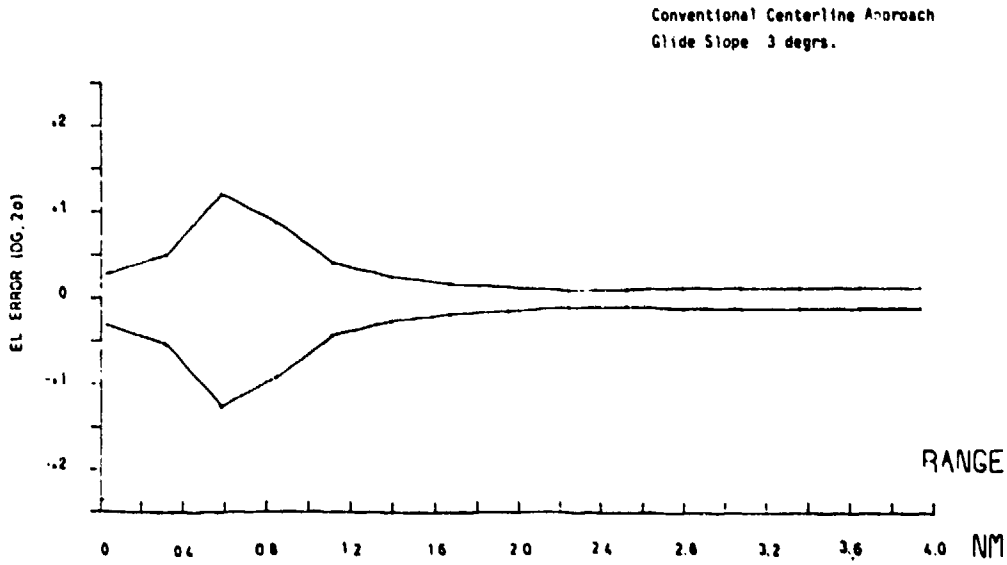

Fig. 8.3.8 Accuracy for the Elevation Angle to the Test Aircraft

Fig. 8.3.9 shows the results of measurements which were taken during conventional centerline approches. In the figure the difference between the y-components of the DLS signal and the reference is displayed in rectangular coordinates. The reference trajectory in this case has been calculated by smoothing the cinetheodolite data with the INS. The mean value of this difference is very small: 0.42 m. The standard deviation (1σ) is also very small, as can be seen in this figure: 0.75 m. The error of the reference system is certainly not correlated with the DLS error, so that it is correct to assume that the random error of the reference (1σ) is not greater than 0.75 m. But the structure of the difference signal clearly indicates that the main part of this error is due to the DLS system because the reference trajectory cannot contain such high frequency errors. The conclusion can be drawn that the integrated reference system can provide an accuracy of the order of 50 cm, with cinetheodolites measurements taken every 8 seconds.

The overall results which have been obtained during the DLS testing campaign have shown that the approach of an integrated measuring system for the flight path using optimal smoothing techniques is both economic with respect to the evaluation workload and provides very high accuracies.

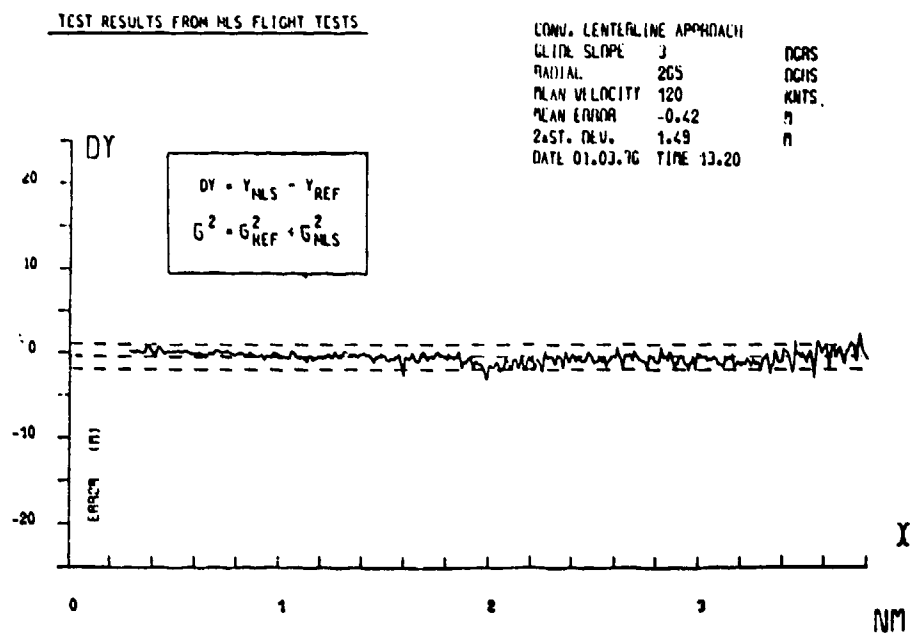

Fig. 8.3.9 Difference between the DLS Signal and Reference System Measurement

8.3.2 Hybrid Reference System for the Flight Testing of a Doppler Navigation System

The flight testing of Doppler navigation systems is another example of the successful application of a hybrid measuring system. In general for the evaluation of such flight tests, the aircraft position, velocity and sometimes also attitude and heading have to be known with very high accuracy. A hybrid measuring system consisting of ground equipment (tracking radars) and on-board sensors (inertial navigation systems, INS) can provide this accuracy. This fact will be illustrated by a few test results presented in this section.

For the Doppler navigation system tests the DFVLR test aircraft HFB 320 (Fig. 8.3.10)had been used. This aircraft contains advanced on-board instrumentation (Fig. 8.3.11, see also Section 9.4):

- fly-by-wire system
- general purpose on-board computer
- INS
- magnetic tape with high storage capacity
- quick-look capability
- several attitude reference systems, etc.

For the Doppler tests the main on-board instruments used were the Litton LN3 inertial platform, the Sperry SYP-820 attitude and heading reference system and three different types of Doppler radars (stabilized and fixed antennas, pulse and CW Dopplers). The measurements of these sensors were recorded on magnetic tape at high frequency (10 times per second).

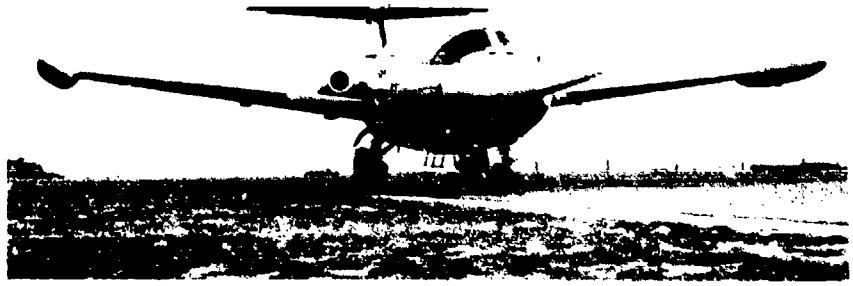

Fig. 8.3.10 HFB 320 Test Aircraft

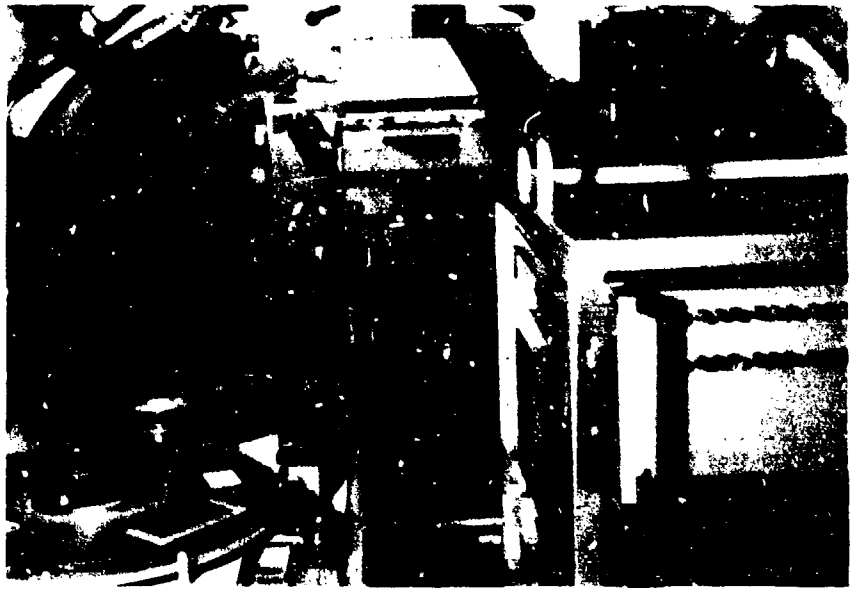

Fig. 8.3.11 HFB 320 On-Board Instrumentation

As a typical example of a flight profile for long range tests, Fig. 8.3.12 shows a flight from Hannover airport, via Meppen, Norderney and Helgoland back to Hannover. The flight track lies partly within the range of three tracking radars, at Hannover (L 4/3), Meppen (MPS-36) and Norderney (Fledermaus). Usually radar measurements are recorded every 10 seconds and stored on magnetic tapes.

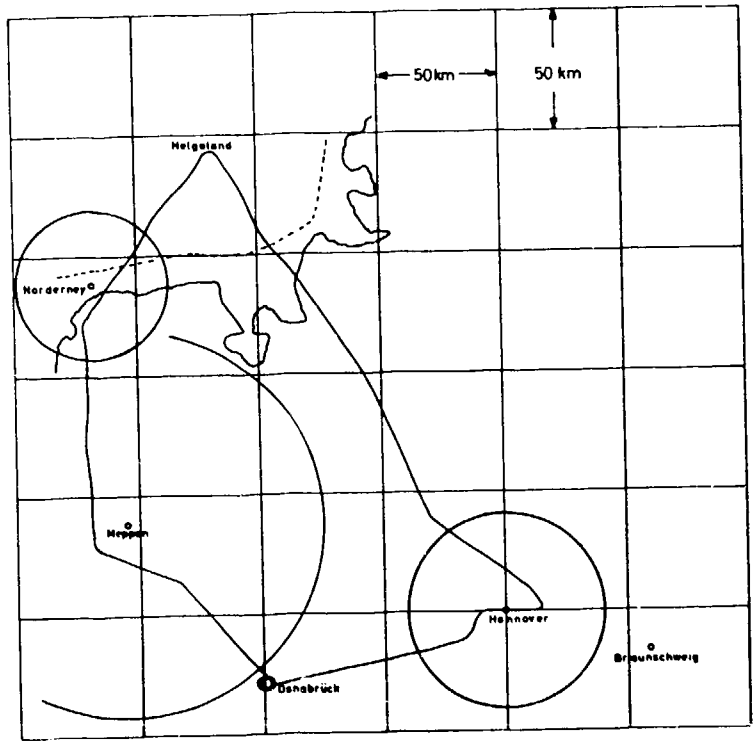

Fig. 8.3.12 Long Range Test Flight

The time synchronization of the on-board and the ground based sensors is accomplished off-line with the aid of a time code which is also recorded on the magnetic tapes.

For the Kalman filter and optimal smoothing calculations, the error models for the INS, radar and cine-theodolites described in the preceding chapters have been used. The error of a Doppler radar signal has been illustrated in Fig. 8.1.1. The predominant error is the Doppler fluctuation, which can be observed clearly in this figure in comparison with the very smooth inertial velocity. Velocity scale factor error and heading error are also contained in the Doppler navigation system error model.

The reference system for the Doppler navigation system testing is realized in the same way as described in Section 8.3.1, i.e. by combining off-line the measurements of the tracking radars with the inertial on-board measurements. The accuracy of this reference system is illustrated in Figs. 8.3.13 to 8.3.16. They show the accuracy obtained by forward Kalman filtering and by backward smoothing. The improvement introduced by optimal smoothing is clearly visible. When the aircraft flies out of the radar coverage the errors of velocity and position increase, as it can be observed in Figs. 8.3.13 and 8.3.14. This increase is much less for the smoother because the "gaps" between two radar coverages are closed from both sides. Under tracking radar coverage the roll and pitch angles are measured to 10 arc sec, the heading to 1.5 arc min, the velocity to 0.03 m/s and the position to 2 - 8 m accuracy (1σ) by the hybrid reference system, consisting of an INS and a tracking radar. Fig. 8.3.15 shows the difference between the reference trajectory (obtained by smoothing the tracking radar data for the long range flight with the LN3 inertial platform) and the radar measurements (curve 1). The accuracies (1σ) of the tracking radars (curve 2) and the reference trajectory (curve 3) are also shown. This figure demonstrates that the measurements of the three tracking radars

- L4/3
- MPS-36
- Fledermaus

have approximately the same error dynamics. This can be explained by the fact that these errors are mainly caused by the radar fluctuations on the test aircraft HFB 320.

The accuracy that would be obtained if Doppler radar, rather than the INS, were used to smooth the tracking radar data has also been analysed. This is shown with the help of Fig. 8.3.16. This figure gives a comparison of the position measuring accuracy (smoothed estimates) of the two reference systems

- INS and tracking radar
- Doppler and tracking radar

for the long range flight shown in Fig. 8.3.12. Fig. 8.3.16 shows the higher accuracy obtained with the INS under radar coverage in comparison with the Doppler system. Outside the radar coverage both systems have similar errors. In long periods between radar coverage the reference system with a Doppler has a higher accuracy than with an INS (in Fig. 8.3.16 between 4500 and 5500 s), though it should be realised that the Doppler heading reference system (SYP 820) was initially aligned to north with the aid of the LN3 system.

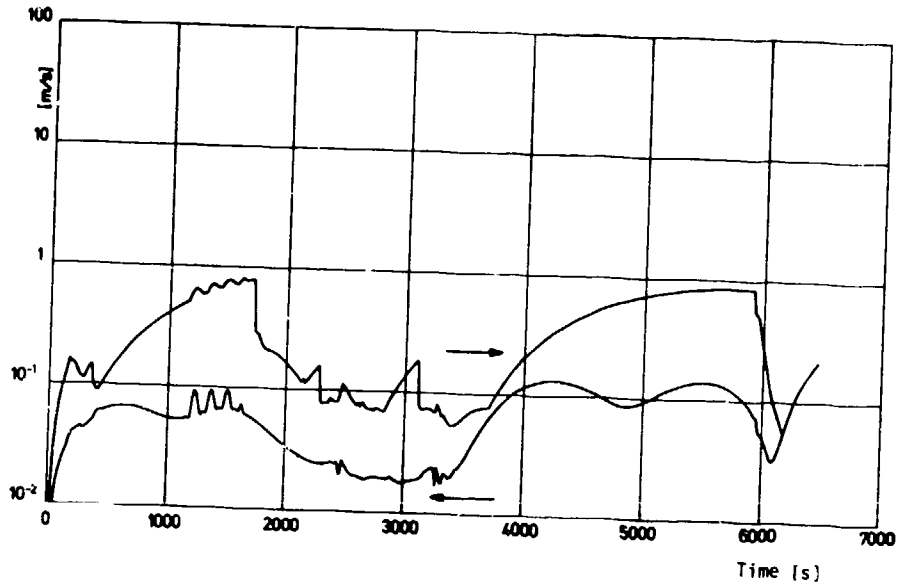

Fig. 8.3.13 Velocity Error of the Hybrid System (1σ)

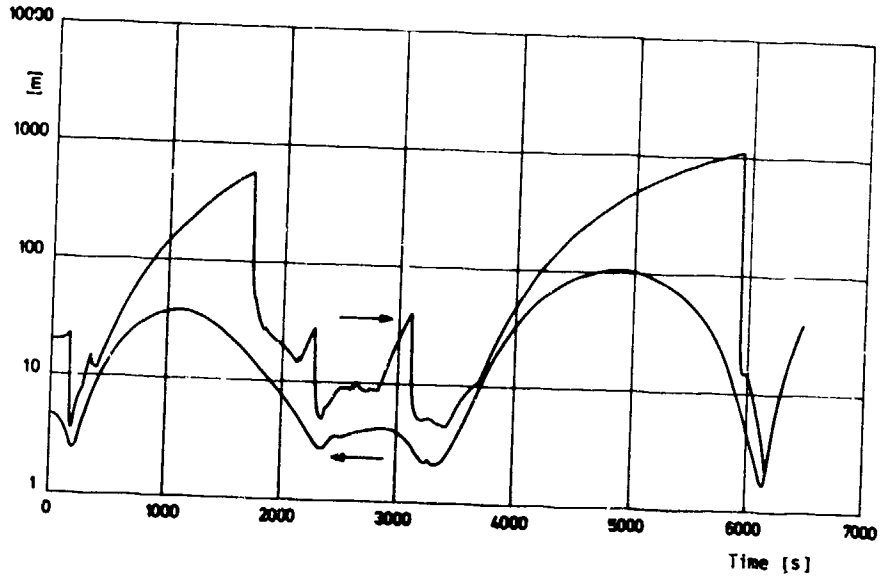

Fig. 8.3.14 Position Error of the Hybrid System (1σ)

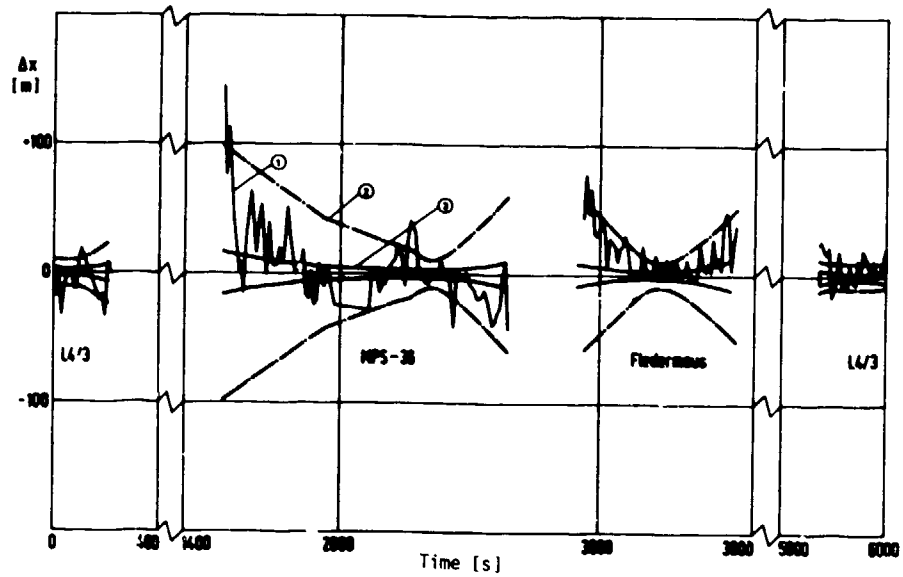

Fig. 8.3.15 ① Difference between Reference Trajectory and Radar Measurements
② Accuracy of the Tracking Radar (1σ)
③ Accuracy of the Reference Trajectory (1σ)

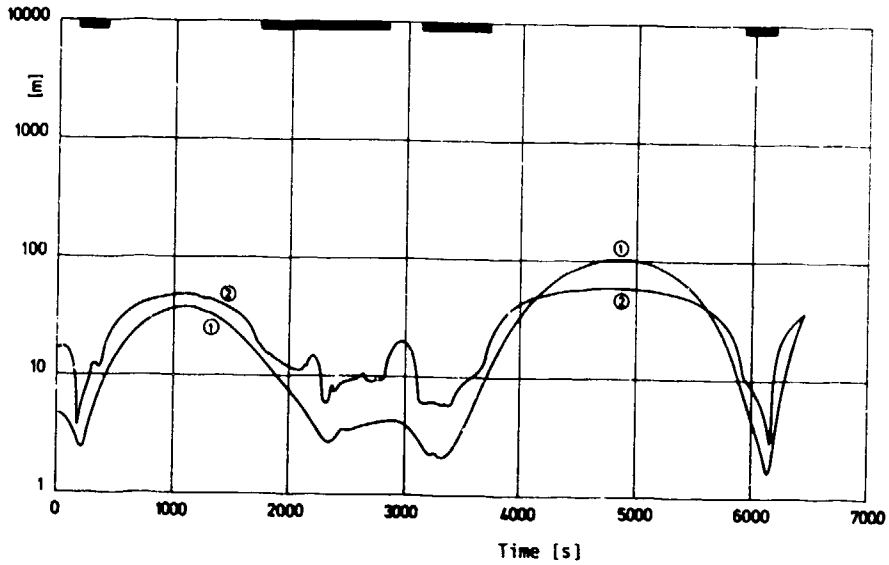

Fig. 8.3.16 Accuracy of the Smoothed Estimates of two Hybrid Reference Systems
① INS and Tracking Radar
② Doppler and Tracking Radar

As examples of the results of flight tests, Figs. 8.3.17 and 8.3.18 are shown. Fig. 8.3.17 shows the difference between the Doppler radar measurement and the reference velocity for a flight period of 90 s. This is a part of the sample function measured in a flight over flat land. The mean value of this sample function has been computed over 200 s, which corresponds to a distance flown of 12 nm at 110 m/s. The mean value of the sample function was 0.067 m/s, which is negligibly small. The standard deviation of this sample function is σ = 2 m/s, a value which is several orders of magnitude greater than the reference velocity accuracy, so that it can be stated that this error is due to the Doppler radar measurement only.

Another sample function has been taken over water. Fig. 8.3.18 shows the difference between the Doppler radar measurement and the reference velocity for 90 s flight time. The same analysis has been carried out for this sample function showing a mean error of 2.2 m/s and a standard deviation σ = 1.4 m/s. The large

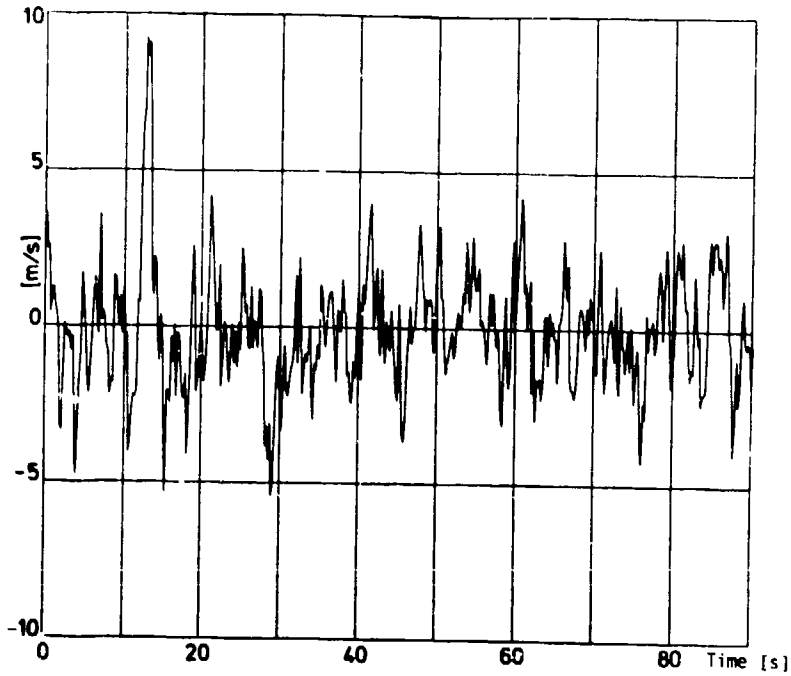

Fig. 8.3.17 Doppler Radar Error Fine Structure as Measured with the Help of a Hybrid Reference System over Land

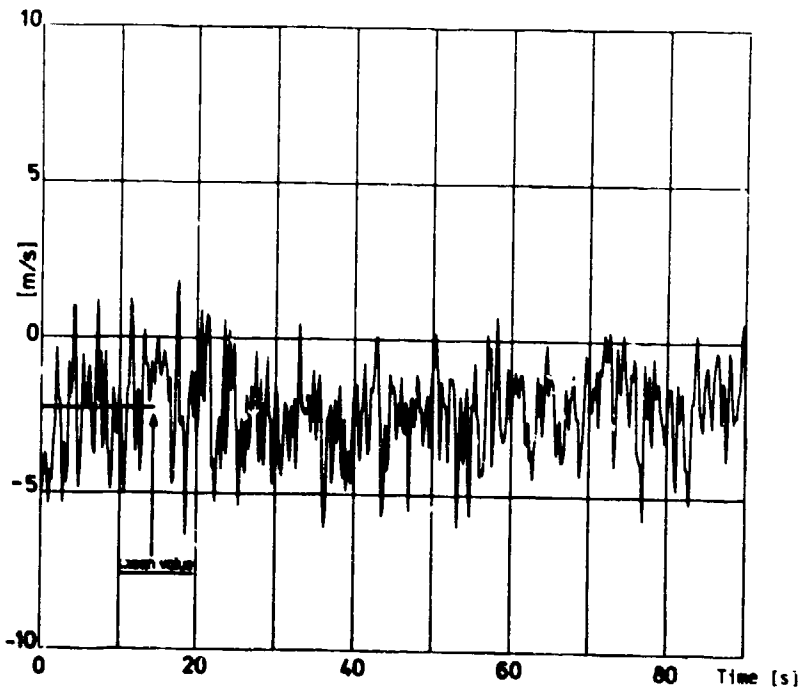

Fig. 8.3.18 Doppler Radar Error over Water

mean error present in the sample function is due to the land/sea calibration shift. The sample functions show that the fluctuation error over sea has smaller amplitudes than over land. The statements made so far refer to the velocity measured in the aircraft's longitudinal axis. Similar results have been obtained for the cross-track velocity.

The results which have been obtained in several campaigns of flight testing navigation systems of high accuracy have shown that hybrid systems can provide reference information about the aircraft attitude, heading, velocity and position with highest accuracy, if advanced software techniques such as optimal smoothing are combined with advanced instrumentation.

References for Chapter 8

[8.1] Oppelt, W. — Kleines Handbuch technischer Regelvorgänge. Chemie-Verlag Weinheim/Bergstraße, 3. Aufl., 1960.

[8.2] Gelb, A. (Editor) — Applied Optimal Estimation. The M.I.T. Press, Cambridge, (Mass.), USA, 1974.

[8.3] Sage, A. P. and Melsa, J. L. — Estimation Theory with Applications to Communications and Control. McGraw-Hill Book Company, New York, 1971.

[8.4] Rauch, H. E., Tung, F., Striebel, C. T. — Maximum Likelihood Estimates of Linear Dynamic Systems. AIAA Journal, Vol. 3, No. 8, 1965.

[8.5] Drohan, W.A., et.al. — Airborne Flight Inspection Inertial Locator Equipment Development and Flight Evaluation. FAA Report RD-71-88, May 1971.

[8.6] Abbink, F.J. and Krijn, R. — Navaid Calibration Evaluation with a Computer-Controlled Avionics Data Aquisition System. NLR Report MP78030U, 1978.

9. APPLICATION OF GYROSCOPIC INSTRUMENTS TO FLIGHT TESTING OF AIRCRAFT

Flight testing of an aircraft is carried out for a number of reasons such as:

- New or modified aircraft must be certified.
- Research objectives are studied with experimental aircraft.
- The aircraft is used as a "flying platform" for the evaluation and calibration of airborne or ground equipment.
- Research and teaching in a "flying classroom".

The aim of the flight test of a new or modified aircraft is to demonstrate that the airplane or subsystems of it perform in accordance with certain specifications or requirements (Mil. Specs., requirements of national airworthiness authorities, etc.) or to measure the deviation from these specifications. Tests are required for

- Stability and control ("flying qualities").
- Aircraft performance.
- Systems (including avionics and navigation).
- Structure (loads and flutter).

The same tests are often accomplished with experimental aircraft to satisfy basic research objectives. Flight tests can be made in steady state or in non-steady (dynamic) flight conditions. The variety of parameters which are involved in flight testing makes the design and integration of the instrumentation system a rather complex task. A comprehensive analysis of the principles and problems of the design of flight test instrumentation is presented in Volume 1 of this AGARDograph [9.1]. The general ideas laid down in Volume 1 are also valid for the gyroscopic instrumentation subsystems under consideration. In addition, we have to consider the special requirements which exist for the applications in dynamic flight testing.

9.1 Requirements for the Gyroscopic Instruments

The application of gyroscopic instruments in aircraft stability, control and performance flight tests and for the calibration of airborne and ground systems places a number of requirements on these transducers [x]. These requirements are expressed in terms of measurement range, frequency response and accuracy. It has already been discussed in Chapter 1 that the non-steady flight test techniques which are used to identify aircraft parameters in dynamic flight conditions, together with advanced mathematical evaluation procedures, have increased these requirements in the last decade.

The kinematic and dynamic quantities which are of interest in these flight tests and which can be measured with inertial transducers are:

- the angular rates in aircraft body axes (roll, pitch, yaw)
- the aircraft angles measured with respect to local level (attitude) and north (heading)
- the linear accelerations, in aircraft body axes and also with respect to local level and north.

From these measured quantities, the aircraft ground speed and position can be computed by dead reckoning (see Chapter 7). The requirements for the inertial transducers largely depend on the characteristics of the physical quantities to be measured:

- the frequency spectrum of the signal of interest, which depends on the type of aircraft and mission flown in the flight test, and
- the frequencies of the noise corrupting this signal.

The noise can be generated within the transducers (e.g. angular or linear vibrations, pickoff noise) or it can be introduced by the electronics or the digitizing process (see Chapters 3 and 4).

In order to illustrate the physical structure of the quantities which have to be measured in the flight tests, we present several sample functions of these quantities obtained during flight tests with the DFVLR test airplanes (DO 28 and HFB 320; Figures 8.3.2 and 8.3.10). These sample functions exemplify the difficulty of separating the signal of interest from unwanted overlying noise. This separation has to be accomplished by appropriate filtering of the sample functions.

9.1.1 Sample Functions of the Measurements Obtained with Strapdown Gyros and Accelerometers

Figures 9.1 to 9.3 show sample functions of the angular rates (yaw, pitch and roll) as measured, before and after touch down, without any filtering, on shock mounts in the DO 28 airplane by the experimental strapdown system MOSY (s. Section 7.4.4.4). The digital data (angle increments divided by the time increment) were sampled and have been plotted with a frequency of 50 Hz. One can observe that the high frequency part of the angular rate (>1 Hz) increases after touch-down during the ground roll.

The angular rates have been integrated in the MOSY strapdown computer to obtain the aircraft angles. The results are shown in Figures 9.4 to 9.6 (the roll, pitch and heading angles). One can observe that, by the integration process, the high frequency content of the measured signals has been considerably diminished.

The corresponding linear accelerations for the same airplane and the same flight period are shown in Figures 9.7 to 9.9 in aircraft body axes, measured by strapdown accelerometers (Litef B 250) and without any filtering. Here again, the high frequency part (> 1 Hz) of the accelerations increases after touch-down.

The sample functions of these measurements obtained with strapdown gyros and accelerometers of high accuracy illustrate the difficulty of distinguishing the useful signal (angular velocity, attitude and heading

[x] For the application in structural tests see Chapter 1, for systems testing Chapter 8.

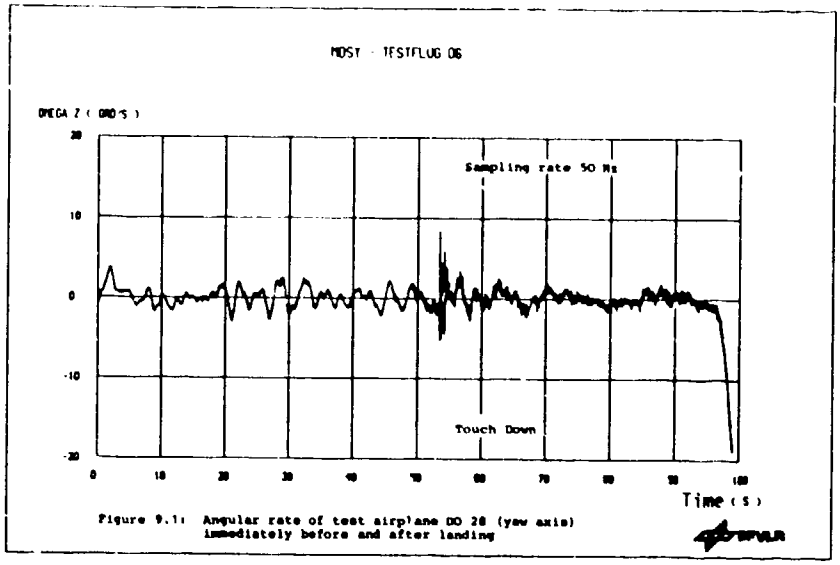

Figure 9.1: Angular rate of test airplane DO 28 (yaw axis) immediately before and after landing

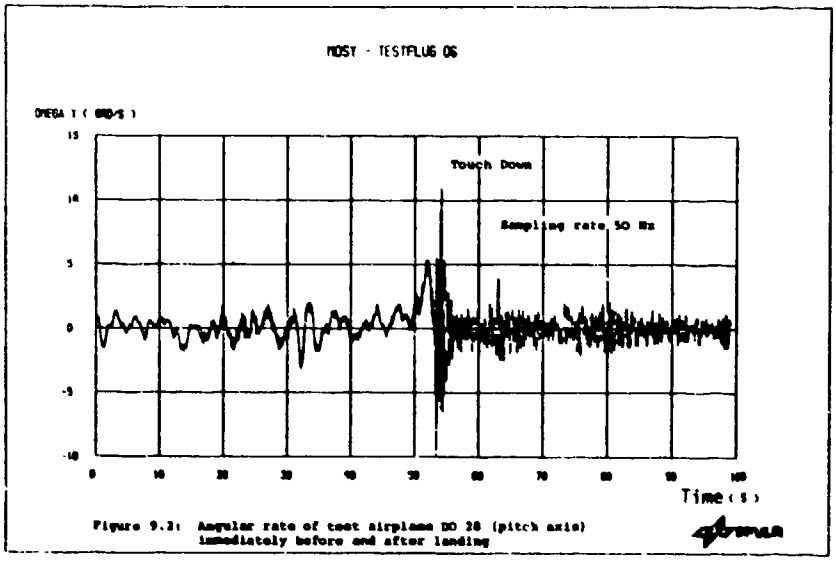

Figure 9.2: Angular rate of test airplane DO 28 (pitch axis) immediately before and after landing

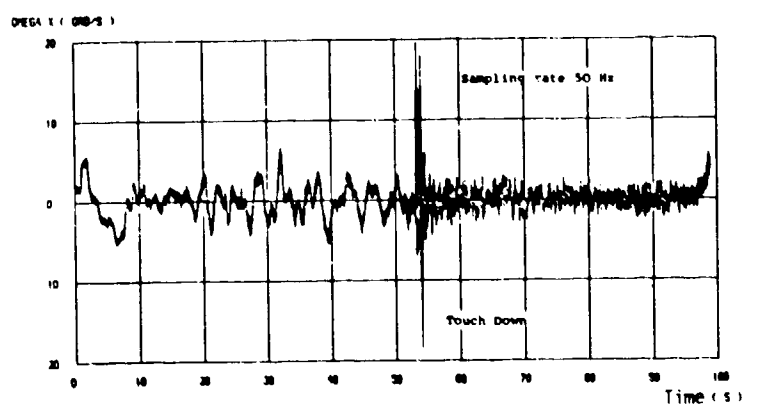

Figure 9.3: Angular rate of test airplane DO 28 (roll axis) immediately before and after landing

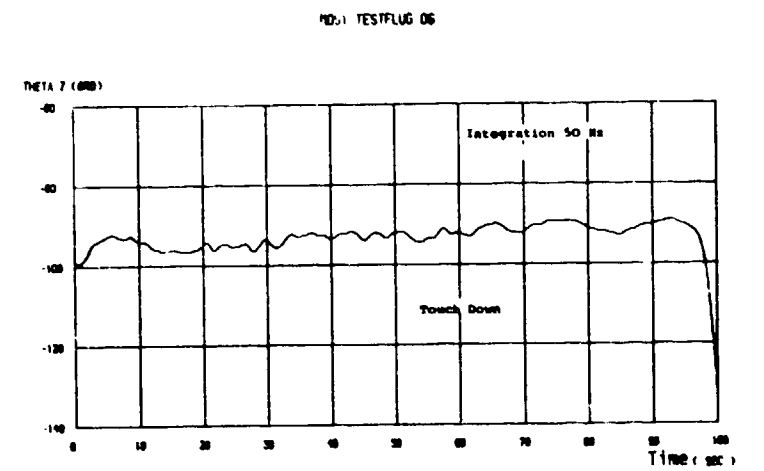

Figure 9.4: Heading of test aircraft DO 28 (by integration of yaw rate Figure 9.1)

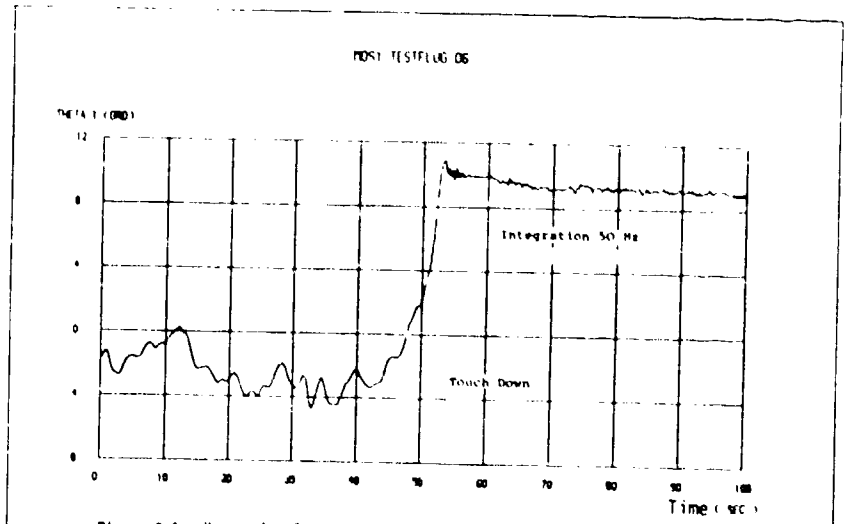

Figure 9.5: Yaw angle of test aircraft DO 28 (by integration of yaw rate Figure 9.2)

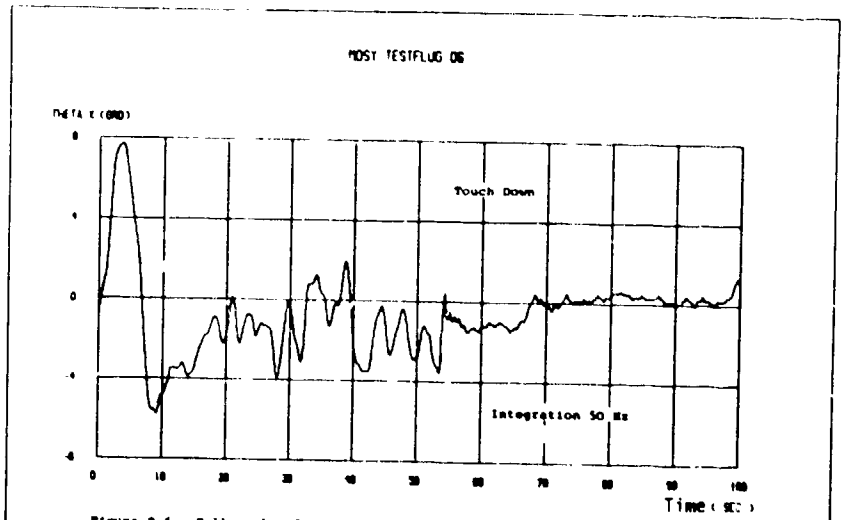

Figure 9.6: Roll angle of test aircraft DO 28 (by integration of roll rate Figure 9.3)

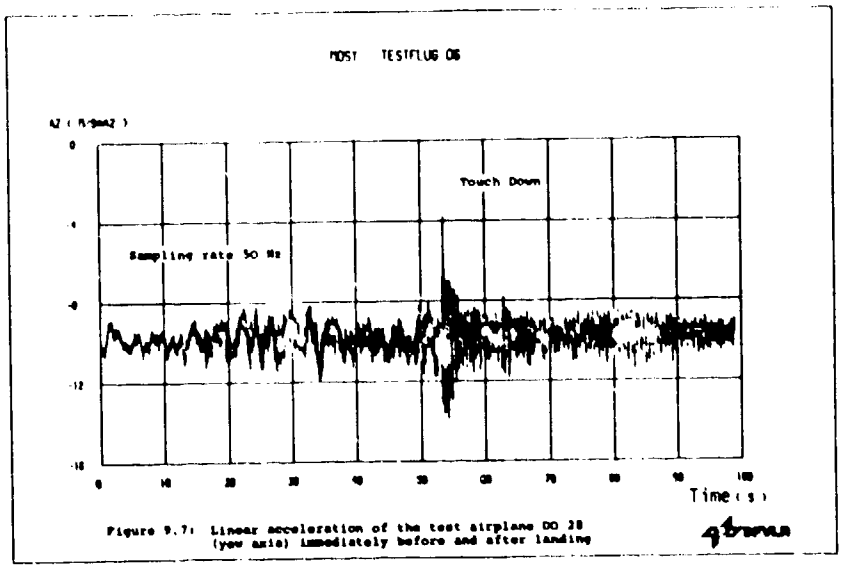

Figure 9.7: Linear acceleration of the test airplane DO 28 (yaw axis) immediately before and after landing

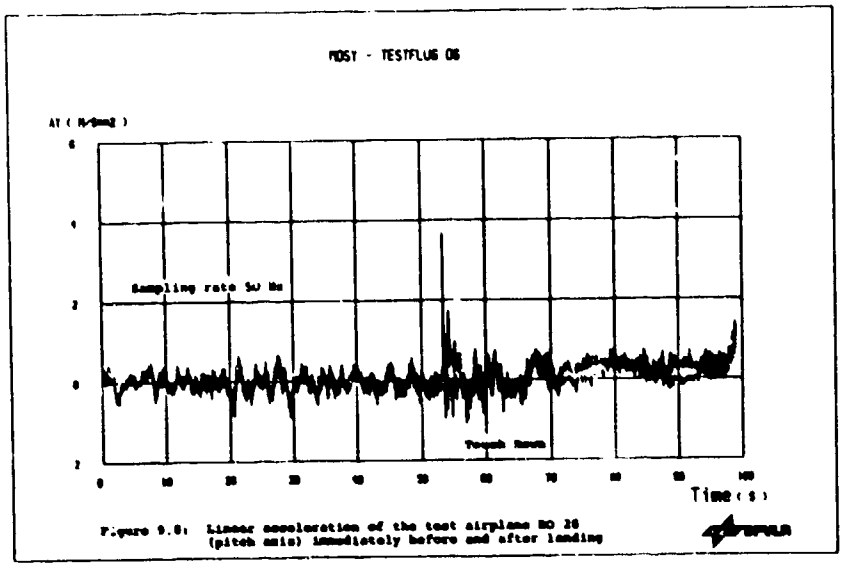

Figure 9.8: Linear acceleration of the test airplane DO 28 (pitch axis) immediately before and after landing

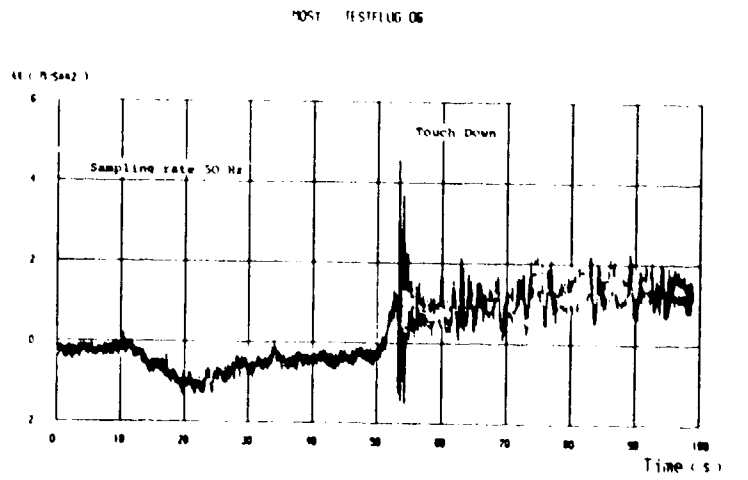

Figure 9.9: Linear acceleration of the test airplane DO 28 (roll axis) immediately before and after landing

and acceleration of the airplane) from what is regarded as noise (e.g. aircraft vibrations). This fact is particularly obvious in the increase of the noise level in the Figures 9.1 to 9.3 after touch-down, when the aircraft is rolling on the grass field. The "noise" in these figures partly corresponds to angular vibrations of the aircraft, partly to effects in the transducers induced by vibrations or other sources and finally, to effects in the readout system.

The effect of a simple integration process on the noise level can be observed in comparing the angles (Figures 9.4 to 9.6) with the angular rates (Figures 9.1 to 9.3). A similar effect can be seen when the accelerations (Figures 9.7 to 9.9) are integrated to obtain the velocities. It should be noted here that the integration process does not reduce the noise to nothing, but builds up a "random walk" stochastic process, with a variance increasing with time (see Section 4.3).

9.1.2 Sample Functions of Measurements Obtained with an Inertial Platform

The sample functions shown in Figures 9.10 and 9.11 have been obtained with the LN3-2A inertial platform system during a laboratory experiment. The platform was coupled with a digital computer via an interface with two 12 bit A/D converters for the accelerations. The navigation equations were programmed in this computer, and the loop was closed in feeding the computed gyro torquing signals back into the platform through a 12 bit D/A interface. As a means of obtaining clear effects in this experiment, the platform was not aligned very accurately (1 to 2 minutes of arc misalignment in the horizontal axes and 10 to 12 minutes of arc in the azimuth) and a north accelerometer bias of the order of 10^{-2} m/s^2 as well as a vertical gyro drift of 0.5 °/h was not compensated. The INS was installed in the laboratory and no external accelerations or angular rates applied to it. Thus the accelerometer output is a measure of the earth gravity sensed by the accelerometers in accordance with their angular orientation and of the acceleration measuring errors. Figure 9.10 shows sample functions of the horizontal accelerations and the computed ground speeds recorded during the first seven minutes (reading interval 0.2 seconds). An interesting feature is the fine structure of the errors, particularly of the acceleration errors: One can clearly recognize quantization effects. The accelerometer noise excites "quantum jumps" in the A/D converters at the level of the last bit. It is also remarkable how quickly the clearly visible bias of the north accelerometer is integrated into a large speed error (V_N).

It should be pointed out that the large platform errors introduced to make the effects visible lead to navigation errors that lie about one order of magnitude above the errors of the calibrated LN3-2A system.

In Figure 9.11, the acceleration indicated by the north accelerometer is again plotted with a reading interval of 14 seconds. Together with this sample function, the best estimate of the gravity component ($-g \cdot \varepsilon_E$) acting upon the accelerometer due to its angular orientation is shown. This estimate was obtained by applying the optimal smoothing technique (Chapter 8) to all the information obtained from the inertial platform during the experiment. This Figure 9.11 may be considered as a sample function showing the acceleration signal together with the noise corrupting this signal.

The physical structure of the output signals of an inertial navigation system in flight is illustrated

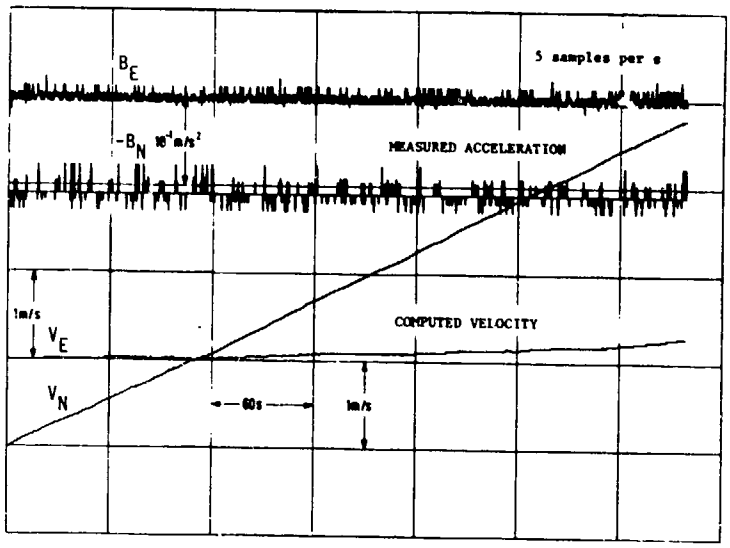

Fig. 9.10 Fine structure of the accelerations measured by a LN3-2A INS in a laboratory experiment, and the corresponding velocities

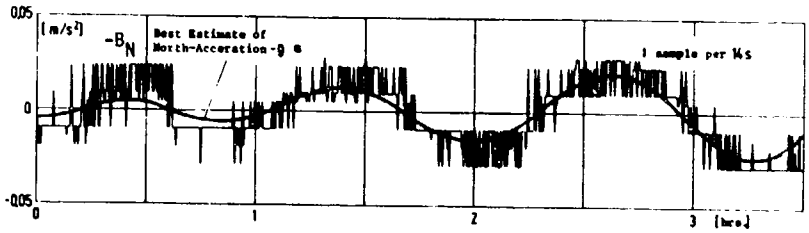

Fig. 9.11 North acceleration as measured by the LN3-2A INS together with the best estimate of the gravity component acting upon the accelerometer

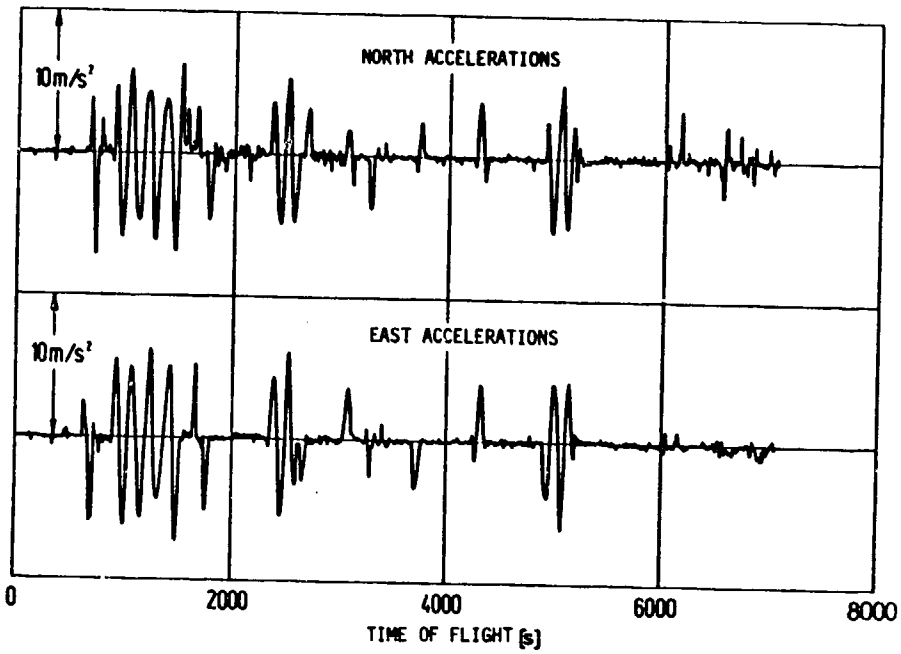

Fig. 9.12 Horizontal accelerations measured by a LN3-2A INS during a test flight

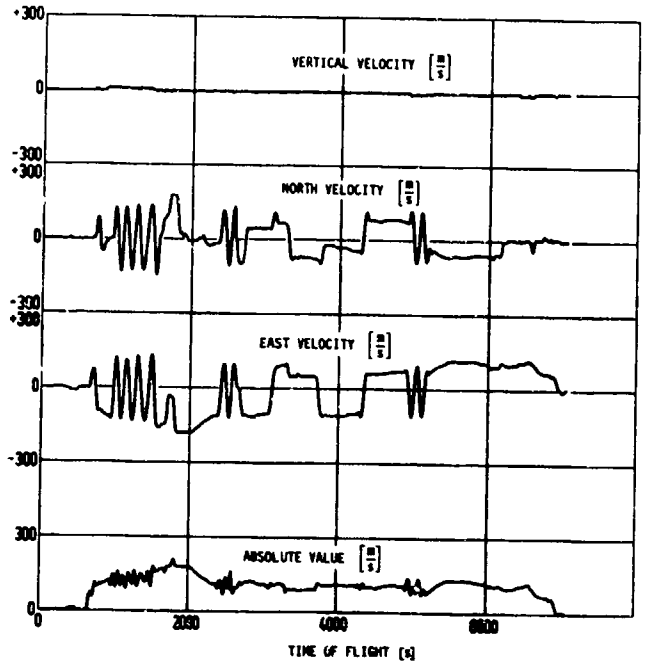

Fig. 9.13 Velocities measured by a LN3-2A INS during a test flight

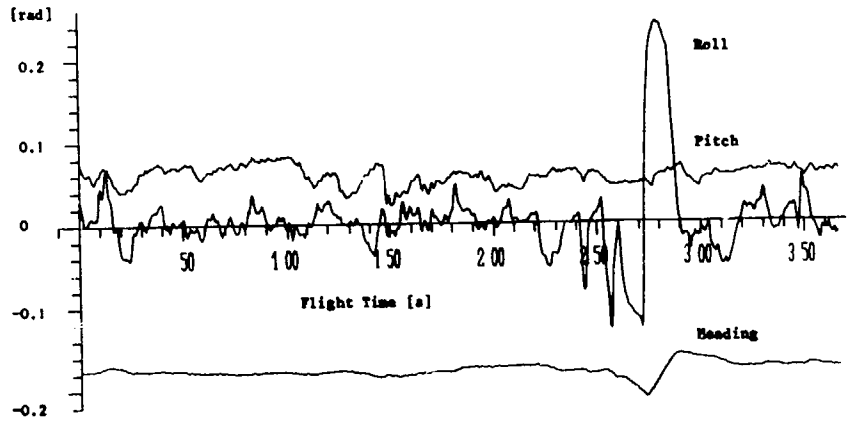

Fig. 9.14 The platform angles measured during a 6-min-interval of a flight test

by the Figures 9.12 to 9.14. These figures have been obtained in flight with the DFVLR HFB 320 test airplane using the LN3-2A INS. Figure 9.12 shows the north and east accelerations measured during a typical test flight of two hours duration. Figure 9.13 shows the corresponding velocities. (The vertical velocity was measured with a baro-inertial loop). The platform angles are plotted for a different flight in the Figure 9.14 for a flight period of 6 minutes.

9.1.3 General Conclusions on the Requirements for the Gyrocopic Transducers

The sample functions of measurements of aircraft angular rates, attitude and heading and linear accelerations, which have been presented in the preceding sections, demonstrate that these physical quantities are highly dynamic functions of time. In addition, they are corrupted with overlying noise induced bv aircraft vibrations or by the measuring process itself. Several general requirements for the design ot the instrumentation with respect to measurement range, dynamic response and accuracy can be formulated.

The measuring range of the gyroscopic transducers should be as small as allowable, in order to maximize the output signal level and consequently the resolution of the measurement. The allowable range is determined by the input signals which are expected from the aircraft motion and from the vibration level. Thus the range of the measurement depends on the type of aircraft used for the flight test and its manoeuverability. For yaw attitude (heading) a range of 360° is required. Roll and pitch attitude may be ± 180° and ± 90° respectively for fighter aircraft and ± 45° for transport aircraft. For fighter aircraft pitch and yaw rates up to ± 100 °/s and roll rates up to several hundreds of °/s have to be measured.

The frequency spectrum of the physical quantities to be measured (angles and angular rates) or to be computed (angle and rate dependent parameters) has to be studied in advance of the measurement. In general, gyroscopic instrumentation has sufficiently rapid response for the medium frequency range of up to 10 Hz, and also for the somewhat greater bandwidth of fighter aircraft of up to 20 Hz (see Sections 3.3 and 3.4). Not only the gyroscopic sensor but also the signal conditioning, the recording system and synchronization techniques employed have to be chosen with sufficiently high response frequencies in order to obtain an adequate measurement of the physical quantity of interest. In digital systems the rules for sampling signals must also be satisfied (see Section 4.4). Special attention has to be given to the problem of separation of the signal of interest from the overlying stochastic errors (see Sections 4.3 and 8.2).

The accuracy requirements span a wide range. Gyroscopic instruments of low or medium accuracy are normally required for aircraft flight tests under steady flight conditions (0.1° for the angles; 1 % of full scale for the angular rates). For performance testing and system identification under dynamic flight conditions gyroscopic equipment of inertial quality is necessary (a few arc minutes for the angles; 0.1 to 0.01% of full scale for the angular rates). These accuracies have to be achieved under severe conditions: heavy g-loads in manoeuvers, linear and angular vibrations and shocks, electromagnetic interference, temperature effects, electrical system noise, etc.

9.2 Conventional Instrumentation Systems

In the following sections we shall describe typical sets of inertial sensors which are in use as part of the overall instrumentation systems for the flight testing of aircraft.

A typical conventional instrumentation system as used for stability and contr. flight testing of aircraft contains the following set of inertial transducers:

3 Accelerometers (Section 3.6)
1 Vertical gyro (Section 6.1)
1 Directional gyro (Section 6.2)
3 Rate gyros (Section 3.3).

In addition to these inertial sensors, transducers are required for the angles of attack and sideslip, for air pressure and temperature, for the position of the aerodynamic surfaces, for engine parameters and strain gages for load measurements, etc.

The package of inertial transducers measures:

- the linear accelerations in the aircraft body axes
- the aircraft attitude and heading with respect to local level and north
- the angular rates in the aircraft body axes.

For performance tests earth-referenced measurements are often taken in addition to the on-board measurements, using tracking radars or cinetheodolites, to reconstruct the aircraft flight path in dynamic manoeuvers with high precision. With this set of on-board and ground instrumentation, the aircraft dynamic state vector:

- the position of the center of gravity
- the velocity of the center of gravity
- the aircraft attitude and heading

with respect to an earth-referenced coordinate system and

- the linear aircraft accelerations
- the aircraft angular rates

in aircraft body axes, can be measured with the accuracy provided by the sensors used. This accuracy is determined by carrying out an error analysis for the inertial sensor package using the error models developed in the Sections 6.1 (for the vertical gyro) and 6.2 (for the directional gyro) and in Section 3.2 (for mechanical gyros). The specific data for the sensors are specified by the producer of this equipment. Typical accuracy figures for the conventional type of instrumentation are:

Measurement	Accuracy
Acceleration	10^{-3} g
Attitude	0.5^{o}
Heading	1°
Angular rate	1 % of full scale

9.3 Instrumentation Systems Using an Inertial Platform

For performance flight testing and in experimental aircraft inertial platform systems are used more and more as basic sensors of the instrumentation system [9.2]. There are several factors which favor the use of an inertial platform system for flight testing - in particular their high accuracy (see Chapter 7). These systems have also become cheaper and more reliable during the two decades of their application to military and civilian navigation. They are insensitive to accelerations - in contrast to the vertical gyro - and thus more suited for dynamic flight testing. The aircraft and their avionics systems to be flight-tested have become more and more complex, and the accuracy required for their testing can only be achieved with instrumentation systems employing an inertial platform system. Finally a reference system for the aircraft attitude, heading, velocity and position requiring extreme accuracies is always centered around an INS, which is aided by external measurements (see Section 7.1 and Chapter 8).

A typical instrumentation system of this kind contains at present the inertial platform and three rate gyros. (The computation of the angular rates from the platform angles may not be sufficiently accurate because of the limited angle read-out accuracy, even if sophisticated mathematics like curve fitting is employed.) The measurement output list of this instrumentation system will contain the following parameters (air data must be provided by an air data computer):

Parameter	Typical Accuracy
Baro-inertial altitude	depending on air data accuracy
True airspeed	depending on air data accuracy
Ground speed	3 m/s
Latitude	1 nm per hour of flight time
Longitude	1 nm per hour of flight time
Wind direction	depending on air data accuracy
Wind speed	depending on air data accuracy
Track angle	0.5^{o}
Drift angle	0.5^{o}
North velocity	1 m/s
East velocity	1 m/s
Vertical velocity	1 m/s

Parameter	Typical Accuracy (continued)
North acceleration	10^{-3} g
East acceleration	10^{-3} g
Vertical acceleration	10^{-3} g
True heading	20 arc min
Pitch	6 arc min
Roll	6 arc min
Yaw rate	0.1 % of full scale
Pitch rate	0.1 % of full scale
Roll rate	0.1 % of full scale

If the platform is not located at the aircraft center of gravity, these data must be corrected for accelerations and velocities induced by aircraft rotations around its center of gravity. The calculation of the flight path can then be performed. Using additional air speed measurements, the angles of attack and sideslip can be calculated. With these data, aerodynamic and performance data can be computed and converted from an earth-referenced coordinate system to the aircraft body axes - using the platform angles - and to flight path axes - using the angles of attack, sideslip and the flight path angle.

The use of redundant information from other sources (e.g. Doppler Radar, VOR/DME, DME/DME, etc.) in combination with the INS, using the hybrid techniques described in Chapter 8 or just mere update methods, can considerably improve the accuracies in the above table. Examples of such applications in aircraft flight tests are [9.7] and [9.8]. In [9.7] the INS is aided using VOR/DME and barometric altitude measurements; in [9.8], the INS-updates are obtained from points of standstill of the aircraft on the ground and from knowledge of the runway profile during the ground run of the aircraft.

9.4 Examples of Modern Instrumentation Systems

In this Section three examples of modern instrumentation systems are discussed. These systems employ an inertial platform system together with rate gyros, body-mounted accelerometers and air data sensors to obtain performance and aerodynamic data in dynamic flight tests. The application of these instrumentation systems involves the two main factors which have influenced the design of flight test instrumentation during the last decades: Dynamic manoeuvers are flown, and complex mathematical tools are employed to extract aircraft parameters - unobservable in steady-state flights - from the measured data. So the requirements for the gyroscopic sensors are very stringent.

9.4.1 DyMoTech Instrumentation System

DyMoTech (Dynamic Modeling Technology) is a program [9.3] which was undertaken by the US Air Force at the Air Force Flight Test Center (AFFTC) at Edwards Air Force Base. The objective of DyMoTech is to develop dynamic flight test techniques and the necessary modeling techniques for the identification of the performance characteristics of aircraft. The test aircraft is the F-4C.

The locations of the transducers used in the DyMoTech instrumentation system are shown in the Figure 9.15a. Figure 9.15b shows a block diagram of this system. Several sensor packages are mounted on the airplane.

1. The Noseboom Instrumentation Unit (NBIU), with Sundstrand Q-flex accelerometers, which comprise the flight path accelerometer (FPA).
2. An air data system with 20 bit Garrett digital quartz pressure transducers.
3. Two sets of body-mounted accelerometers mounted in the nose and tail sections of the fuselage to determine body bending as well as longitudinal acceleration at the center of gravity.
4. An LTN-51 inertial navigation system with the usual output of position, velocity and angles. The platform was modified to obtain acceleration and gimbal angles directly. The vertical channel is aided by pressure altitude (see Chapter 8).
5. A high accuracy three-axis rate gyro package to measure the angular rates. An angular accelerometer for pitch acceleration.
6. Engine instrumentation and sensors for the aerodynamic control surface movements.

The accelerometer outputs are sampled at sixty samples per second as are the angles of attack and sideslip, the rate gyros and the angular accelerometer. The aerodynamic surface positions are sampled at thirty samples per second and the engine parameters at five samples per second. The INS data are also output at five samples per second. For highly dynamic maneuvers the INS accelerations, velocities and angles might be required at a higher rate.

The DyMoTech program was started in 1974 and the F-4C test aircraft was instrumented in 1978. The instrumentation is obviously redundant, so that different methods for extracting the flight path acceleration simultaneously from separate measurement systems can be compared in flight. The instrumentation has the required high accuracy to obtain the aircraft performance data from dynamic flight maneuvers.

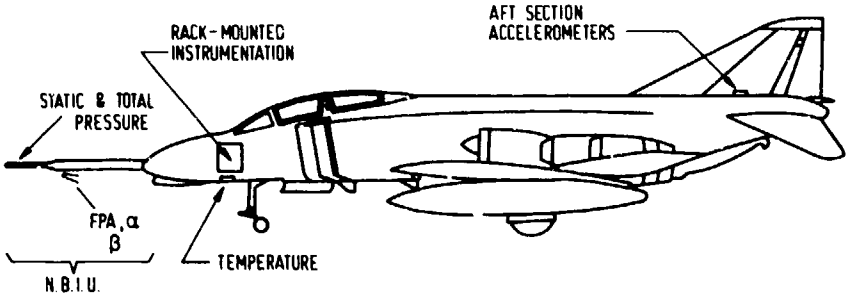

Figure 9.15a: DyMoTech Instrumentation System

Rack mounted instrumentation includes:
- o INS (LTN-51)
- o Rate gyro package
- o Angular accelerometer
- o FWD section accelerometer

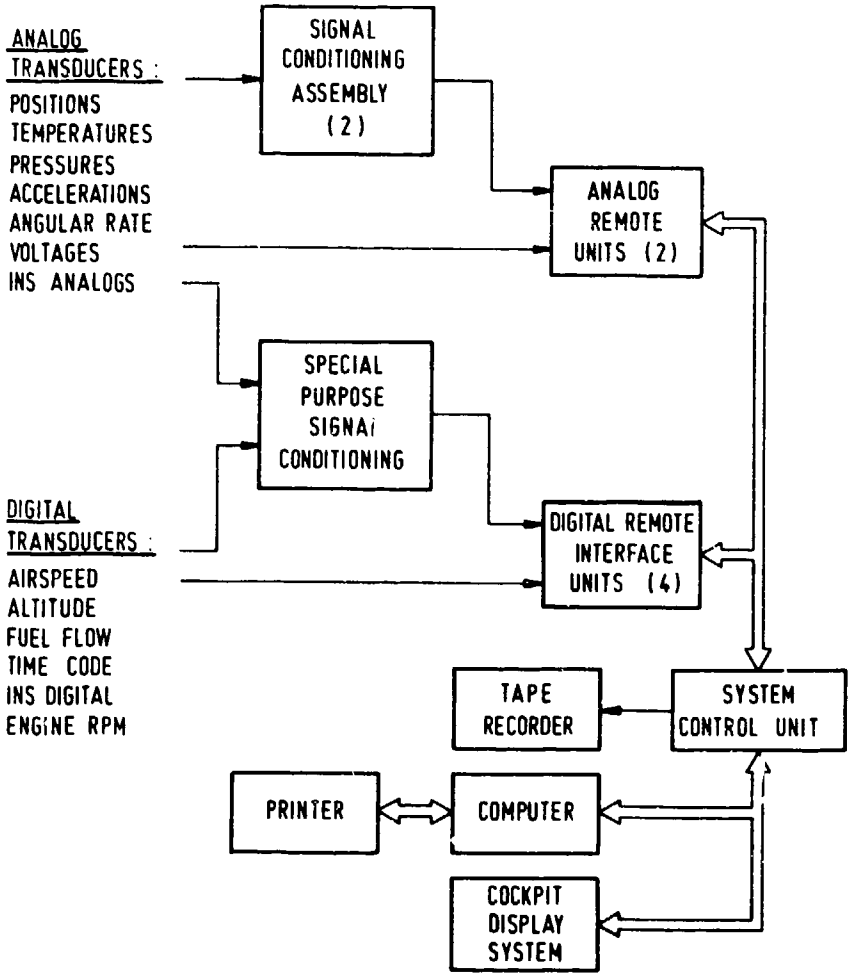

Fig. 9.15b Block diagram of the DyMoTech Instrumentation System

9.4.2 Instrumentation for Dynamic Testing at the National Aerospace Laboratory (NLR)

A different system for dynamic testing has been developed and flight-tested by the Delft University of Technology and the National Aerospace Laboratory (NLR) in the Netherlands [9.4]. This equipment has been flight-tested and improved in different airplanes since 1967 (DHC-2 Beaver, Hawker Hunter MK VII and Fokker F28 Fellowship). The purpose of these flight tests was to study the influence of

- the aircraft input signal (dynamic maneuvers),
- the instrumentation system, and
- the data analysis technique

on the accuracy of the aircraft parameter determination from a single dynamic maneuver [9.5] and [9.6]. As an example of this measuring technology, the instrumentation system developed by the NLR for the Fokker F28 Fellowship will be considered. This instrumentation system is shown in Figure 9.16a. Figure 9.16b shows a block diagram of this system. It consists of

1 Inertial Measurement and Conditioning System (IMAC)
1 Air Data Measurement System (DRUM)
4 Flight Data Acquisition Units (FDAU) (to measure engine parameters, control surface deflections, etc.)
1 Litton LTN-58 Inertial Sensor System (ISS)
1 Avionics Data Acquisition System (CADAS)
and a tape recorder for data storage.

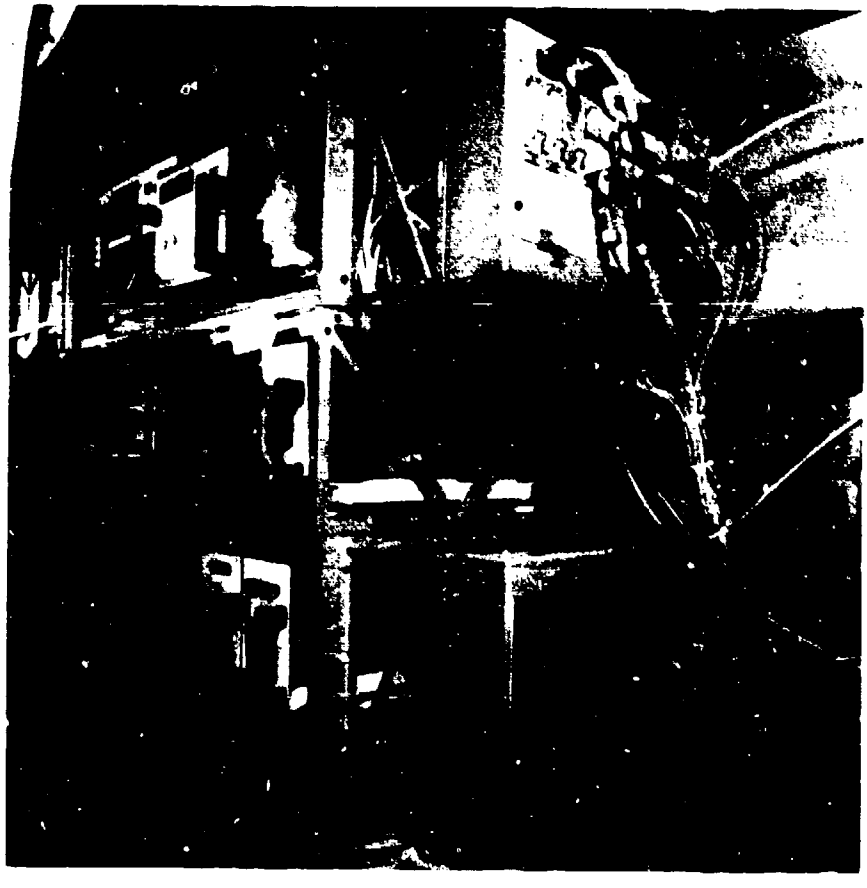

Fig. 9.16a NLR Instrumentation System for the F28 Aircraft

The IMAC contains three accelerometers (SAGEM 10625 A) and three rate gyroscopes (Honeywell DGG87B7) in a temperature controlled environment. The alignment accuracy of the sensor axes with respect to the aircraft axes is in the order of 0.01 degrees. The IMAC is mounted near the center of gravity of the airplane in order to eliminate the effect of elastic deformation of the aircraft on the measurement. The output signals are synchronized to within 1 ms. The six output channels are sampled at a rate of 64 samples per second, and converted from analog to digital using 16 bit A/D converters. Static accuracies of 10^{-4} g and 10^{-3} degrees/second are reached with these sensors. The measurement range is $\pm$ 10 degrees/second and $\pm$ 2.5 g.

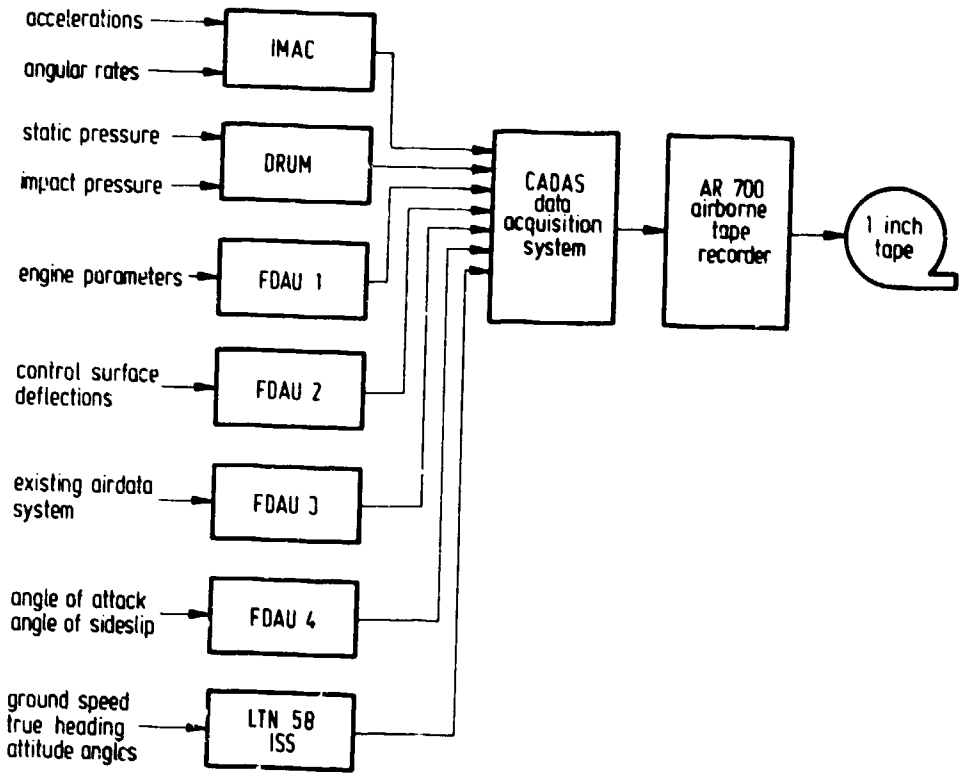

Fig. 9.16b Block Diagram of the NLR Instrumentation System

The DRUM system contains pressure transducers for static pressure, for impact pressure and for change of static pressure since the start of the maneuver (static pressure minus pressure in a flask closed at that moment). The static accuracies are 50, 10 and 1 Pa, respectively. Static pressure is obtained from a trailing cone with a time constant of 1 to 2 seconds, which can be estimated with an accuracy of about 5 %.

Data from IMAC and DRUM are processed in a Kalman filter/smoother, which provides an accurate estimate of the state vector during the maneuver: three air velocity components, three attitude angles and altitude. The Kalman filter assumes that the wind speed and direction are constant during the maneuver. This assumption can be checked later by a comparison of the calculated air velocities with the ground velocities measured by the LTN-58.

From the state vector the angles of attack and sideslip can be calculated with an accuracy of 0.05 degrees. Further calculations can provide lift and drag coefficients and stability derivatives.

9.4.3 Integrated Instrumentation System Used at DFVLR

The DFVLR is operating the twin-jet HFB 320 (see Figure 8.3.10) at Braunschweig as an experimental aircraft for research projects in the fields of guidance and control and flight mechanics. This aircraft has a digital electrohydraulic control system (fly-by-wire system) and a complex flight control unit for fully automatic control of the aircraft movements. The aircraft is used for flight tests of

- digital integrated flight control systems
- integrated navigation systems
- new operational procedures (steep approaches, 4D-command control, flight procedures with an MLS, etc.)
- improved handling qualities through digital control (direct lift control)
- methods for aircraft state and parameter identification in dynamic flight conditions.

The aircraft is equipped with an instrumentation system (Figures 8.3.11 and 9.17a) containing the inertial transducers

1 Vertical gyro (Sperry VG3007)
1 Directional gyro (Sperry C12, s. Section 6.2)
3 Rate gyros (Honeywell GG1111)
3 Accelerometers (Systron Donner 4311A)
1 Inertial platform (Litton LN3-2A).

The sensor package with VG, DG rate gyros and accelerometers is shown in Figure 9.17a. Figure 9.17b shows a block diagram of the DFVLR instrumentation system.

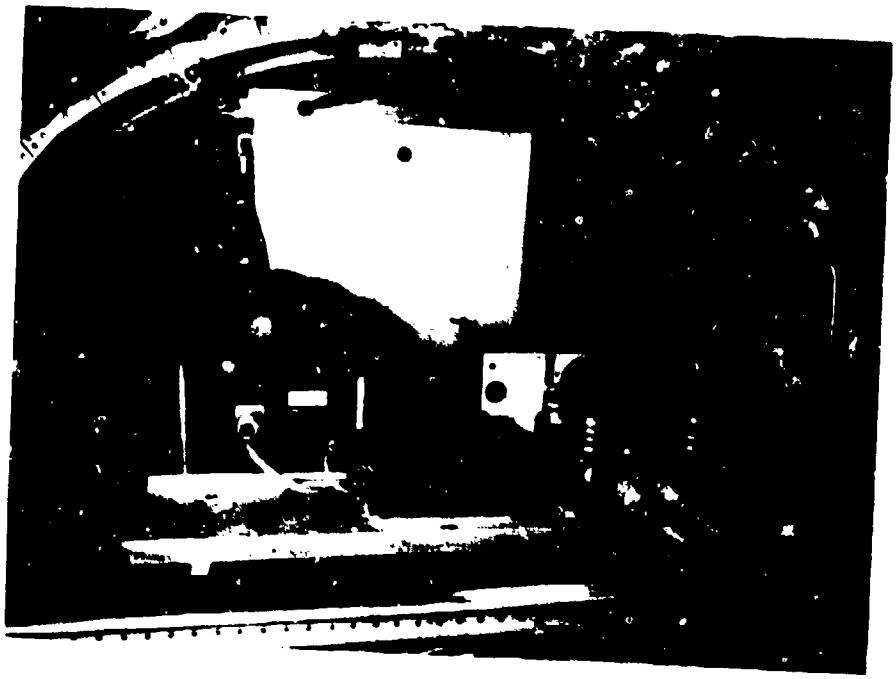

Fig. 9.17a Sensor Packages of the DFVLR Instrumentation System
- o VG and DG (left and right)
- o Rate gyros (back, right)
- o Accelerometers (front, middle)

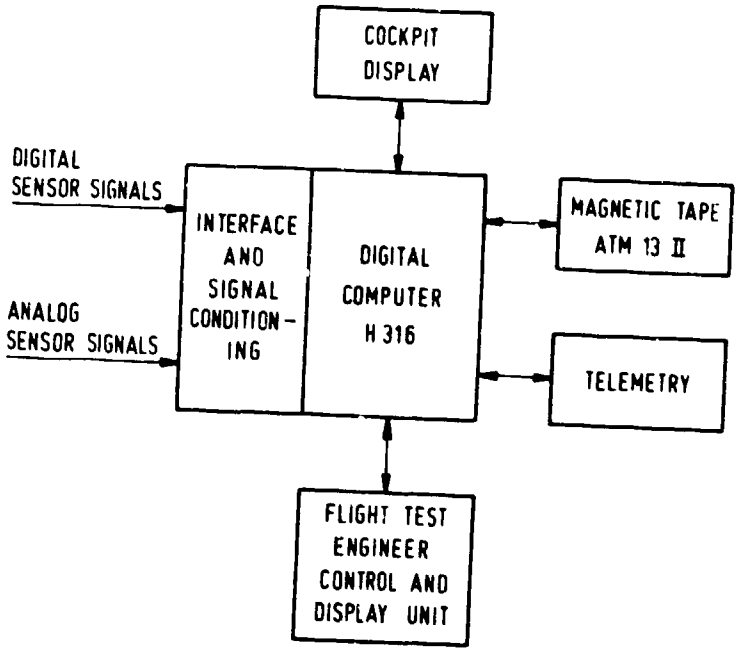

Fig. 9.17b Block diagram of the DFVLR Instrumentation System

The inertial transducers provide the following outputs:

- angular rates
- accelerations in the body axes
- attitude and heading from VG and DG and INS
- accelerations in earth-referenced axes from the INS (east, north, vertical)
- ground speed components
- position data (longitude and latitude).

The accuracies of these measurements are shown in the following table:

Parameter		Accuracy
Angular rates		0.5 - 0.8 % of full scale
Body acceleration		0.2 % of full scale
Attitude (VG)		0.5^0 unaccelerated flight
Heading (VG)		0.25 - 0.5^0 (free or slaved to compass)
	attitude	0.1^0
	heading	0.3^0
INS	acceleration	better than 0.1 % of full scale
	velocity	3 m/s (unaided)
	position	2 nm (unaided)

The (analog) navigation computations of the LN3-2A platform have been replaced by a digital algorithm in the on-board computer, including the capability of aiding the INS by external (radio) sensors, like VOR/DME, multiple DME or Doppler radar. In this aided mode the data provided by the platform are improved (see Chapter 8) corresponding to the accuracy of the external sensors.

9.5 Future Trends

The introduction of Control Configured Vehicle (CCV) technology in military and civilian aircraft will intensify the tendency to more sophisticated integrated instrumentation systems. Future aircraft will contain complex digital guidance and control and avionics systems, the flight testing of which will increase the requirements for accuracy and dynamic performance of the transducers to be used. Flight testing of these aircraft under dynamic conditions and the application of advanced mathematical methods to obtain the aircraft parameters and their derivatives with high precision and for a minimum of flight test time will promote the introduction of inertial navigation systems (platform and especially strapdown systems) as flight test instruments

When the strapdown systems (Section 7.4.4) have reached the same state of maturity as the platform systems of today they will become the ideal inertial instrumentation system for flight test use. These systems provide the complete set of inertial information which is of interest to the flight test engineer

- the angular rates,
- the aircraft angles,
- the linear accelerations,
- the ground velocities, and
- the aircraft position (the flight path).

These data are well synchronized and of high accuracy, and contain frequencies up to 5 or 10 Hz (see Table 7.7.1b). For flutter measurements in the very high frequency range, linear and angular accelerometers and rate gyros will still be used.

For very high required accuracies in the low frequency range the strapdown systems can be velocity or position aided (see Chapter 8) by means of external sensors, like Doppler radars, radio navigation systems, tracking radars, etc. In these hybrid systems, the complete set of inertial information is improved with respect to accuracy.

With the introduction of laser gyros for the new generation of transport aircraft (A310, B767), these sensors will also become mature for applications in flight testing. The laser gyros tend to eliminate the disadvantage of mechanical gyros - their sensitivity to vibrations. Strapdown systems (attitude and heading reference systems and navigation systems) with laser gyros will then find their application in the flight testing of aircraft.

References for Chapter 9

[9.1] A. Pool and D. Bosman, Ed. — Basic Principles of Flight Test Instrumentation Engineering. AGARDograph No. 160, Volume 1, 1974.

[9.2] James N. Olhausen — The Use of a Navigation Platform for Performance Instrumentation of the YF-16 Flight Programm. AIAA Aerospace Meeting, Pasadena, California, January 1975.

[9.3] L.P. Plews — Use of an Inertial Navigation System as Airborne Instruments for Performance Flight Testing. Tenth Transducer Workshop, Range Commander Council, Colorado Springs, Colorado, June 1979.

[9.4] J.H. Breeman and J.L. Simons — Evaluation of a Method to Extract Performance Data from Dynamic Manoeuvers for a Jet Transport Aircraft. 11th Congress of the International Council of Aeronautical Sciences, Lisboa, Sept. 1978.

[9.5] O.H. Gerlach — The Determination of Stability Derivatives and Performance Characteristics from Dynamic Manoeuvers. AGARD CP No. 85, 1971 (VTH-163),

[9.6] J.J. Horsten, H.L. Jonkers and J.A. Mulder — Flight Path Reconstruction in the Context of Nonsteady Flight Testing. Proc. of the AGARD-Cranfielf Short Course on Flight Test Instrumentation, May 1979.

[9.7] V. Adam and R. Onken — Evaluation of a New Flight Path Command Control Concept. Proc. of the Tenth Congress of the International Council of the Aeronautical Science (ICAS), October 1976.

[9.8] A. Pool, J.L. Simons, G.J.H. Wensink and A.J.L. Willekens — A Method for Measuring Take-Off and Landing Performance of Aircraft Using an Inertial Sensing System. NLR Report MP 800 36 U (also published in AGARD CP 299), October 1980.

REPORT DOCUMENTATION PAGE

1. Recipient's Reference	2. Originator's Reference	3. Further Reference	4. Security Classification of Document
	AGARD-AG-160 Volume 15	ISBN 92-835-1433-5	UNCLASSIFIED

5. Originator Advisory Group for Aerospace Research and Development
North Atlantic Treaty Organization
7 rue Ancelle, 92200 Neuilly sur Seine, France

6. Title GYROSCOPIC INSTRUMENTS AND THEIR APPLICATION TO FLIGHT TESTING

7. Presented at

8. Author(s)/Editor(s)	9. Date
B.Stieler and H.Winter	September 1982

10. Author's/Editor's Address	11. Pages
	216

12. Distribution Statement This document is distributed in accordance with AGARD policies and regulations, which are outlined on the Outside Back Covers of all AGARD publications.

13. Keywords/Descriptors

Flight tests
Test equipment
Flight instruments
Gyroscopes
Gyrostabilizers
Accelerometers
Inertial navigation

14. Abstract

This AGARDograph is the 15th of the AGARD Flight Test Instrumentation Series and discusses gyroscopic instruments and their application to flight testing. Gyroscopic instruments are used in flight tests to measure the aircraft angular accelerations and rates, attitude and heading and – in combination with accelerometers – the linear acceleration, the ground velocity and the position. This volume describes the measuring principles, the technical lay-out and the error behaviour of the sensors and systems used for these measurements: gyroscopes, accelerometers, attitude and heading references and inertial navigation systems. Attention is also given to integrated and hybrid sensor systems, as they are in use in modern instrumentation systems. Examples of actual flight instrumentation systems are described and the requirements for the gyroscopic sensors in these systems are discussed for applications in aircraft stability and control flight tests, in performance tests and in airborne and ground systems calibration and testing.

This AGARDograph has been sponsored by the Flight Mechanics Panel of AGARD.

and the position. This volume describes the measuring principles, the technical lay-out and the error behaviour of the sensors and systems used for these measurements: gyroscopes, accelerometers, attitude and heading references and inertial navigation systems. Attention is also given to integrated and hybrid sensor systems, as they are in use in modern instrumentation systems. Examples of actual flight instrumentation systems are described and the requirements for the gyroscopic sensors in these systems are discussed for applications in aircraft stability and control flight tests, in performance tests and in airborne and ground systems calibration and testing.

This AGARDograph has been sponsored by the Flight Mechanics Panel of AGARD.

ISBN 92-835-1433-5

and the position. This volume describes the measuring principles, the technical lay-out and the error behaviour of the sensors and systems used for these measurements: gyroscopes, accelerometers, attitude and heading references and inertial navigation systems. Attention is also given to integrated and hybrid sensor systems, as they are in use in modern instrumentation systems. Examples of actual flight instrumentation systems are described and the requirements for the gyroscopic sensors in these systems are discussed for applications in aircraft stability and control flight tests, in performance tests and in airborne and ground systems calibration and testing.

This AGARDograph has been sponsored by the Flight Mechanics Panel of AGARD.

ISBN 92-835-1433-5

and the position. This volume describes the measuring principles, the technical lay-out and the error behaviour of the sensors and systems used for these measurements: gyroscopes, accelerometers, attitude and heading references and inertial navigation systems. Attention is also given to integrated and hybrid sensor systems, as they are in use in modern instrumentation systems. Examples of actual flight instrumentation systems are described and the requirements for the gyroscopic sensors in these systems are discussed for applications in aircraft stability and control flight tests, in performance tests and in airborne and ground systems calibration and testing.

This AGARDograph has been sponsored by the Flight Mechanics Panel of AGARD.

ISBN 92-835-1433-5

and the position. This volume describes the measuring principles, the technical lay-out and the error behaviour of the sensors and systems used for these measurements: gyroscopes, accelerometers, attitude and heading references and inertial navigation systems. Attention is also given to integrated and hybrid sensor systems, as they are in use in modern instrumentation systems. Examples of actual flight instrumentation systems are described and the requirements for the gyroscopic sensors in these systems are discussed for applications in aircraft stability and control flight tests, in performance tests and in airborne and ground systems calibration and testing.

This AGARDograph has been sponsored by the Flight Mechanics Panel of AGARD.

ISBN 92-835-1433-5

AGARDograph No.160 – Volume 15
Advisory Group for Aerospace Research and Development, NATO
GYROSCOPIC INSTRUMENTS AND THEIR APPLICATION TO FLIGHT TESTING
by B.Stieler and H.Winter
Published September 1982
216 pages

This AGARDograph is the 15th of the AGARD Flight Test Instrumentation Series and discusses gyroscopic instruments and their application to flight testing. Gyroscopic instruments are used in flight tests to measure the aircraft angular accelerations and rates, attitude and heading and – in combination with accelerometers – the linear acceleration, the ground velocity

P.T.O.

AGARD-AG-160 Vol.15

Flight tests
Test equipment
Flight instruments
Gyroscopes
Gyrostabilizers
Accelerometers
Inertial navigation

AGARDograph No.160 – Volume 15
Advisory Group for Aerospace Research and Development, NATO
GYROSCOPIC INSTRUMENTS AND THEIR APPLICATION TO FLIGHT TESTING
by B.Stieler and H.Winter
Published September 1982
216 pages

This AGARDograph is the 15th of the AGARD Flight Test Instrumentation Series and discusses gyroscopic instruments and their application to flight testing. Gyroscopic instruments are used in flight tests to measure the aircraft angular accelerations and rates, attitude and heading and – in combination with accelerometers – the linear acceleration, the ground velocity

P.T.O.

AGARD-AG-160 Vol.15

Flight tests
Test equipment
Flight instruments
Gyroscopes
Gyrostabilizers
Accelerometers
Inertial navigation

AGARDograph No.160 – Volume 15
Advisory Group for Aerospace Research and Development, NATO
GYROSCOPIC INSTRUMENTS AND THEIR APPLICATION TO FLIGHT TESTING
by B.Stieler and H.Winter
Published September 1982
216 pages

This AGARDograph is the 15th of the AGARD Flight Test Instrumentation Series and discusses gyroscopic instruments and their application to flight testing. Gyroscopic instruments are used in flight tests to measure the aircraft angular accelerations and rates, attitude and heading and – in combination with accelerometers – the linear acceleration, the ground velocity

P.T.O.

AGARD-AG-160 Vol.15

Flight tests
Test equipment
Flight instruments
Gyroscopes
Gyrostabilizers
Accelerometers
Inertial navigation

AGARDograph No.160 – Volume 15
Advisory Group for Aerospace Research and Development, NATO
GYROSCOPIC INSTRUMENTS AND THEIR APPLICATION TO FLIGHT TESTING
by B.Stieler and H.Winter
Published September 1982
216 pages

This AGARDograph is the 15th of the AGARD Flight Test Instrumentation Series and discusses gyroscopic instruments and their application to flight testing. Gyroscopic instruments are used in flight tests to measure the aircraft angular accelerations and rates, attitude and heading and – in combination with accelerometers – the linear acceleration, the ground velocity

P.T.O.

AGARD-AG-160 Vol.15

Flight tests
Test equipment
Flight instruments
Gyroscopes
Gyrostabilizers
Accelerometers
Inertial navigation

B145
4

AGARD

NATO OTAN

7 RUE ANCELLE · 92200 NEUILLY-SUR-SEINE

FRANCE

Telephone 745.08.10 · Telex 610176

DISTRIBUTION OF UNCLASSIFIED AGARD PUBLICATIONS

AGARD does NOT hold stocks of AGARD publications at the above address for general distribution. Initial distribution of AGARD publications is made to AGARD Member Nations through the following National Distribution Centres. Further copies are sometimes available from these Centres, but if not may be purchased in Microfiche or Photocopy form from the Purchase Agencies listed below.

NATIONAL DISTRIBUTION CENTRES

BELGIUM
Coordonnateur AGARD – VSL
Etat-Major de la Force Aérienne
Quartier Reine Elisabeth
Rue d'Evere, 1140 Bruxelles

CANADA
Defence Science Information Services
Department of National Defence
Ottawa, Ontario K1A 0K2

DENMARK
Danish Defence Research Board
Østerbrogades Kaserne
Copenhagen Ø

FRANCE
O.N.E.R.A. (Direction)
29 Avenue de la Division Leclerc
92320 Châtillon sous Bagneux

GERMANY
Fachinformationszentrum Energie,
Physik, Mathematik GmbH
Kernforschungszentrum
D-7514 Eggenstein-Leopoldshafen 2

GREECE
Hellenic Air Force General Staff
Research and Development Directorate
Holargos, Athens

ICELAND
Director of Aviation
c/o Flugrad
Reykjavik

ITALY
Aeronautica Militare
Ufficio del Delegato Nazionale all'AGARD
3, Piazzale Adenauer
Rome/EUR

LUXEMBOURG
Sur Belgium

NETHERLANDS
Netherlands Delegation to AGARD
National Aerospace Laboratory, NLR
P.O. Box 126
2600 A.C. Delft

NORWAY
Norwegian Defence Research Establishment
Main Library
P.O. Box 25
N-2007 Kjeller

PORTUGAL
Direcção do Serviço de Material
da Força Aérea
Rua da Escola Politécnica 42
Lisboa
Attn: AGARD National Delegate

TURKEY
Department of Research and Development (ARGE)
Ministry of National Defence, Ankara

UNITED KINGDOM
Defence Research Information Centre
Station Square House
St. Mary Cray
Orpington, Kent BR5 3RE

UNITED STATES
National Aeronautics and Space Administration (NASA)
Langley Field, Virginia 23365
Attn: Report Distribution and Storage Unit

THE UNITED STATES NATIONAL DISTRIBUTION CENTRE (NASA) DOES NOT HOLD STOCKS OF AGARD PUBLICATIONS, AND APPLICATIONS FOR COPIES SHOULD BE MADE DIRECT TO THE NATIONAL TECHNICAL INFORMATION SERVICE (NTIS) AT THE ADDRESS BELOW.

PURCHASE AGENCIES

Microfiche or Photocopy
National Technical
Information Service (NTIS)
5285 Port Royal Road
Springfield
Virginia 22161, USA

Microfiche
Space Documentation Service
European Space Agency
10, rue Mario Nikis
75015 Paris, France

Microfiche or Photocopy
British Library Lending
Division
Boston Spa, Wetherby
West Yorkshire LS23 7BQ
England

Requests for microfiche or photocopies of AGARD documents should include the AGARD serial number, title, author or editor, and publication date. Requests to NTIS should include the NASA accession report number. Full ordering-which references and abstracts of AGARD publications are given in the following journals:

Scientific and Technical Aerospace Reports (STAR)
published by NASA Scientific and Technical
Information Facility
Post Office Box 8757
Baltimore/Washington International Airport
Maryland 21240, USA

Government Reports Announcements ( )
published by the National Technical
Information Service, Springfield
Virginia 22161, USA

Printed by Technical Editing and Reproduction Ltd
5-11 Bleeding Street, London W1N 7RH

ISBN 92-835-1431-5